AD NUMBER

AD846599

NEW LIMITATION CHANGE

TO

Approved for public release, distribution unlimited

FROM

Distribution authorized to U.S. Gov't. agencies and their contractors; Critical Technology; DEC 1968. Other requests shall be referred to Air Force Rocket Propulsion Laboratory, ATTN: RPPR/STINFO, Edwards AFB, CA 93523.

AUTHORITY

AFRPL ltr dtd 27 Oct 1971

AFRPL-TR-68-132
Rocketdyne No. R-4521

FRACTURE MECHANICS APPROACH TO CUMULATIVE DAMAGE

J. S. Noel
J. D. Burton
B. C. Harbert

FINAL REPORT
15 May 1967—19 August 1968
Contract No. F04611-67-C-0103

DECEMBER 1968

ROCKETDYNE
A DIVISION OF NORTH AMERICAN ROCKWELL CORPORATION
SOLID ROCKET DIVISION
McGREGOR, TEXAS

AFRPL-TR-68-132
Rocketdyne No. R-4521

FRACTURE MECHANICS APPROACH TO CUMULATIVE DAMAGE

J. S. Noel
J. D. Burton
B. C. Harbert

FINAL REPORT
15 May 1967—19 August 1968
Contract No. F04611-67-C-0103

DECEMBER 1968

ROCKETDYNE
A DIVISION OF NORTH AMERICAN ROCKWELL CORPORATION
SOLID ROCKET DIVISION
McGREGOR, TEXAS

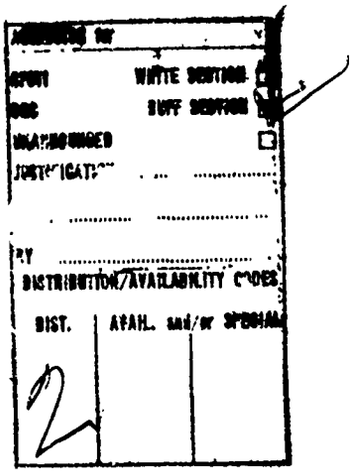

"When U.S. Government drawings, specifications, or other data are used for any purpose other than a definitely related Government procurement operation, the Government thereby incurs no responsibility nor any obligation whatsoever, and the fact that the Government may have formulated, furnished, or in any way supplied the said drawings, specifications, or other data, is not to be regarded by implication or otherwise, or in any manner licensing the holder or any other person or corporation, or conveying any rights or permission to manufacture, use, or sell any patented invention that may in any way be related thereto."

FOREWORD

This report documents the effort accomplished at Rocketdyne under Contract No. F04611-67-C-0103 for the period 15 May 1967 to 19 August 1968. The program was sponsored by the Air Force Rocket Propulsion Laboratory, Research and Technology Division, Edwards, California, Air Force Systems Command, United States Air Force. Air Force Project Engineers were Mr. Donald Saylak anc Captain Scott Beckwith.

The program to study the applicability of viscoelastic fracture equations to the problem of cumulative damage in solid rocket propellants was a portion of a broader study of cumulative damage in which the Air Force has sponsored several parallel approaches by separate contractors. It is expected that the reports, taken together, will provide new insight into the applicability and appropriateness of the several techniques. In addition to this program, Lockheed Propulsion Company investigated the volumetric response mechanisms of the propellant and have reported their work (as well as the propellant characterization data) in AFRPL-TR-68-130. Aerojet-General Corporation (Sacramento) investigated various damage mechanisms using a linear cumulative damage approach. Their work is reported in AFRPL-TR-68-131.

The consulting services of Dr. M. L. Williams, University of Utah; Dr. P. J. Blatz, North American Rockwell Science Center; and Mr. W. B. Jones, also of the University of Utah, are gratefully achknowledged. Their intuitions and judgments, constrained by technical understanding gained after long experience with rocket propellants, have provided the ideas for the bulk of this program.

This technical report has been reviewed and is approved.

Donald Saylak (RPMCB)
Project Engineer

Scott W. Beckwith (RPMCB)
Captain, USAF
Project Engineer

ABSTRACT

This report documents a 12-month program conducted by Rocketdyne to study cumulative structural damage in solid rocket propellant. Tests conducted and experimental data obtained therefrom are described, and conclusions drawn from the study are presented. The theory of fracture in viscoelastic materials provides the analytical expressions for evaluating damage to propellant during loading histories comparable to those which might be experienced by rocket motor grains. Poker chip and biaxial strip tensile tests were used to simulate the states of stress typically occurring in actual motors. Simple constant rate tests were used to evaluate the constants necessary to apply the fracture equations to histories involving sequences of loadings.

Page iv is blank

CONTENTS

CONTENTS

(Continued)

FIGURES

TABLES

Page xii is blank

SECTION I

INTRODUCTION

This report describes the experimental work, the analytical calculations, and the resulting conclusions of the portion of the Cumulative Damage Study Program that was performed at Rocketdyne. The program was funded by the Air Force Rocket Propulsion Laboratory on Contract No. F04611-67-C-0103.

The program was designed specifically to test the applicability of the recently developed viscoelastic fracture techniques to the prediction of crack-type propellant failures following loading histories characteristically experienced by rocket motor grains. Such histories usually involve sequences of loadings, each differing from the other, until the motor either satisfactorily performs its mission or prematurely fails. Current failure analyses, however, are only valid following elementary loadings such as constant loads or constant loading rates or constant amplitude and frequency vibrations. The customary procedure is to select the dominant loading and analyze the structural capability of the grain following its application. Then, judgment is used to modify the solution to account for damages incurred by earlier loadings. It was felt that the viscoelastic fracture techniques might well provide an analytical vehicle for making engineering evaluations of the effect of the earlier loadings.

Accordingly, the experimental test phase of this program was oriented to evaluate this technique. It should be noted, however, that all test results showing sensitivity to damage accumulation are invaluable for the study of the applicability of any analysis procedure and consequently, are reported in descriptive detail.

SUMMARY OF THE THEORY

A theory of fracture applicable to linear viscoelastic materials has been formulated by Williams and his coworkers (1, 2, 3).* The approach utilizes an energy balance as originally proposed and demonstrated by Griffith (4) for brittle fracture in elastic materials.

Griffith postulated that fracture always originates at defects or flaws which exist throughout real materials. This explanation readily accounted for the fact that glass and similar brittle crystalline materials always fail at stresses much smaller than those known to be necessary

*Numbers in parentheses, i.e., (1, 2, 3), refer to the tabulated references on page 235.

to rupture the interatomic or intermolecular bonds. He was successful in showing that the rupture stress in glass increased in proportion to the inverse of the existing flaw size.

Griffith's approach utilized a mathematical solution derived by Inglis (5) for the stresses and strain energy in an initially cracked thin plate. The initial flaw located at the center of an infinite plate was assumed to be elliptically shaped but with the major axis taken to be very long in comparison with the minor axis, giving the effect of a line crack. This specimen is illustrated in Fig. 1.

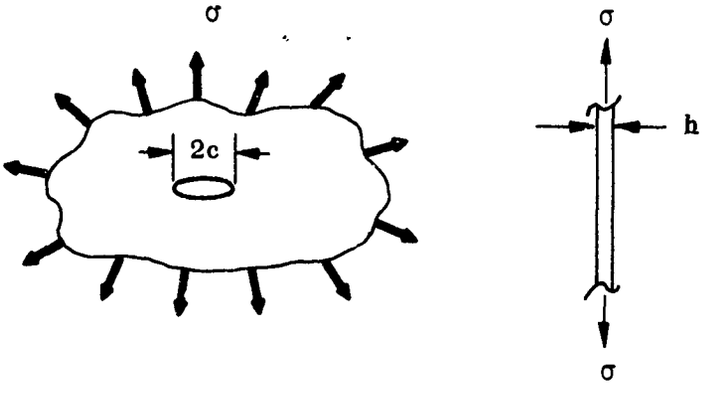

Figure 1. An Infinite Tensile Specimen With An Initial Elliptically Shaped Crack

According to Griffith's plane stress analysis, fracture will occur if and when

$$\frac{d}{dA}(V + A\gamma) = 0 \qquad (1)$$

where V is the potential energy of the system (see (6, p 382) for a definition of potential energy), A is the free surface area of the specimen which increases as the crack grows, and γ is the free surface energy per unit of new surface area. The form taken by the terms of Eq. 1 depend upon the boundary conditions. For the important case where the applied

stress, σ, (some distance away from the crack) is held constant and the crack length is 2c

$$\frac{d}{dc}\left[\left(-\frac{\sigma^2 \pi c^2}{E} + 4\gamma c\right)\right] \leq 0 \qquad (2)$$

Here the first term reflects the lowering of the strain energy due to the increase in the crack length while the second reflects the increase in surface energy due to the increase in the free surface area. A plot which schematically shows these two terms is given in Fig. 2. When the derivative is evaluated, one finds the most common and well known form of the Griffith criterion

$$\sigma_{cr} = \sqrt{\frac{4E\gamma}{\pi (2c)}} \qquad (3)$$

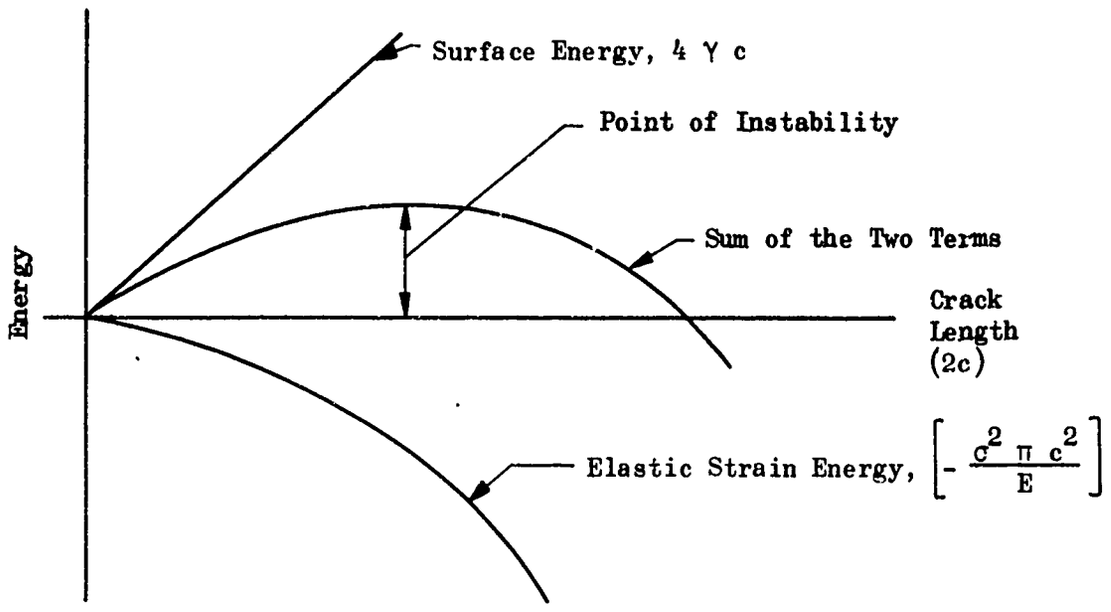

Figure 2. Energy Criterion For a Plate With a Crack of Length 2c

The suggestion that the energy balance equations might prove valuable for predicting the onset of fracture in elastomeric materials has been studied and tested extensively. A brief survey of the monograph edited by Rosen (7) on the subject reveals the extent of the variety and success of these explorations.

During the 1950's, exploratory efforts to apply the energy balance approach to amorphous polymers were pioneered by Rivlin and Thomas (8). Their studies clearly indicated the existence of a characteristic energy for the initiation of crack growth defined (just as in Eq. 1) as:

$$-\frac{\partial F}{\partial A}(c)\Big|_u = \gamma \qquad (4)$$

where F is the total stored strain energy and the subscript u indicates that the derivative is evaluated with the boundary displacements held constant. But, taking the lead established by Irwin and Orowan (9, 10), Rivlin and Thomas emphasized the point that γ must not, for these materials, necessarily be interpreted as a free surface energy.

Later Greensmith and Thomas (11) hypothesized, as a result of extensive experimentation, that the characteristic tearing energy depended strongly upon both the temperature and the time rate associated with the straining history. However, constant moduli (in time) were used in the calculations supporting this conclusion.

The generalization of the energy balance concept to the prediction of crack type failures in viscoelastic materials is possible primarily because simplified flaw geometries are hypothesized. The assumption that the flaws are either spherical or cylindrical in shape, centered in a spherical or cylindrical body of incompressible material has been made to find a tractable expression for incipient flaw growth. Because of the time-dependent nature of the material properties, a balance of the time rate of change of the energy (power) rather than a simple energy balance is necessary. This balance leads to criticality expressions quite similar in nature to Eq. 3 except that viscoelastic material properties replace the constant Young's modulus. The form with which these time-varying properties enter the equation is dependent upon the loading history, which allows the balance theory to be used in evaluating cumulative damage. The time to failure following essentially any loading history, including sequences of completely different types of loadings (such as a step strain followed by a superposed vibratory load) can, therefore, be conveniently predicted.

The formulation of an energy balance criterion with expressions reflecting viscoelastic material properties is especially attractive because it provides the expressions necessary to evaluate the influence of the time or rate of loading, the order of loading, the material properties, the state of stress, and perhaps even temperature on crack initiation in a viscoelastic material. This unifying idea motivated the Rocketdyne approach to cumulative damage.

Derivations of the analytical expressions for criticality following practical loading histories are shown in Section II. Those used in this report are summarized. These criticality equations, pp 30 and 33 present the unified theory of failure for viscoelastic materials.

Dr. Paul Blatz of the North American Rockwell Science Center, has conducted supplementary research activity while serving as a consultant to this program. A portion of his efforts is reported in Appendix I. These studies have been directed toward determining the importance of finite strains relative to the interpretation of the fracture results, interpretation of the triaxial poker chip test data after the many growing internal flaws have effectively rendered the specimen into a sponge, and whether or not the fundamental assumptions on which the flaw growth expressions are based can be modified to improve or refine the resulting predictions.

As the applicability of a fracture theory is widened, either by providing a more fundamental basis or by experimentally extending the range, its value to the practicing stress analyst is likewise enhanced. So a fracture criterion capable of evaluating many if not all of the influences on the initiation of a propellant grain crack is a very important contribution to the rocket motor industry.

SUMMARY OF THE TESTING

The laboratory experimental investigations were designed specifically to test the applicability of the spherical and cylindrical flaw theories to the prediction of cracking in propellants. Those parameters which were believed to be the most influential were selected to vary as extensively as possible. The tests provided a wide variation in loading rates and times, the state of stress, and the various kinds of loadings, including temperature. The propellant utilized for the tests was the STV propellant furnished by Lockheed Propulsion Company. It was an 86.5% solids-loaded CTPB formulation typical of the state of the art. A summary of the testing program is presented in Table I.

The tests shown in the table fall into two categories: first, the single environment or elemental tests and, second, multiple environment tests. The elemental tests (conducted early in the program) were designed specifically to provide the data necessary for a numerical evaluation of the arbitrary constants required by the analytics. Following these experiments, multiple loading tests were conducted to check the feasibility of using the theory to predict cracking following practical loading histories. The consistencies between the various elemental tests also provided a check on the reliability and applicability of the energy balance expressions to propellant cracking.

TABLE I. SUMMARY OF TESTS

a. Triaxial Poker Chip Tests

Type Test Specimen	Type Test	Temperatures	No. of Tests	Purpose of Test
Triaxial 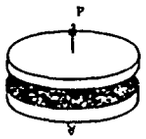	Constant Stress Rate $\dot{\sigma}_1$ (Fast Rate) 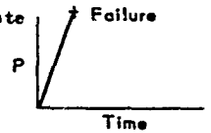	T_1 = 0 F	1	Generate data to determine theoretical constants for equations of theory under conditions of constant strain rate and temperature
		T_2 = 77 F	1	
		T_3 = 140 F	1	
	$\dot{\sigma}_2$ (Intermediate Rate) 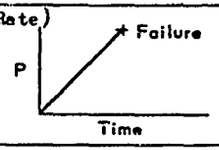	T_1 = 0 F	1	Determine statistical variability of propellant
		T_2 = 77 F	6	Evaluate individually the influence of strain rate and temperature
		T_3 = 140 F	2	
	$\dot{\sigma}_3$ (Slow Rate) 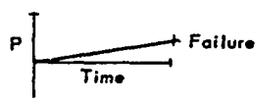	T_1 = 0 F	1	
		T_2 = 77 F	1	
		T_3 = 140 F	2	
Triaxial 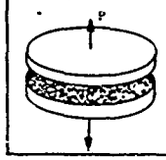	Bilinear Stress Rates to Failure 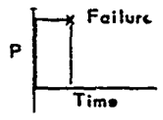	T = Constant = 77 F Conditions Load (P)		Instantaneous loads were applied and the time for the center load cell to indicate failure was noted
		600 lb	1	X-ray pictures of the internal flaw growth were taken during these tests
		750 lb	1	
		900 lb	1	

TABLE I. Continued

b. Static Biaxial Strip Tests

Type Test Specimen	Type Test	Temperatures	No. of Tests	Purpose of Test
Biaxial  This group of constant rate tests to failure was performed by Lockheed by using their 7.5- X 1.5-inch specimen	$\dot{\epsilon}_1$, (X-head Rate = 0.01 in./min)	T_1 = -100 F T_2 = -65 F T_3 = -40 F T_4 = 0 F T_5 = 40 F T_6 = 77 F T_7 = 100 F T_8 = 150 F T_9 = 200 F	One at each temp	Generate data to determine theoretical constants for the energy balance expressions under conditions of constant strain rate and temperature
	$\dot{\epsilon}_2$, (X-head Rate = 0.1 in./min)		One at each temp	Evaluate individually the influence of strain rate and temperature
	$\dot{\epsilon}_3$, (X-head Rate = 1.0 in./min)		One at each temp	
	$\dot{\epsilon}_4$, (X-head Rate = 10 in./min)		One at each temp	
Biaxial 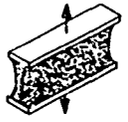	Bilinear Strain Rates to Failure 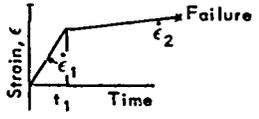	T = Constant = 140 F Conditions 0.6 in./in./min to 2.98 X 10^{-4} in./in./min 0.000294 in./in./min to 2.76 in./in. min	2	Determine applicability of theories for prediction of failure following a sequence of two constant strain rates on a biaxial specimen
Biaxial 	Constant Strain Rate $\dot{\epsilon}$ = Constant 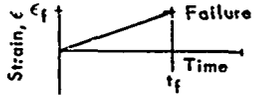	Variable with Time $\dot{T}$ = Constant = 3F/hr 70 to -80 F 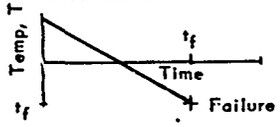	2	Prediction of failure for series of constant strain rate tests in which specimen temperature is varied as function of time, thus simulating history of propellants on inner bore of motor during cooldown to failure. The value of the strain rate can be related to the web fraction of the simulated motor

TABLE I. Continued

c. Oscillatory Biaxial Strip Tests

Type Test Specimen	Type Test	Temperature	Conditions			Purpose of Test
Biaxial (Fatigue) 	Constant Strain at Constant Frequencies of Mechanical Fatigue Testing ϵ_{max} = Constant; ω = Constant 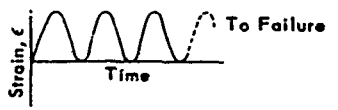	T = Constant = 140 F	cps	Max. Strain	No. of Tests	Generate data to determine constants in equations for time to failure under various levels of maximum strain at fixed frequency fatigue testing. Specimen surface temperature held constant.
			5	6% 7 8	6 5 3	
			15	6 7 8	3 4 3	
			47	6 7 8	4 2 3	
			Total 33			
Biaxial (Fatigue) 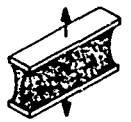	Constant Load at Constant Frequencies of Mechanical Fatigue Testing Load (max) = Constant; ω = Constant 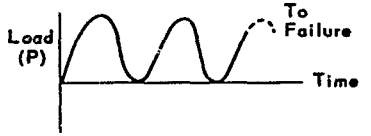	T = Constant = 140 F	cps	P_{max}, lb	No. of Tests	Same as above
			5	200 235 270	1 1 1	
			15	200 235 270	1 1 1	
			47	200 235	1 1	
			Total 8			
Biaxial (Fatigue) 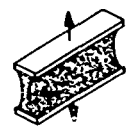	Dual Frequency to Failure Under Constant Maximum Strain $\omega = \omega_1$ $0 < t < t_1$ $\omega = \omega_2$ $t_1 < t$ ϵ_{max} = Constant 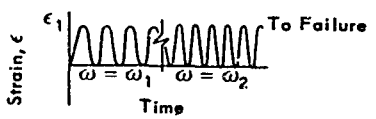	T = Constant = 140 F	cps	Strain	No. of Tests	Prediction of failure for biaxial specimen subjected to mechanical cycling following a history with two different strain amplitudes
			5 to 47	8%	4	
			47 to 5	8	1	
			Total 5			
Biaxial (Fatigue) 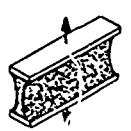	Dual Strain Levels to Failure at Constant Frequency ω = Constant 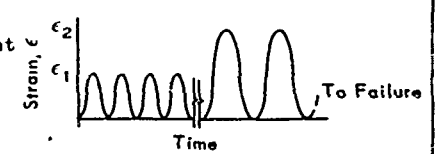	T = Constant = 140 F	cps	Strain	No. of Tests	Prediction of failure for biaxial specimen subjected to constant amplitude strain cycling but with a sequence of two different frequencies
			5	6--8% 8--6	3 3	
			47	6--8 8--6	1 1	
			Total 8			

TABLE I. Concluded

d. Hilzinger's Microphotography

Type Test Specimen	Type Test	Temperatures	No. of Tests	Purpose of Test
Hollow Cylinder (Machined Surface) 0.8-Inch OD 1/8-Inch Wall 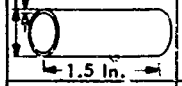	Internal Pressurization to Failure at Constant Rate 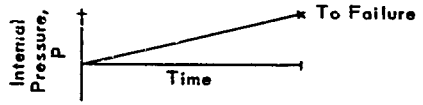	77 F	4	Microphotos of actual particle-to-binder dewetting in biaxial stress field typical of constant strain rate tests
Hollow Cylinder (Machined Surface) 0.5-Inch OD 1/8-Inch Wall 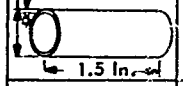	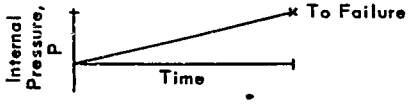	77 F	1	Microphotos of dewetting on a machined surface for direct comparison with the microphotos of a cast surface on the like specimens described below
Hollow Cylinder (Cast Surface) 0.5-Inch OD 1/8-Inch Wall 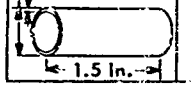	Internal Pressurization to Failure at Constant Rate 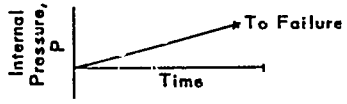	77 F	4	Specimens cast using the Saylak tensile specimen mold Microphotos of a cast surface during straining and cracking failure

The triaxial tests of the program which are most applicable to the evaluation of the spherical flaw portion of the theory were conducted using the poker chip specimens. These circular thin flat specimens, bonded between two platens, were pulled at constant crosshead rates in Instron machines. Load cells were installed at the center of one platen in each test and were used to monitor the center bond stresses.

As shown in Table I, 16 of these tests were conducted, some at an intermediate crosshead rate and room temperature and others across a spectrum of rates and temperatures. Forces, platen displacements, and center load cell outputs were recorded during all of the tests. The center load cell output provided a sensitive measure of the time of failure during the tests. In addition to the constant stress rate tests of the poker chip, three constant load tests of the poker chip specimens were also conducted. These three tests represent multiple environmental conditions in that they essentially had the load applied instantaneously and then held constant for the duration of the test. This provided a limiting case of a bilinear stress rate type loading history. A significant amount of time elapsed from the time the load was applied until failure occurred. It was possible to X-ray the cross section (X-ray exposures take up to 5 minutes on the poker chip) to observe the internal mechanisms. These X-rays were most informative; they enabled a sound technical explanation of the constant load test results. In addition, they provided insight into the meaning of the center load cell readings during constant stress rate tests.

Because cracks usually originate in the center ports of rocket grains and because these center ports are frequently in essentially the same state of stress as the biaxial strip tensile specimen, major attention was given to tests of this nature. Constant rate tests of biaxial strip specimens were run during the propellant characterization by Lockheed. The data from these tests, both failure stress and failure strains, were used as elemental tests in the Rocketdyne program.

In addition, vibration fatigue tests with both displacement- and force-specified boundaries were conducted using the new Cumulative Damage tester at Rocketdyne. This testing machine provided the capability of imposing sinusoidal platen displacements on the biaxial strip specimen. The capability of pre-programming any required thermal history (-75 to 250 F) was provided with an environmental box surrounding the specimen. Other testing capabilities of the machine included bi-linear rates (strain or stress), combinations of fatigue tests involving different frequencies or different amplitudes, and the very practical test involving simultaneous changes in strains and temperatures. As shown in Table I, most of these capabilities were exploited on the program.

A sequence of four tests involving small, hollow propellant cylinders were performed by Hilzinger at Rocketdyne Research (Canoga Park). Photomicrographs showing the behavior of binder and failure during these constant pressure rate tests were taken. Close-up movies were also made. These pictures provided a basic understanding of the propellant behavior before and during the actual fracturing processes.

Appendix II summarizes work performed by J. E. Hilzinger. He was able to capture on film the initiation and propagation of cracks in the STV propellant following a constant stress rate loading history. The specimens used for these studies were small, hollow cylinders subjected to internal pressurization. Perhaps the most significant finding was the basic difference in the behavior of the specimens with cast surfaces from that of specimens with machined surfaces.

Page 12 is blank

SECTION II

THEORY OF VISCOELASTIC FRACTURE

Until about 1960, the primary contribution to the study of failure in amorphous viscoelastic media (e.g., polymers) was the work of Rivlin and Thomas (8) which extended the Griffith fracture hypothesis (see Section I) to the rupture of rubber. The rupture (or tearing) was shown to result from strain energy being released at a greater rate than it can be transferred into surface free energy or other dissipative mechanisms. Their results showed the change in strain energy, F, with respect to the area of a cut in a thin sheet, A, computed with fixed displacement over the boundary where forces are prescribed is given by

$$(\partial F/\partial A)\Big|_u = \gamma \qquad (5)$$

where γ is the characteristic energy of tearing. Although the form of the result is similar to Griffith's criterion, γ includes other dissipative mechanisms than surface free energy. In particular, at long-time rubbery and short-term glassy conditions, surface energy effects will be predominant. In the transition region, a significant amount of dissipation and resultant heat flow will absorb the energy. These phenomena qualitatively agree with the observations of Greensmith and Thomas (11) that the characteristic tearing energy is strongly dependent on the tearing rate and temperature.

In a review article (1) in 1963, Williams related the findings to date to include evaluation of the effects of load and crack tip geometry at fracture initiation, the prediction of crack acceleration and stable propagation, and the results observed in triaxial stress fields. Further, he discussed an approach to cumulative damage based on superposition analogous to Miner's hypothesis for fatigue or vibration in metals.

Williams later proposed (2) a qualitative expression of the Griffith critical stress formulation as

$$\sigma_{crit} = k\sqrt{(E/2c)\,(\gamma_b + \gamma_d + \gamma_v + \ldots} \qquad (6)$$

where E is the material modulus; ℓ, the crack length; and the subscripts b, d, v, . . . stand for the brittle, ductile, and viscoelastic dissipative processes, respectively. Pursuing the application of the thermodynamic theory of fracture presented earlier (1), equations of criticality were established for general conditions of loading and specimen geometry. The following development of criticality formulas is based on this approach.

THE ENERGY APPROACH TO FAILURE

The elemental nature of the Griffith approach to failure is intrinsically attractive since it overcomes the indeterminancy of the infinite strain-stress state at the crack tip (i.e., an infinitesimal area). Of further benefit is the fact that energy is a scalar quantity and may be summed directly as in Eq. 6. Considering the case of the viscoelastic material and neglecting kinetic energy, which will be small for slow velocities of crack propagation, one has

$$\dot{I} = \dot{F} + 2D + \dot{SE} \tag{7}$$

where $\dot{I}$ is the rate at which work is being done on the body (power input), $\dot{F}$ is the rate of increase of strain energy, 2D is the viscous dissipation (work converted to heat), and $\dot{SE}$ is the rate of increase of the surface energy.

Neglecting work done by the body forces, and assuming a volume constant body of volume τ and surface S, (6)

$$\frac{d}{dt}(I) = \int_{S_\sigma + S_\epsilon} \overset{\nu}{T}_i \dot{u}_i \, ds \tag{8}$$

where $\overset{\nu}{T}_i$ are the surface forces prescribed over the surface S_σ and the u_i are the displacements prescribed over the remaining surface S_ϵ.

$$\frac{d}{dt}(\dot{SE}) = \frac{d}{dt} \int_S \gamma ds \tag{9}$$

where γ is the characteristic tearing energy. Finally, due to the viscoelastic nature of the material, the remainder of the power input, typically denoted as free energy must be accounted for in terms of elastic strain energy and viscous dissipation. Thus

$$\frac{d}{dt}(F) = \frac{d}{dt} \int_\tau \int_0^t \sigma_i \dot{\epsilon}_i dt d\tau - 2D \tag{10}$$

where F is the stored strain energy and $\int_\tau \int_0^t \sigma_i \dot{\epsilon}_i dt d\tau$ is the volume integral of the strain energy density. Using this formulation of the energy approach, it is now pertinent to inquire into the conditions for which $\dot{I}$ exceeds $\dot{F}$ + 2D and resulting flaw growth occurs.

ELASTIC ANALYSIS FOR VISCOELASTIC MEDIA

The problem of analytical determination of the stress-strain state in even a simple geometry is complicated by the time-temperature dependence of the material properties when the material is of a viscoelastic nature. Historically, two approaches to the solution of viscoelastic problems are available. A thorough discussion of the representation of the material properties is presented in (12). Of interest here for subsequent application is the analogy between viscoelastic and elastic response.

In principle, with zero initial conditions, the Laplace or Fourier time-transformed linear viscoelastic field equations and boundary conditions are equivalent with the equations of an elastic body with the same geometry. This analogy, essential to the pursuit of viscoelastic stress analysis, was expressed by Lee (13) for isotropic materials and Biot (14) for anisotropic materials. Of special importance to the application of this concept are the requirements for linear viscoelasticity, special stress distribution independent of material properties, and separation of space and time dependence of prescribed loads and displacements. By way of illustration, take the case of an elastic uniaxial specimen loaded at constant rate of displacement

$$\frac{\sigma}{\epsilon} = E \tag{11}$$

Now, consider a constant strain test of a viscoelastic uniaxial specimen

$$\sigma_{rel}(t) = E_{rel}(t)\ \epsilon_o \tag{12}$$

Applying the Laplace transform,

$$\overline{\sigma_{rel}}(p) = \overline{E_{rel}}(p)\ \overline{\epsilon}_o \tag{13}$$

or

$$\frac{\overline{\sigma_{rel}}(p)}{\overline{\epsilon}_{rel}} = \overline{E_{rel}}(p) = \frac{p\bar{\sigma}(p)}{\epsilon_o} \tag{14}$$

Next, consider the constant strain rate test (Rate = R) on the viscoelastic specimen. The ratio of the transform of the strain input to that for the constant strain test is

$$\frac{\bar{\epsilon}_{tens}}{\bar{\epsilon}_{rel}} = \frac{\frac{R}{p^2}}{\frac{\epsilon_o}{p}} = \frac{R}{\epsilon_o p} \tag{15}$$

From the thermodynamic considerations of linear viscoelastic materials (15) one obtains

$$\frac{\bar{\sigma}_{tens}}{\bar{\sigma}_{rel}} = \frac{\bar{\epsilon}_{tens}}{\bar{\epsilon}_{rel}} = \frac{R}{\epsilon_o p}$$

or

$$\frac{\bar{\sigma}_{rel}}{\bar{\epsilon}_o} = \overline{E_{rel}}(p) = \frac{p\bar{\sigma}_{tens}}{R} \tag{16}$$

which may be written as

$$\bar{\sigma}_{tens}(p) = \overline{E_{rel}}(p)\,\frac{R}{p} = \bar{E}_{rel}(p)\; p\; \bar{\epsilon}(p) \tag{17}$$

which is the transform of the viscoelastic stress response to the constant strain rate input. To complete the solution,

$$\begin{aligned} \sigma(t) &= L^{-1}\left\{\bar{\sigma}(p)\right\} = L^{-1}\left\{p\overline{E_{rel}}(p)\;\bar{\epsilon}(p)\right\} \\ &= L^{-1}\left\{\overline{E_{rel}}(p)\cdot\frac{\dot{\epsilon}}{p}\right\} \\ &= E_{rel}(t) * \frac{d\epsilon}{dt} = \int_o^t E_{rel}(t-\tau)\,\frac{d\epsilon}{d\tau}\,d\tau \end{aligned} \tag{18}$$

It is worthwhile to note that the elastic analysis is valid to the point of obtaining a transformed solution. The final step, inversion of the transformed solution to the real-time plane, is generally not directly available and must be accomplished through approximate methods as described in (16). In the present analysis, direct inverse transformation is adequate.

A final area of note in the treatment of viscoelastic materials is that of time-temperature interdependence. From qualitative consideration of the molecular behavior of amorphous polymers (17), it is possible to infer an equivalence relation on the time-temperature mode of material response. From empirical information obtained from the reduction of relaxation data, Tobolsky, (18) suggested that those data could be adequately represented by

$$\frac{\log E_{rel}(t) - \log E_e}{\log E_g - \log E_e} = \frac{1}{2}\left[1 - \operatorname{erf}\left(h \log \frac{t}{K(T)}\right)\right] \qquad (19)$$

where K (T) is the value of f(T) at which the reduced time parameter, t/f (T) equals unity and h is $\frac{\text{standard deviation}}{\sqrt{2}}$. Plotting K (T) against T revealed an inflection point at the temperature T_D, usually about 10 F above the glass transition temperature. A useful approximation of Tobolsky's result is given by

$$\log \frac{K(T)}{K(T_D)} = \frac{-16\ (T - T_o)}{100 + T - T_D} \qquad (20)$$

for T in degrees Farenheit. A different representation was given by Williams, Landel and Ferry (19) which resulted in placing the glassy relaxation behavior near the unit reduced time $t/a_T = 1$. Subsequent trends in application have shown that it is desirable to determine the shift factor a_T such that $a_T = 1$ occurs at 77 F, the point at which most laboratory data are obtained. The form of the equivalence remains

$$\log a_T = \frac{-C_1\ (T - T_s)}{C_2 + (T - T_s)} \qquad (21)$$

where T_s is the temperature at which $a_T = 1$. Using Eq. 21 it is possible to handle temperature dependency as a time function in viscoelastic analysis.

VISCOELASTIC FRACTURE ANALYSIS

Equipped with the energy concept and the elastic-viscoelastic xy (and keeping in mind the limitations and assumptions) the analysis fracture initiation in viscoelastic bodies will now be considered. this point, the analysis will be further limited to infinitesimal . n theory.

Three principal geometries of interest are illustrated in Fig. 3. The spherical flaw subjected to uniform loading at infinity is at once a simple geometry for analysis as well as one of practical interest in the analysis of void growth in triaxial stress fields. The cylindrical flaw geometries in both plane strain and plane stress fields are analogous to rocket motor geometries as well as laboratory test specimens. The subsequent derivations follow the methods reported in (2 and 20).

STRESS BOUNDARIES

Consider a long, circular cylinder with a concentric circular flaw. The material is incompressible, linearly viscoelastic, and will respond with infinitesimal strain to the prescribed loadings and, $\epsilon_z = 0$.

For a boundary condition specified by $\sigma(b,t) = \sigma_o f(t)$ one has

$$u(b,t) = \frac{3}{2} \frac{\sigma_o f(t)}{bE\left[\frac{1}{a^2} - \frac{1}{b^2}\right]} \tag{22}$$

Since

$$r\,u(r,t) = b\,u(b,t)$$

$$u(r,t) = \frac{3}{2} \frac{\sigma_o f(t)}{rE\left[\frac{1}{a^2} - \frac{1}{b^2}\right]} \tag{23}$$

From elastic theory,

$$\sigma_r(r,t) = \frac{2E}{3} \frac{u(b,t)}{a^2}\, b \left[1 - \frac{a^2}{r^2}\right] \tag{24}$$

a. Spherical Flaw Geometry

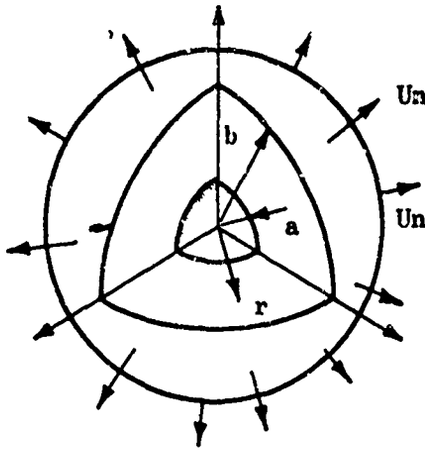

Uniform Boundary Stress, σ_o f(t)

or

Uniform Boundary Displacement, u_o g(t)

b. Cylindrical Flaw Geometry; Plane Strain

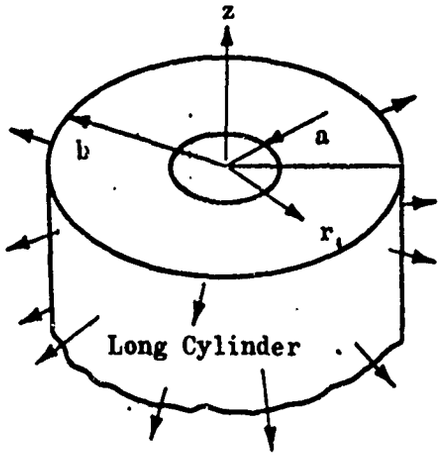

Uniform Boundary Stress, σ_o f(t)

or

Uniform Boundary Displacement, u_o g(t)

c. Cylindrical Flaw Geometry; Plane Stress

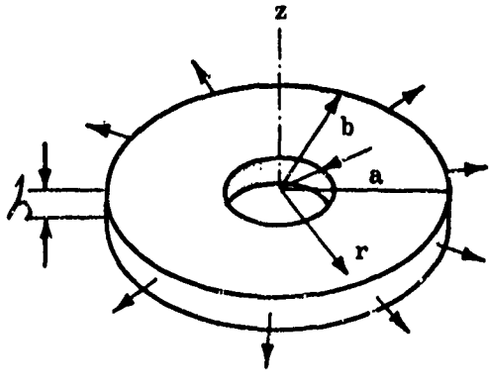

Uniform Boundary Stress, σ_o f(t)

or

Uniform Boundary Displacement, u_o g(t)

Figure 3. Initial Flaw Geometrics

and

$$\sigma_\theta(r,t) = \frac{2E}{3} \frac{u(b,t)}{a^2} b \left[1 + \frac{a^2}{r^2}\right] \tag{25}$$

or in terms of the prescribed stress

$$\sigma_r(r,t) = \sigma_o f(t) \frac{1 - \frac{a^2}{r^2}}{1 - \frac{a^2}{b^2}} \tag{26}$$

and

$$\sigma_\theta(r,t) = \sigma_o f(t) \frac{1 + \frac{a^2}{r^2}}{1 - \frac{a^2}{b^2}} \tag{27}$$

The strains are given by

$$\begin{aligned} \epsilon_r &= \frac{3}{2} \frac{\sigma_o f(t)}{(1 - \frac{a^2}{b^2})} D \left[-\frac{a^2}{r^2}\right] \\ &= \frac{3}{4} D \left[\sigma_r(r,t) - \sigma_\theta(r,t)\right] \end{aligned} \tag{28}$$

and

$$\begin{aligned} \epsilon_\theta &= \frac{3}{2} \frac{\sigma_o f(t)}{(1 - \frac{a^2}{b^2})} D\left[\frac{a^2}{r^2}\right] \\ &= \frac{3}{4} D \left[\sigma_\theta(r,t) - \sigma_r(r,t)\right] = -\epsilon_r \end{aligned} \tag{29}$$

where D is the elastic compliance.

Further defining

$$\left[\frac{a(t)}{a_o}\right]^2 = \alpha;\ k = \frac{a_o}{b}\ ;\ R(t) = -\frac{3}{2}\ \frac{\alpha a_o^2 f(t)}{1 - \alpha k^2} \tag{30}$$

one has

$$\sigma_r - \sigma_\theta = \frac{4\sigma_o}{3r^2}\ R(t) \tag{31}$$

From Eq. 7 and considering geometry and boundary conditions we note that

$$\dot{I} = 2\pi b\ \sigma_r(b,t)\ \dot{u}\ (b,t) \tag{32}$$

$$\dot{F} + 2\dot{D} = \frac{d}{dt}\int_a^b \int_o^t 2Q\pi r\ dtdr \tag{33}$$

where Q = stored strain energy per unit volume or

$$Q = \sigma_r \dot{\epsilon}_r + \sigma_\theta \dot{\epsilon}_\theta + \sigma_z \dot{\epsilon}_z \tag{34}$$

and

$$\dot{SE} = 2\pi \dot{a}\gamma \tag{35}$$

Thus, for an elastic body, Eq. 7 becomes

$$0 = \dot{a}\gamma + \frac{d}{dt}\int_{a(t)}^b \int_o^t Qr\ dtdr - b\sigma_r(b,t)\ \dot{u}\ (b,t) \tag{36}$$

To facilitate the solution of Eq. 36 for the viscoelastic body, we employ the Laplace transform analogy so that

$$\bar{\sigma}_r(p) - \bar{\sigma}_\theta(p) = \frac{4\sigma_o}{3r^2}\ \bar{R}\ (p) \tag{37}$$

and

$$\bar{\epsilon}_r(p) = -\bar{\epsilon}_\theta(p) = \frac{\sigma_o}{r^2}\, p\, \bar{D}_{crp}(p)\, \bar{R}(p) \tag{38}$$

likewise

$$\bar{u}(b,p) = -\frac{\sigma_o}{b}\, p\, \bar{D}_{crp}(p)\, \bar{R}(p) \tag{39}$$

so

$$\frac{1}{p}\bar{\bar{Q}}(p) = (\bar{\sigma}_r(p) - \sigma_\theta(p))\, \bar{\epsilon}_r(p) \tag{40}$$

$$= \frac{4\sigma_o^2}{3r^4}\, p\, \bar{D}_{crp}(p)\, \bar{R}(p)^2 \tag{41}$$

For obtaining the inverse transform

$$\frac{1}{p}\bar{\bar{Q}}(p) = \frac{4\sigma_o^2}{3r^4} \left\{ \bar{\bar{R}}(p) \left[p\, \bar{D}(p)\, \bar{R}(p) \right] \right\}$$

and

$$\int_o^t Q(\cdot) = \frac{4\sigma_o^2}{3r^4} \int_o^t R(t) \frac{\partial}{\partial \xi} \left[D_g R(\xi) + \int_o^\xi \frac{\partial D(\xi - \tau)}{\partial \tau} R(\tau)\, d\tau \right] d\xi \tag{42}$$

Then, the total stored energy per unit length is

$$\int_{a(\cdot)}^{b} \int_o^t Q\, dt\, 2\pi r\, dr$$

$$= \frac{4\pi\sigma_o^2}{3} \left[\frac{1}{b^2} - \frac{1}{a^2} \right] \int_o^t R(\xi) \frac{\partial}{\partial \xi} \left[D_g R(\xi) + \int_o^\xi \frac{\partial D_{crp}(\xi - \tau)}{\partial(\xi - \tau)} R(\tau)\, d\tau \right] d\xi \tag{43}$$

And differentiating with respect to time,

$$\dot{\gamma} + 2\dot{D} = \frac{4\pi\sigma_o^2}{3}\left\{-\frac{2\dot{a}}{a^3}\int_o^t R(\xi)\frac{\partial}{\partial\xi}\left[D_g R(\xi) + \int_o^\xi \frac{\partial D_{crp}(\xi-\tau)}{\partial(\xi-\tau)} R(\tau)\,d\tau\right]d\xi + \left[\frac{1}{b^2}-\frac{1}{a^2}\right]R(t)\frac{\partial}{\partial t}\left[D_g R(t) + \int_o^t \frac{\partial D_{crp}(t-\tau)}{\partial(t-\tau)} R(\tau)\,d\tau\right]dt\right\} \tag{44}$$

Similarly, for the power input, Eq. 32 gives

$$p\,\bar{I}(p) = -2\pi\sigma_o^2\left[p\,\bar{f}(p)\,\bar{D}_{crp}(p)\,\bar{R}(p)\right] \tag{45}$$

and inverting

$$\dot{I} = 2\pi\sigma_o^2 f(t)\frac{\partial}{\partial t}\left[D_g R(t) + \int_o^t \frac{\partial D_{crp}(t-\tau)}{\partial(t-\tau)} R(\tau)\,d\tau\right] \tag{46}$$

which exactly equals the second term in Eq. 44.

Combining Eq. 44, 46, and 35,

$$0 = \dot{a}\left\{\gamma - \frac{4\sigma_o^2}{3a^3}\int_o^t R(\xi)\frac{\partial}{\partial\xi}\left[D_g R(\xi) + \int_o^\xi \frac{\partial D_{crp}(\xi-\tau)}{\partial(\xi-\tau)} R(\tau)\,d\tau\right]d\xi\right\} \tag{47}$$

Up to initiation of flaw growth, $\dot{a} = 0$. Thus, the condition of criticality is

$$\gamma = \frac{4\sigma_o^2}{3a^3}\int_o^t R(\xi)\frac{\partial}{\partial\xi}\left[D_g R(\xi) + \int_o^\xi \frac{\partial D_{crp}(\xi-\tau)}{\partial(\xi-\tau)} R(\tau)\,d\tau\right]d\xi \tag{48}$$

Further, since $\dot{a} = 0$, it is possible to simplify Eq. 48 to

$$\gamma = \left[\frac{1}{2}\,\frac{a}{(1-k^2)^2}\right] 2\sigma_o^2 \left\{\int_o^{t_o} f(\xi)\,\frac{\partial}{\partial\xi}\left[D_g\, f(\xi) + \int_o^{\xi} \frac{\partial D_{crp}(\xi-\tau)}{\partial(\xi-\tau)}\, f(\tau)\, d\tau\right] d\xi\right\} \quad (49)$$

or

$$\left[\frac{2}{3}(1-k^2)^2\right]\frac{\gamma}{a_o} = 2\sigma_o^2 \int_o^{t_o} f(\xi)\,\frac{\partial}{\partial\xi}\, L^{-1}\left\{p\,\bar{D}_{crp}(p)\,\bar{f}(p)\right\} d\xi \quad (50)$$

Equation 50 is especially useful in that it may be shown that the right side of the equation is independent of geometry (within the three cases being considered) and the term multiplying γ/a_o is a function only of the geometry. The use of the inverse transform notation will be shown to be practical when considering various prescribed loading functions.

For the plane stress cylindrical flaw problem, a process similar to that above yields

$$\left[\frac{1}{2}(1-k^2)^2\right]\frac{\gamma}{a_o} = 2\sigma_o^2 \int_o^{t_o} f(\xi)\,\frac{\partial}{\partial\xi}\, L^{-1}\left\{p\,\bar{D}_{crp}(p)\,\bar{f}(p)\right\} d\xi \quad (51)$$

while for the spherical flaw problem one has

$$\left[\frac{16}{9}(1-k^3)^2\right]\frac{\gamma}{a_o} = 2\sigma_o^2 \int_o^{t_o} f(\xi)\,\frac{\partial}{\partial\xi}\, L^{-1}\left\{p\,\bar{D}_{crp}(p)\,\bar{f}(p)\right\} d\xi \quad (52)$$

DISPLACEMENT BOUNDARIES

We will now follow a similar process to that described for the stress boundary to a plane strain cylinder with applied displacements at the boundaries.

As before,

$$u(r,t) = \frac{b}{r}\,u(b,t) = \frac{b}{r}\,u_o g(t) \quad (53)$$

with the strains

$$\epsilon_r(r,t) = -u_o g(t) \frac{b}{r^2} \tag{54}$$

and

$$\epsilon_\theta(r,t) = u_o g(t) \frac{b}{r^2} = -\epsilon_r(r,t) \tag{55}$$

The principal stress difference is given by

$$\begin{aligned} \sigma_r(r,t) - \sigma_\theta(r,t) &= -\frac{4u_o}{3a^2} E\, g(t)\, b \left[\frac{a^2}{r^2}\right] \\ &= -\left(\frac{4}{3}\right) u_o E\, g(t) \left[\frac{b}{r^2}\right] \end{aligned} \tag{56}$$

Utilization of the Laplace transform and the inversion to obtain Q results in

$$Q = \frac{4}{3} \frac{u_o^2 b^2}{r^4} \frac{\partial g(t)}{\partial t} \left[E_g\, g(t) + \int_o^t \frac{\partial E_{rel}\,(t-\tau)}{\partial (t-\tau)} g(\tau)\, d\tau \right] \tag{57}$$

and

$$\int_{a(t)}^{b} \int_o^t Q dt\, 2\pi r dr = \frac{4\pi u_o^2 b^2}{3} \left[\frac{1}{a^2(t)} - \frac{1}{b^2}\right] \int_o^t \frac{\partial g(\xi)}{\partial \xi} \left[E_g g(\xi) + \int_o^\xi \frac{\partial E\,(\xi-\tau)}{\partial(\xi-\tau)} g\,(\tau)\, d\tau \right] d\xi \tag{58}$$

Differentiating with respect to time,

$$\dot{F} + 2D = \frac{4\pi u_o^2 b^2}{3} \left\{ \frac{-2\dot{a}}{a^3} \int_o^t \frac{\partial g(\xi)}{\partial \xi} \left[E_g g(\xi) + \int_o^\xi \frac{\partial E(\xi-\tau)}{\partial(\xi-\tau)} g(\tau)\, d\tau \right] d\xi + \left[\frac{1}{a^2} - \frac{1}{b^2}\right] \frac{\partial g(t)}{\partial t} \left[E_g g(t) + \int_o^t \frac{\partial E(t-\tau)}{\partial(t-\tau)} g\,(\tau)\, d\tau \right] \right\} \tag{59}$$

The rate of energy input,

$$\dot{I} = 2\pi b\sigma_r(b,t)\,\dot{u}\,(b,t) = \frac{4\pi b^2 u_o^2}{3}\left[\frac{1}{a^2} - \frac{1}{b^2}\right]\frac{\partial g(t)}{\partial t}\left\{E_g g(t) + \int_o^t \frac{\partial E(t-\tau)}{\partial(t-\tau)}\, g(\tau)\, d\tau\right\} \tag{60}$$

which again is equal to the second term of Eq. 59.

And finally,

$$\dot{SE} = 2\pi a\dot{a}\gamma \tag{61}$$

Substituting into the power balance equation,

$$0 = \dot{a}\left\{\gamma - \frac{4u_o^2 b^2}{3a^3}\int_o^{\xi} \frac{\partial g(\xi)}{\partial \xi}\left[E_g g(\xi) + \int_o^{\xi} \frac{\partial E_{rel}(\xi-\tau)}{\partial(\xi-\tau)}\, g(\tau)\, d\tau\right] d\xi\right\} \tag{62}$$

As before, up to flaw growth $\dot{a} = 0$ and the condition for criticality may be expressed as

$$\left[\frac{\pi}{2}k^4\right]\frac{\gamma}{a_o} = 2\left(\frac{u_o}{b}\right)^2 \int_o^t \frac{\partial g(\xi)}{\partial \xi}\left[E_g g(\xi) + \int_o^{\xi} \frac{\partial E_{rel}(\xi-\tau)}{\partial(\xi-\tau)}\, g(\tau)\, d\tau\right] d\xi \tag{63}$$

The right side of Eq. 63 is independent of the geometry whereas the multiplier of γ/a_o is entirely a function of geometry. Following the methods above one may deduce for the plane stress cylindrical flaw

$$\left[\frac{1}{2}(1-k^2)^2\right]\frac{\gamma}{a_o} = 2\left(\frac{u_o}{b}\right)^2 \int_o^t \frac{\partial g(\xi)}{\partial \xi}\left[E_g g(\xi) + \int_o^{\xi} \frac{\partial E_{rel}(\xi-\tau)}{\partial(\xi-\tau)}\, d\tau\right] d\xi \tag{64}$$

and for the spherical flaw

$$\left[\frac{4}{3}(1-k^3)\right]^2\frac{\gamma}{a_o} = 2\left(\frac{u_o}{b}\right)^2 \int_o^t \frac{\partial g(\xi)}{\partial \xi}\left[E_g g(\xi) + \int_o^{\xi} \frac{\partial E_{rel}(\xi-\tau)}{\partial(\xi-\tau)}\, d\tau\right] d\xi \tag{65}$$

Utilizing the expression for stress and displacement boundaries we will now consider the correlation of criticality for a variety of loading conditions.

CONDITIONS OF CRITICALITY FOR FLAW GROWTH

Stress Boundaries

Utilizing the expressions of Eq. 50 and 52, one may deduce the "energy" available for creation of surface for stress boundary loadings. It is necessary only to evaluate the right hand side of each expression to determine the "criticality" for all three geometries. In practice, it is necessary to determine the value of the "energy" as a function of time and infer the time to failure by intersecting the resultant curve with the left side of the expression for each geometry.

One case of special interest is that of the step input

$$\sigma(b,t) = \sigma_o \, 1(t) \tag{66}$$

From above, we wish to evaluate

$$2\sigma_o^2 \int_o^{to} f(\xi) \frac{\partial}{\partial \xi} \; L^{-1}\left\{ p \, \overline{D}\,(p) \, \overline{f}\,(p) \right\} \tag{67}$$

which is

$$\begin{aligned} &2\sigma_o^2 \int_o^{t_o} 1(\xi) \frac{\partial}{\partial \xi}\left[D_g \, 1(\xi) + \int_o^{\xi} \frac{\partial D_{crp}(\xi - \tau)}{\partial (\xi - \tau)} \, 1(\tau) \, d\tau \right] d\xi \\ &= 2\sigma_o^2 \int_o^{t_o} \frac{D_g}{2} \frac{\partial}{\partial \xi}\left[(\overline{1}(\xi))^2 \, d\xi + \int_o^{\xi} \frac{\partial D_{crp}(\tau)}{\partial \tau} 1(\xi - \tau) d\tau \right] d\xi \\ &= 2\sigma_o^2 \left[\frac{D_g}{2} + \int_o^{t_o} \frac{\partial D_{crp}(\xi)}{\partial \xi} d\xi \right] = 2\sigma_o^2 \left[\frac{D_g}{2} + D_{crp}(t_o) - D_g \right] \\ &= \sigma_o^2 \left[2D_{crp}(t_o) - \frac{D_g}{2} \right] \end{aligned} \tag{68}$$

Let us next consider a bilinear stress function

$$\sigma\,(b,t) = \begin{cases} \sigma_o C_1 t & , \; t < t_1 \\ \sigma_o \left[C_1 t + (C_2 - C_1)\,(t - t_1) \right] & , \; t \geq t_1 \end{cases} \tag{69}$$

From Eq. 67 we have

$$2\sigma_o^2 \left\{ f(\xi)\, L^{-1}\left\{ p\, \bar{D}_{crp}(p)\, \bar{f}(p) \right\} - \int_o^{t_o} L^{-1}\left\{ p\, \bar{D}_{crp}(p)\, \overline{f(p)} \right\} \frac{\partial f(\xi)}{\partial \xi}\, d\xi \right. \tag{70}$$

and for the loading, Eq. 69

$$L^{-1}\left\{ p\, D_{crp}(p) \left[\frac{c_1}{p^2} + \frac{c_2 - c_1}{p^2} e^{-t_1 p} \right] \right. \tag{71}$$
$$= c_1 \int_o^{\xi} D(\tau)d\tau + (c_2 - c_1) \int_{t_1}^{\xi} D(\tau - t_1)d\tau$$

and we obtain

$$\begin{aligned} 2\sigma_o^2 \Bigg\{ & c_1^2\, \xi \int_o^{\xi} D(\tau)d\tau \Big|_o^{t_1} - c_1^2 \int_o^{t_1} \int_o^{\xi} D(\tau)d\tau \\ & + \left[c_1 \xi + (c_2 - c_1)(\xi - t_1) \right] \left[c_1 \int_o^{\xi} D(\tau) + (c_2 - c_1) \int_{t_1}^{\xi} D(\tau - t_1)d\tau \right] \Big|_{t_1}^{t_o} \\ & - c_2 \int_{t_1}^{t_o} c_1 \int_o^{\xi} D(\tau)d\tau - c_2(c_2 - c_1) \int_{t_1}^{t_o} \int_{t_1}^{\xi} D(\tau - t_1)d\tau \Bigg\} \\ & - 2\sigma_o^2 \Big\{ \left[c_1 t_o + (c_2 - c_1)(t_o - t_1) \right] \left[c_1 D^{(1)}(t_o) + (c_2 - c_1) D^{(1)}(t_o - t_1) \right] \\ & - c_1 c_2 D^{(2)}(t_o) - c_1 (c_1 - c_2) D^{(2)}(t_1) - c_2 (c_2 - c_1) D^{(2)}(t_o - t_1) \Big\} \end{aligned} \tag{72}$$

where the $D^{(n)}(t_o - t_1)$ notation follows that demonstrated by Jones and others (21). For the simpler case of a ramp function,

$$\sigma(b,t) = \sigma_o ct \tag{73}$$

merely set $c_1 = c_2 = c$ in Eq. 72 and obtain

$$2\sigma_o^2 \left\{ c^2 t_o D^{(1)}(t_o) - c^2 D^{(2)}(t_o) \right\} \tag{74}$$

For a ramp-to-constant loading, typical of an approximation of a step loading in a real test, set $c_2 = 0$ in Eq. 72 with the result

$$2\sigma_o^2 \left\{ c_1^2 t_1 \left[D^{(1)}(t_o) - D^{(1)}(t_o - t_1) \right] - c_1^2 D^{(2)}(t_1) \right\} \tag{75}$$

where

$$\sigma(b,t) = \begin{cases} \sigma_o c_1 t, & t < t_1 \\ \sigma_o c_1 t_1, & t \geq t_1 \end{cases}$$

These results and those for other loadings of interest are summarized in Table II.

Displacement Boundaries

The evaluation methods used above are now to be applied to Eq. 63--65 for prescribed displacement boundaries. The equation of interest is

$$2\left(\frac{u_o}{b}\right)^2 \left\{ \int_o^t \frac{\partial g(\xi)}{\partial \xi} \left[E_g g(\xi) + \int_o^\xi \frac{\partial E_{rel}(\tau)}{\partial \tau} g(\xi - \tau) d\tau \right] d\xi \right\} \tag{76}$$

or in alternate notation

$$2\left(\frac{u_o}{b}\right)^2 \left\{ \int_o^t \frac{\partial g(\xi)}{\partial \xi} L^{-1} \left\{ p \overline{E_{rel}}(p) \bar{f}(p) \right\} d\xi \right. \tag{77}$$

Consider now the constant displacement boundary,

$$u(b,t) = u_o \, 1(t), \text{ i.e., } g(t) = 1 \tag{78}$$

which gives in Eq. 76

$$\begin{aligned} 2\left(\frac{u_o}{b}\right)^2 & \left\{ \int_o^t \frac{\partial g(\xi)}{\partial \xi} E_g g(\xi) \, d\xi + \int_o^t \frac{\partial g(\xi)}{\partial \xi} \int_o^\xi \frac{\partial E(\tau)}{\partial \tau} g(\xi - \tau) \, d\tau d\xi \right\} \\ & = 2\left(\frac{u_o}{b}\right)^2 \left\{ \frac{1}{2} E_g + \int_o^t \frac{\partial E(\tau)}{\partial \tau} d\tau - \int_o^t \frac{\partial}{\partial \xi} \int_o^\xi \frac{\partial E(\tau)}{\partial \tau} d\tau \right. \\ & = 2\left(\frac{u_o}{b}\right)^2 \left\{ \frac{1}{2} E_g + \left[E(t) - E_g \right] - \left[E(t) - E_g \right] = \left(\frac{u_o}{b}\right)^2 E_g \right. \end{aligned} \tag{79}$$

TABLE II. CRITICALITY CRITERIA FOR STRESS LOADINGS

Geometry	Spherical Flaw	Plane Strain Cylindrical Flaw	Plane Stress Cylindrical Flaw
Criticality Constant	$\left[\frac{4}{3}(1-k^3)\right]^2 (\gamma/a_o)$	$\frac{2}{3}(1-k^2)^2 (\gamma/a_o)$	$\frac{1}{2}(1-k^2)^2 (\gamma/a_o)$

Loading History	Criticality Variable for Failure at Time, t_o
Constant Stress $\sigma(\gamma,t) = \sigma_o 1(t)$ 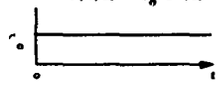	$\sigma_o^2 \left\{2D_{crp}(t_o) - D_g\right\}$
Bilinear Rate $\sigma(b,t) = \begin{cases} \sigma_o c_1 t & t < t_1 \\ \sigma_o\left[c_1 t + (c_2 - c_1)(t - t_1)\right] & t > t_1 \end{cases}$ 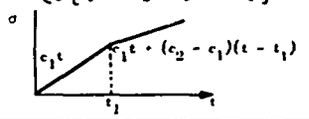	$2\sigma_o^2 \left\{\left[c_1 t_o + (c_2 - c_1)(t_o - t_1)\right]\left[c_1 D^{(1)}(t_o) + (c_2 - c_1)D^{(1)}(t_o - t_1)\right] - c_1 c_2 D^{(2)}(t_o) + c_1(c_2 - c_1)D^{(2)}(t_1) - c_2(c_2 - c_1)D^{(2)}(t_o - t_1)\right\}$
Linear Rate $c_1 = c$, $c_2 = c$, $\sigma(b,t) = \sigma_o ct$	$2\sigma_o^2 \left\{c^2 t_o D^{(1)}(t_o) - c^2 D^{(2)}(t_o)\right\}$
Ramp-to-Constant $\sigma(b,t) = \begin{cases} \sigma_o ct & t < t_1 \\ \sigma_o ct_1 & t \geq t_1 \end{cases}$ $c_2 = 0$ above	$2\sigma_o^2 \left\{c^2 t_1\left[D^{(1)}(t_o) - D^{(1)}(t_o - t_1)\right]\right\}$
Quadratic Stress $\sigma(b,t) = \sigma_o\left[c_1 t + c_2 t^2\right]$ 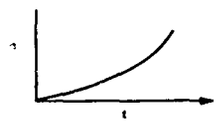	$\sigma_o^2 (c_1 t_o + c_2 t_o^2)^2 \left\{\frac{2}{\left(1 + \frac{c_2}{c_1} t_o\right)} D^{(1)}(t_o) - \frac{(1 - 2\frac{c_2^2}{c_1^2} t_o^2)}{(1 + \frac{c_2}{c_1} t_o)^2} \frac{2}{t_o^2} D^{(2)}(t_o) - \frac{4}{3} \frac{(\frac{c_2}{c_1} t_o)^2}{(1 + \frac{c_2}{c_1} t_o)^2} \frac{6}{t_o^3} D^{(2)}(t_o) + \frac{1}{3} \frac{(\frac{c_2}{c_1})^2 t_o}{(1 + \frac{c_2}{c_1} t_o)^2} \frac{24}{t_o^4} D^{(4)}(t_o)\right\}$
Sinusoidal $\sigma(b,t) = \sigma_o \sin \omega t$, $D(t) = D_g + \sum_{i=1}^{n} D_i e^{-t/\tau_i}$ 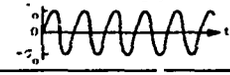	$\sigma_o^2 \left\{D_g \sin^2 \omega t_o - \sum_{i=1}^{n} D_i \frac{\omega t_o}{1 + (\omega\tau_i)^2} + 2 \sum_{i=1}^{n} D_i \frac{(\omega\tau_i)^2}{\left[1 + (\omega\tau_i)^2\right]^2} (1 - e^{-t_o/\tau_i} \cos \omega t_o) - 2 \sum_{i=1}^{n} D_i \frac{\omega\tau_i}{\left[1 + (\omega\tau_i)^2\right]^2} e^{-t_o/\tau_i} \sin \omega t_o + \sum_{i=1}^{n} D_i \frac{\sin 2\omega t_o - \sin^2 \omega t_o}{1 + (\omega\tau_i)^2}\right\}$

Next we consider the bilinear displacement rate loading

$$u(b,t) = \begin{cases} u_o c_1 t, & t < t_1 \\ u_o \left[c_1 t + (c_2 - c_1)(t - t_1) \right], & t \geq t_1 \end{cases} \tag{80}$$

As before

$$L^{-1}\left\{ p\, \overline{E_{rel}}(p)\, \overline{g}(p) \right\} = L^{-1}\left\{ p\, \overline{E_{rel}}(p) \left[\frac{c_1}{p^2} + \frac{c_2 - c_1}{p^2} e^{-t_1 p} \right] \right\}$$

and

$$\begin{aligned} & 2\left(\frac{u_o}{b}\right)^2 \int_o^{t_o} \frac{\partial g}{\partial \xi} L^{-1}\left\{ p\, \overline{E_{rel}}(p)\, \bar{r}(p) \right\} d\xi \\ & = 2\left(\frac{u_o}{b}\right)^2 \left\{ \int_o^{t_1} c_1^2 \int_o^{\xi} E(\tau) d\tau\, d\xi + \int_{t_1}^{t_o} c_2 \int_o^{\xi} c_1 E(\tau) d\tau\, d\xi \right. \\ & \left. + \int_{t_1}^{t_o} c_2 \int_{t_1}^{\xi} (c_2 - c_1) E(\tau - t_1)\, d\tau\, d\xi \right\} \\ & = 2\left(\frac{u_o}{b}\right)^2 \left\{ c_1^2 E^{(2)}(t_1) + c_1 c_2 \left[E^{(2)}(t_o) - E^{(2)}(t_1) \right] \right. \\ & \left. + c_2 (c_2 - c_1) E^{(2)}(t_o - t_1) \right\} \end{aligned} \tag{81}$$

which agrees with the earlier published result (21). For the constant displacement rate case, setting $c_2 = c_1 = c$, one obtains

$$2\left(\frac{u_o}{b}\right)^2 \left\{ c^2 E^{(2)}(t_o) \right\} \tag{82}$$

As a final example, consider the case of a quadratic displacement loading

$$u(b,t) = u_o \left[c_1 t + c_2 t^2 \right] \tag{83}$$

Utilizing, Eq. 77,

$$2\left(\frac{u_o}{b}\right)^2 \int_o^{t_o} \left[c_1 + 2c_2\,\xi\right] L^{-1}\left\{c_1 \frac{1}{p} E(p) + 2c_2 \frac{1}{p^2} E(p)\right\} d\xi$$

$$- 2\left(\frac{u_o}{b}\right)^2 \int_o^{t_o} \left[c_1 + 2c_2\,\xi\right] \left\{c_1 \int_o^{\xi} E(\tau)\, d\tau + 2c_2 \int_o^{\xi} E(\tau)\,(\xi - \tau) d\tau\right\} d\xi$$

$$- 2\left(\frac{u_o}{b}\right)^2 \left\{c_1^2 \int_o^{t_o}\int_o^{\xi} E(\tau) d\tau + 2c_1c_2\left[\int_o^{t_o}\int_o^{\xi} E(\tau)(\xi - \tau) d\tau + \int_o^{t_o} \xi \int_o^{\xi} E(\tau) d\tau\right] d\xi\right.$$

$$\left. + 4c_2^2 \int_o^{t_o} \xi \int_o^{\xi} E(\tau)\,(\xi - \tau)\, d\tau\, d\xi\right\}$$

$$- 2\left(\frac{u_o}{b}\right)^2 c_1^2 \left\{\left(1 + \frac{2c_2 t_o}{c_1}\right) E^{(2)}(t_o) + 4\left(\frac{c_2}{c_1}\right)^2 t_o E^{(3)}(t_o) - 4\left(\frac{c_2}{c_1}\right)^2 E^{(4)}(t_o)\right\}$$

$$- \left[\left(\frac{u_o}{b}\right) c_1 t_o \left(1 + \frac{c_2}{c_1} t_o\right)\right] 2\left\{\frac{\left(1 + 2\frac{c_2}{c_1} t_o\right)}{\left(1 + \frac{c_2}{c_1} t_o\right)^2} \frac{2}{t_o^2} E^{(2)}(t_o) + \frac{4\left(\frac{c_2}{c_1}\right)^2 t_o^2}{3\left(1 + \frac{c_2}{c_1} t_o\right)^2} \frac{6}{t_o^3} E^{(3)}(t_o)\right.$$

$$\left. - \frac{\left(\frac{c_2}{c_1}\right)^2 t_o^2}{3\left(1 + \frac{c_2}{c_1} t_o\right)^2} \frac{24}{t_o^4} E^{(4)}(t_o)\right\}$$

(84)

the final expression being the one of greatest applicability in reducing actual test data where the failure displacement and ratio of constants, c_2 to c_1, are known. Again, these results are summarized along with others of interest in Table III.

The applications of the conditions of criticality derived here are reported in subsequent chapters in the interpretation of test results. It is pertinent at this point however to interpret and evaluate the significance of the theoretical results.

TABLE III. CRITICALITY CRITERIA FOR DISPLACEMENT LOADINGS

Geometry	Spherical Flaw	Plane Strain Cylindrical Flaw	Plane Stress Cylindrical Flaw
Criticality Constant	$(k^3)^2\ (\gamma/a_o)$	$\frac{3}{2}\ (k2)^2\ (\gamma/a_o)$	$\frac{1}{8}\ (1 + 3k^2)^2\ (\gamma/a_o)$

Loading History	Criticality Variable for Failure at Time, t_o
Constant Displacement $u(b,t) = u_o\, 1(t)$ 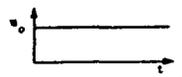	$2\left(\frac{u_o}{b}\right)^2 \left\{\frac{K_a}{2}\right\}$
Bilinear Rate $u(b,t) = \begin{cases} u_o c_1 t & , t < t_1 \\ u_o\left[c_1 t - (c_1 - c_2)(t - t_1)\right] & t > t_1 \end{cases}$ 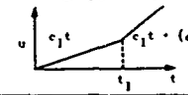	$2\left(\frac{u_o}{b}\right)^2 \left\{c_1^2\, F^{(2)}(t_1) + c_1 c_2\left[F^{(2)}(t_o) - F^{(2)}(t_1)\right] + c_2 (c_2 - c_1)\, F^{(2)}(t_o - t_1)\right\}$
Linear Rate $c_1 = c_1\ \ c_2 = c$ $u(b,t) = u_o c t$	$2\left(\frac{u_o}{b}\right)^2 \left\{c^2\, F^{(2)}(t_o)\right\}$
Quadratic Displacement $u(b,t) = u_o(c_1 t + c_2 t^2)$ 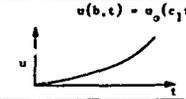	$\left(\frac{u_o}{b}\right)^2 (c_1 t_o + c_2 t_o^2)^2 \left\{\frac{\left(1 + 2\frac{c_2}{c_1} t_o\right)}{\left(1 + \frac{c_2}{c_1} t_o\right)^2} \frac{2}{t_o^2} F^{(2)}(t_o) + \frac{1}{3} \frac{\left(\frac{c_2}{c_1} t_o\right)^2}{\left(1 + \frac{c_2}{c_1} t_o\right)^2} \frac{6}{t_o^3} F^{(3)}(t_o) - \frac{1}{3} \frac{\left(\frac{c_2}{c_1} t_o\right)^2}{\left(1 + \frac{c_2}{c_1} t_o\right)^2} \frac{24}{t_o^4} F^{(4)}(t_o)\right\}$
Sinusoidal $u(b,t) = u_o \sin \omega t$ $E(t) = E_e + \sum_{i=1}^{n} E_i\, e^{-t/\tau_i}$ 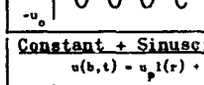	$2\left(\frac{u_o}{b}\right)^2 \left\{\frac{E_e}{2} \sin^2 \omega t_o + \sum_{i=1}^{n} \frac{E_i(\omega\tau_i)}{1 + (\omega\tau_i)^2}\left[\frac{\omega t_o}{2} + \frac{\sin 2\omega t_o}{4} + \frac{\omega\tau_i}{1 + (\omega\tau_i)^2}\left(\frac{\sin^2 \omega t_o}{2} - 1 + e^{-t_o/\tau_i} \cos \omega t_o\right) - \frac{(\omega\tau_i)^2}{1 + (\omega\tau_i)^2} e^{-t_o/\tau_i} \sin \omega t_o\right]\right\}$
Constant + Sinusoidal $u(b,t) = u_p 1(t) + u_o \sin \omega t$ 	$2\left(\frac{u_o}{b}\right)^2 \left\{\left(\frac{u_p}{u_o}\right)^2 \frac{K_a}{2} + \left(\frac{u_p}{u_o}\right) E_e \sin \omega t_o + \left(\frac{u_p}{u_o}\right) \sum_{i=1}^{n} \frac{E_i(\omega\tau_i)}{1 + (\omega\tau_i)^2}\left[1 - e^{-t_o/\tau_i} \cos \omega t_o + \frac{(\omega\tau_i)}{1 + (\omega\tau_i)^2} e^{-t_o/\tau_i} \sin \omega t_o\right]\right\}$

TABLE III. Concluded

Geometry	Spherical Flaw	Plane Strain Cylindrical Flaw	Plane Stress Cylindrical Flaw
Criticality Constant	$(k3)^2\ (\gamma/a_o)$	$\frac{3}{2}\ (k2)^2\ (\gamma/a_o)$	$\frac{1}{8}\ (1 + 3k^2)^2\ (\gamma/a_o)$

Loading History	Criticality Variable for Failure at Time, t_o
Bifrequency Sinusoidal $u(b,t) = \begin{cases} u_o \sin \omega t, & t < t_1 \\ u_o \sin \theta t, & t > t_1 \end{cases}$ $u(b,t_1) = 0$, i.e. $\theta t_1 = n\pi$ 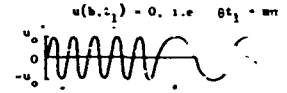	$2\left(\frac{u_o}{b}\right)^2 \left\{ \frac{E_o}{4}(2 - \cos^2 \omega t_1 - \cos 2\theta t_o) + \sum_{i=1}^{n} \frac{E_i(\omega\tau_i)}{1 + (\omega\tau_i)^2}\left[\frac{\omega t_1}{2} + \frac{\sin 2\omega t_1}{4}\right] + \sum_{i=1}^{n} \frac{E_i(\theta\tau_i)}{1 + (\theta\tau_i)^2}\left[\frac{\theta(t_o - t_1)}{2} + \frac{\sin 2\theta t_o}{4}\right] \right.$ $+ \sum_{i=1}^{n} \frac{E_i(\omega\tau_i)^2}{4\left[1 + \omega\tau_i\right]^2}(1 - \cos 2\omega\tau_i) + \sum_{i=1}^{n} \frac{E_i(\theta\tau_i)^2}{4\left[1 + (\theta\tau_i)^2\right]}(1 - \cos 2\theta t_o) - \sum_{i=1}^{n} \frac{E_i(\omega\tau_i)^3}{\left[1 + (\omega\tau_i)^2\right]^2} e^{-t_o/\tau_i} \sin \omega t_1$ $- \sum_{i=1}^{n} 2 \frac{E_i(\theta\tau_i)^3}{\left[1 + (\theta\tau_i)^2\right]^2} e^{-\frac{t_o - t_1}{\tau_i}} \left[\sin \theta(t_o - t_1) + \sin \theta(t_o + t_1)\right] - \sum_{i=1}^{n} \frac{E_i(\omega\tau_i)^2}{\left[1 + (\omega\tau_i)^2\right]^2}(1 - e^{-t_1/\tau_i} \cos \omega t_1)$ $\left. \sum_{i=1}^{n} \frac{E_i(\theta\tau_i)^2}{\left[1 + (\theta\tau_i)^2\right]^2}\left[1 - e^{-\frac{(t_o - t_1)}{\tau_i}} \frac{\cos \theta(t_o - t_1) + \cos \theta(t_o + t_1)}{2}\right] \right\}$

CRITIQUE OF VISCOELASTIC FRACTURE THEORY

Due to the limitations and assumptions required to develop the solutions presented, it is worthwhile to investigate the implications of some of these limitations to the application of the results to real materials in typical test situations.

CRACK GEOMETRY

The spherical and cylindrical flaws analyzed here for the purpose of obtaining a simple stress distribution are somewhat limited in analogy with typical crack type failures. However, the ability to separate energy and geometry for these limited cases suggests the applicability of the results to crack-type flaw geometries. Also, for the elastic case, it has been shown (2) that up to a geometrical constant, the critical stress for the crack geometries with crack length a_0 is of the same form as the spherical or cylindrical flaws of radius a.

Using quasi-elastic analytical techniques, Rocketdyne (22), has demonstrated the applicability of the fracture mechanics technique to predicting thermal bore cracking in propellant grains. Similar approaches have been pursued by Swanson (23) and others.

EFFECTS OF FINITE STRAINS

Although the effects of finite strains on the viscoelastic solution are presently beyond the state of analytical capability, some insight into the effects of large strains on the criticality for a spherical flaw have been obtained (24) for a body of neo-Hookean material. The essence of the result of that analysis is that for small cavities one needs to account for the finite strains. Williams has suggested an extension of the finite elastic strain result through

$$\sigma(\lambda,t) = E_{rel}(t)\, f(\lambda) \tag{85}$$

where $\lambda = 1 + \epsilon$ for small strains. These effects are currently under investigation (24).

Flaw Growth

Since body forces were neglected, a degree of limitation was placed on the analysis for flaw growth. Blatz has investigated the result for both Hookean and a neo-Hookean body with a spherical flaw including

inertial effects (25) and found (for the Hookean material) that the initial crack velocity is linear in time and proportional to the square of the shear wave speed in the material.

An additional limitation of the present analysis arises from the flaw geometry. The propagation of the flaw by uniform increase of the radius could be of significant quantitative difference from that by cracking although qualitative similarities may exist (1).

SURFACE ENERGY AND CUMULATIVE DAMAGE

In the foregoing results, we were able to express the criticality criteria for a given geometry and boundary condition in terms of an equality between "constant" terms and time-temperature-loading history dependent terms. From a purely theoretical standpoint, it is not possible to deduce a dependency on time or temperature on the characteristic surface energy, γ. In any event, it would appear sufficient to establish γ for the failure condition only since its role in the power balance up to failure is nil. Thus, the "energy" term involving the time dependent material properties and the loading history will account for the cumulative effects.

SECTION III

POKER CHIP TESTS AND ANALYSES

The first tests run on the Cumulative Damage program were tensile tests in which poker chip specimens were used. Specimens, 4-inch diameter by 1/3-inch thick, are bonded between two rigid steel platens. When the platens are separated, a tensile strain is generated in the direction of the thin specimen dimension, and an essentially hydrostatic stress field is induced in the center portion of the incompressible material (26). This is a particularly appealing test because the hypothesized stress field of the spherical flaw derivations, a uniform triaxial tension, matches that of the specimen.

The experimental technique, including data collection, is described in this section; and data interpretations and quantitative comparisons with the analytical expressions are made.

EXPERIMENTAL PROGRAM

The poker chip specimens, each with an oversized diameter, were milled flat on a specially modified Van Norman 12 Universal Milling Machine from bulk propellant furnished by Lockheed. Loose oxidizer particles were removed from the bond surfaces by impregnating a layer of surgical gauze with an epoxy resin in contact with the propellant surface. After a 30-minute cure, the epoxy resin was easily removed from the specimen, and the loosely imbedded oxidizer crystals adhered to the epoxy resin.

It is normally possible to prime the bonded surfaces at this point and subsequently to assemble the specimen to the steel platens using the same epoxy adhesive. However, it was necessary to expose this particular propellant to pure oxygen for 48 hours before an adequate bond could be obtained. Specimens for all tests reported herein were exposed to oxygen in this manner before they were primed with Eastman's adhesive. The Eastman 910 primer layer was air dried for 12 hours followed by 1 hour at 170 F. The specimen was then bonded to the steel platen while being aligned in a special bonding fixture such as that shown in Fig. 4. A light pressure was maintained on the assembly while the epoxy adhesive was curing. The assembly was placed in instrumentation rings (Fig. 5) after the edges of the propellant had been trimmed. The specimen was then subjected to tensile loads on a 20,000-pound Model TTD Instron tester at the desired rate and temperature.

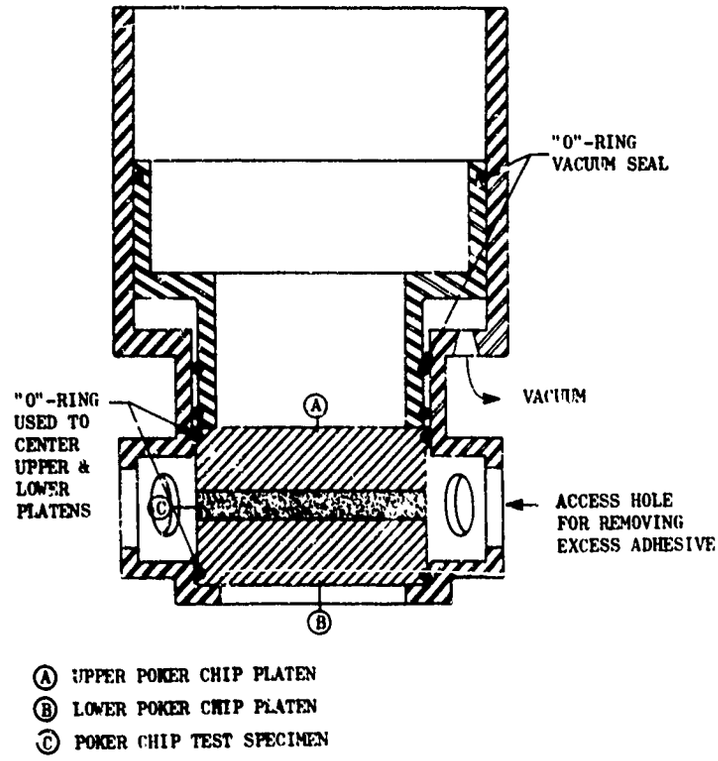

Figure 4. Poker Chip Bonding Fixture

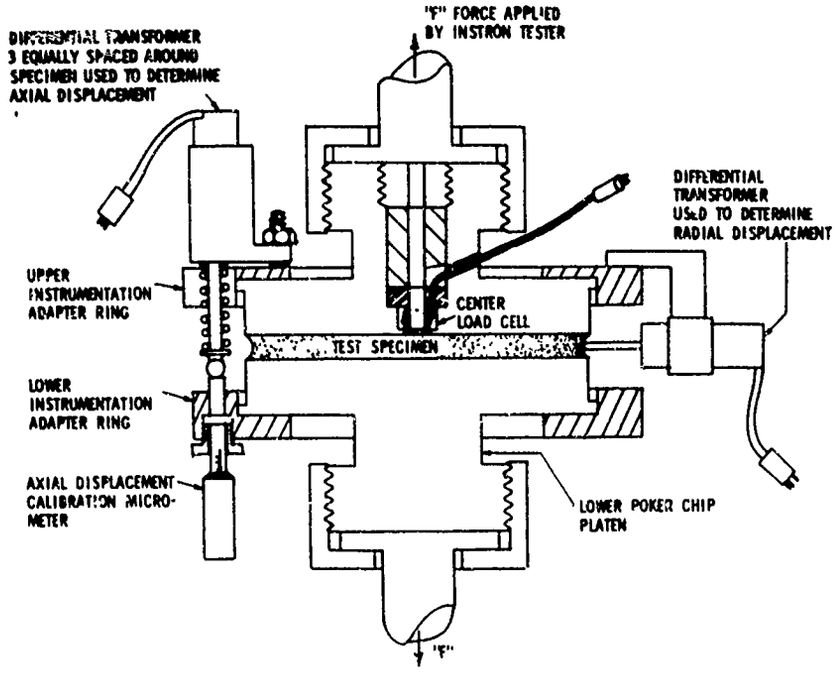

Figure 5. Poker Chip Assembly Installed In Instrumentation Rings Ready for Testing

A typical data acquisition trace is shown in Fig. 6. These data are recorded as a function of time. The three LVDT traces indicate the amount of displacement in the direction of the pull at three points equally spaced around the specimen. These traces must be parallel to ensure achieving a uniform separation during the test. The output from the Instron load cell is indicated by the over-all load trace which represents the total load exerted over the entire cross section of the specimen. The fifth trace shown is the output from a center load cell located at the center of one of the steel end platens. This cell has an area of 0.1 sq in. and is bonded to the propellant specimen. The element is flush with the surface of the platen and is very stiff so there are essentially no modifications in the stress distribution due to the presence of the cell. The output from the center load cell reached a peak well ahead of the peak in the "over-all load" as indicated by the Instron load cell.

This phenomenon has been noted in many constant stress rate tests with a variety of composite propellants over the past few years. In general, during constant stress rate tests it has been noted that the center load cell stress is greater than the average stress P/A, usually by a factor just less than 2:1. An elastic analysis relating this ratio to the material properties and specimen geometry has been given by Lindsey, et al (26), and Messner (27). The ratio appears to hold essentially constant to the point where microvoids begin to grow, generally at internal points distant from the edges, resulting in changes in the load distribution. The point of maximum output on the center load cell trace has previously been interpreted as the point of failure (see Fig. 6, Point a). However, during the work with constant loads (Page 33), X-rays of specimens revealed that the growth of numerous small voids on the order of 0.040-inch diameter led to the decrease in the load cell reading. Based on these findings, the triaxial failure point has been defined at a point earlier on the curve where it just begins to break from a straight line, Point b, Fig. 6.

There was no visible indication of failure on the outside of the specimen at the point previously discussed. However, the test was continued until the specimen was pulled completely apart. A typical surface after complete separation is shown in Fig. 7; the propellant layer is thin over most of the top platen. Such separations were encountered quite frequently; however, flaw growth failures near the center of the specimen in other tests produced essentially the same terminal results. Therefore, the actual plane of separation is not deemed pertinent to the test results.

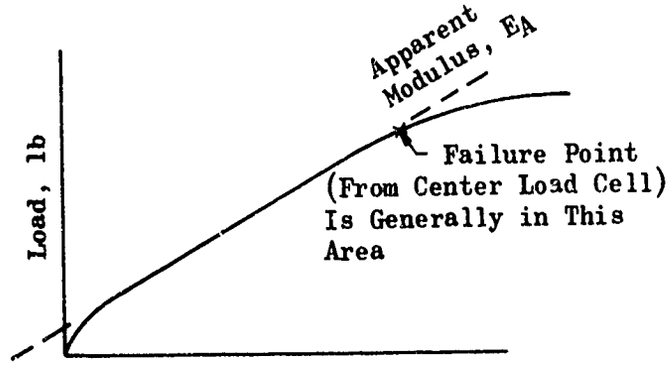

a. Typical X-Y Plot (Moseley Autograph Recorder). These Data Obtained Simultaneously with That Collected with the CEC Recorder

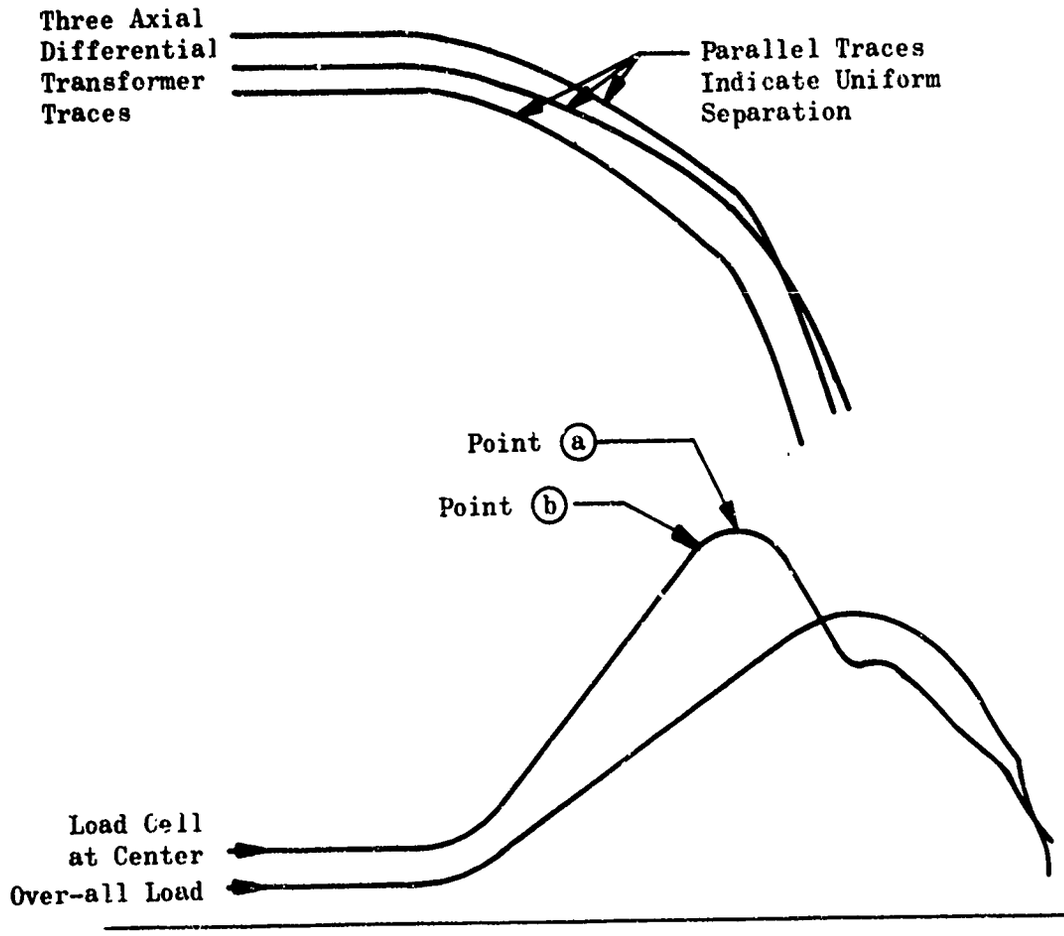

b. Typical CEC Oscillograph Record

Figure 6. Data Traces Collected During Poker Chip Tests

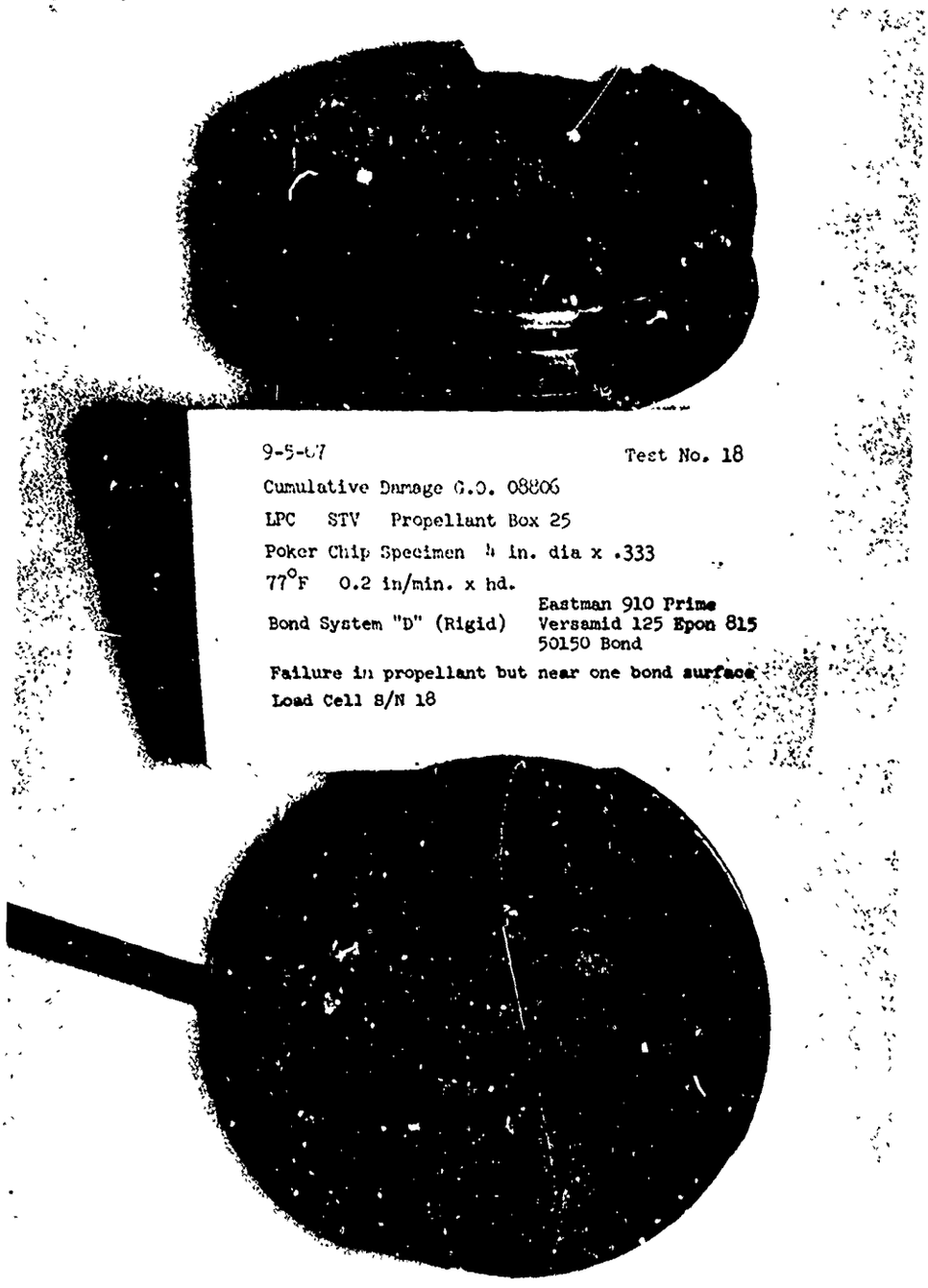

Figure 7. Typical Surface Following Complete Separation of Platens

DATA INTERPRETATION

Experimental test results from the elemental poker chip tests are summarized in Table IV. These experimental data can be analyzed in several ways insofar as the use of the spherical flaw theory is concerned. In Tables II and III (a summary of the criticality equations) it is seen that either stress or displacement strain histories can be used. These equations have been derived from both linear and quadratic (in time) histories. When an attempt is being made to evaluate a new theory, it would be most desirable to use the simplest case possible for the experimental input, namely the expression for linear displacement. Two factors, however, influenced the selection of the expression for the quadratic stress history for determining the failure parameter, γ/a_o.

TABLE IV. SUMMARY OF EXPERIMENTAL TEST RESULTS FOR THE ELEMENTAL POKER CHIP TESTS

Test No.	Test Temp, deg F	Nominal Crosshead Rate, in./min	Linear Stress Rate, psi/sec	Time to Failure, sec	Center Stress at Failure	Average Strain at Failure, in./in.
35	77	0.02	1.9	92.0	175	0.0080
17	77	0.2	17.5	12.5	218	0.0084
18	77	0.2	20.1	11.5	223	0.0082
29	77	0.2	16.5	14.5	200	0.0069
31	77	0.2	17.6	12.5	220	.77
32	77	0.2	19.2	11.9	228	.0084
33	77	0.2	19.2	10.8	208	0.0070
34	77	20.0	2950.0	0.120	354	0.0041
42	0	0.02	2.3	127.0	286	0.0050
41	0	0.2	24.5	15.3	374	0.0044
43	0	20.0	4690.0	0.145	650	0.0023
38	140	0.02	1.7	75.0	124	0.0090
36	140	0.2	18.5	8.2	152	0.0081
40	140	0.2	19.2	8.1	156	0.0088
37	140	20.0	2235.0	0.135	302	0.0085
39	140	20.0	2435.0	0.103	250	0.0069

First, it was noted that the strain history imposed on the poker chip specimens in the Instron tester were not linear as one would expect to result from a constant rate of crosshead displacement. It was determined that this was caused by the relatively low compliance of the test machine and linkage as compared to the stiffness of the propellant specimen. (The detailed investigation into this problem is reported in Appendix IV.) The extent of this influence is shown in Fig. 8 and 9, typical stress and strain time relationships. Dotted lines represent the linear rate corresponding to the failure points that would have been obtained if such a history had been possible.

The stress history was then selected because the geometric parameter, k, can conveniently be omitted from the calculation without causing excessive error. From Tables II and III, the expression for criticality of the spherical flaw following a stress-prescribed history can be written in the form Critical Stress = $(1 - k^3)$ f(mechanical properties and geometry); but following a displacement-prescribed history, critical Strain = (k^3) g(mechanical properties and geometry).

Because k, the ratio of the initial flaw size, a_o, to the outer radius of the sphere, b, used for the mathematical derivations is expected to be rather small (< 1), it is readily apparent that it may be neglected in the equation for stress loading but not for displacement loading.

Therefore, the first analysis of poker chip test results for γ/a_o utilizes the equation

$$\left[\frac{4}{3}(1 - k^3)\right]^2 \left(\frac{\gamma}{a_o}\right) =$$

$$\sigma_o^2 (c_1 t_o + c_2 t_o^2) \left\{ \frac{2}{\left(1 + \frac{c_2}{c_1} t_o\right)} D^{(1)}_{crp}(t_o) - \frac{\left(1 - 2\frac{c_2}{c_1} t_o^2\right)}{\left(1 + \frac{c_2}{c_1} t_o\right)^2} \frac{2}{t_o^2} D^{(2)}_{crp}(t_o) - \frac{4}{3} \frac{\left(\frac{c_2}{c_1} t_o\right)^2}{\left(1 + \frac{c_2}{c_1} t_o\right)^2} \frac{6}{t_o^3} D^{(2)}_{crp}(t_o) \right.$$

$$\left. + \frac{1}{3} \frac{\left(\frac{c_2}{c_1}\right)^2 t_o}{\left(1 + \frac{c_2}{c_1} t_o\right)^2} \frac{24}{t_o^4} D^{(4)}_{crp}(t_o) \right\} \qquad (86)$$

the expression for the time, t_o, to incipient flaw growth following a stress history of the form

$$\sigma(t) = \sigma_o \left(C_1 t + C_2 t^2\right) \tag{87}$$

The meaning of the various terms is as described in Section II.

Table V shows corresponding calculated values for γ/a_o for the 16 tests. These data reflect temperature and rate changes in the experimental condition from 0 to 140 F and from 0.02 to 20.0 in./min nominal crosshead speeds. Values assigned to the creep compliance integrals, $D^{(n)}_{crp}(t_o)$, were calculated using uniaxial relaxation data supplied by Lockheed. (These calculations are described and results are shown in Appendix V.) Times to failure were shifted using the a_T values also taken from the uniaxial data mentioned. From the values calculated for γ/a_o, it appears possible that temperature and rate influence the parameter. For example, at 0 F the average γ/a_o was 64.8 in.-lb/in.^{3}; while at 77 F the average value had dropped to 48.3 in.-lb/cu in., and at 140 F the average was down to 40.4 in.-lb/cu in. The influence of rate effects is not quite so evident, but there seems to be a tendency for the higher rates to exhibit a higher γ/a_o at each temperature. It should be noted that utilization of the uniaxial stress relaxation modulus data in the triaxial (or biaxial near the flaws) stress fields in arriving at the values for γ/a_o may actually be responsible for these apparent effects

LINEAR VS NONLINEAR ANALYSIS

It was observed that the loading rate for these tests varied as shown in Fig. 8 and 9. Because these histories are probably typical for poker chip tests, it was desirable to determine the influence of the variation if a linear history to failure had been assumed and the data interpreted accordingly. Therefore, the failure data were substituted into the equation (from Table II):

$$\frac{\sigma_o c t_o}{1-k^3} = \frac{4}{3}\sqrt{\frac{\gamma/a_o}{2\left[\frac{1}{t_o} D^{(1)}_{crp}(t_o)\right] - \left[\frac{2}{t_o^2} D^{(2)}_{crp} t_o\right]}} \tag{88}$$

which was then solved for γ/a_o. (Again, the various terms are described in Section II.)

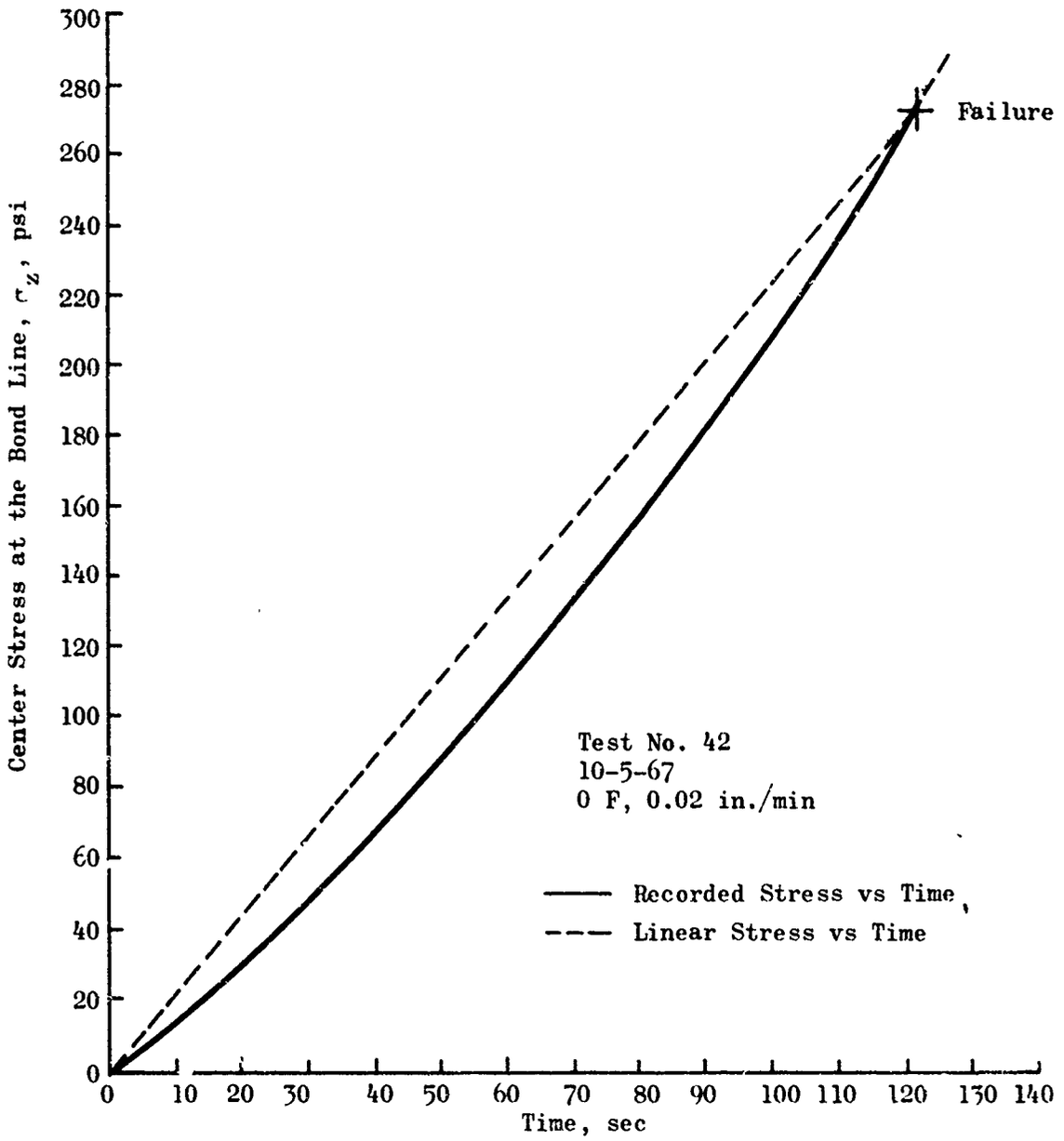

Figure 8. Typical Stress-vs-Time Relationship for Poker Chip Test

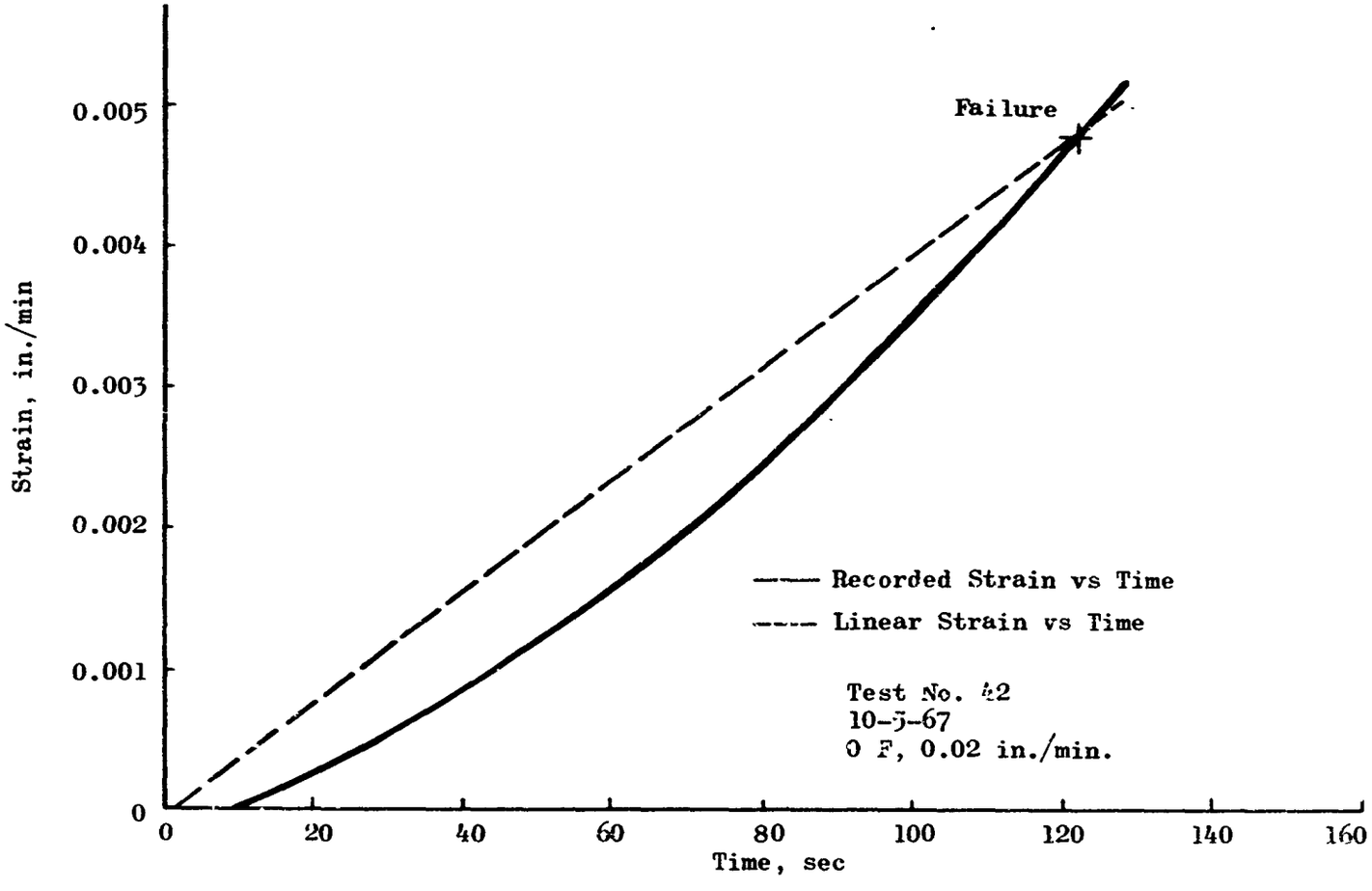

Figure 9. Typical Strain-vs-Time Relationship for Poker Chip Test

TABLE V. SUMMARY OF VALUES FOR THE FAILURE PARAMETER γ/a_o FROM POKER CHIP TESTS USING A QUADRATIC VARYING STRESS ANALYSIS

Test No.	Time to Failure, Min	Log t_o/a_T	Stress - Time History: Assuming a Linear Stress History $\sigma(t) = \sigma_o c_1 t$ — $\sigma_o c_1$, psi/min	Stress - Time History: Assuming a Quadratic Stress History $\sigma(t) = \sigma_o c_1 t + \sigma_o c_2 t^2$ — $\sigma_o c_1$, psi/min	$\sigma_o c_2$, psi/min^2	Stress at Failure, psi	$\frac{c_2}{c_1}$	$\left(\frac{c_2}{c_1}\right)^2$	$\left(\frac{c_2}{c_1} t_o\right)^2$	$\frac{1}{t_o} D^{(1)}_{crp}(t_o)$	$\frac{2}{t_o^2} D^{(2)}_{crp}(t_o)$	$\frac{6}{t_o} D^{(3)}_{crp}(t_o)$	$\frac{24}{t_o} D^{(4)}_{crp}(t_o)$	γ/a_o, in.-lb/in.^{3}
Temperature = 0 F														
42	2.18	-1.8632	130.8	91.2	21.56	286	0.2364	0.0558	0.2651	1.1×10^{-3}	1.0×10^{-3}	9.5×10^{-4}	9.0×10^{-4}	52.1
41	0.255	-2.7932	1470	942	2098.8	374	2.228	4.96	0.3225	7.6×10^{-4}	6.4×10^{-4}	6.7×10^{-4}	6.5×10^{-4}	61.47
43	0.00242	-4.8154	2682	243,000	15,336,000	650	63.11	3982.8	0.02329	3.2×10^{-4}	2.9×10^{-4}	2.7×10^{-4}	2.52×10^{-4}	81.17
Temperature = 77 F														
35	1.53	0.1846	114.6	108	4.75	175	0.0439	0.0019	0.0044	2.4×10^{-3}	2.2×10^{-3}	2.1×10^{-3}	2.0×10^{-3}	44.08
17	0.209	-0.6798	1,044	930	669.6	218	0.7200	0.5184	0.0226	1.75×10^{-3}	1.6×10^{-3}	1.52×10^{-3}	1.45×10^{-3}	49.89
18	0.193	-0.7145	1,242	882	1681.2	223	1.9061	3.63	0.1352	1.73×10^{-3}	1.58×10^{-3}	1.50×10^{-3}	1.43×10^{-3}	49.8
29	0.242	-0.6162	828	582	2077.2	200	3.569	12.737	0.745	2.82×10^{-3}	1.68×10^{-3}	1.6×10^{-3}	1.52×10^{-3}	41.4
31	0.209	-0.6798	1,050	786	1389.6	220	1.7679	3.125	0.136	1.75×10^{-3}	1.6×10^{-3}	1.52×10^{-3}	1.45×10^{-3}	49.54
32	0.198	-0.7034	1,152	954	1098	228	1.1509	1.324	0.0519	1.73×10^{-3}	1.58×10^{-3}	1.54×10^{-3}	1.43×10^{-3}	52.11
33	0.180	-0.7448	1,152	888	1558.8	208	1.755	3.08	0.0995	1.7×10^{-3}	1.57×10^{-3}	1.5×10^{-3}	1.40×10^{-3}	43.82
34	0.0020	-2.699	177,000	55,320	56,880,000	354	1028.1	1,056,989	4.22	8.0×10^{-4}	7.2×10^{-4}	6.8×10^{-4}	6.3×10^{-4}	55.1
Temperature = 140 F														
38	1.25	1.0969	99.0	99.6	0	124	0	---	---	3.3×10^{-3}	3.0×10^{-3}	2.9×10^{-3}	2.8×10^{-3}	31.1
36	0.1367	0.1357	1,110	936	1231.2	152	1.315	1.7292	0.032	2.4×10^{-3}	2.2×10^{-3}	2.1×10^{-3}	2.0×10^{-3}	33.02
40	0.135	0.13033	1,158	1,077.6	640.8	156	0.5946	0.3535	0.00644	2.4×10^{-3}	2.2×10^{-3}	2.1×10^{-3}	2.0×10^{-3}	35.19
37	0.00225	-1.6479	134,400	26,124	47,988 [illegible]	302	1836.93	3,374,311.8	16.87	1.22×10^{-3}	1.1×10^{-3}	1.02×10^{-3}	9.9×10^{-4}	61.25
39	0.0018	-1.7448	146,400	61,200	47,880,000	250	782.35	612,071	1.958	1.18×10^{-3}	1.1×10^{-3}	1.0×10^{-3}	9.6×10^{-4}	41.8

Table VI shows the results which vary only slightly from those computed in Table V. The conclusion must be that the slightly different loading histories involved in these tests do not essentially influence failure stresses and strains or the parameter γ/a_0.

The critical values for γ/a_0 represent the failure criteria for the corresponding rates and temperatures. Therefore, a composite of these data would represent the failure envelope over the range of the tests. Figures 10 and 11 show these failure envelopes for different γ/a_0 values. Figure 10 shows failure predictions using an average γ/a_0 of 51.1 (the average value for the 77 F data-linear analysis). The use of this value assumes that there is no temperature effect on γ/a_0. Therefore, the experimental points for 0 and 140 F do not fall on the failure envelope. The curve indicates the prediction error expected as a result of temperature effects on γ/a_0. Figure 11 presents the failure envelopes at different temperatures using the corresponding γ/a_0 for the temperatures shown. As expected, the experimental data points fit the envelope better since the values for the corresponding γ/a_0 were determined using averages from the data at each temperature.

Having obtained γ/a_0, it is now possible to calculate the value for k. The equation for criticality following a second order displacement history provides the necessary tool. Using the average γ/a_0 for the 77 F data (51.1 in.-lb/in.^{3}) and the second order strain history equation, values for k were calculated. These values are shown in Table VII. If the effective outer sphere radius, b, is assumed to be one-half the poker chip thickness, 0.167 inch, an estimate for the characteristic flaw size can be deduced from the calculations of Table VII.

$$\frac{a_0}{b} \simeq 0.3 \qquad b \simeq 0.167 \qquad \therefore \; a_0 \simeq 0.055 \text{ inch}$$

It seems logical that the assumed value for b is an upper limit (for the poker chip specimen), implying that the calculated value for the flaw size is also an upper limit. This flaw size seems to be reasonable because the larger solid particles within the propellant are of the order of 600 microns (0.024 inch) in diameter. The small variation between the several calculated k values also adds to the credibility of the calculations.

TABLE V

SUMMARY OF VALUES FOR THE FAILURE PARAMETER γ/a_o FROM POKER CHIP TESTS ASSUMING A LINEAR STRESS HISTORY

Test No.	Time To Failure, min	Stress at Failure, $\sigma_o ct_o$	$\text{Log } \frac{t_o}{a_T}$	$2\left[\frac{1}{t_o} D^{(1)}_{crp}(t_o)\right]$	$\frac{2}{t_o^2} D^{(2)}_{crp}(t_o)$	$\frac{\gamma}{a_o}$	Average $\frac{\gamma}{a_o}$
Temperature = 0 F			Log a_T = 2.2	a_T = 158.5			
42	2.18	286	-1.8632	2.2×10^{-3}	1.01×10^{-3}	55.2	
41	0.255	374	-2.7932	1.516×10^{-3}	6.9×10^{-4}	64.3	66.8 x 3 = 200.4
43	0.00242	650	-4.8154	6.2×10^{-4}	2.85×10^{-4}	81.0	
Temperature = 77 F			Log a_T = 0	a_T = 1.0			
35	1.5300	175	0.1846	4.8×10^{-3}	2.2×10^{-3}	44.8	
17	0.209	218	-0.6798	3.5×10^{-3}	1.6×10^{-3}	50.7	
18	0.193	223	-0.7145	3.48×10^{-3}	1.6×10^{-3}	52.2	
29	0.242	200	-0.6162	3.64×10^{-3}	1.62×10^{-3}	45.0	51.13 x 8 = 409.1
31	0.209	220	-0.6798	3.56×10^{-3}	1.6×10^{-3}	53.3	
32	0.198	228	-0.7034	3.58×10^{-3}	1.6×10^{-3}	57.8	
33	0.180	208	-0.7448	3.42×10^{-3}	1.58×10^{-3}	44.7	
34	0.002	354	-2.6990	1.58×10^{-3}	7.2×10^{-4}	60.6	
Temperature=140 F			Log a_T = -1.0	a_T = 0.1			
38	1.25	124	1.0969	6.4×10^{-3}	3.0×10^{-3}	29.4	
36	0.1367	152	0.1357	4.76×10^{-3}	2.18×10^{-3}	33 5	
40	0.135	156	0.1303	4.8×10^{-3}	2.18×10^{-3}	35.8	42.6 x 5 = 213.0
37	0.00225	302	-1.6479	2.44×10^{-3}	1.10×10^{-3}	68.7	822.5
39	0.0018	250	-1.7448	2.38×10^{-3}	1.08×10^{-3}	45.6	Average = 51.4

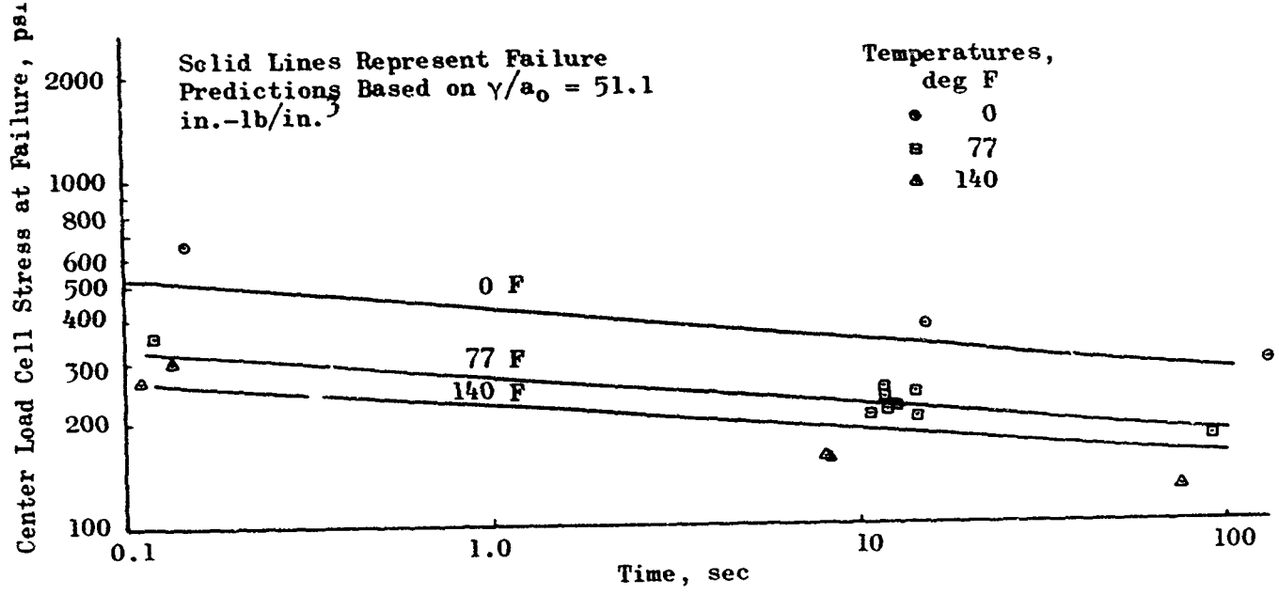

Figure 10. Failure Predictions Based on Average γ/a_o

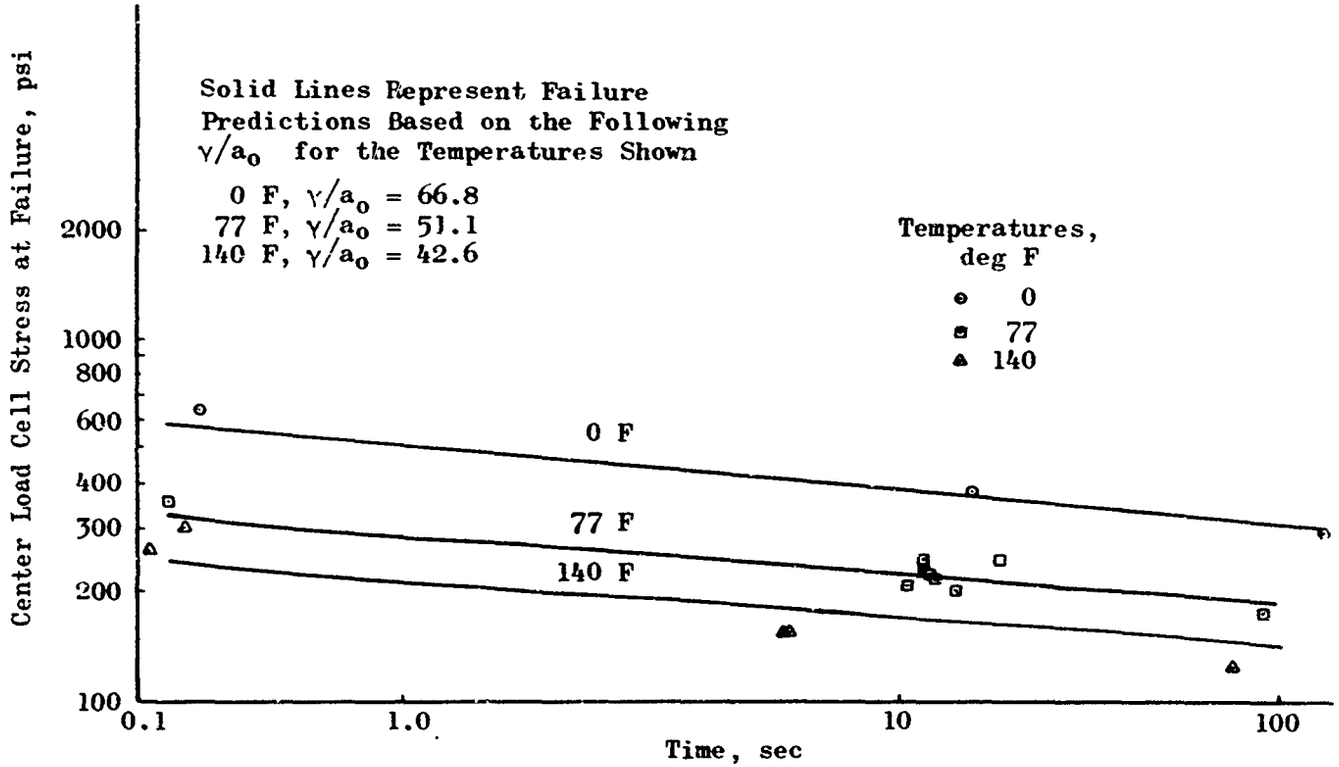

Figure 11. Failure Predictions Based on Various γ/a_o Values

TABLE VII

CALCULATION OF VALUES FOR k USING THE NON-LINEAR STRAIN HISTORY ANALYSIS (USING $\gamma/a_o = 51.1$)

Test No.	Time to Failure, min (t_o)	Log t_o/τ_1	Strain-Time History (Assuming a Quadratic Strain History) $\epsilon(t) = \epsilon_o C_1 t + \epsilon_o C_2 t^2$		$\frac{u_o(C_1 t_o + C_2 t_o^2)}{b}$	$\frac{C_2}{C_1}$	$\left(\frac{C_2}{C_1}\right)^2$	$\left(\frac{C_2}{C_1} t_o\right)^2$	$\frac{1}{t_o} E^{(1)}_{rel}(t_o)$	$\frac{2}{t_o^2} E^{(2)}_{rel}(t_o)$	$\frac{6}{t_o^3} E^{(3)}_{rel}(t_o)$	$\frac{24}{t_o^4} E^{(4)}_{rel}(t_o)$	k, $\left(\frac{\tau_2}{b}\right)$
			$\epsilon_o C_1$, in./in./min	$\epsilon_o C_2$, in./in./min^2	Strain at Failure, in./in.								
Temperature = 77 F													
35	0.153	0.1846	0.00403	0.000972	0.0080	0.241	0.0580	0.00135	389	400	418	422	0.282
17	0.209	-0.6798	0.02856	0.0756	0.0084	2.647	7.006	0.3060	542	580	610	630	0.305
18	0.193	-0.7145	0.0225	0.1188	0.0082	5.327	28.37	1.056	550	585	615	635	0.308
29	0.242	-0.616	0.0135	0.10908	0.0069	8.08	65.28	3.823	525	565	595	615	0.341
31	0.209	-0.6798	0.0211	0.09108	0.0077	4.316	18.62	0.8133	532	575	600	620	0.296
32	0.198	-0.7034	0.0259	0.09288	0.0084	3.586	12.85	0.503	541	580	615	632	0.305
33	0.180	-0.7448	0.0242	0.1058	0.0070	4.371	19.10	0.618	555	590	625	645	0.286
34	0.002	-2.699	0	1089.36	0.0041	-	-	-	1200	1280	1350	1450	0.275

One further interesting calculation can be made using the value for a_0 found above. Again using $\gamma/a_0 = 51.1$ in.-lb/in.^{3} and $a_0 = 0.055$ inch, one finds the characteristic strain energy release rate to be

$$\gamma = (51.1 \text{ in.-lb/in.}^3)(0.055 \text{ inch}) = 2.81 \text{ in.-lb/in.}^3 \quad (89)$$

which one should also interpret as an upper limiting value based on the rather gross assumptions that have been described.

CONSTANT LOAD CONFIRMATORY TESTS

Three constant load poker chip tests were conducted to confirm failure prediction based on critical values for γ/a_0. These tests represent a more complex loading history than the simple pulls used in determining the failure parameter. Loads of 900, 750, and 600 pounds were applied, relatively instantaneously (loading time < 15 seconds), across the specimens. The loads exerted an average stress of P/A as indicated in Fig. 12 for each test. Data collected during these tests included the output of the center load cell and displacement across the specimen in the direction of the pull. Center load cell output was used to calculate the stress at the center of each specimen.

The rapid drop early in the 900- and 750-pound tests indicated that failure had occurred. The specimen was X-rayed perpendicular to the axis of symmetry during the 750-pound test to verify this interpretation. Data revealed by X-ray are presented schematically as a function of time in Fig. 13. It is generally considered that flaws 0.01 of the propellant thickness (in this case 0.04 inch) are the smallest that can be detected by X-ray. By extrapolating back to the smaller (undetectable) flaws, one can surmise that the initial flaw size must have been on the order of 0.025 inch which is consistent with previous findings. The flaws continued to grow in both size and number for the duration of the test.

Figure 14 shows test results compared to those predicted. The predicted values of 0.25 and 2.4 minutes agree quite well for the 900- and 750-pound tests, respectively. The failure point was taken to be the time when the slope of the center load cell output first became negative. The prediction for the time to failure in the 600-pound test did not materialize--the specimen had not failed after 3000 minutes, and the test was discontinued.

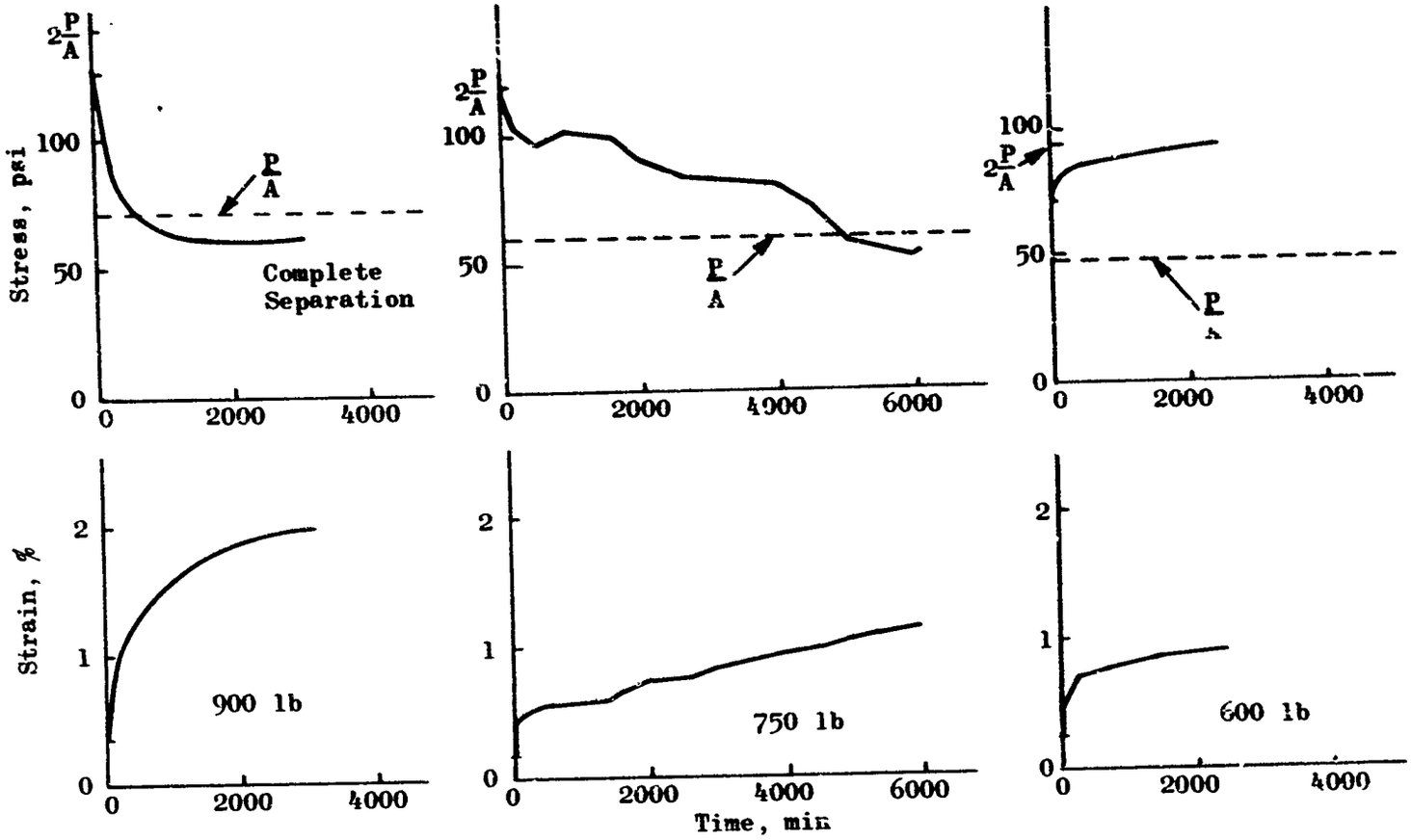

Figure 12. Center Stresses and Average Strains During Three Constant Load Poker Chip Tests

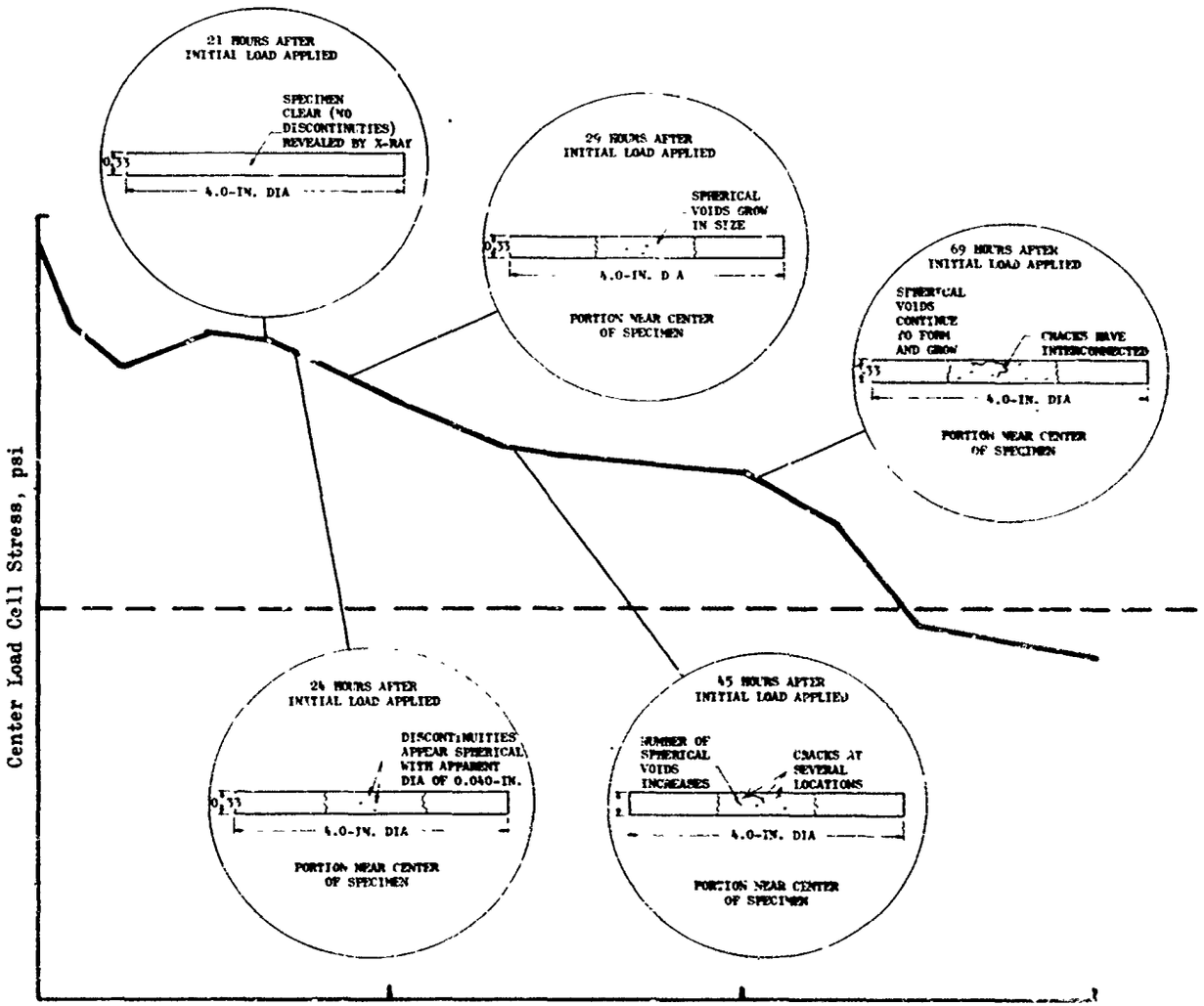

Figure 13. Schematic of X-Ray Views at Various Times During 750-Pound Constant Load Test

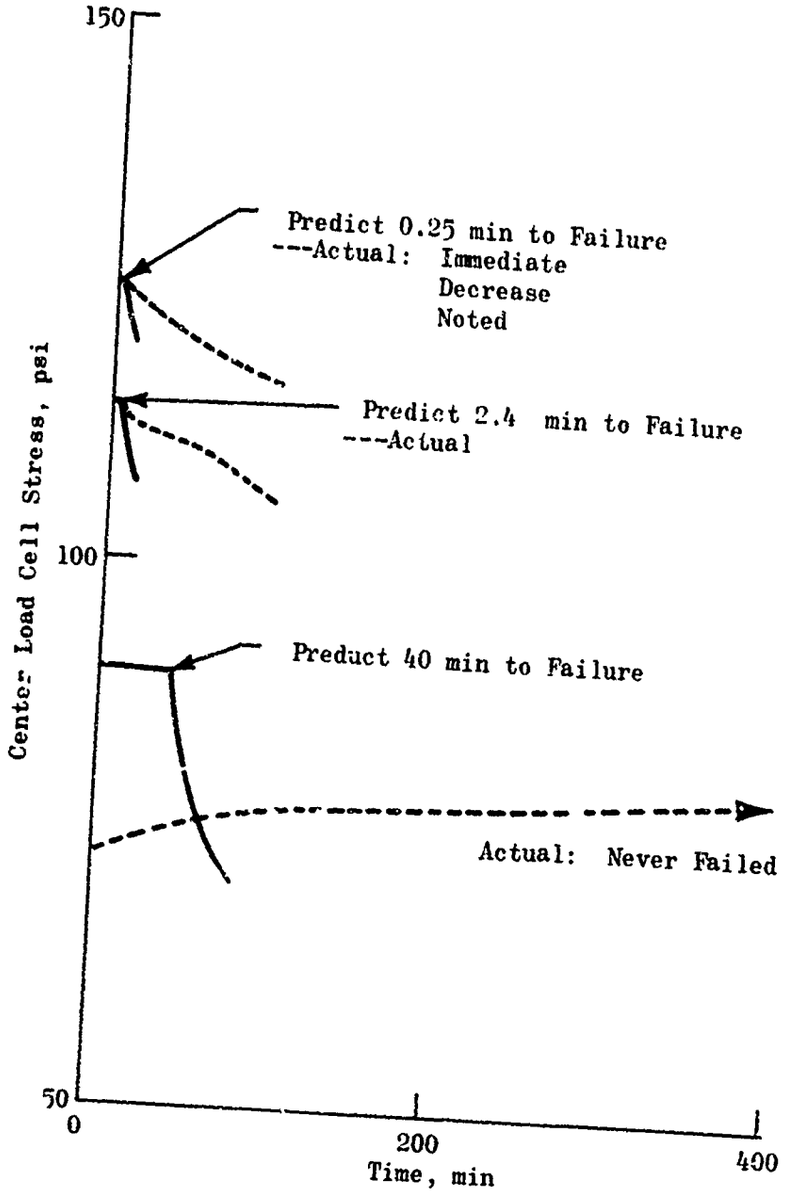

Figure 14. Theory-vs-Test Results for Constant Load Poker Chip Tests (Predictions based on γ/a_o = 51.1 in.-lb/in.^{3} deduced from constant stress rate tests at 77 F)

One other significant aspect of the curves in Fig. 12 involves the plots resulting from the 600-pound test. The output of the center load cell continued to rise throughout this test. The more incompressible the specimen material is (i.e., $K \gg G$), the larger the center load cell output will be (28). The limiting value will be 2 x P/A when $K \to \infty$ or $G \to 0$. The continuing increase in the center load cell reading in the 600-pound test was interpreted to indicate that no flaw-type failures were present and that the shear modulus, G, was relaxing at a decidedly faster rate than the bulk modulus, K.

Calculations of predicted times to failure during these tests were based on the criticality formula for the time to failure, t_o, following a constant stress test

$$\frac{\sigma_o}{1-k^3} = \frac{4}{3}\sqrt{\frac{\gamma/a_o}{2\,D_{crp}\,(t_o) - D_g}} \qquad (90)$$

although the stress history as recorded by the center load cell was certainly not constant. However, this calculation should provide a reasonable estimate of the times to failure.

Page 58 is blank

SECTION IV

STATIC LOADINGS ON BIAXIAL STRIP SPECIMENS

In the previous discussion and interpretation of the poker chip results it was shown that small deviations from a linear loading history, of either the stress or strain, exert little influence on the failure stresses and strains predicted on the basis of the straightline history. This provided the license necessary to draw conclusions about the values of theoretical parameters with only the point values of failure stresses and strains following constant strain rate tests of biaxial strips. Several of these tests were conducted and reported by Lockheed. Interpretation of the resulting data to obtain the fracture parameters appropriate for the biaxial specimen will be discussed first. Then by using the results of the elemental tests the analytical expressions of Tables II and III make it possible to predict the time to failure following the bilinear strain histories. Two tests of this nature were performed, and the measured and predicted failures are indicated.

CONSTANT RATE TESTS

The failure data on which the calculations of these sections are based were collected by Lockheed during the characterization phase of the Cumulative Damage program. The small biaxial strip specimens, which measured 7.5 x 0.25 x 1.5 inches long, were tested in tension in an Instron machine. Strain rates were varied over a 4-decade range by setting the crosshead speeds to 0.01, 0.1, 1.0 and 10.0 in./min. Their magnitudes were calculated by dividing these speeds by the specimen length, 1.5 inches. The tests were run at nine temperatures varying from -100 to 200 F. Some of those tests run at 1 in./min (three replicate specimens at each temperature) were stopped when the strain level reached 2.5%, and the resulting force relaxation was monitored with time. After a pause of about 10 minutes, the constant rate loading was resumed and continued until failure. No variation could be detected between the results of the continuous and the interrupted tests.

In general, the maximum stress was used as the criterion for failure. Observers at Lockheed reported only slight differences from the time of the observation of the first crack and the maximum stress level. The reported failure stresses and failure strains were plotted against temperature in Fig. 15 which was taken directly from (29).

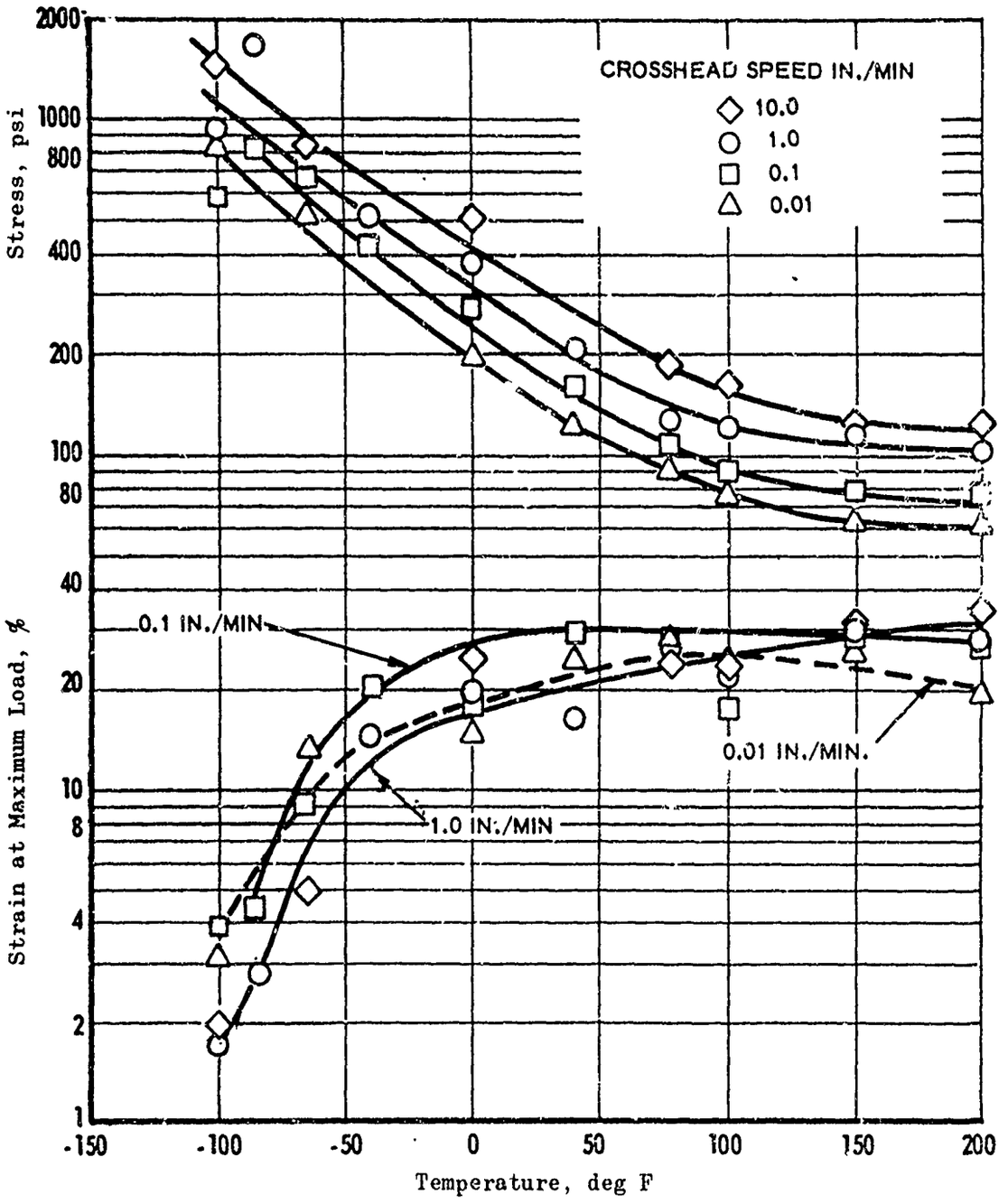

Figure 15. Strip Biaxial Failure Stress and Strain vs Temperature-0064-61E Control Propellant

DATA INTERPRETATION

Knowing both the failure stresses and strains, it is possible, providing the loading history is known, to use the fracture equations of Tables II and III to solve for both γ/a_o and k. The exact time history of neither the stress nor the strain was available. However, because the strains were imposed by a constant crosshead movement rate, because the strip specimen is small, and because the propellant is relatively compliant it seems reasonable to assume a constant strain rate history. The force response to a linear strain history on a biaxial strip at room temperature, shown in Fig. 6 , Appendix IX, reveals that under this condition the viscoelastic effects are not too great and the force is relatively linear in time. Linear rates were assumed for both stress and strain because slight variations from a linear history are believed to make only slight differences in the results (see Section III). Hence, the formulas for criticality of a flaw in a plane stress body (Tables II and III) following linear histories were applied.

Since both failure stresses and strains are reported, two equations can be written for each test, i.e., equations having the two unknowns, k and γ/a_o. By assuming that the time-temperature shift was appropriate for the material properties, data at all temperatures were used. The values used in the calculations are summarized in Table VIII for the strain boundary and Table IX for the stress boundary. The two simultaneous equations originate with the criticality expressions of Tables II and III. The expression for the incipient growth of a cylindrical flaw in a plane strain body following a linear strain history is given by

$$\frac{\gamma}{8a_o}\left(1 + 3k^2\right)^2 = \left(\frac{u_o\, c\, t_o}{b}\right)^2 \left(\frac{2}{t_o^2}\right) E_{rel}^{(2)}\,(t_o) \tag{91}$$

and following a linear stress history by

$$\frac{\gamma}{2a_o}\left(1 - k^2\right)^2 = \left(\sigma_o\, c\, t_o\right)^2 \left\{ 2\left[\frac{1}{t_o} D_{crp}^{(1)}\,(t_o)\right] - \frac{2}{t_o^2} D_{crp}^{(2)}\,(t_o)\right\} \tag{92}$$

TABLE VIII. CALCULATIONS USING BIAXIAL STRIP FAILURE STRAINS

Calculated Strain Rate, in./in./min		Temperature, deg F								
		-100 ($\log a_T = 7.8$)	-65 ($\log a_T = 5.2$)	-40 ($\log a_T = 3.6$)	0 ($\log a_T = 1.7$)	40 ($\log a_T = 0.7$)	77 ($\log a_T = 0.0$)	100 ($\log a_T = -0.5$)	150 ($\log a_T = -1.75$)	200 ($\log a_T = -3.6$)
6.67	ε_f	0.019	0.05		0.246		0.238	0.233	0.309	0.343
	$\dot{\varepsilon} a_T$	42.1×10^{7}	33.4×10^{5}		33.4×10^{1}		6.67	2.11	119×10^{-3}	167×10^{-5}
	t_f/a_T	0.0451×10^{-9}	0.150×10^{-7}		0.000736		0.0357	0.110	2.60	205
	$(2/t_f^2)\, E_{rel}^{(2)}(t_f)$	102,000	32,500		3,700		1,770	1,420	830	442
0.667	ε_f	0.016		0.147	0.183	0.163	0.268	0.225	0.333	0.375
	$\dot{\varepsilon} a_T$	4.21×10^{7}		2.65×10^{3}	3.34×10^{1}	3.34	0.667	0.211	11.9×10^{-3}	16.7×10^{-5}
	t_f/a_T	0.38×10^{-9}		5.55×10^{-5}	0.00548	0.0488	0.402	1.07	28.0	2,228
	$(2/t_f^2)\, E_{rel}^{(2)}(t_f)$	68,000		6,200	2,520	1,680	1,130	870	580	338
0.0667	ε_f	0.039	0.089	0.201	0.176	0.286	0.282	0.172	0.285	0.263
	$\dot{\varepsilon} a_T$	0.421×10^{7}	0.334×10^{5}	0.265×10^{3}	0.334×10^{1}	0.334	0.0667	0.0211	1.19×10^{-3}	1.67×10^{-5}
	t_f/a_T	9.26×10^{-9}	26.6×10^{-7}	75.8×10^{-5}	0.0527	0.856	4.25	8.15	239	15,749
	$(2/t_f^2)\, E_{rel}^{(2)}(t_f)$	35,500	11,300	3,700	1,630	1,000	760	700	440	283
0.00667	ε_f	0.031	0.13		0.147	0.241	0.275	0.245	0.254	0.194
	$\dot{\varepsilon} a_T$	0.0421×10^{7}	0.0334×10^{5}		0.0334×10^{1}	0.0334	0.00667	0.00211	0.119×10^{-3}	0.167×10^{-5}
	t_f/a_T	73.6×10^{-9}	389×10^{-7}		0.440	7.22	41.2	116	2134	115,168
	$(2/t_f^2)\, E_{rel}^{(2)}(t_f)$	23,500	6,700		1,110	710	550	480	3	245

TABLE IX. CALCULATIONS USING BIAXIAL STRIP FAILURE STRESSES

Calculated Strain Rate, in./in./min		Temperature, deg F								
		-100 (log a_T = 7.8)	-65 (log a_T = 5.2)	-40 (log a_T = 3.6)	0 (log a_T = 1.7)	40 (log a_T = 0.7)	77 (log a_T = 0.0)	100 (log a_T = -0.5)	150 (log a_T = -1.75)	200 (log a_T = -3.6)
6.67	σ_f	1455	836		505,000		183	163	123	121
	t_f/a_T	0.0451×10^{-9}	0.150×10^{-7}		0.000736		0.0357	0.110	2.60	205
	$\dot{\sigma}_T$	$364 \times 10^{+11}$	$55.7 \times 10^{+9}$		686,000		5,130	1,480	47.4	0.59
	$2(\frac{1}{t_f})D^{(1)}_{crp}(t_f) - (\frac{2}{t_f^2})D^{(2)}_{crp}(t_f)$	0.000011	0.0000355		0.000312		0.00075	0.00082	0.00142	0.00253
0.667	σ_f	932		516	368	201	123	120	115	102
	t_f/a_T	0.38×10^{-9}		5.55×10^{-5}	0.00548	0.0488	0.402	1.07	28.0	2.230
	$\dot{\sigma}_T$	$24.5 \times 10^{+11}$		$0.930 \times 10^{+7}$	67,500	4,120	306	112	4.10	0.0458
	$2(\frac{1}{t_f})D^{(1)}_{crp}(t_f) - (\frac{2}{t_f^2})D^{(2)}_{crp}(t_f)$	0.0000166		0.000186	0.000455	0.00071	0.00102	0.00132	0.00204	0.0033
0.0667	σ_f	578	679	418	278	158	109	88.6	78.3	72.7
	t_f/a_T	9.26×10^{-9}	26.6×10^{-7}	75.8×10^{-5}	0.0527	0.856	4.23	8.15	239	15,750
	$\dot{\sigma}_T$	$0.624 \times 10^{+11}$	$0.255 \times 10^{+9}$	0.0551×10^{7}	5,270	185	25.8	10.9	0.309	0.00461
	$2(\frac{1}{t_f})D^{(1)}_{crp}(t_f) - (\frac{2}{t_f^2})D^{(2)}_{crp}(t_f)$	0.0000332	0.000103	0.000312	0.000810	0.00117	0.00154	0.00167	0.00255	0.00386
0.00667	σ_f	850	514		195	121	89.3	77.0	63.5	62.7
	t_f/a_T	73.6×10^{-9}	389×10^{-7}		0.440	7.22	41.2	116	2134	116,200
	$\dot{\sigma}_T$	$0.115 \times 10^{+11}$	$0.0132 \times 10^{+9}$		443	16.75	2.17	0.666	0.0298	0.00054
	$2(\frac{1}{t_f})D^{(1)}_{crp}(t_f) - (\frac{2}{t_f^2})D^{(2)}_{crp}(t_f)$	0.0000500	0.000172		0.00105	0.00166	0.00218	0.00235	0.0033	0.0045

Solving Eq. 91 and 92 for the unknown k, one finds

$$k = \sqrt{\frac{1 - \frac{\sigma_o \, c \, t_o}{u_o \, c \, t_o}}{2\left(\frac{u_o \, c \, t_o}{b}\right)} \sqrt{\frac{2\left[\frac{1}{t_o} D^{(1)}_{crp}(t_o)\right] - \frac{2}{t_o^2} D^{(2)}_{crp}(t_o)}{\frac{2}{t_o^2} E^{(2)}_{rel}(t_o)}}}{1 + \frac{3}{2} \frac{\sigma_o \, c \, t_o}{\left(\frac{u_o \, c \, t_o}{b}\right)} \sqrt{\frac{2\left[\frac{1}{t_o} D^{(1)}_{crp}(t_o)\right] - \frac{2}{t_o^2} D^{(2)}_{crp}(t_o)}{\frac{2}{t_o^2} E^{(2)}_{rel}(t_o)}}} \qquad (93)$$

which permits solving either Eq. 91 or 92 for γ/a_o.

These numerical calculations are outlined in Table X and the properties of relaxation modulus and creep compliance used herein were determined by biaxial tests and reported in Appendix V.

The results of the calculations are summarized in Fig. 16 and 17 with k and γ/a_o plotted, respectively, showing a definite influence of both temperature and strain rate. The geometrical parameter, $k (= a_o/b)$, is seen to be fairly constant in all tests. However, γ/a_o fluctuates widely indicating a definite sensitivity to both rates and temperatures. Because the geometrical parameter does not vary widely it was suspected that the initial flaw size a_o was also relatively constant; so most of the variation was credited to the characteristic strain energy release rate, γ. Because of the prevalence of opinion that this term should be a constant, a brief examination of the influences that might make it appear to be time and temperature dependent was made. These considerations included the difference in the stress state in a biaxial strip from the uniform stress assumed for the model, the effects of finite strains, and the error-producing effects that the assumption of incompressibility would give to the apparent γ. Each of these is discussed.

TABLE X. CALCULATION OF BEST γ/a_o AND k TO FIT BIAXIAL STATIC TESTS

Temperature, deg F	Strain Rate, in./in./min	Failure Stress, $c_o c_1 t_o$ psi	Failure Strain, $v_o c_2 t_o/b$, in./in.	$\left[2\left(\frac{1}{t_o}\right) D^{(1)}_{crp}(t_o) - \frac{2}{t_o^2} D^{(2)}_{crp}(t_o)\right]$ sq in./lb	$\frac{2}{t_o^2} E^{(2)}_{rel}(t_o)$, psi	k, in./in.	γ/a_o, in.-lb/cu in.
-100	6.67	1455	0.019	0.0000110	102,000	0.525	88.9
	0.667	932	0.016	0.0000166	68,000	0.480	48.6
	0.0667	578	0.039	0.0000332	35,500	0.659	69.3
	0.00667	850	0.031	0.0000500	23,500	0.355	94.6
-65	6.67	836	0.05	0.0000355	32,500	0.629	136
	0.0667	679	0.089	0.000103	11,300	0.551	196
	0.00667	514	0.130	0.000172	6,700	0.593	216
-40	0.667	516	0.147	0.000186	6,200	0.603	244
	0.0667	418	0.201	0.000312	3,700	0.605	270
0	6.67	505	0.246	0.000312	3,700	0.609	402
	0.667	368	0.183	0.000455	2,520	0.501	219
	0.0667	278	0.176	0.000810	1,630	0.408	180
	0.00667	195	0.147	0.00105	1,110	0.346	103
40	0.667	201	0.163	0.000710	1,680	0.732	267
	0.0667	158	0.286	0.00117	1,000	0.609	148
	0.00667	121	0.241	0.00166	710	0.535	95.2
77	6.67	183	0.238	0.000750	1,770	0.655	144
	0.667	123	0.268	0.00102	1,130	0.688	111
	0.0667	109	0.282	0.00152	760	0.632	100
	0.00667	89.3	0.275	0.00218	550	0.586	80.8
100	6.67	163	0.233	0.000820	1,420	0.639	124
	0.667	120	0.225	0.00132	870	0.582	87.1
	0.0667	88.6	0.172	0.00167	700	0.525	50
	0.00667	77	0.245	0.00235	480	0.566	60.1
150	6.67	123	0.309	0.00142	830	0.645	126
	0.667	115	0.333	0.00204	580	0.584	124
	0.0667	78.3	0.285	0.00255	440	0.579	70.9
	0.00667	63.5	0.254	0.0033	340	0.530	51.5
200	6.67	121	0.343	0.00253	442	0.506	134
	0.667	102	0.372	0.0033	338	0.500	122
	0.0667	72.7	0.263	0.00386	283	0.440	62.5
	0.00667	62.7	0.194	0.0045	245	0.384	48.6

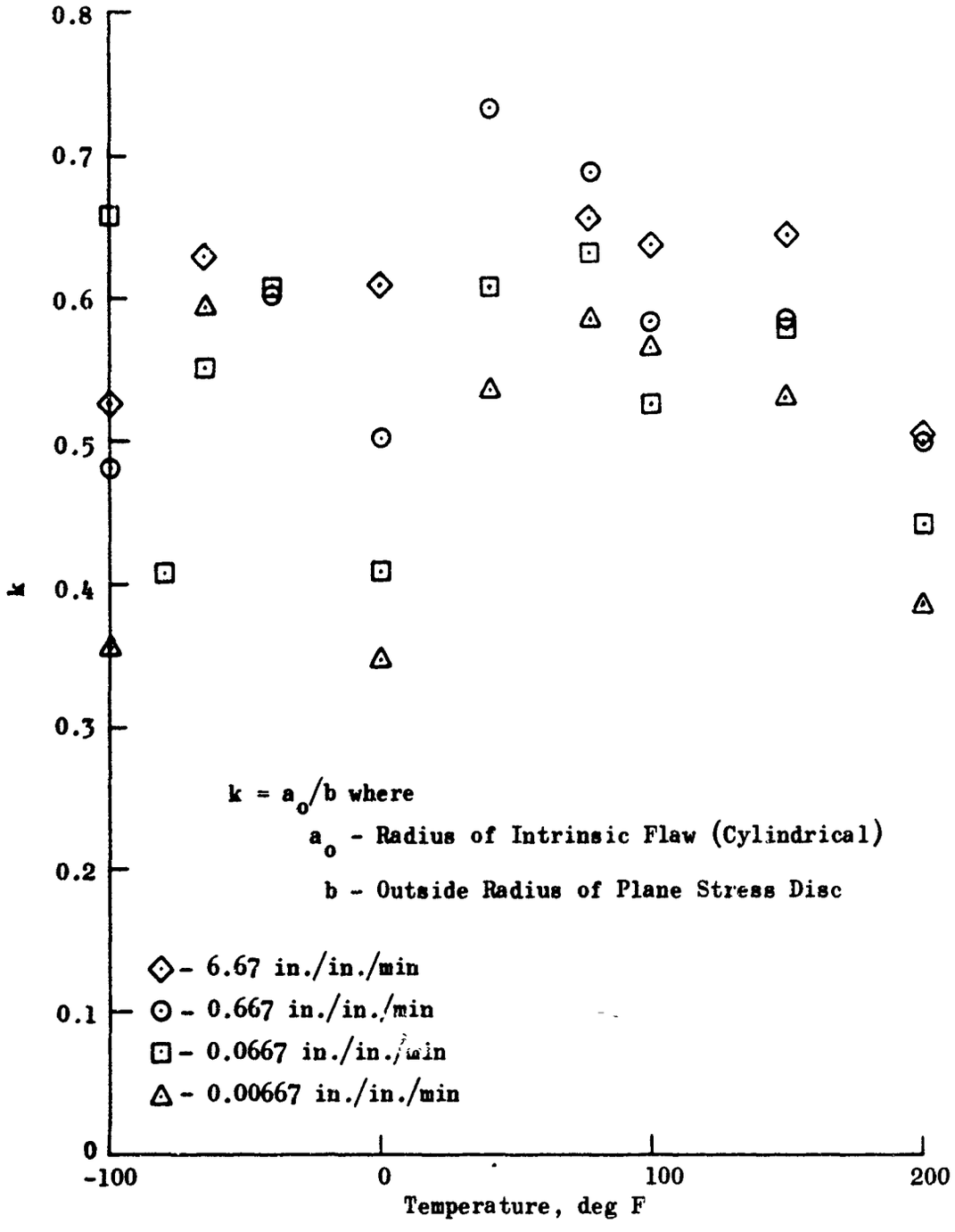

Figure 16. The Values Calculated for k Using Propellant Failure Data Furnished by Lockheed. (The biaxial strip tests were run with the cross-head set to move at a constant rate.)

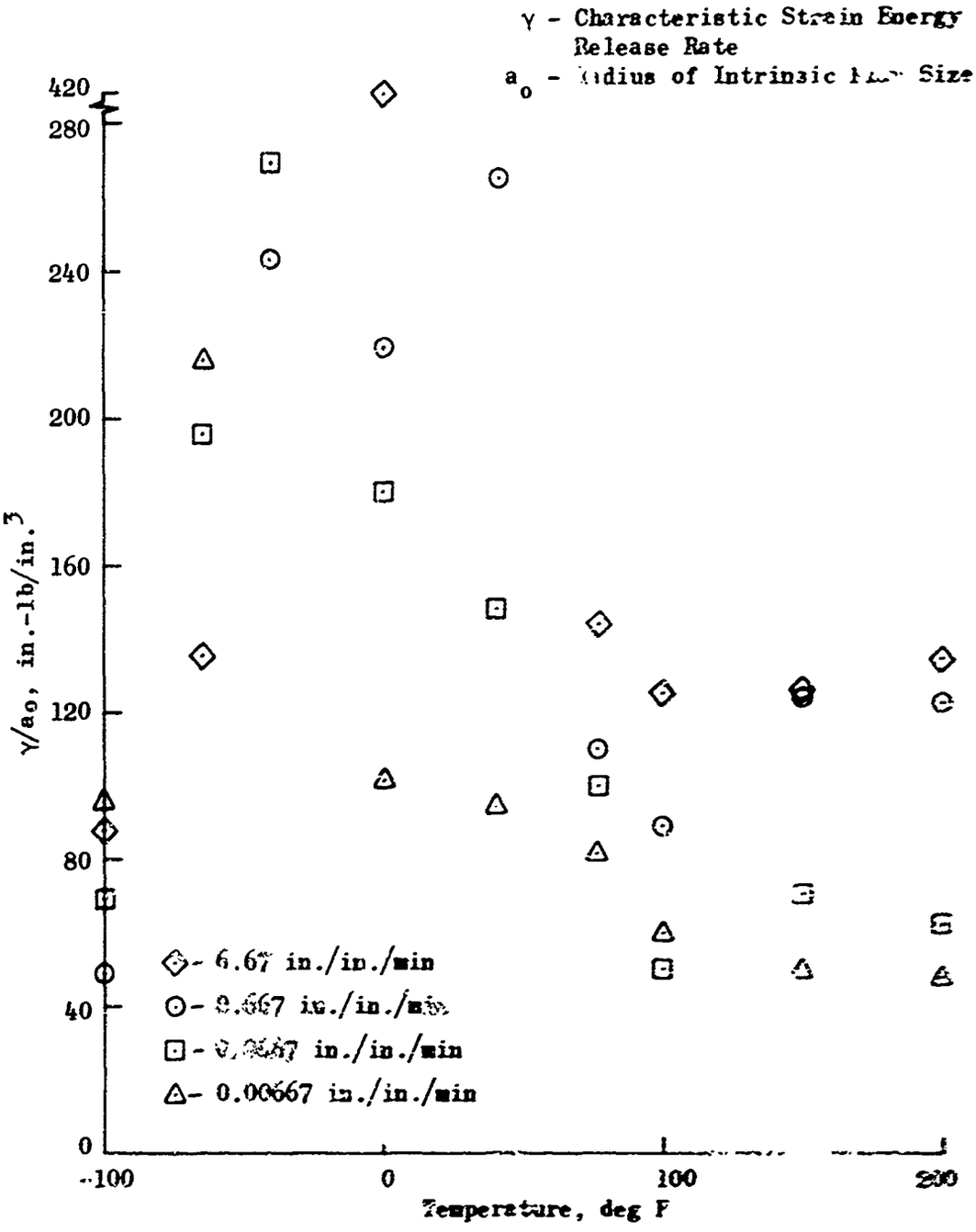

Figure 17. The Values Calculated for γ/a_0 Using Propellant Failure Data Furnished By Lockheed. (The biaxial strip tests were run with the crosshead set to move at a constant rate.)

UNIFORM TENSION ONLY

The basic model from which the mathematics were derived was considered in an effort to determine a plausible explanation for the variability. The axially symmetric geometry (see Fig. 18a) is subjected to a uniform tensile stress. The fact that the resulting stress field is axially symmetric provides the basis for a mathematically tractable solution. It should be noted, however, that the actual state of stress in a biaxial strip specimen is quite different from the hypothesized model. If the strip is considered to be very wide so the strain in the x-direction (i.e., ϵ_x distant from the edges) is taken as zero, the state of stress resulting from a tensile displacement, v, in the y-direction can be deduced. To preserve constancy, Poisson's ratio (ν) is set equal to 0.5. Then using Hooke's law for the plane stress (thin) specimen ($\sigma_z = 0$, where z is the coordinate taken through the thickness of the specimen) one can deduce using

$$\epsilon_x = \frac{1}{E}\left[\sigma_x - \nu\left(\sigma_y + \sigma_z\right)\right] = 0 \qquad (94)$$

that

$$\sigma_x = \nu\,\sigma_y \qquad (95)$$

or with $\nu = 0.5$

$$\sigma_x = \frac{1}{2}\,\sigma_y. \qquad (96)$$

This is the state of stress illustrated in Fig. 18b and is quite different from the uniform stress of the hypothesized model. Just how different can best be visualized by separating the stresses of Fig. 18b into the uniform portion and the shear portion (see Fig. 19). This suggests that the results of the criticality calculations might be improved if only the uniform tension component of the stress state in the biaxial strip were used.

Using this approach, the calculations were simplified by assuming $k = 0.6$. This is a reasonable assumption in view of the values plotted in Fig. 16. The resulting calculations are summarized in Table XI. While

TABLE XI. CALCULATION OF γ/a_o USING ONLY THE UNIFORM STRESS FROM THE BIAXIAL STRIPS

Temperature, deg F	Strain Rate, in./in./min	Failure Stress, $\sigma_o c_1 t_o$, psi	Uniform Stress, $\frac{3}{4}\sigma_o c_1 t_o$, psi	$2\left(\frac{1}{t_o}\right) D_{crp}^{(1)}(t_o) - \frac{2}{t_o^2} D_{crp}^{(2)}(t_o)$, psi	γ/a_o, in.-lb/cu in.
-100	6.67	1,455	1,090	0 10	63.8
	0.667	932	700	0.0000166	39.7
	0.0667	578	434	0.0000332	30.5
	0.00667	850	637	0.0000500	99.1
-65	6.67	836	627	0.0000355	68.1
	0.0667	679	509	0.000103	130
	0.00667	514	385	0.000172	124
-40	0.667	516	388	0.000186	136
	0.0667	418	314	0.000312	150
0	6.67	505	378	0.000312	218
	0.667	368	276	0.000455	169
	0.0667	278	208	0.000810	171
	0.00667	195	146	0.00105	109
40	0.667	201	151	0.000710	79
	0.0667	158	118	0.00117	79.5
	0.00667	121	90.8	0.00166	66.8
77	6.67	183	137	0.000750	68.7
	0.667	123	92	0.00102	42.2
	0.0667	109	81.7	0.00152	49.5
	0.00667	89.3	67	0.00218	47.8
100	6.67	163	122	0.000820	59.6
	0.667	120	90	0.00132	52.2
	0.0667	88.6	66.5	0.00167	36.1
	0.00667	77	57.7	0.00235	38.2
150	6.67	123	92	0.00142	58.7
	0.667	115	86.2	0.00204	74
	0.0667	78.3	58.6	0.00255	42.7
	0.00667	63.5	47.6	0.0033	36.5
200	6.67	121	90.5	0.00253	101
	0.667	102	76.5	0.0033	94.3
	0.0667	72.7	54.6	0.00386	56.2
	0.00667	62.7	47	0.0045	48.5

it is evident that this approach yields γ/a_o values more constant than those indicated in Table X, it is readily obvious that the apparent characteristic strain energy release rates are not nearly constant enough for practical use.

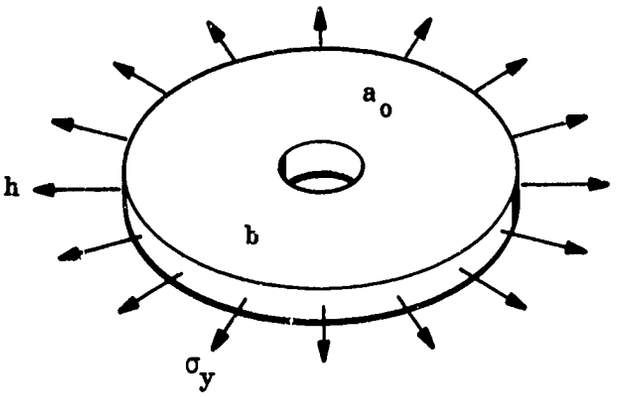

a. Idealized Model on which the Mathematics are Based (Uniform Tensile Stress)

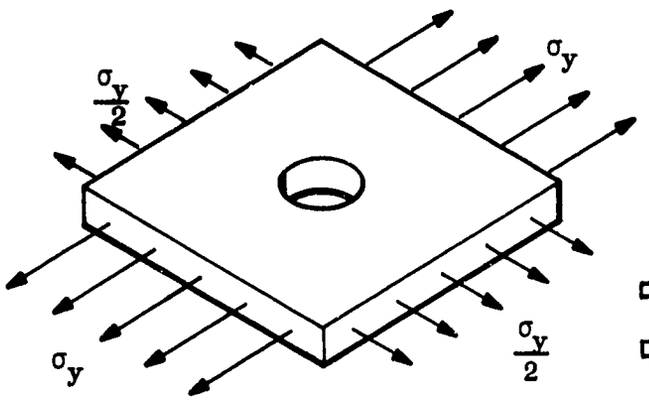

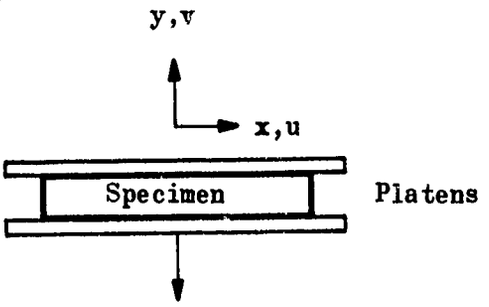

b. Model Appropriate for Biaxial Strip (2:1 Stress Ratio)

Figure 18. States of Stress for Idealized and Realistic Models

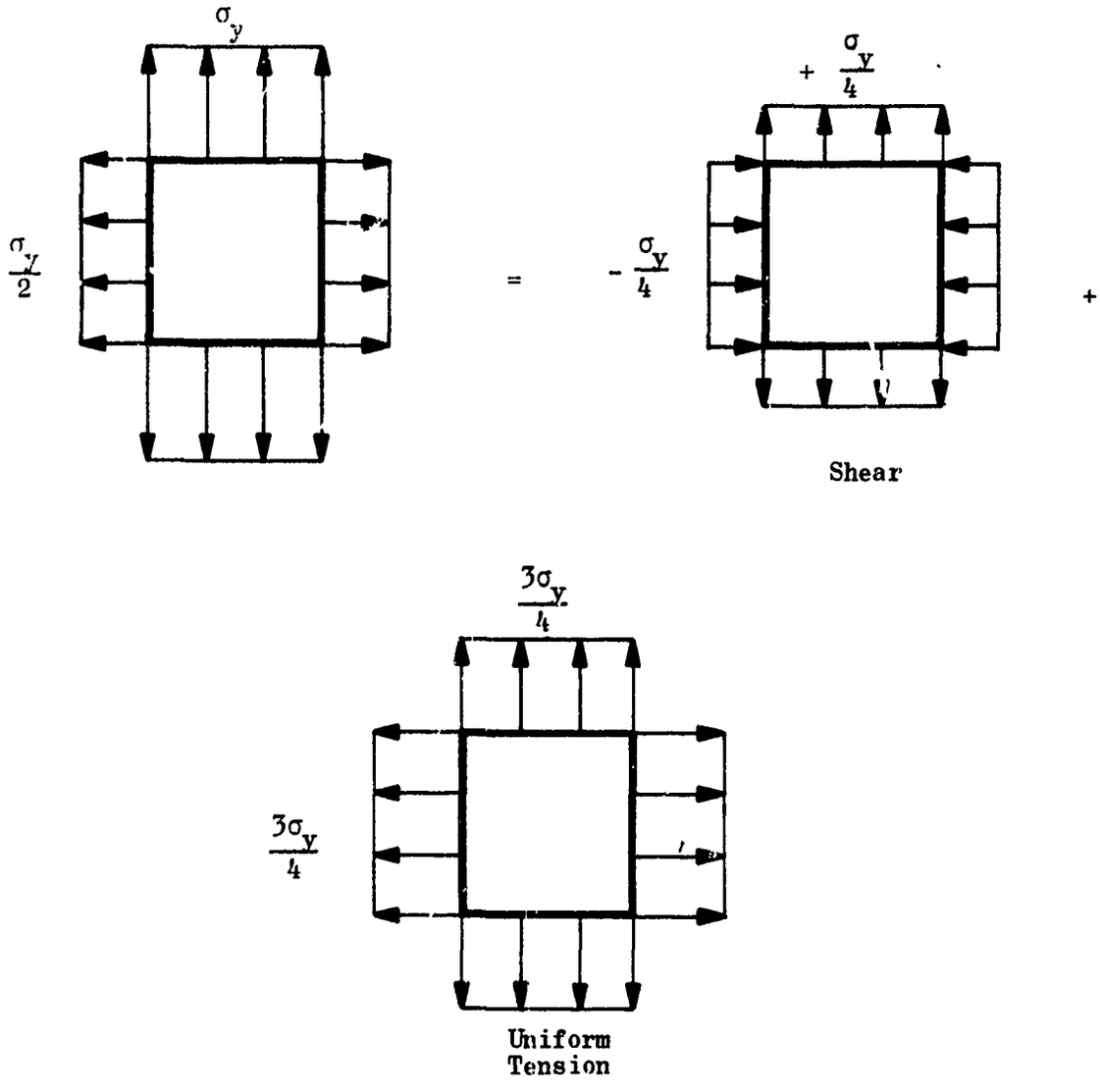

Figure 19. The Stresses of the Biaxial Strip Can Be Separated into a Uniform Tension Portion and a Pure Shear Portion. (Note the value of the uniform tensile stress is $\frac{3\sigma_y}{4}$).

LARGE STRAINS

Another factor certain to influence the results is the inapplicability of the linear viscoelasticity at the higher strain levels inherent in the biaxial strip tests. The importance of accounting for the finite strains, even in the poker chip specimen, is discussed in detail by Blatz in Appendix I. The great significance of the finite strains in the biaxial strip where the gross strain at failure is on the order of 30% is readily apparent, especially when it is contrasted with the poker chip where the gross strain at failure is only about 2%.

One approach to determining the significance of this effect is to contrast the example γ's calculated using Hookean and neo-Hookean formulations in Fig. 3 and 4 in Appendix I. When the modulus is low (higher strains) the solution which takes finite strains into account gives a significantly different, and higher, value for the characteristic strain energy release rate. Consequently, it is believed that large deformations are important to fracture predictions in propellants, especially at free grain boundaries such as the inner port surface. This influence might be a primary one in creating the apparent rate and temperature sensitivity of γ.

COMPRESSIBILITY

Blatz also discussed one other factor which may cause γ to appear time and temperature dependent in these tests. That is the assumption of incompressibility that was made to formulate the criticality equations of Tables II and III.

It is universally agreed that extensive dewetting, hence dilatation, is present in the biaxial strip under large tensile strains. Blatz suggests that to account for the volume change in an elastic material one can simply replace the modulus, E, by $E/[2(1 - \nu)]$. If the dewetting process is a function of time and temperature it is clear that a calculation of γ which disregards this effect will yield values which appear to be functions of these variables even though it might be completely independent of them.

SUMMARY

The implications of each of the three influences are obviously important. But it is clear that definitive statements concerning what appears to be a time and temperature dependence by the characteristic strain energy release rate as deduced from biaxial strip tensile tests cannot be made until a careful study of these effects has been completed.

BILINEAR TESTS

Two bilinear strain rate tests were conducted using a biaxial strip specimen. This specimen, 13.25 x 3/8 x 2.8 inches long, is somewhat larger than that employed at Lockheed; but the proportions are not greatly different. The cumulative damage testing machine, which can be preprogrammed to generate two ramp rates in sequence either for the force or for the platen displacement, was used for the tests.

The two rates were chosen about 4 decades apart in both tests. One was run slow-to-fast, and the other was run fast-to-slow. Even greater rate changes could have been studied, but these variations appeared sufficiently large for study purposes, yet provided a high rate still slow enough to permit the visual observation of failure.

Strain and maximum stress histories of the two tests are given in Fig. 20. Both tests were performed with the specimen at 140 F.

FAILURE PREDICTION (BILINEAR RATES)

Time-to-failure predictions were made using the appropriate expression for criticality and the γ/a_0 and k values found in the constant rate tests. The expression for a plane stress body subjected to a bilinear strain rate is

$$\frac{\gamma}{8a_0}(1 + 3k^2)^2 = \left(\frac{u_0}{b}\right)^2 \left[c_1 (c_1 - c_2) E_{rel}^{(2)}(t_1) + c_1 c_2 E_{rel}^{(2)}(t_f) + c_2 (c_2 - c_1) E_{rel}^{(2)}(t_f - t_1)\right] \quad (97)$$

where t_f represents the time at which the strain buildup changes rate.

The one problem is which value should be appropriately used for γ/a_0 in this calculation. By examining the values deduced from the constant rate tests and plotted in Fig. 17 one can sketch a curve of γ/a_0 vs loading rate as shown in Fig. 21. This curve can then be used to deduce values corresponding to the terminal loading rates in the two bilinear tests. They were found to be

Test No. 114: $\frac{c_2 u_o}{b} = 2.76$ in./in./min, $\frac{\gamma}{a_o} = 160 \frac{\text{in.-lb}}{\text{in.}^3}$

Test No. 116: $\frac{c_2 u_o}{b} = 0.00238$ in./in./min, $\frac{\gamma}{a_o} = 44 \frac{\text{in.-lb}}{\text{in.}^3}$

When substituted into Eq. 97 the values i[illegible] failure times of

Test No. 114: $t_f - t_i = 0.1121$ [illegible]

Test No. 116: $t_f - t_i = 460$ min

these predictions are compared with the [illegible] observed failure strains and times in Fig. 22.

Correlation of the limited observations to the predicted failures is not clearly indicated. However, the experiences of the associated contractors seemed to indicate a definite relationship between the failure stresses (or characteristic strain energy release rate) and the time a specimen surface has been exposed, particularly to humidity. Perhaps exposure variations of a similar order of magnitude as that of the prediction errors are expected merely from the data scatter and the aging effect.

Test No. 114

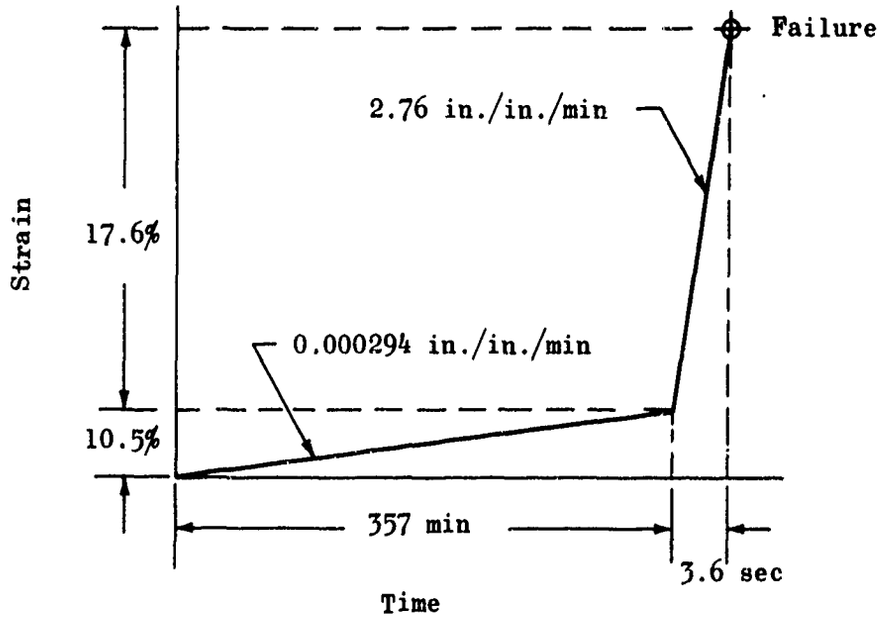

NOTE: Not To Scale

TEMP = 140 F

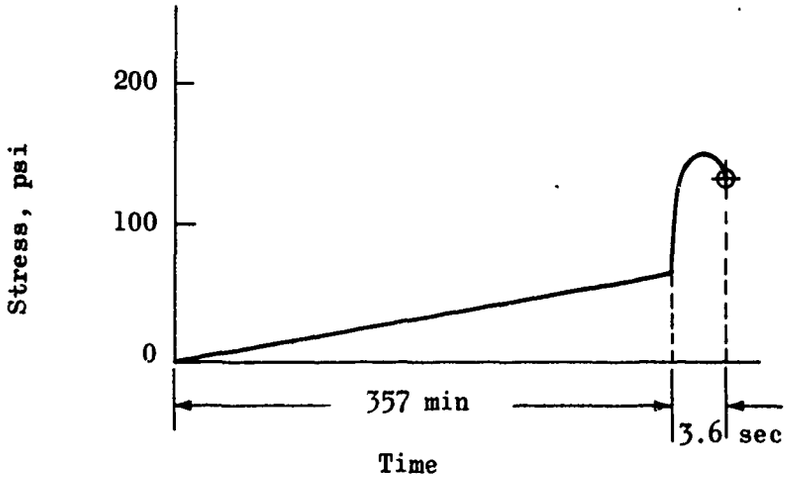

Figure 20. Stress and Strain Histories of the Two Bilinear Strain Rate Tests (biaxial strip specimen)

Test No. 116

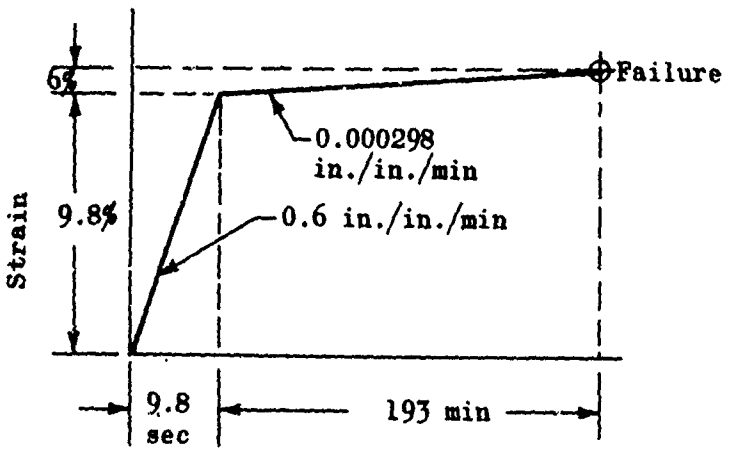

NOTE: Not to Scale

TEMP = 140 F

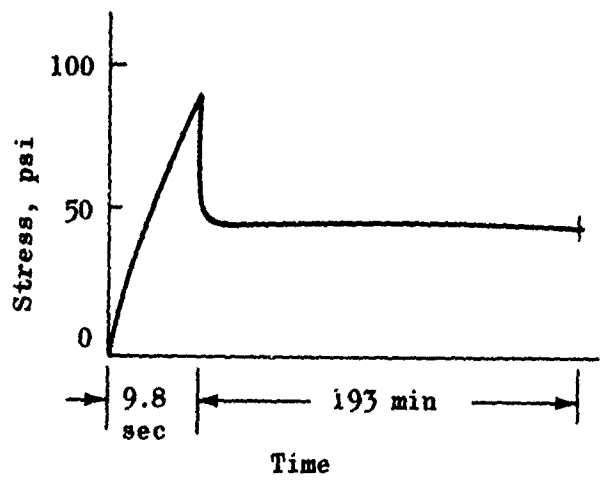

Figure 20. Concluded

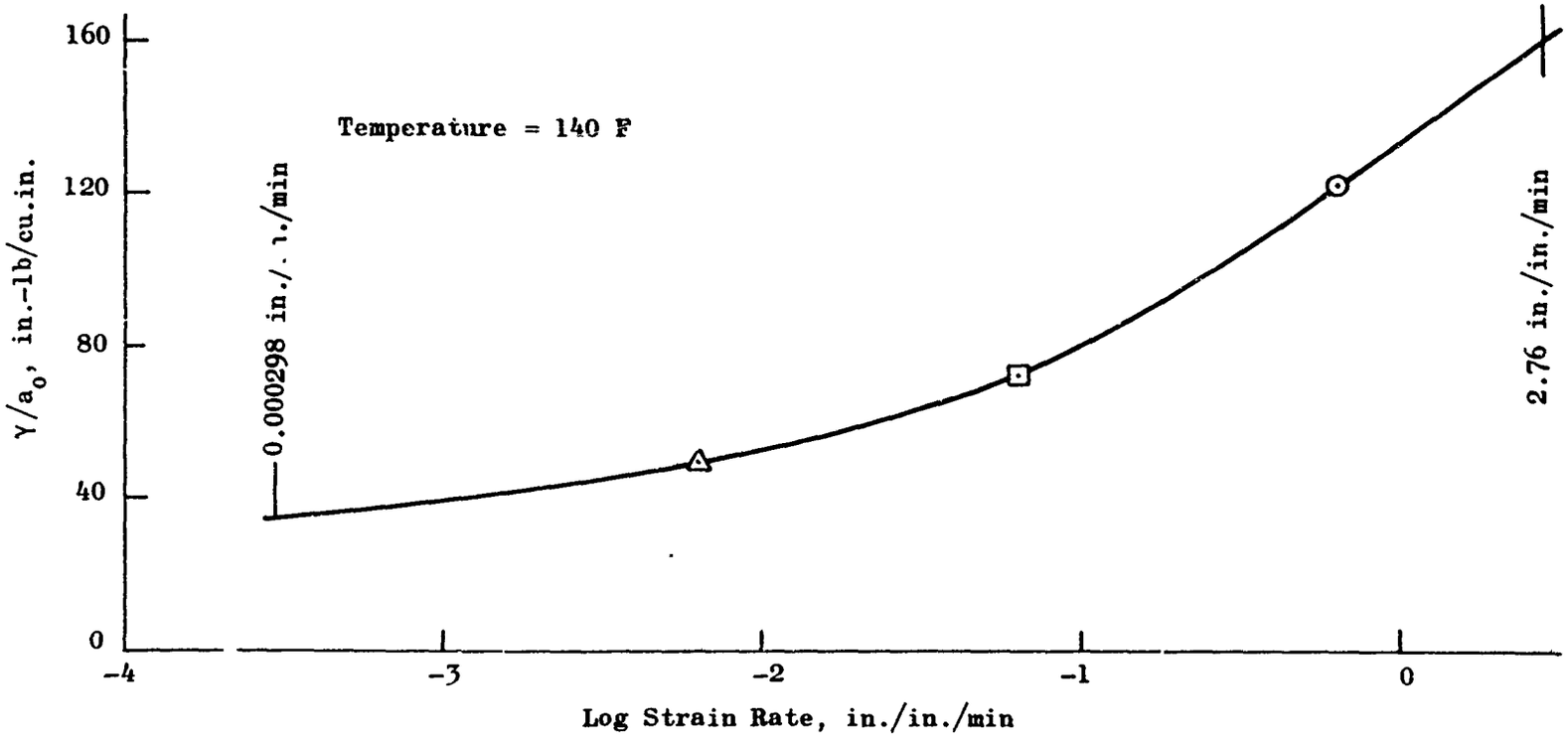

Figure 21. Variation of γ/a_o vs Strain Rate

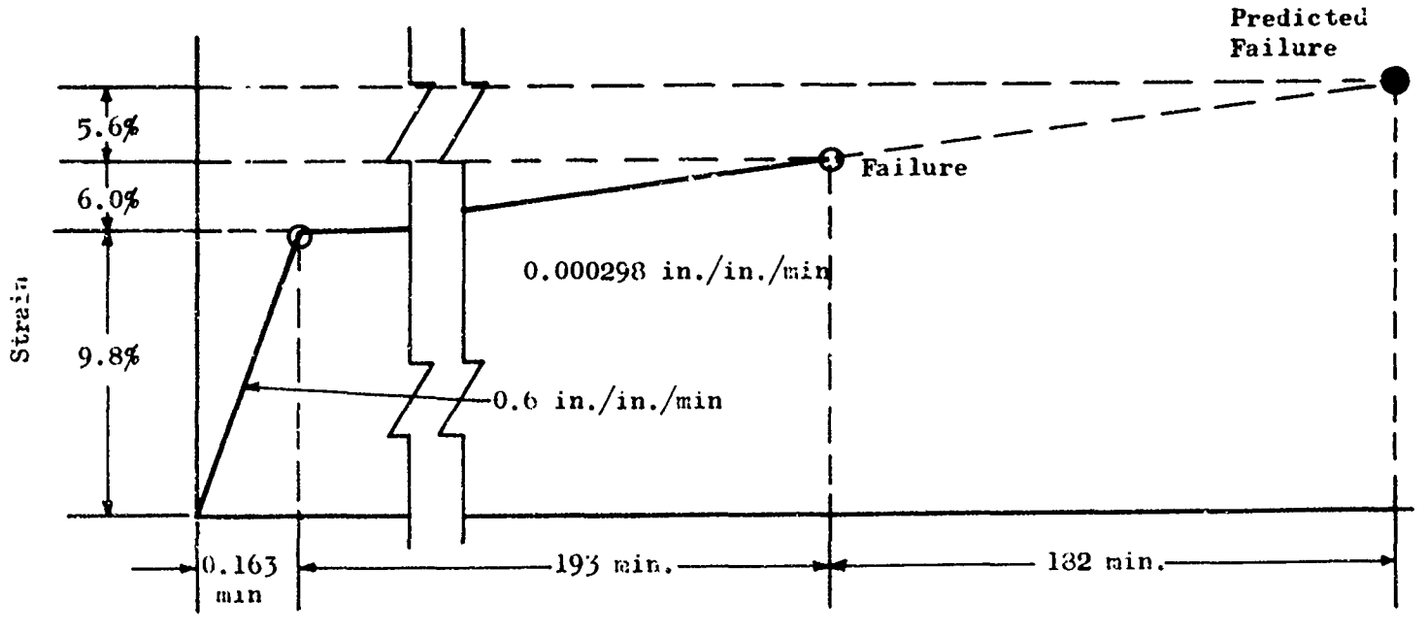

a. Fast-to-Slow

Figure 22. Predicted Failure Strains Compared with Those Observed in the Bilinear Strain Rate Tests

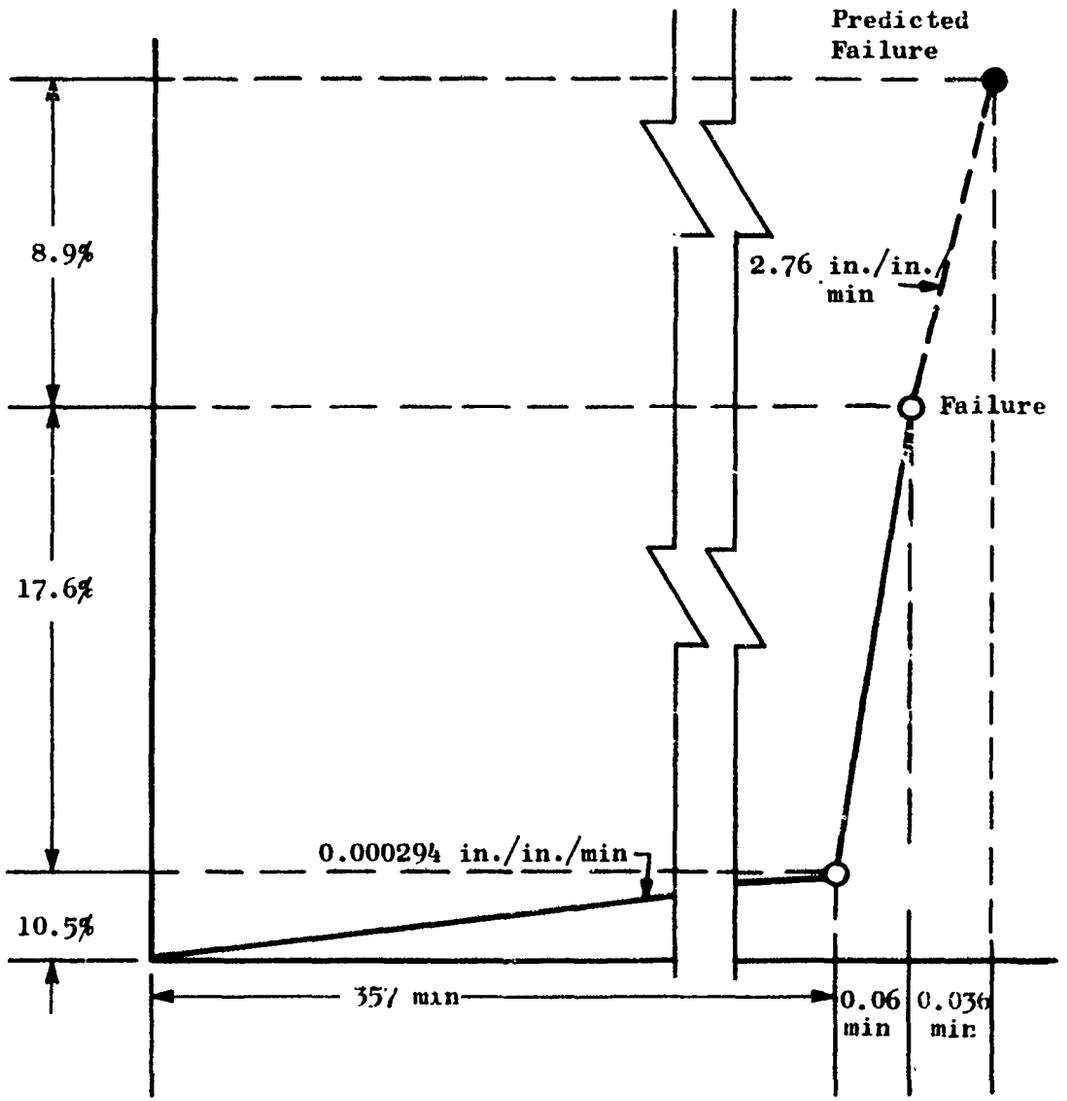

b. Slow-to-Fast

Figure 22. Concluded

Page 80 is blank

SECTION V

VIBRATION FATIGUE

The principal portion of Rocketdyne's effort on the Cumulative Damage program was given to vibration fatigue testing of biaxial strip specimens of propellant. These tests, which were conducted on a Cumulative Damage Tester fabricated by the MTS Corporation especially for this program, are described below. Data from tests having a displacement-controlled input (rather than force) are also reported. (The Cumulative Damage Tester and its capabilities are discussed in Appendix VI, and Data from force-controlled tests are summarized in Appendix VII.)

BIAXIAL FATIGUE TESTING PROGRAM

Three replicate biaxial fatigue tests were conducted at each of three vibration frequencies and three amplitudes to find the parameters γ/a_0 and k necessary to use the viscoelastic fracture expressions for crack initiation. The plan, Table XII, required replicate testing to give a measure of the reproducibility of such tests.

TABLE XII. PLANNED VIBRATION FATIGUE TESTS OF BIAXIAL PROPELLANT STRIPS PLATEN DISPLACEMENTS OF THE FORM

Platen Displacements of the Form:

$$u(t) = u_0 + u_0 \sin\omega t; \quad t > 0$$
$$= 0 \qquad\qquad ; \quad t < 0$$

Displacement, in.	Frequencies, cps		
	5	15	50
0.084	3	3	3
0.098	3	3	3
0.112	3	3	3

SPECIMEN PREPARATION

The biaxial strips, Fig. 23, were 14 x 2.8 x 3/8 inch, providing a length-to-width ratio of 5. However, because of the flared bond surface (the cross section was shaped exactly like a tab-ended JANAF specimen), it was necessary to machine both sides of the specimen.

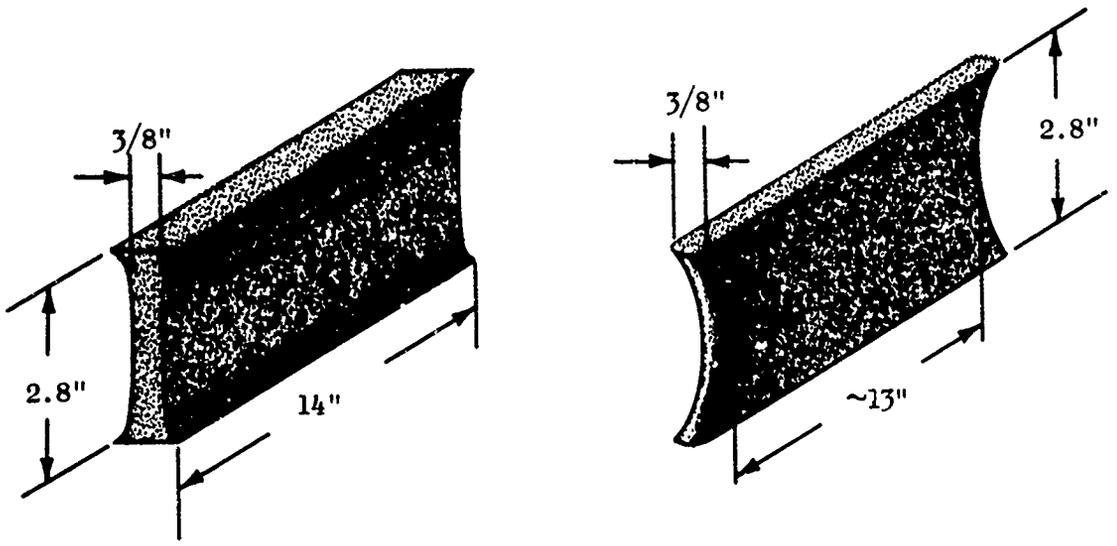

Figure 23. Original Biaxial Strip Specimen Design and the Revised Design Actually Used

Preliminary tests revaled that cracks would more often than not originate from a site within the body of the propellant when the end edges of the specimen were reinforced with a soft rubber, 3M's EC1949, and contoured as shown in Fig. 23b. Preliminary tests also showed that when the rubber was used to form fillets at the bond surfaces with the metal platens the expensive and tedious machining operations could be eliminated. Consequently, specimens used on this program were sawed directly from the bulk propellant blocks furnished by Lockheed. Only a slight and inexpensive milling operation was then required to form flat, parallel sides.

Each specimen was bonded to the platens in a specially constructed fixture which provided for proper alignment and dimensions. While the specimen was in the bonding fixture, a small thermocouple was placed on the flat propellant surface and covered with a thin layer of the EC1949 which was feathered as thin as possible near its edges. The thermocouple was always placed a slight distance from the specimen centerlines, both horizontally and vertically, in an attempt to deter crack initiation near the thermocouple.

Figure 24 shows a specimen mounted between the two platens ready for testing in the cumulative damage tester.

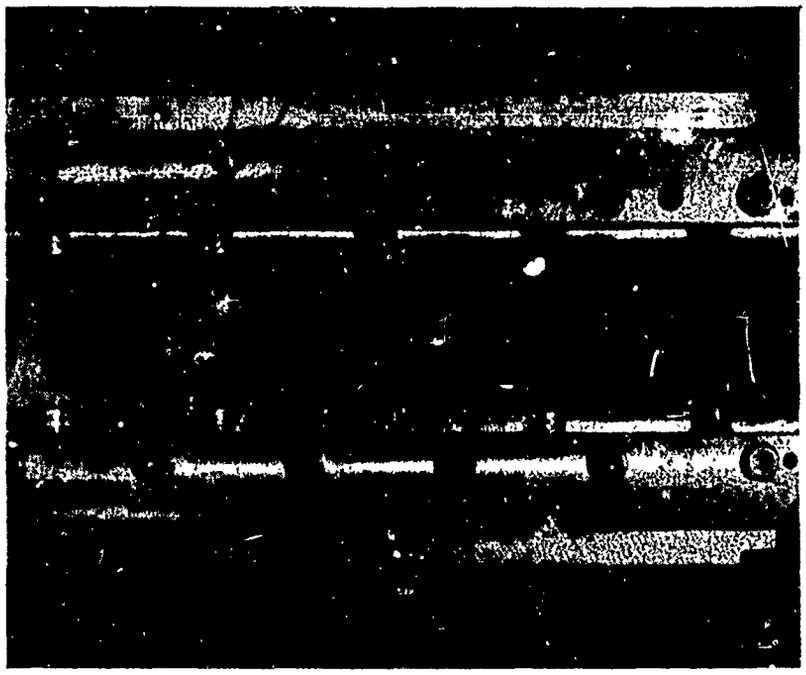

Figure 24. Biaxial Strip Specimen Ready for Vibration Fatigue Test (Edges are reinforced by thin layers of soft EC1949. The small spot of rubber covers a surface-mounted thermocouple from which the temperature was controlled.)

TESTING

The specimen, with the platens, the thermocouple, and the edge-reinforcing EC1949 in place, was mounted in the loading frame of the tester. Ambient temperature within the cabinet was adjusted from the output of the surface-mounted thermocouple to bring the specimen temperature to that required for the test. During all vibration fatigue tests, this specimen surface temperature was held constant at 140 F. Coarse observations of thermocouple output indicated that the temperature varied as much as $\pm$ 3 F between the cycling of the environmental controls.

Figure 25 shows the Cumulative Damage Tester including the loading frame and environment cabinet. Note the observation window and the two ports for hand access.

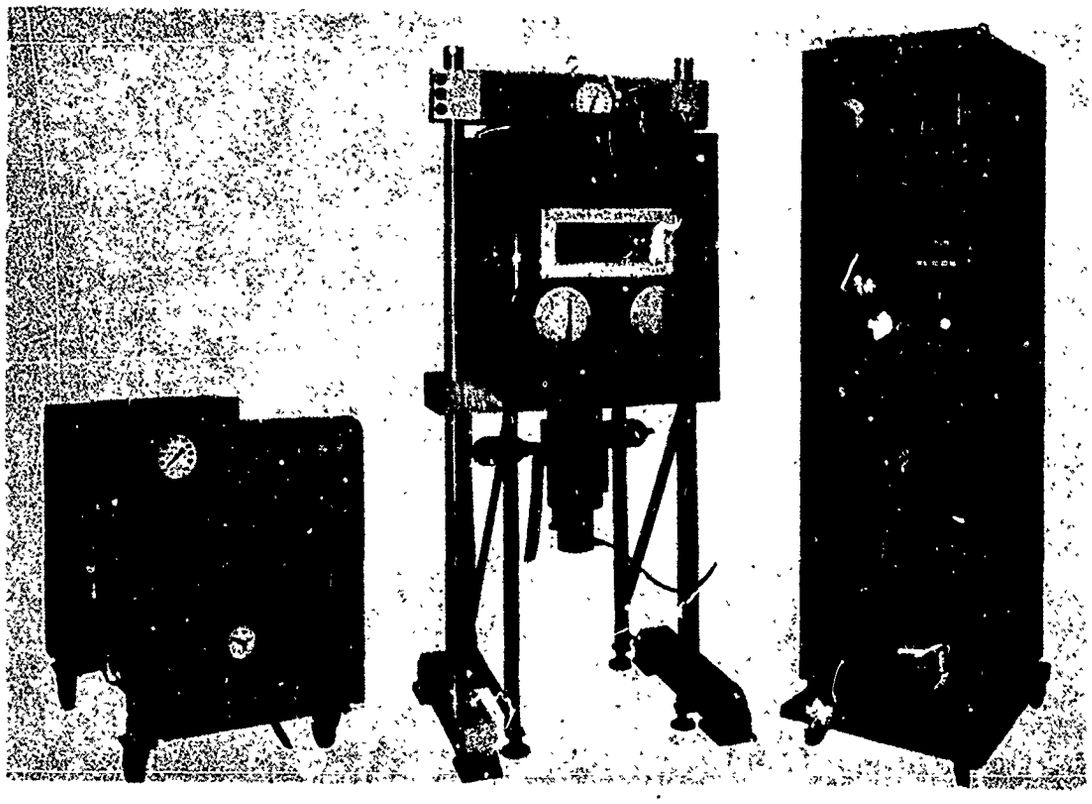

Figure 25. Cumulative Damage Tester

LOADINGS

Since these biaxial strip specimen tests were conducted to evaluate the usefulness of the criticality expressions based on energy balance for predicting the service life of propellant subjected to fatigue-type loadings, it was desirable to apply a strain history that reproduced the strain history assumed for the theoretical derivations as closely as possible. One of the general displacement histories for which a tractable solution for the growth of a spherical or cylindrical flaw is available is

$$u(b,t) = u_p \, 1(t) + u_o \sin \omega t \qquad (98)$$

where

$$1(t) = 0 \quad t < 0$$
$$= 1 \quad t \geq 0$$

which is as shown in Fig. 26.

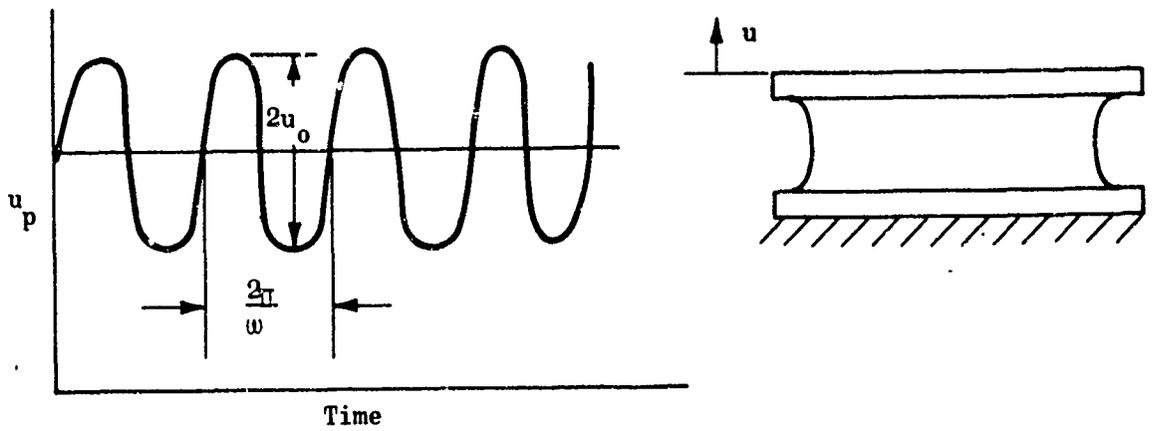

Figure 26. Vibratory Tensile Displacement Input for which a Viscoelastic Fracture Formula is Available

Preprogramming the exact displacement magnitudes, u_p and u_o, was more difficult than had been expected; but precise values could be monitored. Therefore, approximate values were preprogrammed, and calculations and data interpretations were based on the displacements that were actually measured.

Acceptable data were recorded from tests conducted at 5 and 15 cps. But at higher frequencies, the vibration of the loading frame and its foundation caused erroneous data to be recorded. For example, when the lower platen was vibrated at 50 cps at a displacement corresponding to 8% strain with no specimen in place, the force cell above the upper platen gave an oscillating output corresponding to forces of up to 40 pounds. Therefore, testing was suspended until this problem was solved.

FOUNDATION PROBLEM

To provide a seismic foundation for the loading frame, a 11,000-pound mass of concrete was poured into a cork-lined cubicle pit. This structure, which was believed to be highly damped, has a calculated natural frequency approximately midway between 15 and 50 cps, both frequencies at which tests were to be run. (These calculations were subsequently confirmed by tests.) As discussed above, the frame and foundation performed well for tests conducted at 5 and 15 cps; but at higher frequencies they vibrated at unacceptable levels.

Three approaches for alleviating this problem were considered. The first was to increase the mass of the foundation, thus lowering the natural frequency of the foundation-frame system. The second possible approach was to design a tuned energy dissipater that would absorb the input vibration energy during test run at the precise frequency to which it was tuned. Theoretically, this would leave the foundation and attached load frame relatively vibration free. Both of these approaches were discarded--the first because of the expense and time involved, and the second because of the uncertainty associated with its predicted performance.

The solution adopted was to replace the cork lining with pneumatic mountings to provide the vertical support for the concrete foundation. Calculations indicated this should reduce the effective spring constant as required to lower the natural frequency of the spring-mass system (foundation and frame) from about 35 to about 2 cps. These calculations proved to be realistic; the amplitude of the sympathetic responses to a 50 cps input of the moving platen was reduced by a factor of 4 or 5. Figure 27 shows a photograph of one of the pneumatic springs.

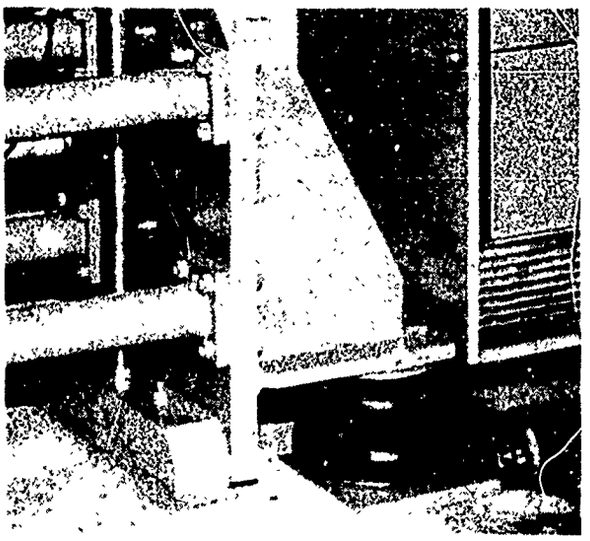

8-2-68-992

Figure 27. One of the Four Pneumatic Springs Used to Soften the Support Structure for the Loading Frame of the Cumulative Damage Tester

TEMPERATURE

There was concern about the cyclic energy input and its effect on thermal gradients across the thickness of the specimen at the higher frequencies and strains. Since the specimen was pre-conditioned to a stable temperature of 140 F before the test was started, cyclic inputs would obviously increase the specimen temperature. To partially compensate for this effect, a thermocouple was attached to the surface of the specimen; and the temperature of the box was controlled automatically so the specimen surface temperature remained at 140 F. This did not ensure that the entire specimen temperature would be held to this temperature, however. Since heat was flowing from the specimen to the air, the temperature of the internal parts of the specimen could become significantly higher than the 140 F surface condition. Therefore, the following calculation was performed to determine the maximum temperature gradient across the specimen during one of the higher frequency and strain tests.

Figure 28 shows a typical Lissajous pattern for the force-displacement relationship during a 47 cps and 6% strain test. By measuring the area of such patterns and converting to energy density, in.-lb/in.^{3}, it is possible to establish a point of equilibrium for the energy input as shown in Fig. 29. The equilibrium energy input, q, can then be used to determine the maximum temperature gradient in the expression

$$T = T_o + \frac{q}{2k} (X_0^2 - X_1^2) \qquad (99)$$

where

T = Temperature
T_o = Surface temperature, 140 F
q = Equilibrium energy input, Btu/in.^{3} hr
k = Conductivity of propellant, ~ 0.25 Btu/hr(ft^2)(deg F/ft)
X = Reference plane located at center of specimen, t/2 = 0.1875 inch

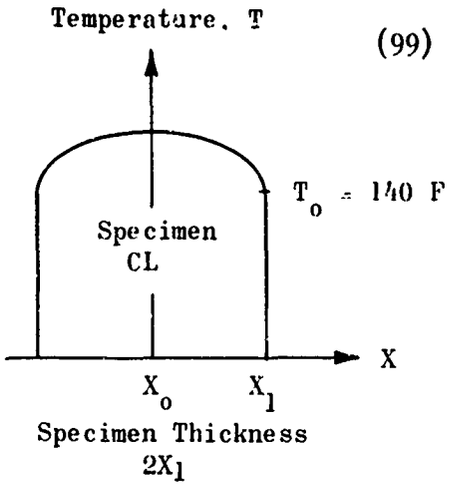

The calculation revealed that the maximum temperature rise for the 47 cps, 6% strain test was 13.8 F, as the maximum temperature at the center was 153.8 F.

The importance of such thermal gradients to the time or number of cycles to failure during such tests remains unknown. The numbers calculated above seem to indicate that gradients arising during 5 and 15 cps (5 F) would be negligibly small. It seems equally likely, however, that the temperature difference might cause measurable differences in results obtained from 47 cps tests.

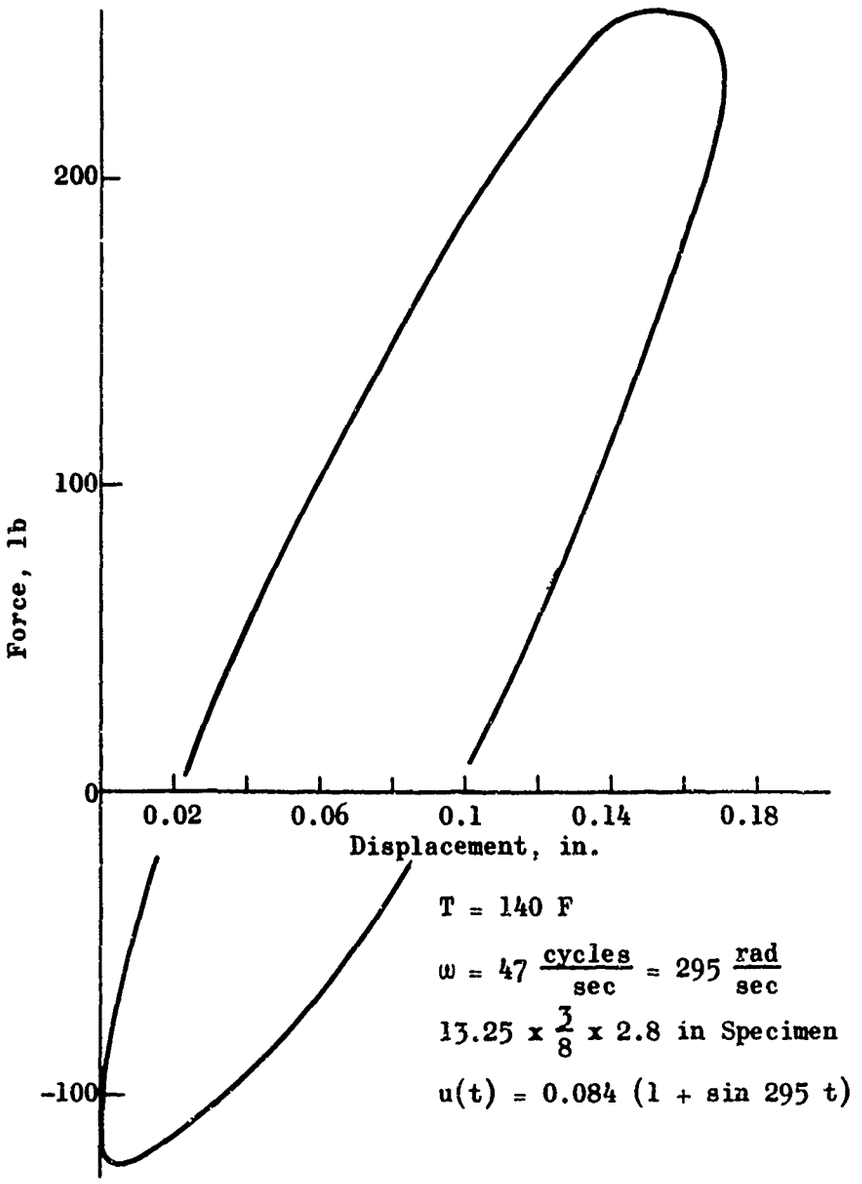

Figure 28. Force-Displacement Trace Taken During a Vibration Fatigue Test on a Biaxial Strip (The area within the ellipse represents total heat loss per cycle)

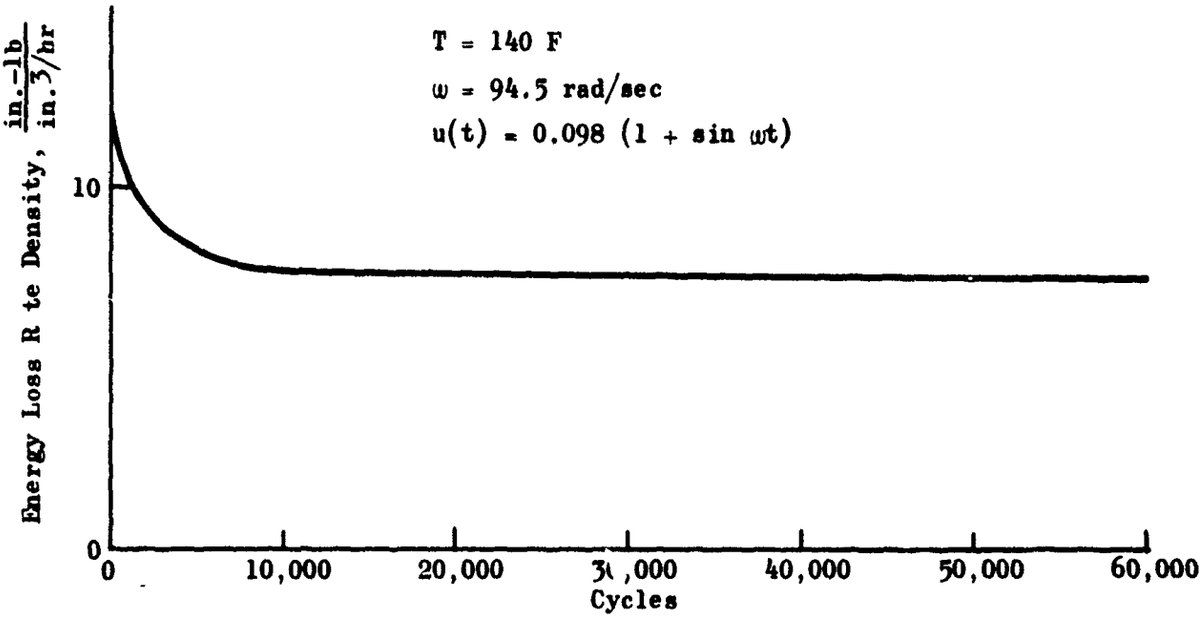

Figure 29. Deterioration in Energy Loss Measured During a Biaxial Strip Vibration Test

DATA COLLECTION

Several items of data including ambient temperature in the conditioning box, platen forces, and platen displacements were collected, all as a function of time, during each test. A counter on the console indicated the number of cycles which was also recorded as a function of time. The time the crack first appeared and the observed rate at which it grew were also recorded. Most of the data were collected by frequent observations.

The environmental cabinet control operates from a feedback system that provides the ambient temperature necessary to maintain the surface-mounted thermocouple at a constant temperature (140 F). A thermometer was used to monitor the ambient temperature of the box. The difference between ambient and surface temperatures is a measure of energy or heat loss from the specimen. Ambient temperature was, therefore, recorded at each observation.

Platen forces and displacements were measured by load cells in the stationary platen support and an LVDT on the moving platen ram, respectively. Output voltages were fed to an oscilloscope where their magnitudes could be displayed separately as a function of time or compared to

provide the so-called Lissajous ellipse on a force-displacement plot. These traces were photographed periodically through every test, indicating both storage and loss properties.

Observations for cracking were made periodically throughout each test. After the beginning of crack growth, the point termed failure in this report, more frequent observations were made to correlate crack length with the number of cycles. These data were noted until the sequence camera was installed to provide a photographic record of crack growth. Results of observations of crack initiation are plotted in the three graphs of Fig. 30. Plotted points are keyed to the box number from which specimens were cut to ascertain whether box-to-box variations were evident from these tests. They were not. Arrows pointing away from some data points indicate that the exact number of cycles at which the crack began is unknown but is bounded in the direction indicated.

Actually, 33 tests rather than the 27 shown in Table XII were successfully completed and are plotted. The extra tests were performed, primarily at the 5 cps frequency, in an effort to narrow the spread of the scattered data.

The ordinates of Fig. 30 are actually the sum of the vibration displacement amplitude, u_o, and the superposed constant displacement, u_p (see Eq. 94). It was intended that they be equal in all tests. However, as shown in Table XIII, they varied slightly from this intended loading.

After actual separation of the specimen, the fracture surface was carefully examined to determine whether the mechanism of failure could be detected visually. Following only one or two tests, it was possible to link the failure to an actual flaw or void. Photographs of an example flaw from which a failure is believed to have originated are shown in Fig. 31.

CAMERA COVERAGE

A 70 mm Hulcher sequence camera was installed to monitor crack initiation and growth. (It was necessary to replace the original door of the conditioning box with a fully transparent plexiglass door to facilitate the use of the camera.) The shutter of the camera opened after a pre-set time interval, and the associated strobe light fired when the displacement reached the next maximum value. Consequently, any cracks present in the specimen were in the strained (open) position as the shutter opened.

TABLE XIII. SUMMARY OF THE DISPLACEMENT BOUNDARY FATIGUE TESTS

Temperature = 140 F $u(t) = u_p + u_o \sin \omega t$

Test No.	Frequency, cps	Nominal Strain, %	Constant Displacement, u_p, in.	Amplitude, u_o, in.	$\frac{u_p + u_o}{2}$, in.	Initial Cracking, Cycles	Specimen Separation, Cycles	Box Number
57	15	7	0.09375	0.1062	0.0999	117,500	133,700	15
59	5	7	0.09575	0.09575	0.09575	315,600	420,300	14
60[a]	5	6	0.0760	0.0813	0.0786	243,100	257,100	14
61	5	8	0.1050	0.114	0.1090	14,000	22,700	14
62	15	6	0.0810	0.0863	0.08360	590,000	636,500	14
63	15	7	0.0920	0.0991	0.0955	87,000	105,300	14
64	15	8	0.1080	0.1680	0.138	21,800	24,700	14
65	5	6	0.077	0.077	0.077	-	184,700	16
66	5	7	0.0980	0.1015	0.099	-	82,100	16
67	5	8	0.1080	0.125	0.116	17,800	31,900	16
68[a]	15	6	0.0815	0.0850	0.0832	287,400	321,200	16
69	15	7	0.0930	0.107	0.100	70,700	80,300	16
70	15	8	0.1120	0.1176	0.1145	23,200	26,500	16
71	5	6	0.0845	0.088	0.086	262,000	315,700	13
72	5	7	0.0955	0.106	0.100	586,200	767,700	13
73	5	8	0.1110	0.1217	0.116	56,000	131,300	13
74[b]	15	6	0.0825	0.1465	0.1145	331,900	392,900	13
75	15	7	0.0915	0.0969	0.0922	52,500	68,700	13
76	15	8	0.106	0.106	0.106	42,800	49,800	13
77	5	6	0.078	0.078	0.078	-	166,800	18
84	5	6	0.081	0.081	0.081	250,000	267,200	3
85	5	7	0.090	0.090	0.090	49,800	56,400	3
86	5	6	0.082	0.082	0.082	172,100	229,300	3
87	5	7	0.090	0.090	0.090	33,100	67,200	3
88	47	8	0.107	0.100	0.104	-	4,300	14
91[b]	47	6	0.095	0.095	0.095	16,500	26,800	14
92	47	6	0.082	0.092	0.087	27,000	31,900	14
93	47	6	0.079	0.079	0.079	46,000	53,900	13
94	47	7	0.095	0.095	0.095	22,100	27,900	13
95[b]	47	8	0.113	0.099	0.106	20,000	22,000	13
96	47	6	0.078	0.085	0.082	26,200	32,800	16
97[c]	47	7	0.090	0.108	0.099	8,200	10,500	16
98[d]	47	8	0.107	0.107	0.107	4,800	6,400	16

a. Electrical Shut Down
b. Data Corrected for Electronic Load of Camera on Head Out
c. Flaw in Specimen (Not visible at outset)
d. Thermal Control Problems

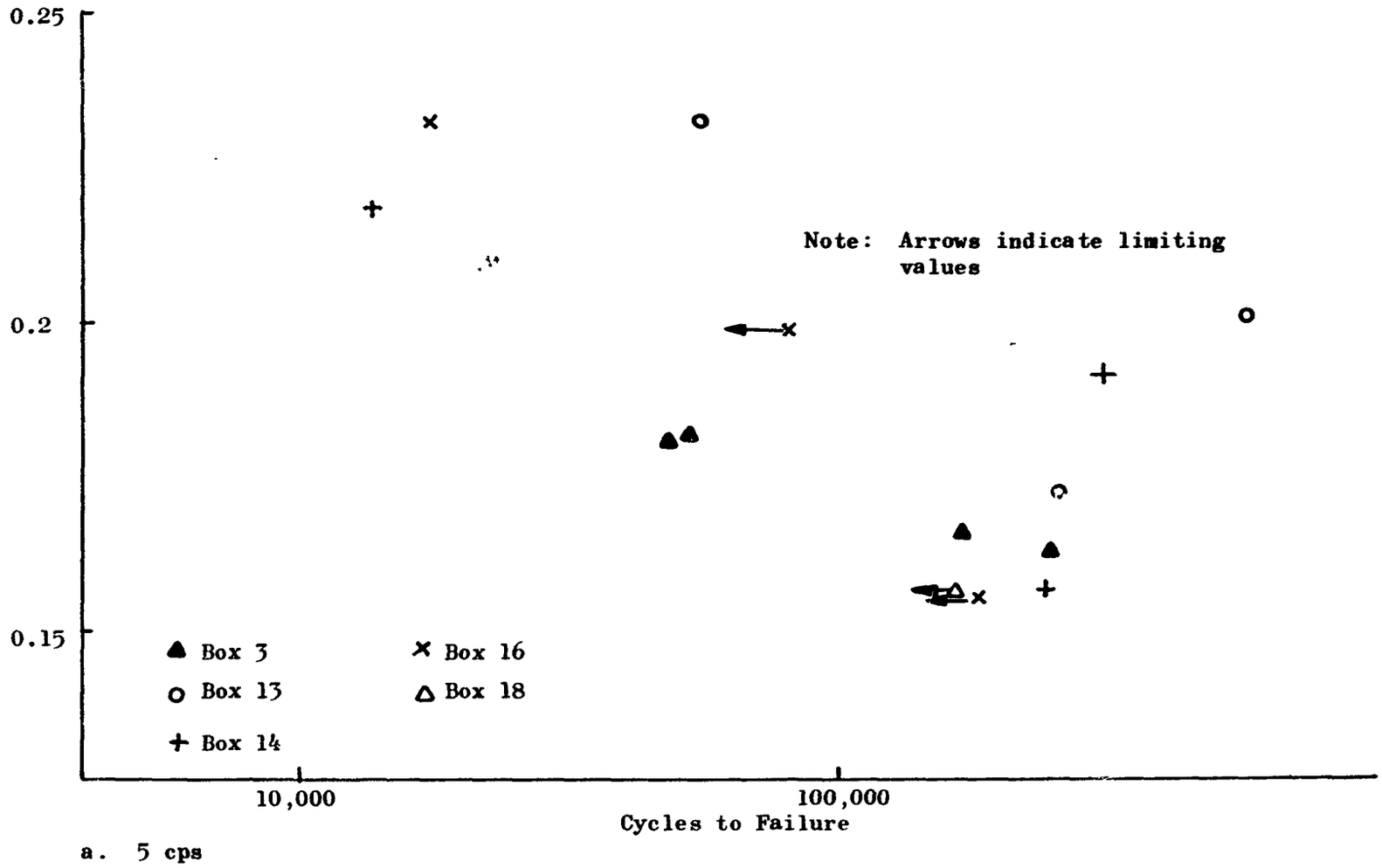

a. 5 cps

Figure 30. Cycles to Failure in Biaxial Strips Following Tensile Displacement Vibration Tests

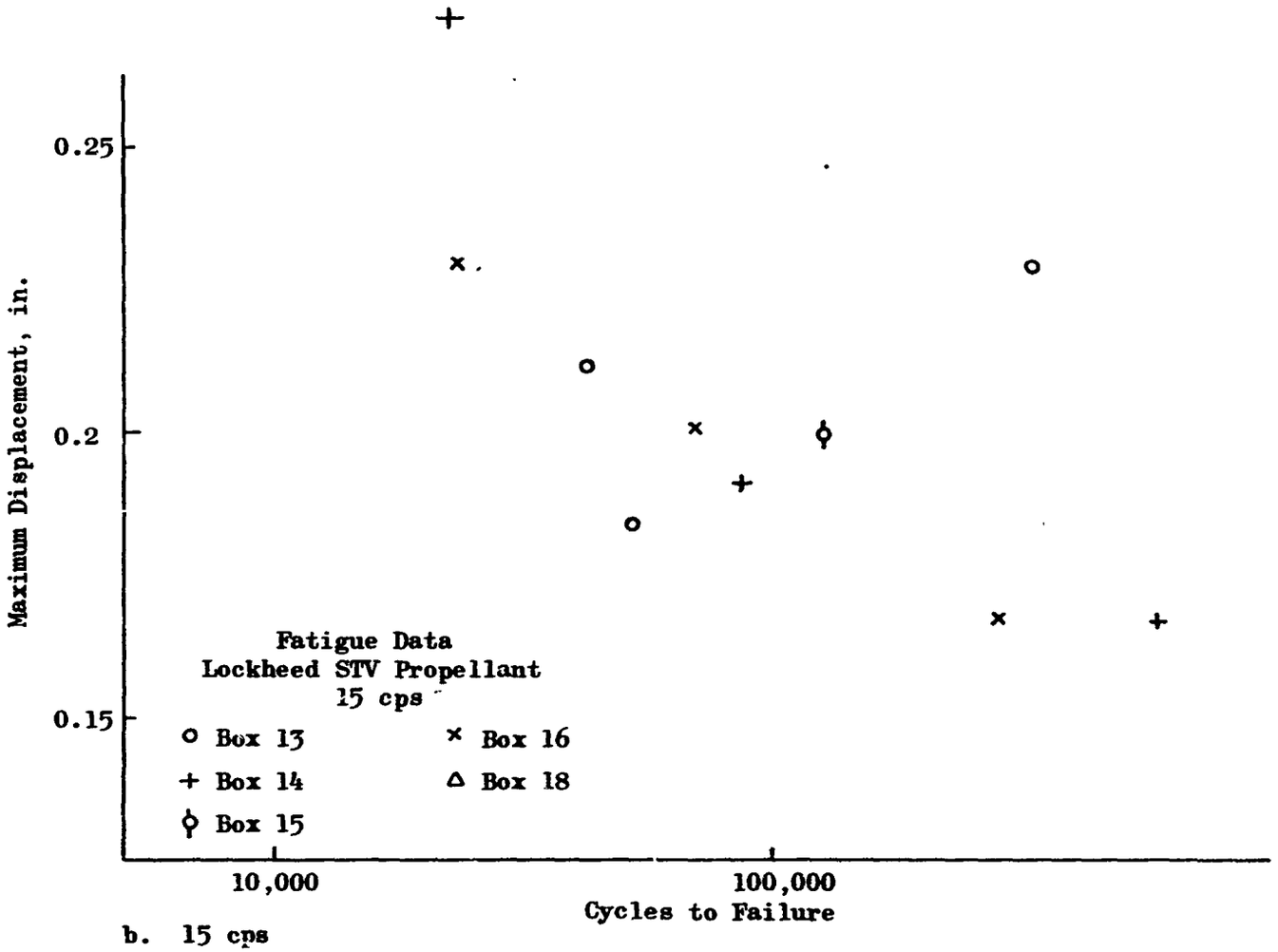

b. 15 cps

Figure 30. Continued

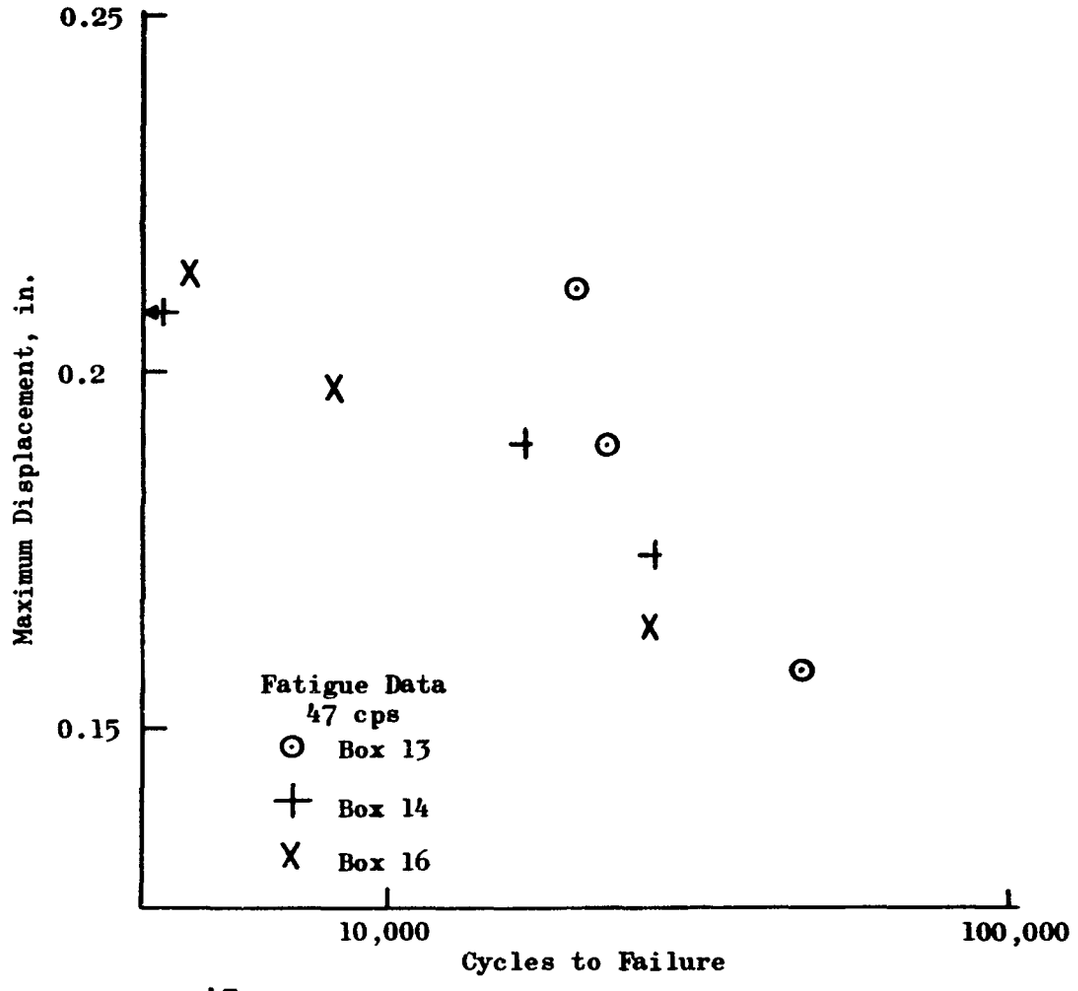

c. 47 cps

Figure 30. Concluded

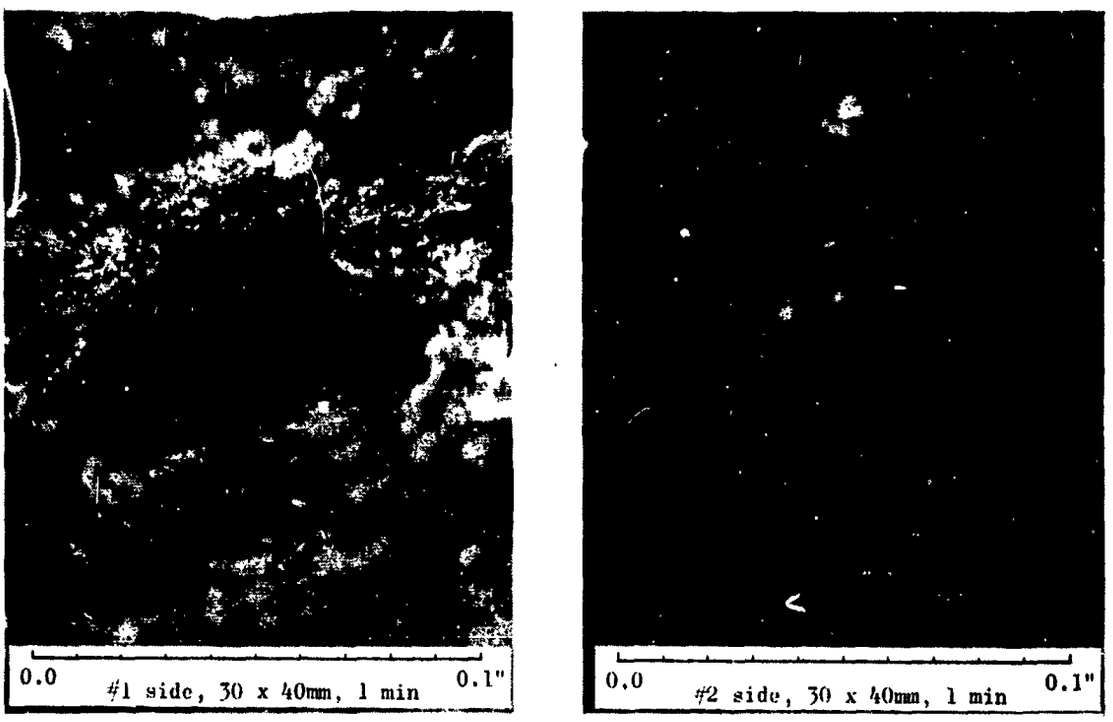

Figure 31. Photomicrographs of a Small Void From Which One Biaxial Test Specimen Failed

Photographic records were made only during the last third of the fatigue testing program. Data collected on film are summarized in the length of crack vs number of cycle curves in Appendix VIII.

The Hulcher camera is not necessarily the best equipment for monitoring the initiation of a crack. However, the availability/schedule impact necessitated its use. A limiting condition of the 70 mm camera is that if it is set far enough away for the entire specimen to be within the field of view, the photograph scale is so large that small initial cracks (0.25 inch) can neither be seen nor measured. This problem was solved by plotting the longer crack-vs-cycle curve then extrapolating the curve backward until it intersected the zero axis. The number of cycles at this point was considered the number of cycles to failure.

ANALYSIS OF RESULTS

Early in the analysis phase of the program it was established that one can hope to predict the initiation of fracture reliably, only if stresses and strains can first be reliably calculated. A failure prediction cannot be better than the stress analysis on which it is based.

Therefore, calculations were made to ascertain just how close analytical stress/strain calculations (based on linear viscoelasticity) came to actual measured forces in the biaxial strip under oscillatory displacement loading. Material properties determined with uniaxial tests were first used in these calculations and were found to predict a quite different force response from that measured on the biaxial strip. This finding led to the exploration reported in Appendix IX where the effective differences between properties determined using uniaxial specimens are contrasted with those using biaxial specimens. It was concluded that it would be best to use biaxially determined properties for all failure predictions concerning biaxial strip specimens.

Figure 32a and b compare predicted and measured vibration responses shortly after the start of a test and after 50,000 cycles, respectively.

Interpreting these propellant fatigue data and the extension to other loadings and sequences of loadings requires that they be fitted to the equations for the criticality of a flaw. The energy balance expression for the initiation of the fracture of a spherical flaw following a loading of this type has been derived by Jones, Wagner, and Williams (11). The derivation incorporates a viscoelastic relaxation modulus expressed in the form of a Prony series. The analogous expression for a cylindrical flaw in a plane stress (very thin) body has been formulated as shown in Table II. That expression, probably most applicable to the biaxial specimen, is written

$$\frac{\gamma}{8a_o}\left[1+3k^2\right]^2 = \left(\frac{u_p}{b}\right)^2 E_g + 2\left(\frac{u_p}{b}\right)\left(\frac{u_o}{b}\right)\sum_{i=1}^{n}\left(\frac{\omega\tau_i}{1+\omega^2\tau_i^2}\right)E_i$$

$$+2\left(\frac{u_p}{b}\right)\left(\frac{u_o}{b}\right)E_e \sin\omega t_f + 2\left(\frac{u_p}{b}\right)\left(\frac{u_o}{b}\right)\sum_{i=1}^{n}\left(\frac{\omega\tau_i}{1+\omega^2\tau_i^2}\right)E_i e^{-t_f/\tau_i}\ x \qquad (100)$$

$$\left(\frac{\omega\tau_i}{1+\omega^2\tau_i^2}\sin\omega t_f - \cos\omega t_f\right)+\left(\frac{u_o}{b}\right)^2 E_e\left(1-\cos^2\omega t_f\right)$$

$$+2\left(\frac{u_o}{b}\right)^2\sum_{i=1}^{n}\left(\frac{\omega\tau_i}{1+\omega^2\tau_i^2}\right)E_i\left[\frac{\omega t_f}{2}+\frac{\sin 2\omega t_f}{4}\right.$$

$$\left.+\left(\frac{\omega\tau_i}{1+\omega^2\tau_i^2}\right)\left(e^{-t_f/\tau_i}\cos\omega t_f - 1 + \frac{\sin^2\omega t_f}{2}\right)-\frac{\omega^2\tau_i^2}{1+\omega^2\tau_i^2}\left(e^{-t_f/\tau_i}\sin\omega t_f\right)\right]$$

The right-hand side of this expression reflects an energy buildup, with time, under the influence of the two elemental loadings of Eq. 97: the instantaneous step displacement, u_p, and a sinusoidally vibrating displacement of amplitude, u_o. The material properties, namely the tensile modulus, enters through the use of coefficients, E_i and τ_i, chosen to give the best fit to the measured relaxation modulus. The surface temperature of the specimen was held constant at 140 F during all the tests. It was assumed that it was permissible simply to shift the property data in accordance with the biaxial time-temperature equivalence factors reported in Appendix V.

A plot of the calculated value of the right-hand side of Eq. 99 vs time for the three loading frequencies of the Rocketdyne tests are shown in Fig. 32. The frequencies 1.288, 0.412, and 0.1374 at 77 F are equivalent to 47, 15, and 5 cps at 140 F. The time scale (the value of t_f in Eq. 99) is unchanged by temperature and represents laboratory time.

The hypothesis is that when the value of the right-hand side becomes just equal to the constant of the left-hand side the flaw begins to grow. The constant value assigned depends upon the geometry and displacement magnitudes and is directly dependent upon the characteristic strain energy release rate, γ, divided by the initial flaw radius, a_o. It was hoped that the values of these parameters, determined in the static tests described in the preceding section, could be used to calculate the constant. For example, if one uses the typical values

$$\frac{\gamma}{a_o} = 50 \quad ; \quad k = 0.5 \quad ; \quad \frac{b}{u_o} = 14.3$$

then the value of the constant is

$$\frac{\gamma}{8a_o}\left(1 + 3k^2\right)^2 \left(\frac{b}{u_o}\right)^2 = 3.9 \times 10^3 \frac{\text{in.lb}}{\text{in.}^3} \qquad (101)$$

But this value is much too small to compare to the curves of Fig. 33.

At least one reason for this problem was the assumption of an instantaneously applied displacement, u_p (= the amplitude, u_o, in these tests), which leads to the large term on the right hand side of Eq. 100. This single term is precisely the term for the critical energy level during a step displacement loading without the sinusoidal vibration. This led to the idea of replacing the term with the equivalent expression for criticality following a ramp loading history. That is, replace the term

$\left(\frac{u_p}{b}\right)^2 E_g$ with $\frac{2}{t_1^2} E^{(2)}_{rel}(t_1)$ where t_1 is the ramp duration time. An estimate of the ramp times can be made by assuming their duration was one-quarter of a cycle. This leads to the ramp times shown in Table XIV. From these times, with the plot of the biaxial relaxation modulus and its integrals in Appendix IX, one can evaluate the critical energy, $\frac{2}{t_1^2} E^{(2)}(t_1)$.

TABLE XIV. APPROXIMATE RAMP LOADING TIMES AND THE CORRESPONDING CRITICAL ENERGY LEVELS AT 77 F

Reduced Frequency, ω/a_T, cps	Ramp Loading Time, t_1, min	$\frac{2}{t_1^2} E^{(2)}_{rel}(t_i)$, psi
1.288	3.24×10^{-3}	2800
0.412	10.1×10^{-3}	2270
0.1322	31.5×10^{-3}	1810

The curves of Fig. 33 are lowered significantly when the critical energy corresponding to a ramp-type loading is used in place of that for a step loading. These calculations resulted in the curves of Fig. 34. However, only a quick calculation indicates that the parameters determined during biaxial static tests do not fit the vibration fatigue data.

As a consequence, earlier parameters were completely disregarded; and new values were chosen to give a reasonable fit to the test data. The predicted failure lines, for 47, 15, and 5 cps, at 140 F are compared to the measured failure points in Fig. 35. Several interesting observations can be made from Fig. 35. First, although the data show the wide scatter characteristic of fatigue failure tests, there is still a rather definite indication of a slope of about -1/4 on the log-log plot. (Broken lines indicating this trend were not calculated numerically. This is in direct contrast to theoretical predictions which have a slope of about -1/2.

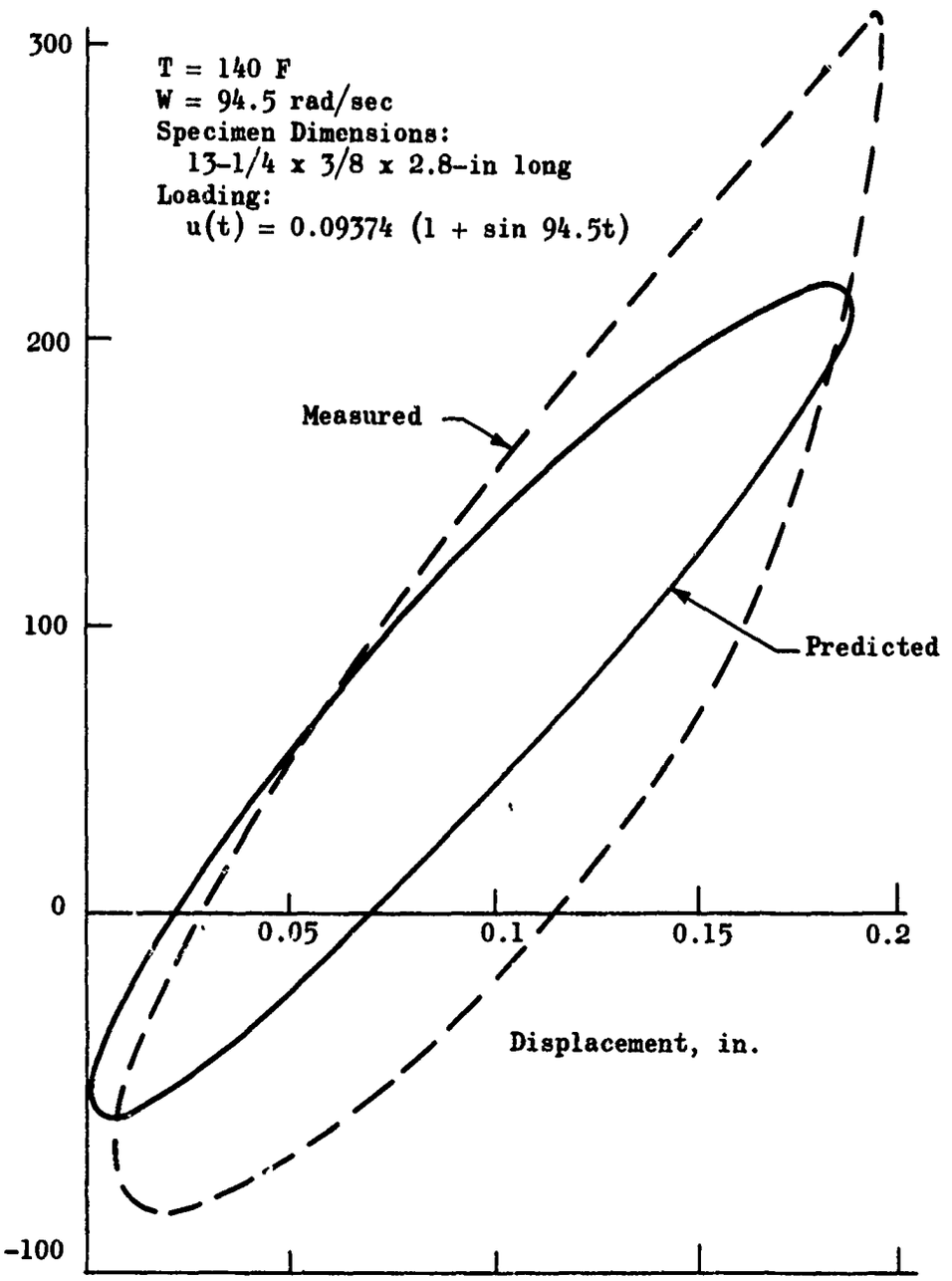

a. After a few cycles of the test (<30)

Figure 32. A Comparison of the Biaxial Force-Displacement Curves as Measured and Predicted (using the biaxial characterization).

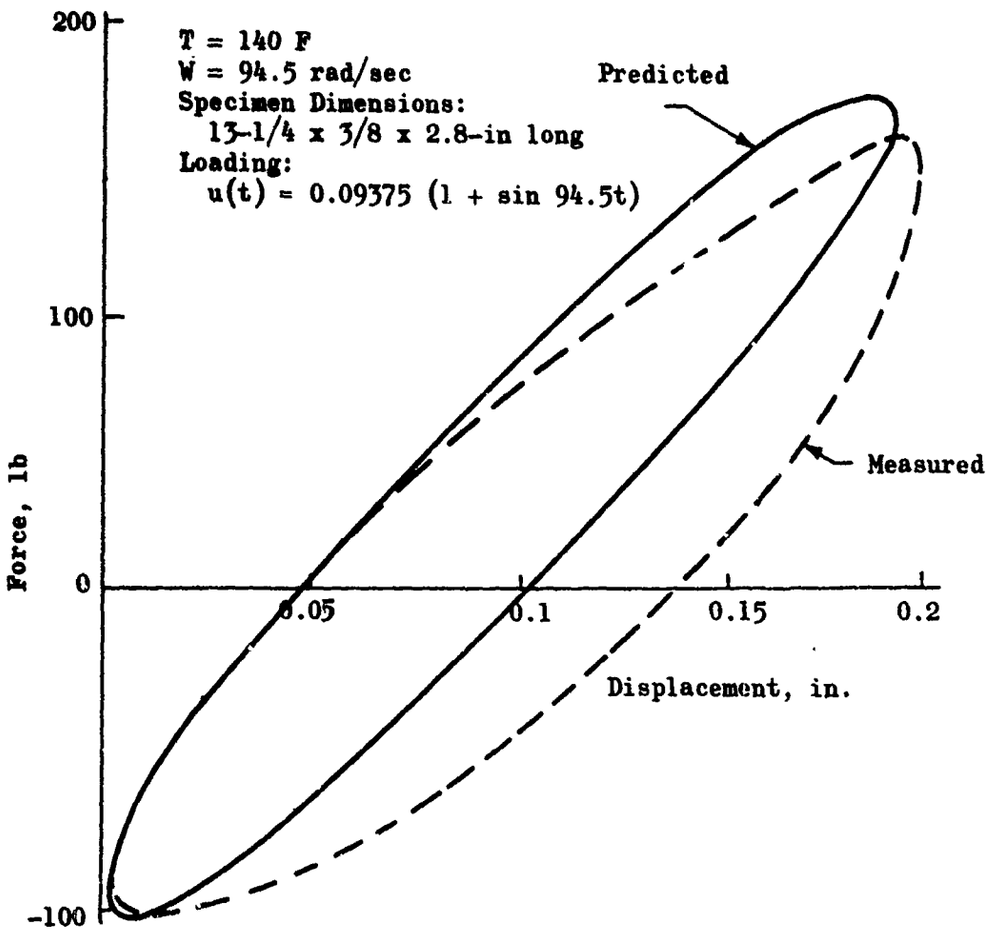

b. After 50,000 cycl of the test

Figure 32. Concluded

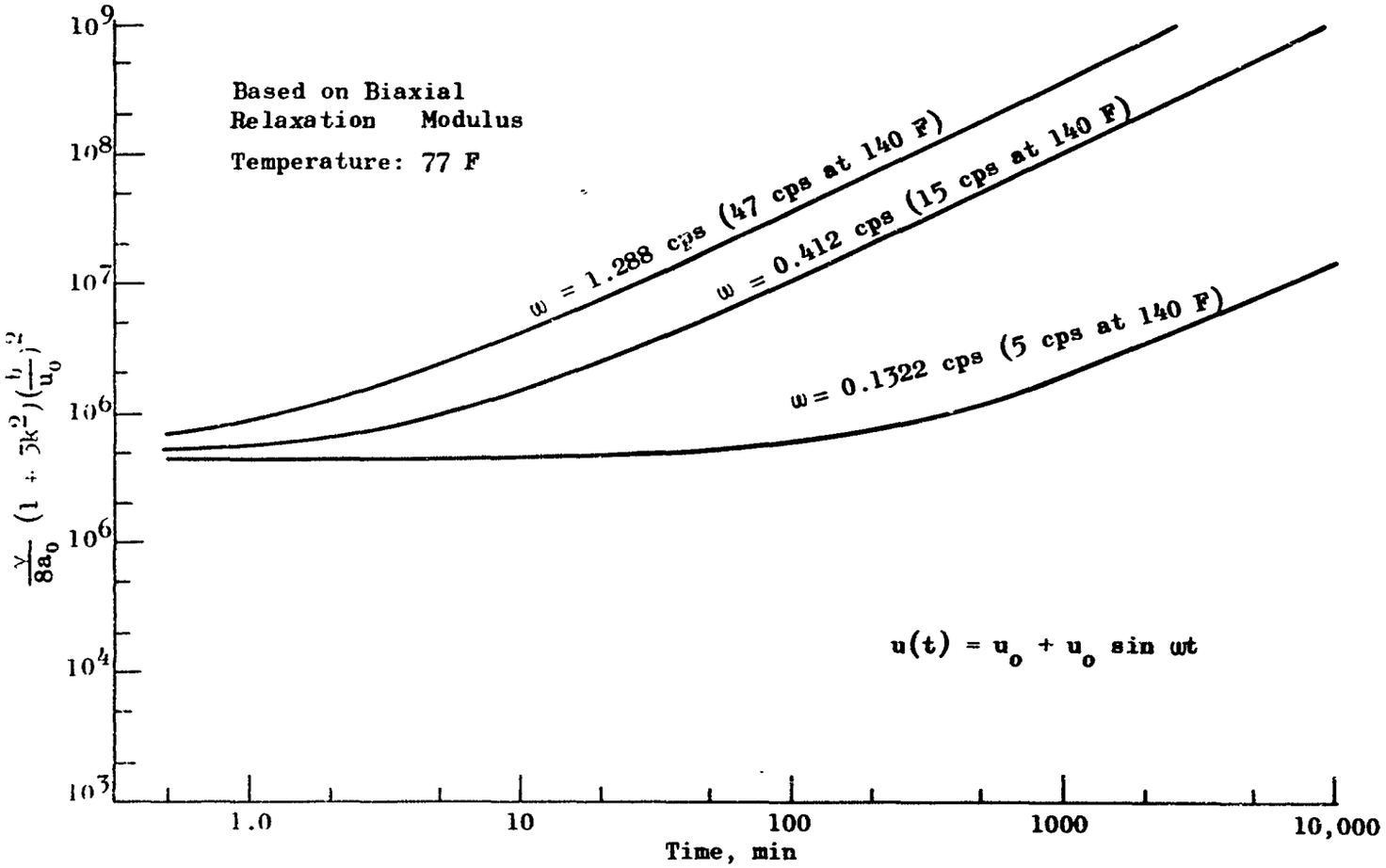

Figure 33. Propagating Flaw Solution for the Sinusoidal Displacements Superposed Upon the Constant Initial Displacement (Step Loading).

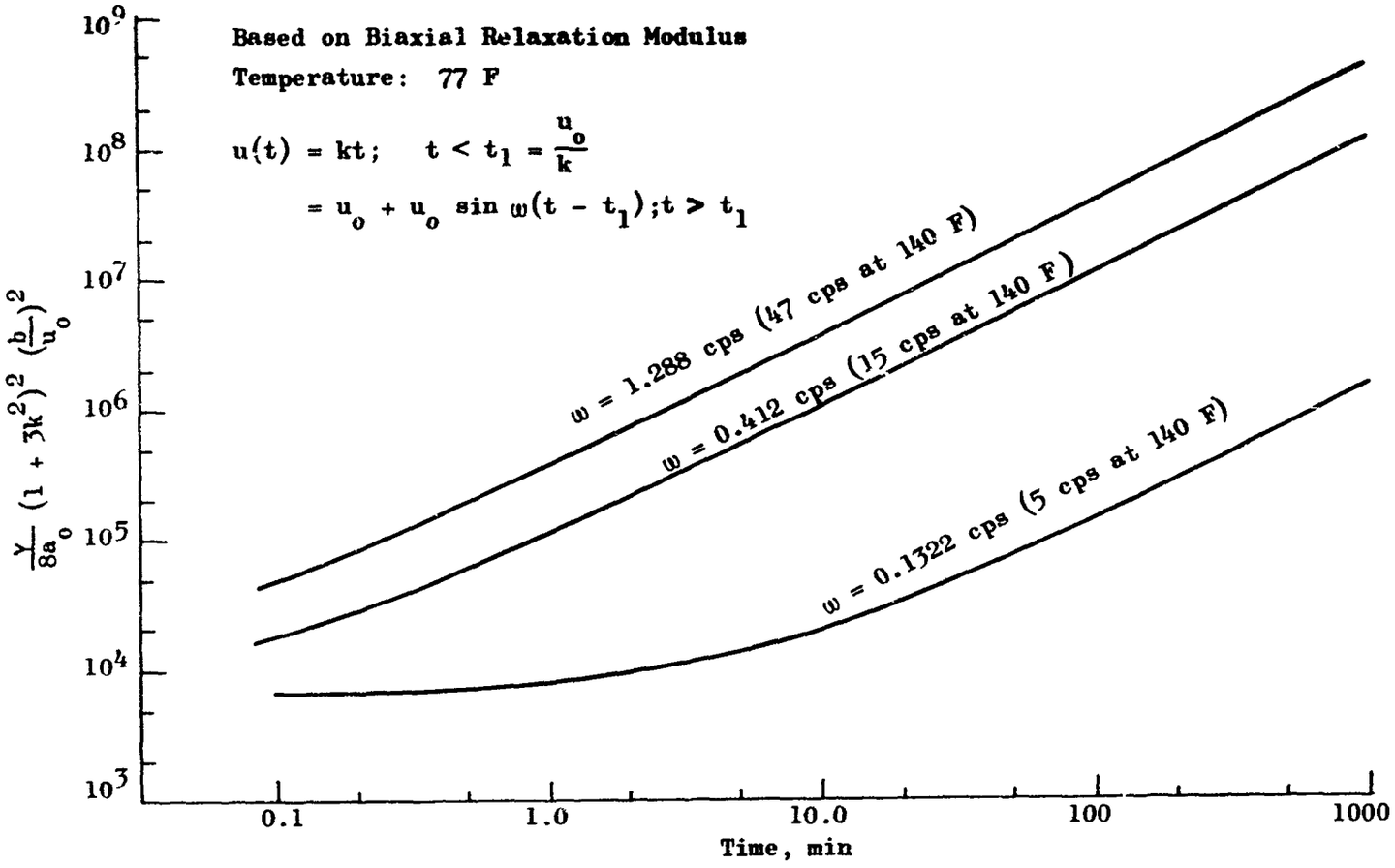

Figure 34. Propagating Flaw Solution for the Sinusoidal Displacements Superposed Upon the Constant Initial Displacement (Ramp Loading)

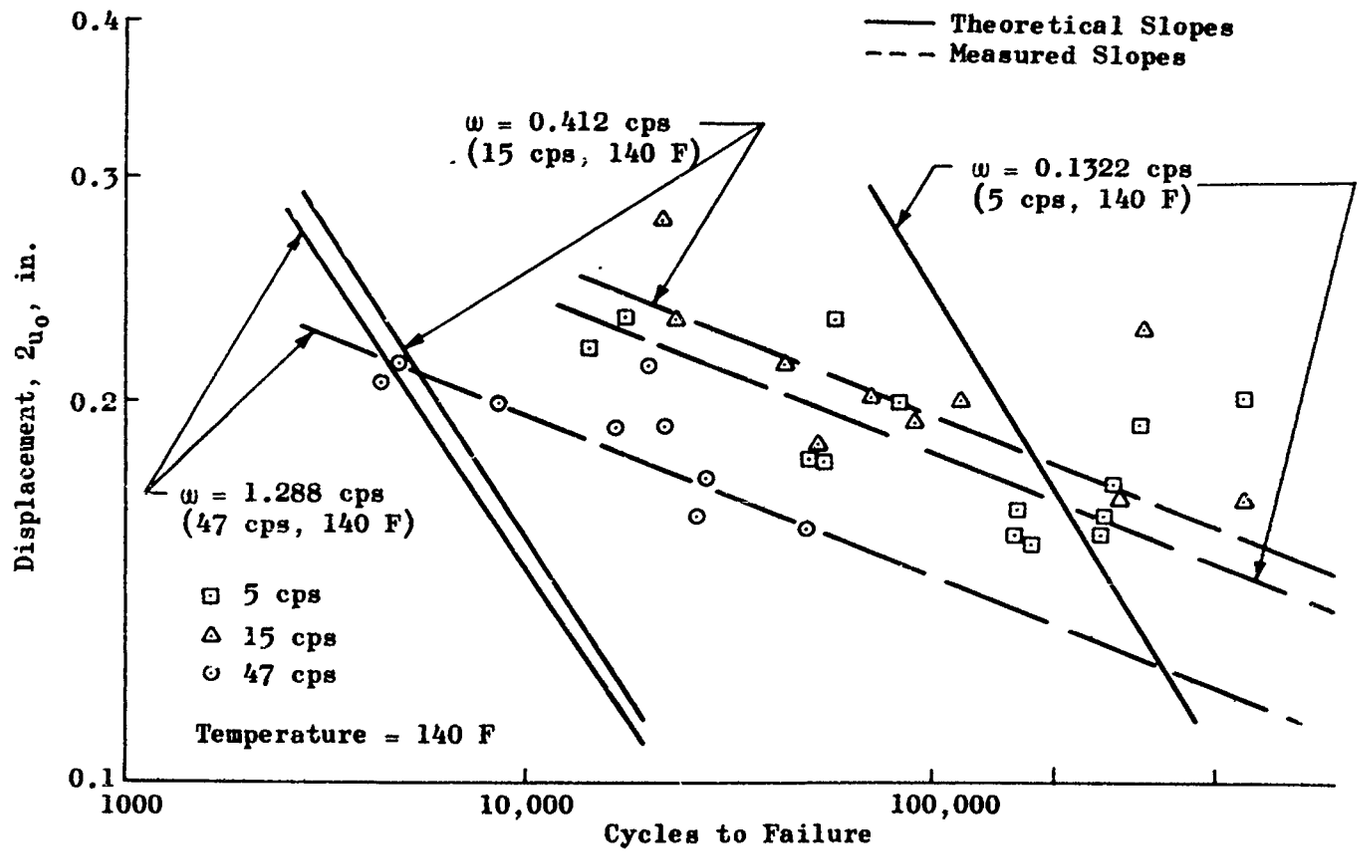

Figure 35. Fatigue Data Collected by Subjecting Biaxial Strips to Vibrating Displacements of the Form $u(t) = u_o + u_o \sin \omega t$

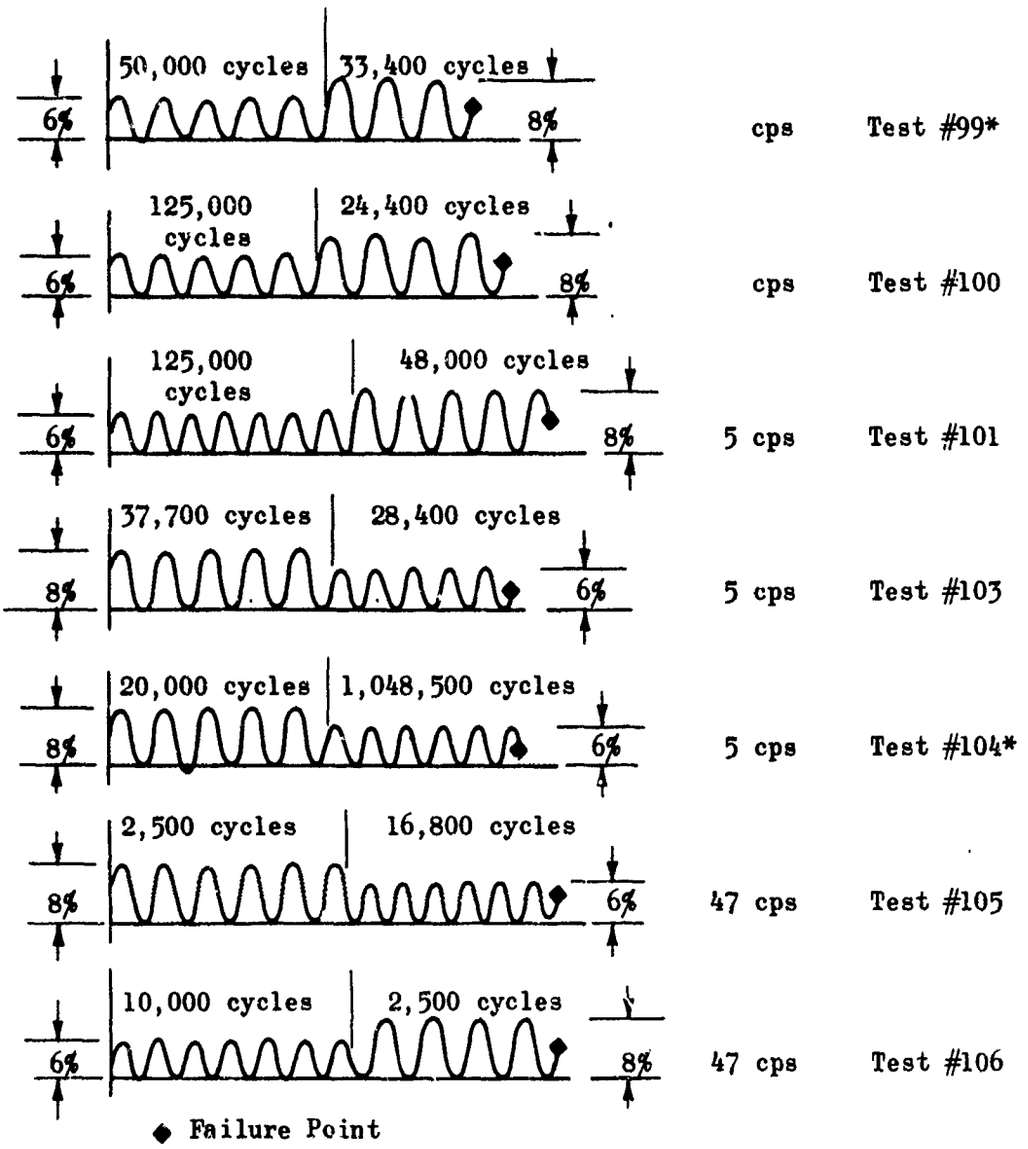

Figure 36. Summary of the Dual Amplitude, Constant Frequency Vibration Fatigue Tests (Biaxial Strip Specimens)

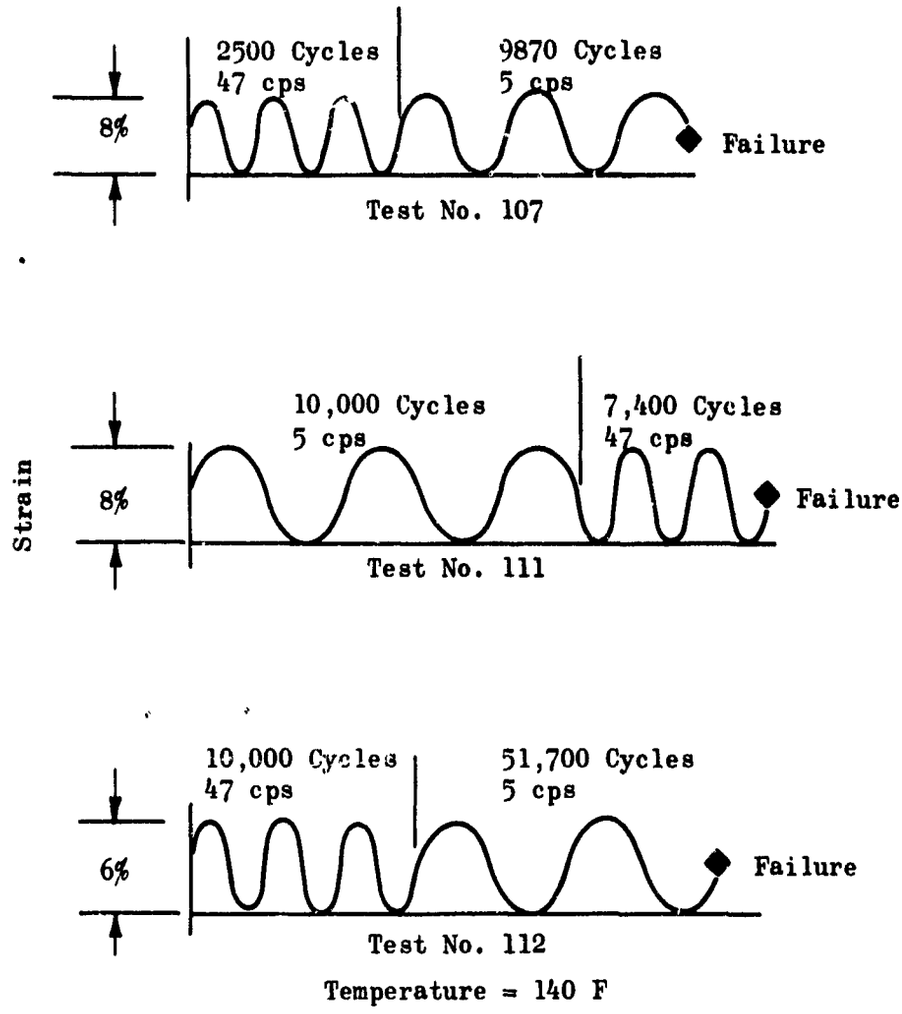

Figure 37. Summary of the Dual Frequency, Constant Amplitude Vibration Fatigue Tests (Biaxial Strip Specimens)

Page 106 is blank

SECTION VI

CONCLUSIONS AND RECOMMENDATIONS

The 1-year program, conducted in association with three other contractors, and coordinated by the AF Rocket Propulsion Laboratory, opened for public view the limitations and capabilities of current grain stress/strain and failure analyses. The concensus must surely be that there are more limitations than capabilities.

The early decision by the Air Force to use a combine of companies exploiting the particular specialties of each proved to be a wise one. Due to frequent coordination conferences, close and interested Government surveillance and a spirit of free exchange of data (both favorable and unfavorable) among the several researchers, maximum use and benefit were derived from the volumunious quantity of data and information generated. Surprisingly few contradictions were found in test results originating from the different organizations, all of which adds to the significance of the conclusions which can be made.

Two salient conclusions are most obvious and important. The first is that if the stresses or even the strains cannot be calculated to within acceptable engineering accuracy, then any attempt to meaningfully predict failure, regardless of the loading history represents merely an analytical exercise. Accordingly the linear viscoelastic analyses based on the elemental properties provided and/or derived proved inadequate even for the most elementary geometries and loadings. The variation in the classical properties due to state of stress and the type of loading were clearly shown by the data on several of the tests. Neither these variations nor their causes are currently understood. However, their relative importance to the working stress analyst must surely provide motivation for their further study. The second is that environmental effects on propellant surfaces are important, perhaps to the point of overshadowing or masking the effects of accumulated damage due to prior structural loadings. The susceptibility of the CTPB propellant failure properties to change as a result of the environment, especially high humidity, is real and must be taken into account in motor grain analyses.

A multitude of specific conclusions are evident from the Rocketdyne portion of the program. Some concern the testing procedures and are listed only to assist other experimenters working with similar specimens or tests. Others are more general and will serve as a guide for those attempting to predict failures using the energy balance techniques. Ordered somewhat by importance they are:

1. The criticality equations for the growth of a spherical or cylindrical flaw in a viscoelastic media can be derived for a wide variety of practical loading histories. These equations at best can be used to predict the loading conditions which will lead to propellant cracking, at worst, can be used to evaluate the significance of the influential parameters on propellant cracking.

2. The triaxial poker chip test results fit the predictions of the viscoelastic fracture equations better than those from any of the various experimental tests. This is reasonable because the state of stress closely simulates that hypothesized for the derivations of the spherical flaw equations and because the problem with surface effects is essentially eliminated.

3. The time to failure in the vibration fatigue tests, like the creep tests, is an extremely sensitive measure and thus exaggerates the statistical spread of failures. However, it is important to the analyst that this variation be quantitatively understood.

4. A reasonable amount of evidence became available to indicate that the characteristic strain energy release rate for propellants is a function of both loading rate and temperature.

5. During the vibration fatigue tests, the propellant response properties change. This change must be taken into account if the crack initiation is to be predicted.

6. The drop off in the center load cell output which has long been observed to precede the ultimate poker chip loading, during constant rate tests, is indicative of the formation and growth of small scattered internal flaws.

7. The cumulative damage testing machine can be used to subject biaxial propellant strips to:

   a. extremely slow stress or strain rates

   b. extremely fast stress or strain rates

   c. simultaneous preprogrammed straining and cooling histories

d. bilinear strain rates

e. vibration fatigue tests (either force or displacement controlled)

8. Premature failures near the edges and bond lines of the biaxial strip specimens can be precluded by careful reinforcement with a soft layer of EC 1949.

These conclusions, while generally encouraging, remain nebulous and unsatisfying to the practicing engineer calculating the margin against failure of his particular motor design. For this reason it is important that careful consideration be given to the direction that similar or related future activities might take. The great expense of the carefully controlled laboratory tests of the completed program dictates that their full meaning be gleaned and presented in a usable and concise format. Such a format would certainly include formulas, graphs, tables, and references to the more detailed origins of the information. The importance of the statistical distributions to the reliability of the resulting calculations should be quantitatively evaluated.

Further testing activities must be promoted to determine more precise information concerning surface effects and environment upon the propellants susceptibility to cracking failure. It is desirable that further tests designed to correlate more directly with actual motors and STV's be designed and perfected. This is especially true for loadings involving thermal changes.

But of first order importance is the necessity to devise a technique adequate for calculating, from laboratory characterizations, meaningful stress and strain magnitudes in any stress field following practical loading histories.

Page 110 is blank

APPENDIX I

FINITE ELASTICITY AND FOAM MECHANICS

BY P. J. BLATZ

Page 112 is blank

APPENDIX I

FINITE ELASTICITY AND FOAM MECHANICS

by P. J. Blatz

FOAM MECHANICS

When a thin disc (poker chip) of propellant is subjected to parallel plate loading and held at some fixed strain, the bonded specimen gradually relaxes the applied load and simultaneously dewets and becomes a foamed or bodied structure. This latter phenomenon was actually observed by X-ray photography (see Poker Chip Tests and Analysis, Section III).

After dewetting, the foamed material should evince a stress-strain behavior characteristic of a foamed material. This should imply, for example, a value of Poisson's ratio equal to 1/4. This latter statement is consistent with the observation that after relaxation ensues and while the material is dewetting the peak stress 2 P/A gradually relaxes to P/A. Accordingly, a constitutive equation, first used by Ko and Blatz (30) was postulated to represent the behavior of this material, namely:

$$\frac{\bar{\sigma}_i}{G} = 1 - \frac{1}{\lambda_i^2 J} \tag{104}$$

where

λ = Extension ratio
J = Volume ratio, V/Vo
G = Shear Modulus
$\bar{\sigma}_i$ = True stress, ith component

The problem of a spherical shell with a small spherical flaw at its center was solved for this particular constitutive equation. In the meanwhile, a triaxial stress-stretch curve was procured on the foamed material. When the data (Fig. 38) became available, it was noted that the range of strain over which the material was tested was only a few per cent, leading to the conclusion that it was no longer necessary to approach the characterization in terms of finite strain theory, but rather that Eq. 104 could take the form:

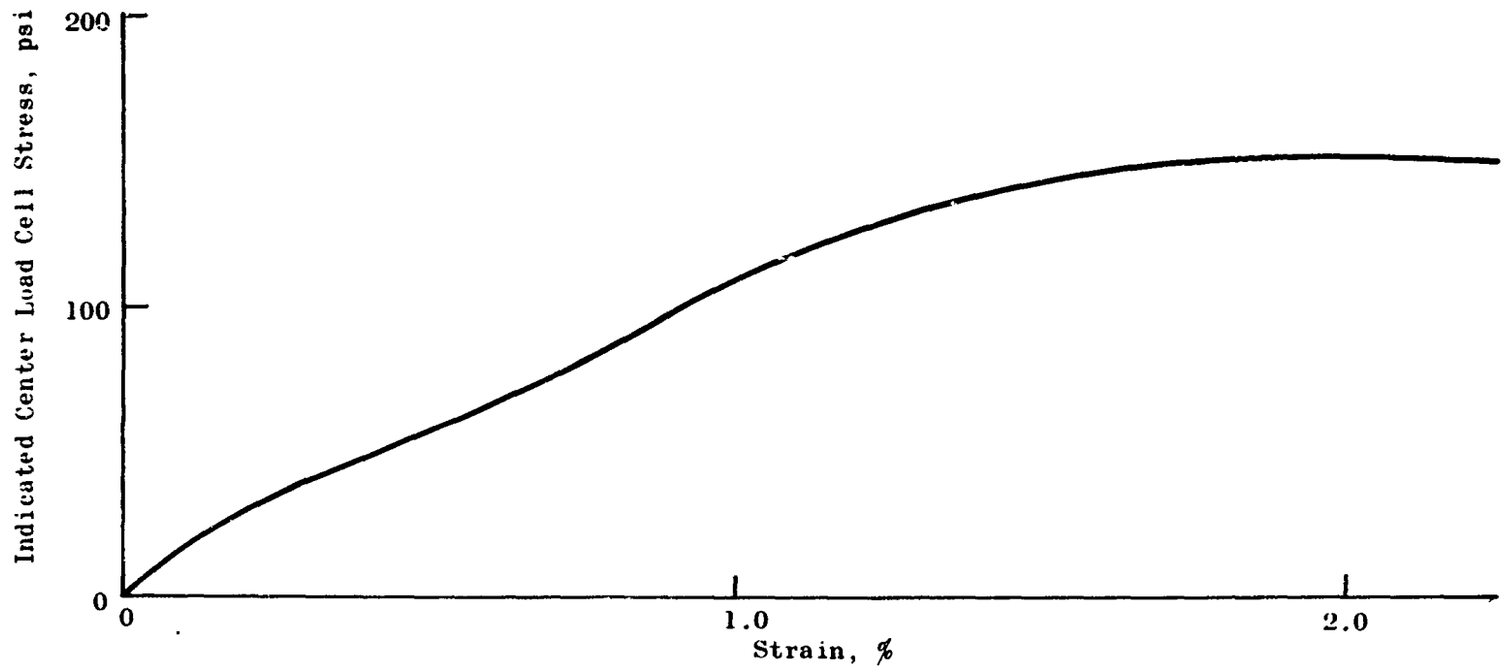

Figure 38. Stress-Strain Curve from Triaxial Test Following Constant Load Test (736 Pounds)

$$\frac{\sigma_i}{G} = 2\epsilon_i + \vartheta \tag{105}$$

where

ϑ = Dilatation = $\epsilon_1 + \epsilon_2 + \epsilon_3$

ϵ_i = ith component of strain

which corresponds to Hooke's law, with $\nu = 1/4$

Furthermore, once the material is foamed, deformation between the parallel plates is purely uniaxial rather than hydrostatic. Therefore:

$$\epsilon_1 = \vartheta = \epsilon \tag{106}$$

$$\epsilon_2 = \epsilon_3 = 0 \tag{107}$$

and

$$\frac{\sigma_1}{G} = 3\epsilon \tag{108}$$

or

$$\frac{\sigma_1}{\epsilon} = 3G \tag{109}$$

From the slope of the data in Fig. 38, it is concluded that the value of the shear modulus of the foamed material is ~3500 psi. Since this value is significantly higher than that of the shear modulus of the undewetted material, the assumption that the material has completely and uniformly dewetted is obviously erroneous.

An alternative procedure is to return to the spherical shell model (i.e., assume that the dewetting is highly localized). Under this assumption, the effective stress-strain behavior of the spherical shell is given by:

$$\epsilon_b = \frac{\sigma_r|_b}{4G} \frac{\frac{2(1-2\nu)}{1+\nu} + \frac{a^3}{b^3}}{1 - \frac{a^3}{b^3}} \tag{110}$$

where

a = Flaw Radius

b = Outer Radius of Spherical Model

If $(1-2\nu)$ is now neglected by the assumption that $\nu \rightarrow 0.5$ in the numerator, Eq. 110 becomes:

$$\epsilon_b = \frac{\sigma_r|_b}{4G} \frac{a^3/b^3}{1-a^3/b^3} \tag{111}$$

or

$$\frac{\sigma_r|_b}{\epsilon_b} = \frac{4G(1-a^3/b^3)}{(a^3/b^3)} \tag{112}$$

Taking G to be 1000 psi, which is typical of Lockheed's STV propellant 0064-61E, leads to the assumption that about 3% of the material has voided, i.e.:

$$\frac{a^3}{b^3} \approx 3\% \tag{113}$$

X-ray photographs indicate that this figure is varying with time as would be predicted using Eq. 110 if values for G and ν were varying with time.

GRIFFITH CRACK THEORY

After Griffith proposed that the critical condition for the growth of a crack can be determined by a power balance between the rate at which mechanical work is done on a body and the rate at which this work is taken up by an increase in strain energy together with an increase in surface energy, cracks of various geometries in bodies of various shapes were analyzed according to this criterion. In such calculations, two precautions must be observed. First, the integral of the strain energy density over the body must exist. This can be ensured by using a superposition principle in which one adds together two problems, one of which involves zero loading at the outer boundary but locally variable throughout and the other involves finite loading at the outer boundary and locally constant stress throughout. The latter problem is trivial and can be added to the solution of the first problem to give a desired result. The first problem is usually one involving pressure in the crack.

The latter problem is trivial and can be added to the solution of the first problem to give a desired result. The first problem is usually one involving pressure in the crack.

The second precaution deals with the question of whether the power balance applied to the infinite body with an infinitesimal crack gives the same result as the power balance applied to the finite body with a finite crack, after which the double limit is taken as the outer boundary moves to infinity and the finite crack becomes a flat or infinitesimal crack. The answer to this question, shown in the following section, is clearly no. The Griffith stress is derived for a finite body between confocal ellipses. First, when correctly done, the result is independent of the position of the outer boundary which can then be taken to be infinite. Second, in the limit as the elliptical crack becomes a flat crack, the Griffith stress becomes infinite.

IMPORTANCE OF FINITE ELASTIC EFFECTS IN THE INSTABILITY OF A SPHERICAL FLAW IN A THICK SPHERICAL SHELL

In stretching a thin disc bonded to two rigid parallel plates in the limit of infinite diameter-to-thickness ratio (so that the strains $\epsilon_x = \epsilon_y = 0$), infinitesimal axial stress is given by:

$$\sigma_z = \left(K + \frac{4}{3} G\right)\epsilon_z \tag{114}$$

where

K = Bulk Modulus

Since, for rubberlike materials

$$K \gg G \tag{115}$$

the stress field is very nearly hydrostatic. On this basis, it is convenient to imagine a spherical shell-like region between the two plates, at the center of which is initiated a spherical flaw that eventually grows to produce the fracture (see sketch below).

a = radius of hole

D = diameter of plate

b = outer radius of sphere

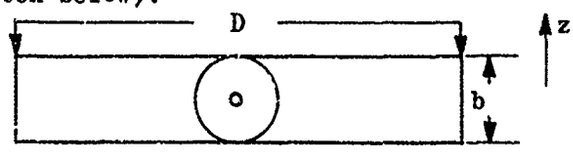

As $\frac{D}{b} \to \infty$ $\quad \sigma_z = (K + 4/3G)\,\epsilon \simeq K\epsilon$, $\therefore$ hydrostatic

Elastostatic Analysis of Parallel-Plate Tension Data

For this geometry it is possible to do an exact general analysis of the instability criterion, for which:

$$\frac{2\gamma}{A} \geq W_a + K_a \tag{116}$$

where

A = Undeformed Radius of Spherical Flaw*

W = Strain Energy + Dissipation Rate Density

γ = Characteristic Strain Energy Release Rate

Since Eq. 116 shows that surface energy depends directly on the strain energy density at the flaw interface, it might be expected that the surface energy calculated from finite elastic theory would differ significantly from that calculated from infinitesimal elastic theory. This statement is poignant because it is precisely at the flaw boundary that large displacement effects are encountered. For example, it will not be uncommon for the deformed radius to be several times larger than the undeformed radius, which means a strain of several hundred per cent. Therefore, γ was calculated from both theories. Kinetic energy effects were not included in the calculation. For moderately slow strain rates, the inertial term is 5--7 orders of magnitude less than the strain energy term.

Assuming that a strain and stress at the point of instability (growth initiation) of the spherical flaw are provided and taking the outer radius of the spherical shell to be 0.5 the disc thickness, the two important material properties, A/B and γ/B, can be calculated** Pertinent equations are:

*The capital A in this equation corresponds to a_0 as used in the body of this report.

**B is the undeformed outer radius of the spherical model.

Neo-Hookean	Hookean	
$\epsilon_a = \dfrac{\frac{\sigma_{r\,b}}{G} - \frac{1}{4}}{\frac{5}{4} - \frac{\sigma_{r\|b}}{G}}$	$\simeq \dfrac{\frac{\sigma_{r\|b}}{G}}{4}$	$\lambda_a \equiv 1 + \epsilon_a$
$\nu = \dfrac{3\epsilon_b}{\lambda_a^3 - 1}$	$\simeq \dfrac{\epsilon_b}{\epsilon_a}$	
$A = B\,\nu^{1/3}$		
$\gamma = \dfrac{E\,A}{12}\left(2\lambda_a^2 - 3 + \dfrac{1}{\lambda_a^4}\right)$	$\simeq E\,A\,\epsilon_a^2$	
$\dfrac{\sigma_{\theta\|a}}{G} = \lambda_a^2 - \dfrac{1}{\lambda_a^4}$	$\simeq 6\epsilon_a$	

In evaluating these quantities, various values of the Young's modulus were chosen to show how sensitive the computed values of γ and A are to that parameter. Tables XV and XVI show the results for a Neo-Hookean and a Hookean material, respectively. When E is 500 psi, which corresponds to the actual test material, the γ calculated from Hookean behavior is only 30% lower than that calculated from Neo-Hookean behavior; whereas A is overestimated by a factor of 2. This says that in a tri-axial, nearly hydrostatic, state of stress, geometrical nonlinearities are not important in an incompressible material. On the other hand, further attention will be paid to the effect of geometrical nonlinearities in uni- or biaxial states of stress. As an expediency, the linear theory will presently be applied to these problems of instability.

TABLE XV. SOLUTIONS USING NEO-HOOKEAN FORMULAS

σ_b = 225 psi		B = 0.3 inch			ϵ_b = 0.00861		
E, psi	270	300	315	337.5	375	450	500
$\bar{\sigma}_{r\|b}$	2.50	2.25	2.14	2.00	1.80	1.50	1.35
λ_a	∞	8.00	5.60	4.02	2.88	2.06	1.81
ν	0	0.0000505	0.000148	0.000404	0.00108	0.00297	0.00434
A, in.	0	0.00437	0.00626	0.00913	0.0121	0.017	0.0192
γ, in.-lb/in.^{2}	∞	14.1	10.2	7.81	5.33	3.65	3.01
$\dfrac{\bar{\sigma}_{\theta\,a}}{G}$	∞	64.0	31.4	16.1	8.28	4.18	3.18

TABLE VII. SOLUTIONS USING [illegible] FORMULAS

E, psi	270	300	315	337.5	375	450	500	
$\sigma_r\|_b/G$	2.50	2.250	2.140	2.00	1.80	1.50	1.350	
ϵ_a	0.625	0.563	0.535	0.500	0.450	0.375	0.338	70% low
ν	0.0138	0.015	0.0161	0.0172	0.0191	0.0230	0.0255	6 fold
A, in.	0.0283	0.0292	0.0298	0.0304	0.0315	0.0335	0.0347	
γ, $\frac{\text{in.-lb}}{\text{in.}^2}$	3.05	3.35	2.77	2.66	2.48	2.2	2.02	γ, $\frac{\text{in.-lb}}{\text{in.}^2}$
$\frac{\bar{\sigma}_R\|_a}{G}$	3.75	3.178	3.21	3.00	2.70	2.25	2.03	50% low

FOAM MECHANICS

When the parallel-plate tensile test under constant load was conducted, it was observed that the disc-shaped specimen gradually became full of voids from 25--50 mils in size. For a foamed material, Blatz (30) has shown that a useful stress-strain law is given by:

$$\frac{\sigma_i\lambda_i}{G} = f\lambda_i^2 - \frac{1-f}{\lambda_i^2} + J\left[4(1-f) - \frac{2(1-f)}{1-2\nu}\right] + J^2\left[\frac{1}{1-2\nu} - 2(1-f)\right] \quad (117)$$

This relation provides a very precise and useful characterization of propellant in the foamed state (i.e., after dewetting). With $\nu = 1/4$, which seems to fit the data best,

$$\frac{\sigma_i\lambda_i}{G} = f\lambda_i^2 - \frac{1-f}{\lambda_i^2} + J\,(1-4f) + 2fJ^2 \quad (118)$$

For this particular choice of Poisson's ratio and for various values of f, the relation between load and extension in the poker chip has been calculated using the flat model.

LINEAR VISCOELASTIC CUMULATIVE DAMAGE

It has been suggested that cumulative damage may be predicted as the viscoelastic creep of a suitably modified flaw in a specimen of propellant subjected to vibratory load or displacement input. This problem was first considered for a vibratory displacement input at the outer boundary of a spherical shell with a spherical flaw.

Neglecting kinetic effects and using the convolution integral to calculate time-dependent stress resulting from a time-dependent strain, Eq. 116 becomes

$$\frac{\gamma}{b} \geq 2 \left(\frac{b}{a}\right)^5 \left[\int_0^t d\epsilon_b(t') \int_0^{t'} E_{rel}(t' - t'')d\epsilon_b(t'')\right] \qquad (119)$$

and

$$\sigma_r|_b = \frac{4}{3}\left(\frac{b^3}{a^3} - 1\right)\int_0^t E_{rel}(t-t')d\epsilon_b(t') \qquad (120)$$

for linearly viscoelastic materials.

Equation 119 reveals that if the quantity in brackets increases with time, a (the flaw radius) must also increase to maintain the product constant and equal to γ/b. From Eq. 120, then, associated stress for a given displacement input can be calculated. The question of the behavior of the quantity in brackets for a specified displacement input then arises.

To evaluate the integral for a chosen sinusoidal input, the following behavior of the relaxation function is noted. First, propellant data are well represented by the form

$$E_{rel} = E_r + (E_g - E_r)\frac{at^{-n}}{\Gamma(1-n)}, \quad E_r < E_{rel} < E_g/10 \qquad (121)$$

The preceding representation is actually an asympototic expansion of the complete function known as Mittag-Leffler (31). Data are fitted with:

$n = 0.194$

$a = 0.00151$ (t in minutes)

With this representation:

$$E^{(k)} \equiv \frac{k}{t^k}\int_o^t E_{rel}(t')t'^{k-1}dt' = E_R + (E_G-E_R)\frac{at^{-n}}{\Gamma(1-n)}\frac{k}{k-n} \qquad (122)$$

so that

$$E^{(k)} \simeq E_{rel} \equiv E^{(0)}, \text{ for all } \underline{k}.$$

With this mild approximation, Eq. 119 may be simplified. In doing this, the integrals must be separated into two parts to remove the discontinuity associated with the initial strain input. In carrying out the integration by parts, no assumption is made that $\underline{t}$ is large, so the result reduces to the correct result as $t \to o$ and is the first term of an ordered expansion that may be made as exact as possible by including higher terms.

Choosing the vibratory input in the form gives:

$$\epsilon_b = \epsilon_{bm}\frac{1+\alpha sn\omega t}{1+\alpha}, \quad 0 < \alpha < 1 \qquad (123)$$

whereupon Eq. 119 becomes:

$$\frac{\gamma_a^5}{b^6} \geq \left(\epsilon_{bm}^2\right)\frac{E_g + (2\alpha sn\omega t + \alpha^2 sn^2\omega t)\,E_{rel}(t)}{(1+\alpha)^2} \qquad (124)$$

The period of the vibratory input is given by:

$$\omega T = 2\pi \qquad (125)$$

and the time to a peak is given by:

$$t = (N + \frac{1}{4})T \qquad (126)$$

so that

$$\omega t = 2\pi N + \frac{\pi}{2} \qquad (127)$$

Insertion of this result in Eq. 124 yields:

$$\frac{\gamma_a^5}{b^6} \geq \left(\epsilon_{bm}^2\right)\frac{E_g + (2\alpha+\alpha^2)E_{rel}\left(\frac{2\pi N}{\psi}\right)}{(1+\alpha)^2} \tag{128}$$

where

N = Number of cycles

As $N \rightarrow 0$, Eq. 128 reduces to:

$$\frac{\gamma_a^5}{2b^6} \geq E_g \epsilon_{bm}^2 \tag{129}$$

which is the correct result for a step input into an elastic material. On the other hand, E_{rel} is a monotonically decreasing function; so Eq. 119 predicts that the flaw radius must decrease with the number of cycles. This means that it achieves its peak on the first cycle and stays constant thereafter. This is to be expected on the basis of thermodynamic behavior of a dissipative material. One can easily take a simple situation in which

$$E_{rel} = E_g^{-kt} \tag{130}$$

and

$$\epsilon_{bm} = \frac{\epsilon_{bm}(1 - \cos \omega t)}{2} \tag{131}$$

In this case there is no discontinuity in the input, and the integrals are exactly calculable. That the peak flaw radius (γ_a^5/b^6) must decrease linearly with N is obvious. This again means that it achieves its peak value on the first cycle and remains constant thereafter.

In summary, a vibratory displacement input of fixed amplitude does not produce cumulative damage under the assumption of Griffith instability. To achieve same, one must input a load history which is ever higher than the value to which the load will relax in the case of constant strain input. Then and only then will cumulative damage ensue. Conversely, a vibratory displacement input of fixed amplitude is known, de facto, to produce cumulative damage, which strongly indicates that other mechanisms besides Griffith instability are involved.

To compute the strain output produced by a specified load input, the flaw radius between Eq. 119 and 120 must be eliminated. Therefore:

$$v_r|_b \simeq \frac{4}{3}\int_o^t E_{rel}(t-t')d\epsilon_b(t')\left[\frac{\gamma/2b}{\int_o^t d\epsilon_b(t')\int_o^t E_{rel}(t'-t'')d\epsilon_b(t'')}\right]^{3/5} \qquad (132)$$

where Eq. 119 has been neglected with respect to (b^3/a^3). Equation 132 in general will have to be integrated numerically because of the nature of the problem involving a moving boundary. In fact, previous statements to the effect that the strain output for a given load must be cast in terms of moments of the creep function are meaningless since, for the spherical flaw (neglecting inertia):

$$\sigma_r = \sigma_r|_b \frac{1 - \frac{a^3}{r^3}}{1 - \frac{a^3}{b^3}} \qquad (133)$$

$$\sigma_\theta = \sigma_r|_b \frac{1 + \frac{a^3}{2r^3}}{1 - \frac{a^3}{b^3}} \qquad (134)$$

and

$$\epsilon_\theta = \frac{\frac{a^3}{r^3}}{4\left(1 - \frac{a^3}{b^3}\right)} J^*\sigma_r|_b \qquad (135)$$

Now the strain energy plus dissipation rate density is given by:

$$W \equiv \int_o^t (\sigma_r' d\epsilon_r' + 2\sigma_\theta' d\epsilon_\theta') = 2\int_o^t (\sigma_\theta' - \sigma_r')d\epsilon_\theta(t') \qquad (136)$$

or

$$W = \frac{3}{8}\int_0^t \left(\frac{\frac{a'^3}{r^3}}{1-\frac{a'^3}{b^3}}\right)^2 \sigma_r|_b' \; d(J^*\sigma_r|_b)' \qquad (137)$$

where the prime designates the value at past time t' and where

$$J^*f(t) \equiv \int_0^t J_{crp}(t-t')df(t') \qquad (138)$$

In general, Eq. 137 cannot be integrated without additional input since the motion of the boundary as expressed by a (t') depends not only on the load history but also on the history of the boundary.

In summary, Eq. 119 and 120 are the only two equations by which relations between load, displacement, and spherical flaw radius can be expressed.

APPENDIX II

PHOTOMICROSCOPIC DOCUMENTATION OF INTERNALLY PRESSURIZED CYLINDERS

Page 128 is blank

APPENDIX II

PHOTOMICROSCOPIC DOCUMENTATION OF INTERNALLY PRESSURIZED CYLINDERS

by
J. E. Hilzinger, Rocketdyne Research

Investigations of the mechanisms resulting in the initiation and propagation of fracture in materials are continuous attempts to reduce the uncertainties associated with failure analyses. The analytical prediction of behavior of actual structures fabricated from some classes of these materials (i.e., brittle, composite) has not been satisfactorily developed, and realistic behavior descriptors, either qualitative and/or quantitative are needed as a basis for practical engineering judgements.

This report describes a study conducted by the author on the behavior of one such material, a composite propellant, under structural and environmental conditions translatable to service applications.

OBJECTIVE

The primary purpose of this effort was the photomicroscopic documentation of the structural behavior of the Lockheed-furnished STV composite propellant under known stress and/or strain states. (Internal pressurization of small hollow cylinders at preselected levels of stress or strain rate and temperature provides outer surface phenomena indicative of the type and extent of microstructural damage associated with a highly filled elastomeric system.)

To achieve this objective, the following were accomplished:

1. Photographic documentation of the surface behavior of both machined and cast surface specimens during a linear increase in stress of 100 psi/min to failure at ambient laboratory conditions

2. A highly detailed record of constant stress rate surface mechanisms for machined and cast surfaces at relatively low stress rates and ambient conditions

PROCEDURE

The preparation of hollow cylindrical test specimens from the CTPB propellant took one of two forms: machining from a cast block, or sectioning of a molded cylindrical tensile specimen. A summary of the

cylinder dimensions (Table XVII) revealed that all test specimens had nominal 1/8-inch wall thickness although minor web variations between and within cylinders resulted from the internal boring operation. Two deliberate changes in cylinder geometry evolved during testing. The initial outside machined diameter of 0.8 inch, although more conducive to good photographic practice, was reduced to 0.5 inch to provide a direct comparison with the cast surface specimens available only in the smaller size. In addition, the length-to-diameter ratio was increased from 1.5/1 to 2/1 when the calculated possibility of substantial end effects reaching the center hoop stress area was confirmed photographically.

Propellant cylinders were closed at each end by Plexiglass fixtures grooved to accept the web thickness and, where applicable, the internal 0.0045-inch latex bladder. An ambient cured epoxy resin was used to bond the propellant into the end fixtures. Eight cylinder assemblies were satisfactorily fabricated in this manner after an initial failure using an inadequate end cap design.

The entire test series was conducted using dry gaseous nitrogen both as a controlled storage medium and as the pressurant for all stress levels. Photographic techniques employed ranged from time lapse methods with 35 mm to 16 mm motion at 128 or 400 frames/second.

RESULTS AND DISCUSSION

Surface phenomena and crack propagation of five hollow propellant cylinders was photographed while the cylinders were being subjected to internal pressurization at a rate of approximately 100 psi/minute. Three of the specimens had machined outer surfaces, and two had cast outer surfaces. The behavior of the machined specimens was consistent and differed from that of the cast specimens. Clear delineation of this difference was obtained by 16 mm photography at a speed of 400 frames/second.

Although all failures were centralized longitudinal cracks, the machined outer surfaces obviously experienced continual structural degradation during a substantial period before failure. Widespread blanching and localized dewetting are visible in the sequence shown in Fig. 39; the internal failure which led to the final fracture occurred at the interface of the larger oxidizer particles. An example of a near surface 400+ micron diameter particle initiating fracture of machined cylinder 004 is shown in detail in Fig. 40. The extent of the surface degradation is indicated by the rapidity of the crack propagation--less than 0.0025 second, or one camera frame.

TABLE XVII. PROPELLANT HOLLOW CYLINDER DESCRIPTIONS

No.	Surface Condition	Test Bladder	Radius (Outside) R_o	Radius (Inside) R_1	Ratio R_1/R_o	Length Dia. L/D_o	Photographic Coverage
001	Machined	Yes	0.3992	0.2441	0.611	1.5/1	35mm Still Sequence and Motion at 128 Fr/Sec
002		Yes	0.4008	0.2566	0.640		35mm Still Sequence and Motion at 128 Fr/sec
003		Yes	0.4045	0.2557	0.632		35mm Still Sequence and Motion at 128 Fr/sec
004		Yes	0.4043	0.2444	0.605	2/1	Dual Motion at 400 Fr/Sec
005		No	0.2490	0.1232	0.495		Still Sequential, Hi Mag
C001	Cast	Yes	0.2643	0.1325	0.501		Dual Motion at 128 Fr/Sec
C002		Yes	0.2668	0.1292	0.484		Dual Motion at 400 Fr/Sec
C003		No	0.2665	0.1147	0.430		Still Sequential, Hi Mag
C004		No	0.2658	0.1197	0.450		Still Sequential, Hi Mag

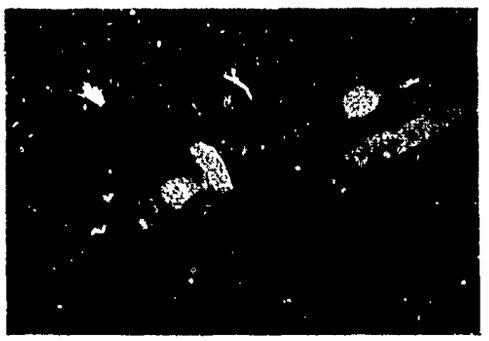

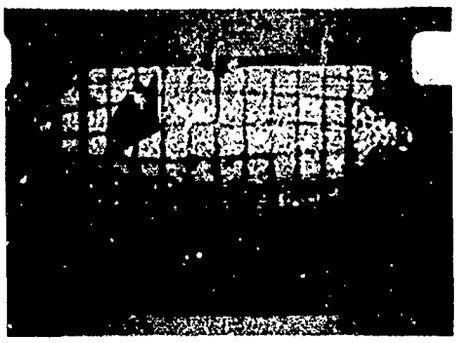

2.5 Msec Before Failure

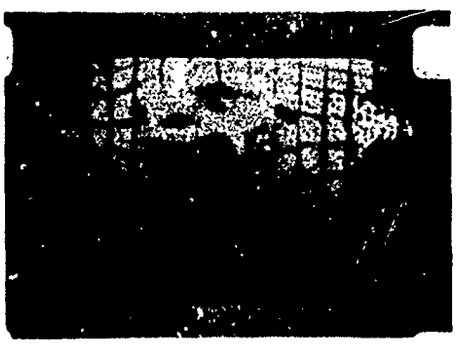

25 Msec Before Failure

Failure

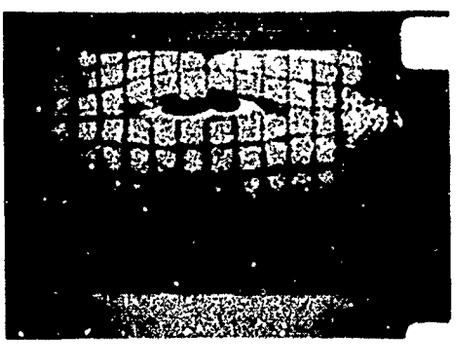

12.5 Msec Before Failure

7.5 Msec After Failure

Figure 39. Cylinder 004: Machined Surface with 0.1-inch Grid, 16mm Motion Photography at 400 Frames/sec

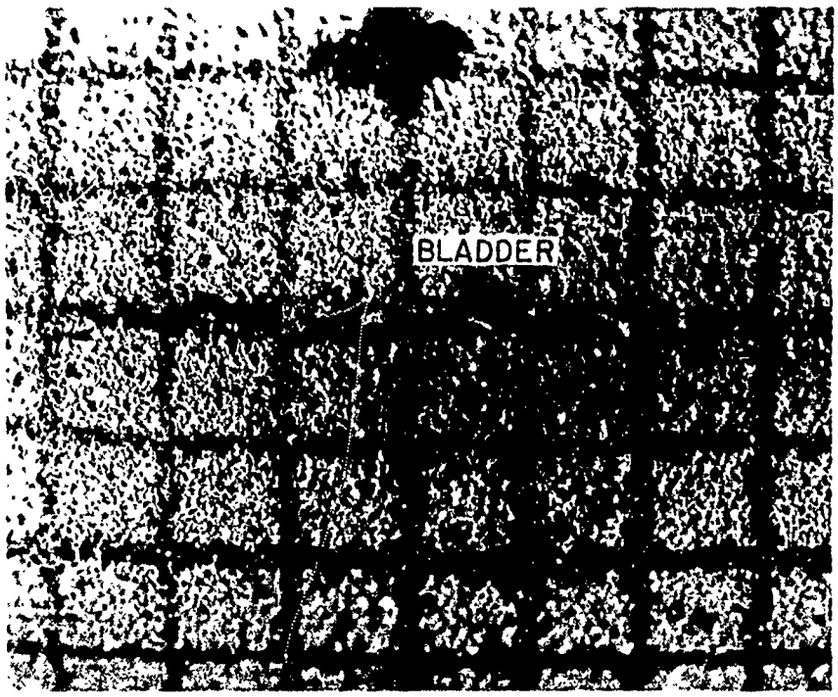

a. Machined Cylinder 004

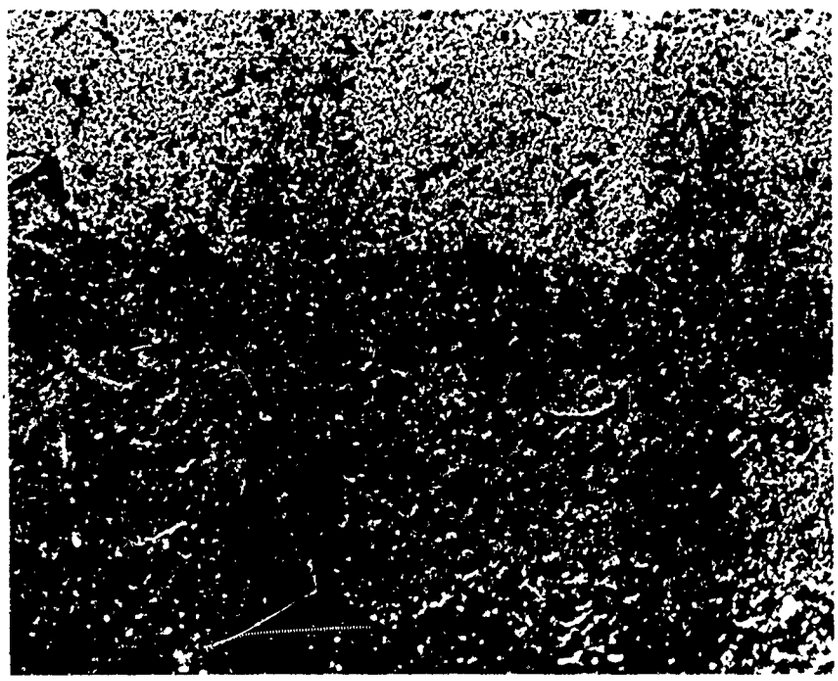

b. Cast Cylinder C-002

Figure 40. Fracture Detail with 0.1-Inch Grid

Cast surfaces, however, produce distinctly different failure phenomena. No surface activity was observed before crack initiation. Perforation of the cylinder wall led to relatively slow (0.100 second) crack propagation, and extensive analysis of the various films indicated the propellant tearing on the innerbore proceeded to the outside surface where the crack propagation was apparently retarded by the binder-rich outer cast surface. This indicated behavior is shown by film sequences in Fig. 41.

A comparison of all fracture areas for the 100 psi/minute pressurization rate (Fig. 42) also indicates another possible condition which the high-speed camera coverage implies but cannot confirm because of film grain limitations. Cylinders 002 and 003 display fractures that apparently pass through oxidizer crystal boundaries in contrast to failure zones that bypass or dewet particles. Consequently, it is not unreasonable to expect highly localized circumferential strains approaching 30% for both types of propellant surfaces.

Results from the second testing phase, Detailed Descriptions of Local Behavior, clarify this particular phenomena. Two cylinders, one machined and one with a cast surface, were pressurized at a relatively slow rate at ambient conditions. A small portion of the surface was photographed using direct magnification of approximately 20 power. This technique provided a viewing area of 0.05 sq in. which included a representative quantity and distribution of oxidizer particles.

The machined surface, Fig. 43 and 44 under comparable conditions suggests that a substantial portion of the exposed oxidizer crystals are actually damaged during machining. Consequently, cleavages occur within the crystal boundaries at relatively low stress levels. These vacancies grow with increasing stress application and for the area observed, this form of stress relief prevails over "conventional" dewetting.

Observation of the cast surface (Fig. 45) during pressurization to failure (Fig. 46)is not particularly revealing. The binder rich "skin" precludes the possibility of directly viewing matrix-filler phenomena, although a number of distinguishing surface characteristics are available for use in measuring local surface strains.

Data from these tests are summarized in Table XVIII.

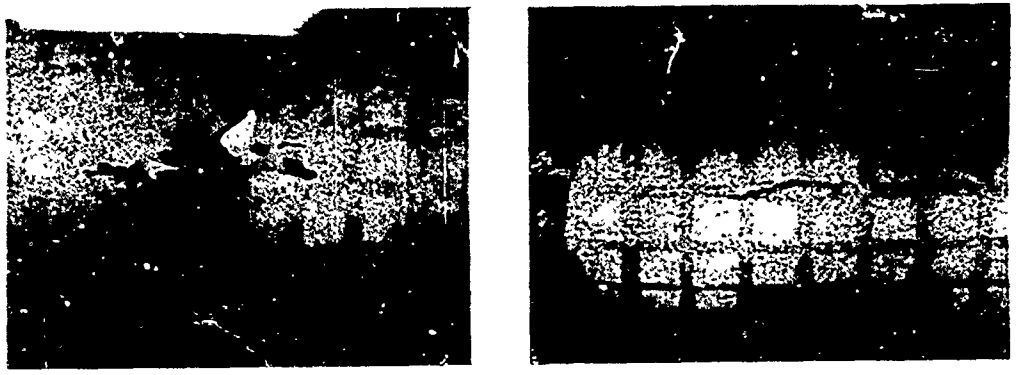

C-001 C-002

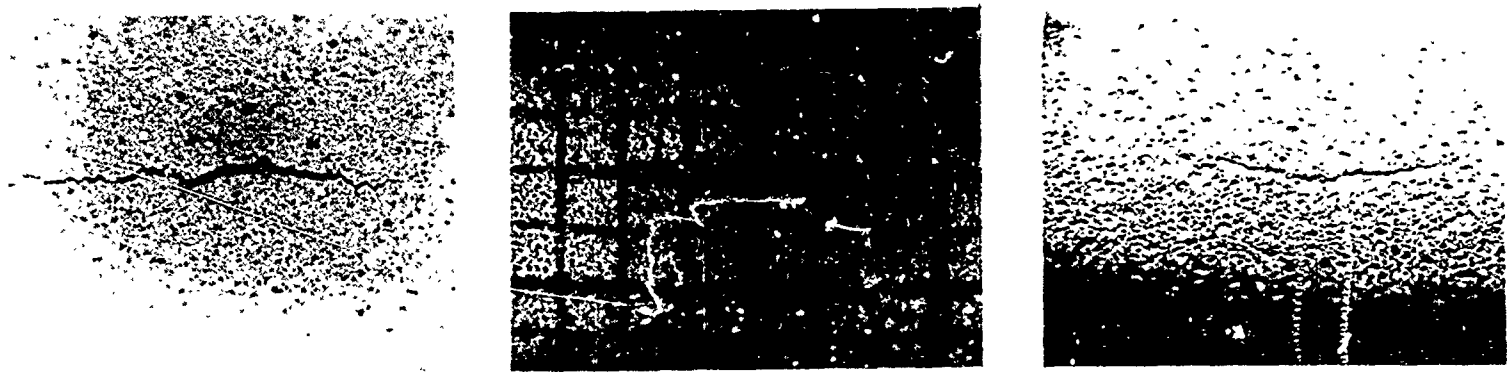

002 004 003

Figure 41. Failure Areas for High Stress Rate: Cast Surfaces C-001 and C-002; Machined Surfaces 002, 003, 004

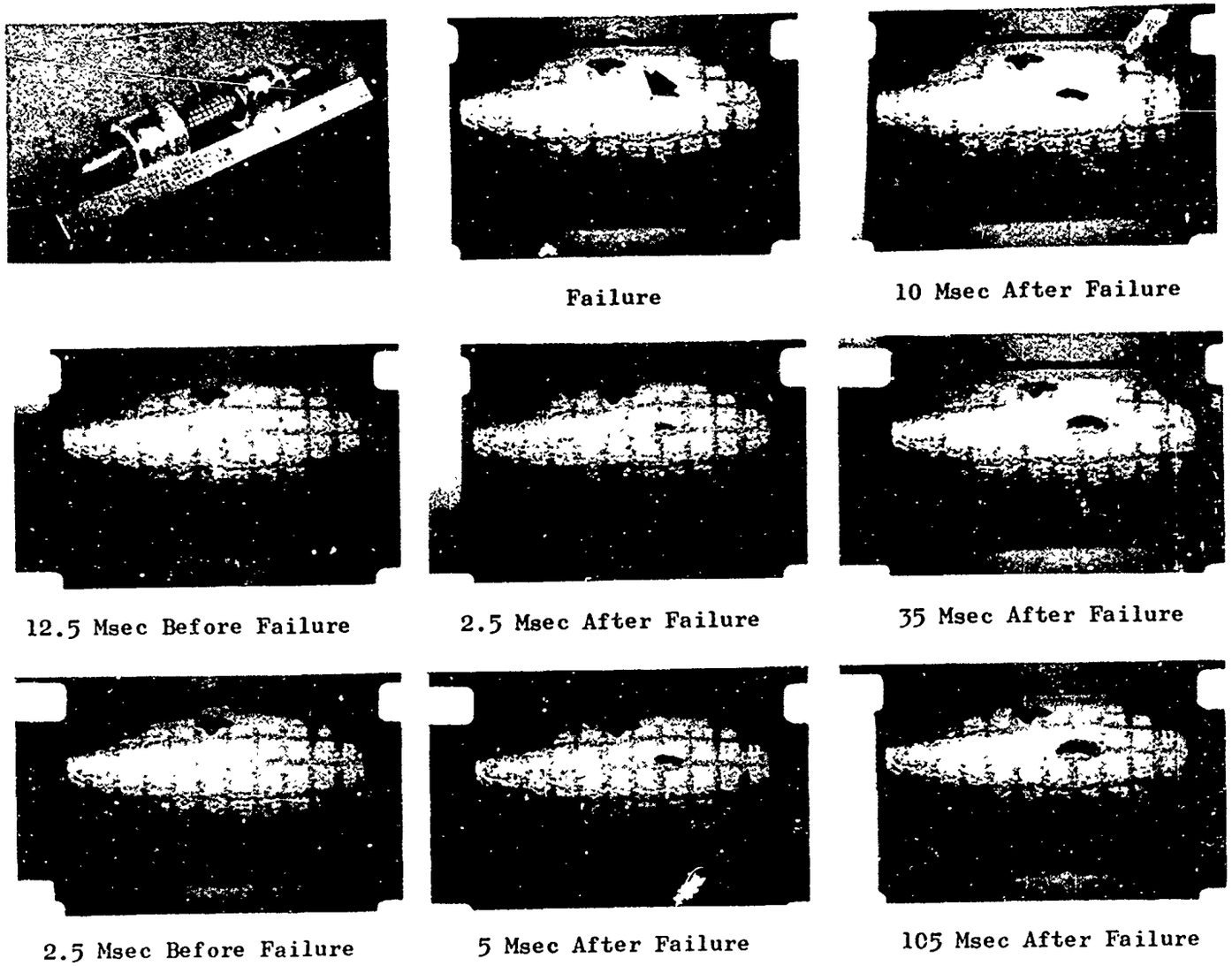

Figure 42. Cylinder C-002: Cast Surface with 0.1-Inch Grid
16mm Motion Photography at 400 Frames/sec

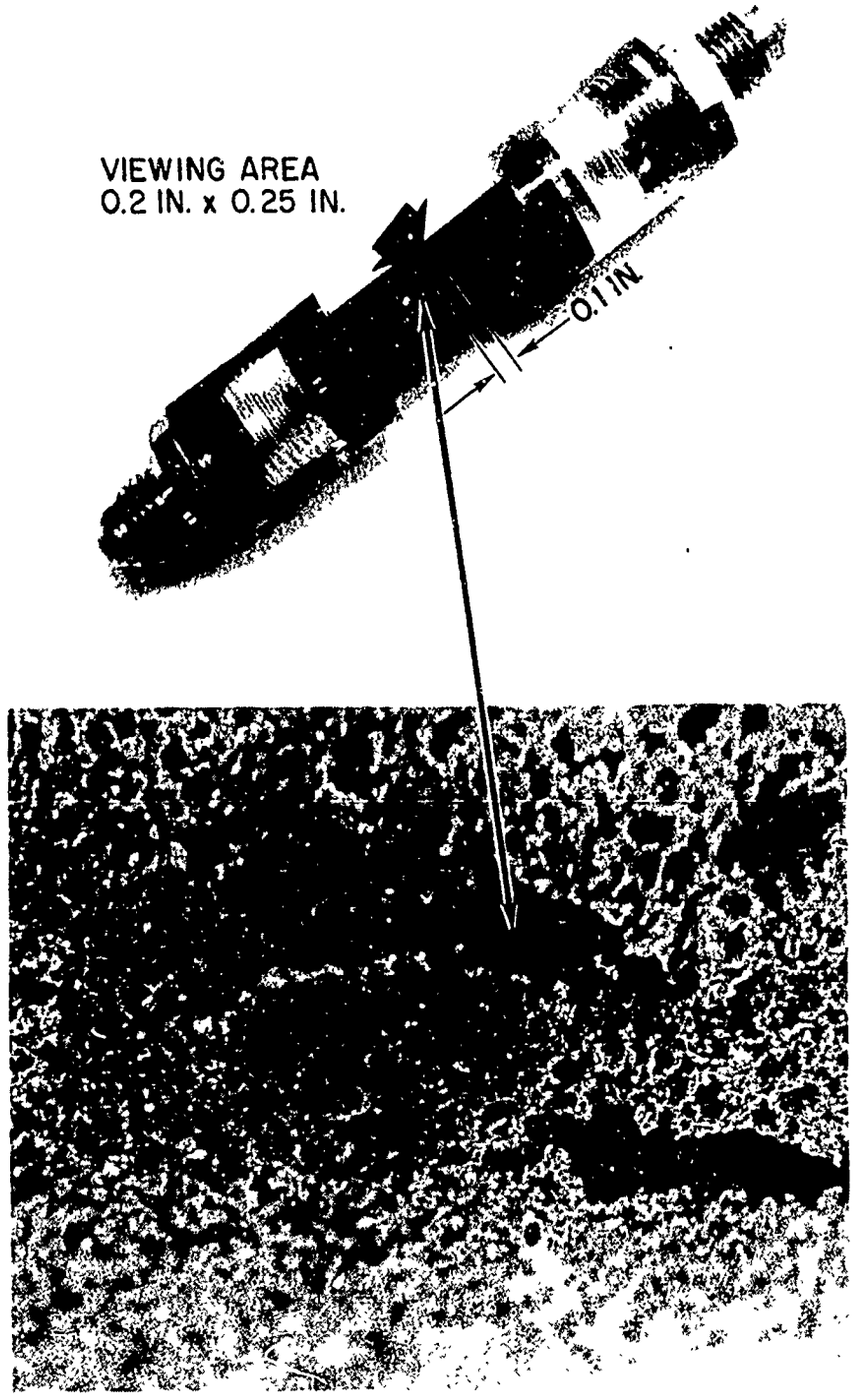

Figure 43. Machined Surface Crack Location, Low Stress Rate, Cylinder 005

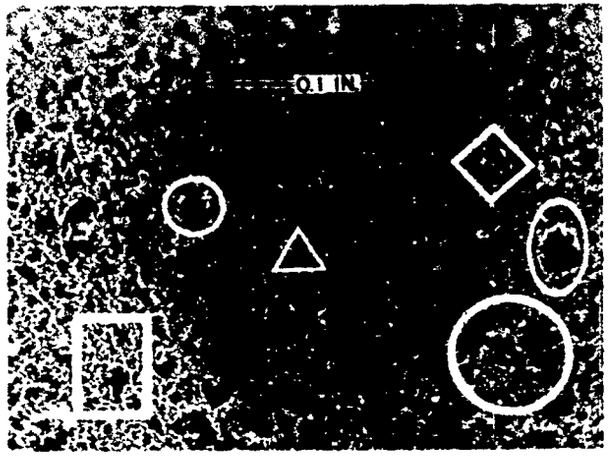

5.0 psi

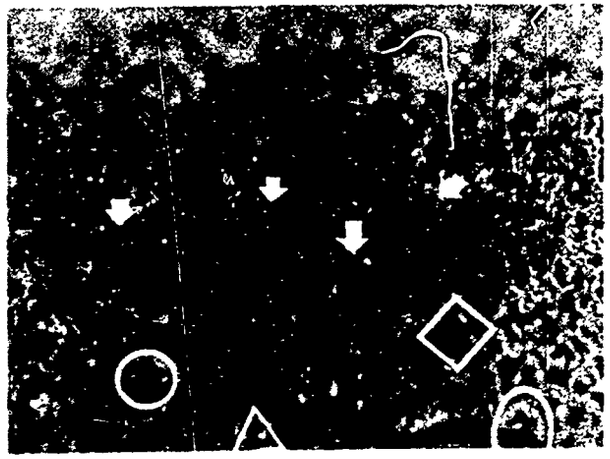

54.6 psi

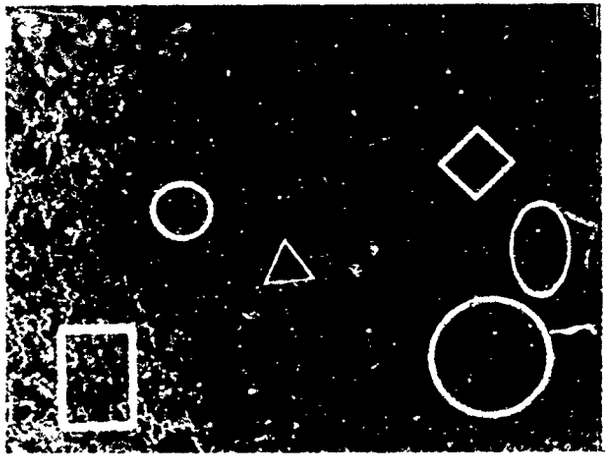

45.2 psi

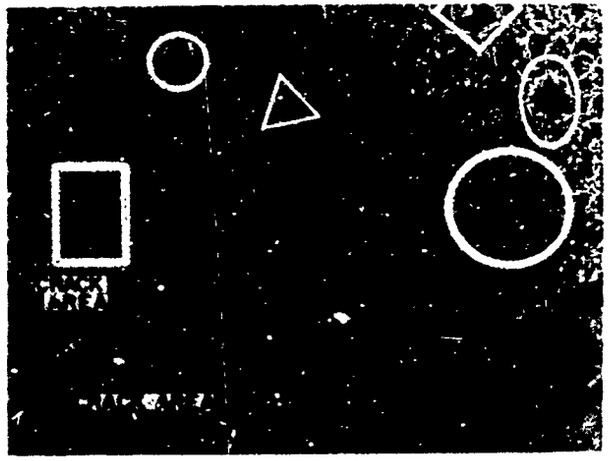

68.2 psi

Figure 44. Machined Surface Detail at High Magnification
Low Stress Rate, Cylinder 005

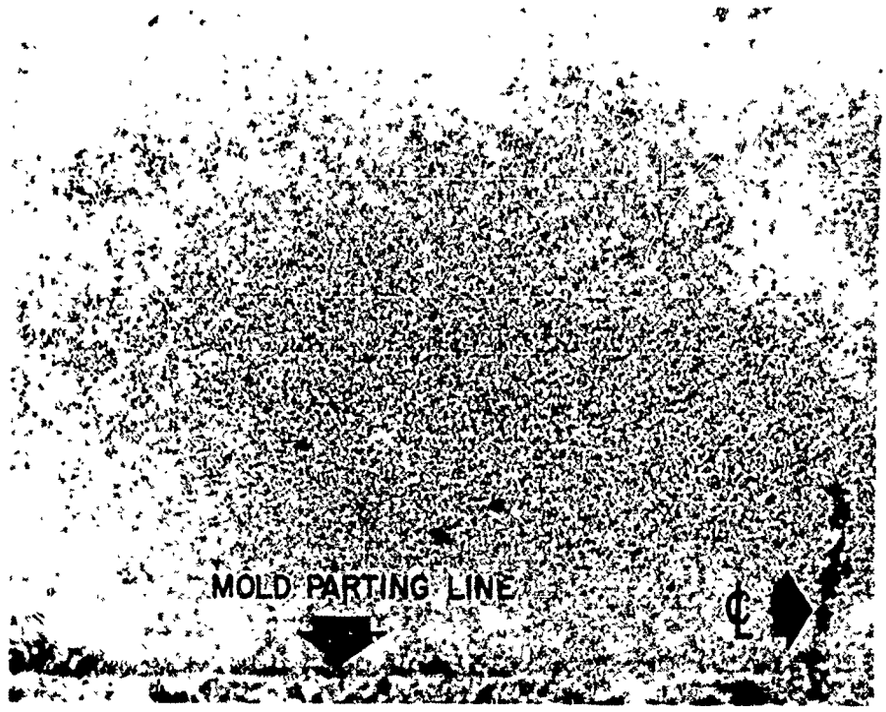

0 psi

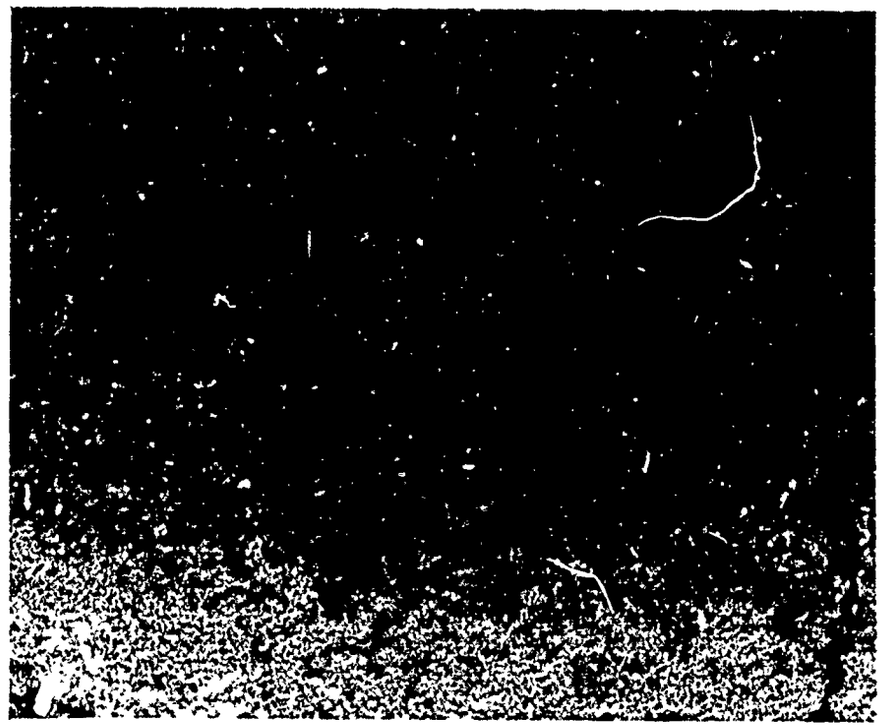

0.2 in.

63.0 psi 18.7 sec Before Failure

Figure 45. Cast Surface Detail Cylinder C-003 High Magnification, Low Stress Rate

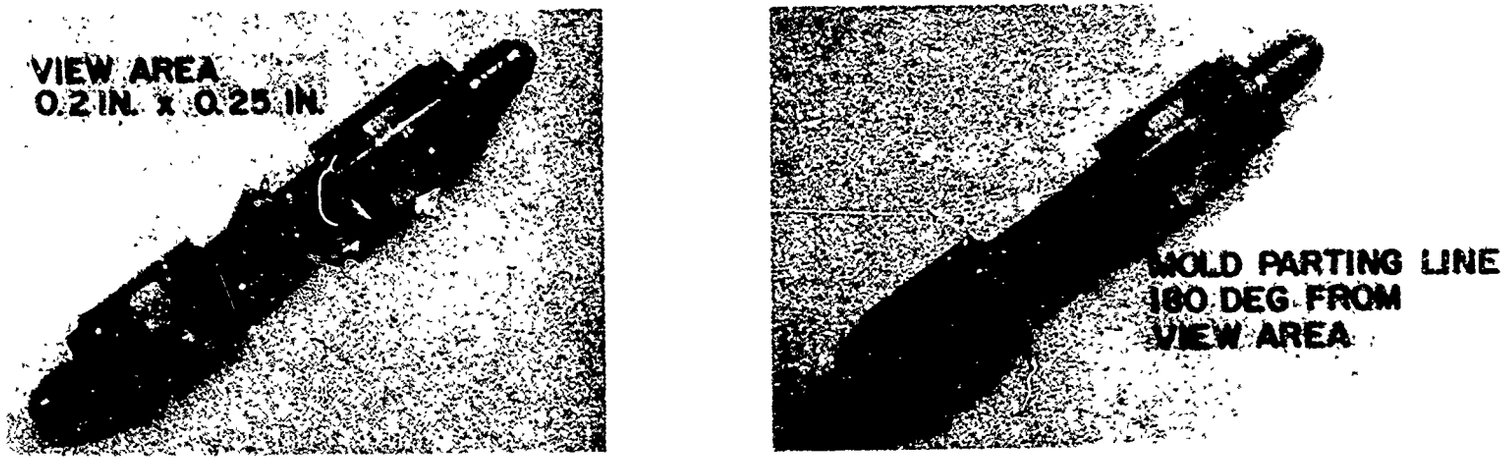

Figure 46. Cast Surface Crack Location, Low Stress Rate, Cylinder C-003

TABLE XVIII. SUMMARY OF TEST RESULTS

No.	Pressure Rate psi ave / minute	P_{max}, psi	Time to Failure, sec	σ_{max} (Lame')	Remarks
001	NA	NA	NA	NA	End Cap Failure
002	108.9	57.4	31.6	137.5	35 mm Sequence of Fracture Area
003	106.1	63.0	35.6	147.0	Fracture at 128 Fr/sec
004	110.2	40.6	22.1	88.5	Fracture Excellent at 400 Fr/sec
005	21.6	71.0	194.3	117.2	Fracture Adjacent to 0.2- x 0.25-Inch View Area
C-001	104.9	71.0	40.6	118.3	Fracture Viewed by Both Camera Stations
C-002	94.0	70.8	45.2	114.3	Fracture Excellent at 400 Fr/sec
C-003	15.6	60.6	232.5	88.5	Fracture at Seam, 180° from View Area
C-004	23.9	70.6	176.9	106.8	Photolite Failure During Sequence

Page 142 is blank

APPENDIX III

SIMULTANEOUS THERMAL AND MECHANICAL STRAINING OF BIAXIAL STRIP SPECIMENS

Page 144 is blank

APPENDIX III

SIMULTANEOUS THERMAL AND MECHANICAL STRAINING

Two tests in which biaxial specimens were stretched and cooled very slowly were run on the Cumulative Damage test machine to simulate the inner bore condition of a strain cylinder during "cooldown" in an attempt to induce failure. During the first test, the specimen was cooled at a rate of 3 F/hour and at a straining rate of 0.00143 in./in./hr. Data collected were: load, displacement across the specimen (inside the environmental box), displacement of the ram (outside the box), and the temperature of the specimen and air inside the box.

Figure 47a is a plot of the results obtained in the first test. The test progressed as expected for 61 hours at which time the load suddenly dropped from 530 to 215 pounds. A careful check after the test was concluded revealed no deficiencies in the system, and the specimen itself was not damaged. It was, therefore, concluded that the clamping arrangement loosened as the temperature dropped, permitting the grip on the specimen to slip until the clamping bolts bottomed out with the holes in the end bar. When a positive mechanical linkage had been re-established, the load started increasing again. The test was allowed to run until the ramp generator completed a full-scale run (87 hours) despite the doubt that the system was working satisfactorily.

The true strain value cannot be precisely determined because of the slippage. However, it possible to estimate the amount of slippage by simply proportioning the loads at the time of slippage since some of the tensile load remained after the slippage occurred. Thus, correcting the final displacement figure, the final strain is estimated to be 8.8%. The peak load is estimated to have been 1450 pounds as indicated by the dotted line, Fig. 47a. The solid line connects the actual data points collected. The peak load was not recorded because it was felt that very little relaxation would occur in the specimen after the test stopped. Since the test terminated in the middle of the night, it was assumed that the reading the next morning would approximate that at the end of the ramp run since the machine would hold the final strain and temperature. It is clear that considerable relaxation occurred at -100 F as indicated by the continued drop in the load. Maximum stress at 87 hours was 308 psi. The stress after 30 additional hours at constant strain and temperature had dropped to 133 psi. The test was discontinued without failure occurring.

In the second test, a higher strain rate was utilized, but the cooling rate was held at the same value. The strain rate in this case was 0.0029 in./in./hr, and the rate in temperature change was 3 F/hr. A positive pull was assured by removing all of the play between the clamping bolts and the holes in the end bar before starting the test. Test results are plotted in Fig. 47b. Failure occurred after 62.5 hours at a stress of 170 psi when the temperature was at -37 F. The strain at the time of failure was 18.2%.

These data are quite encouraging since precise failure data can now be related to both temperature and mechanical strain inputs for the critical biaxial stress condition. Thus, the critical limits for these changes as they affect both mechanical properties and failure can be defined in terms of realistic motor failures.

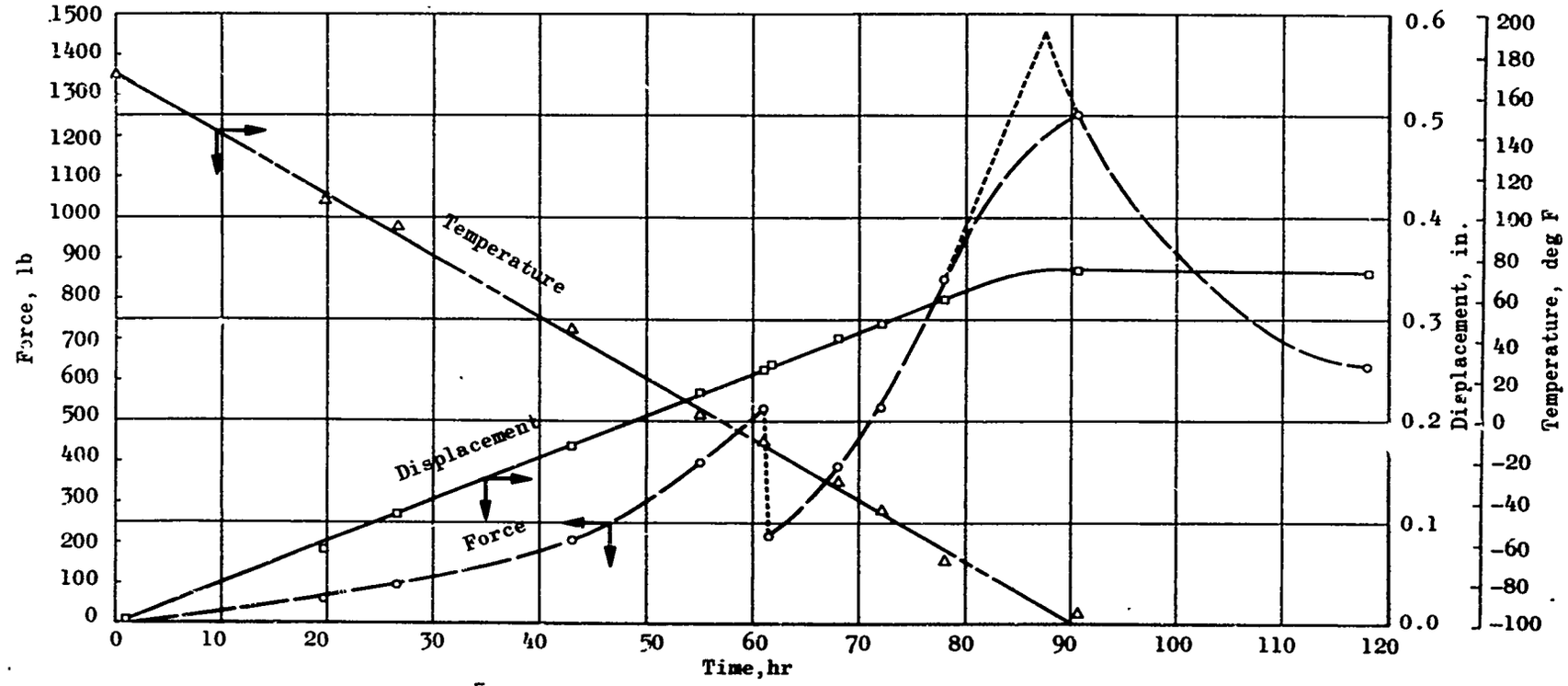

a. Strain Rate = 2.46×10^{-5} in./in./min; Cooling Rate = 3 F/hr; No Failure

Figure 47. Data Traces Taken During Simultaneous Straining and Cooling Tests of Biaxial Strip Specimens 13.5- x 3/8- x 2.8-inch Gage Length).

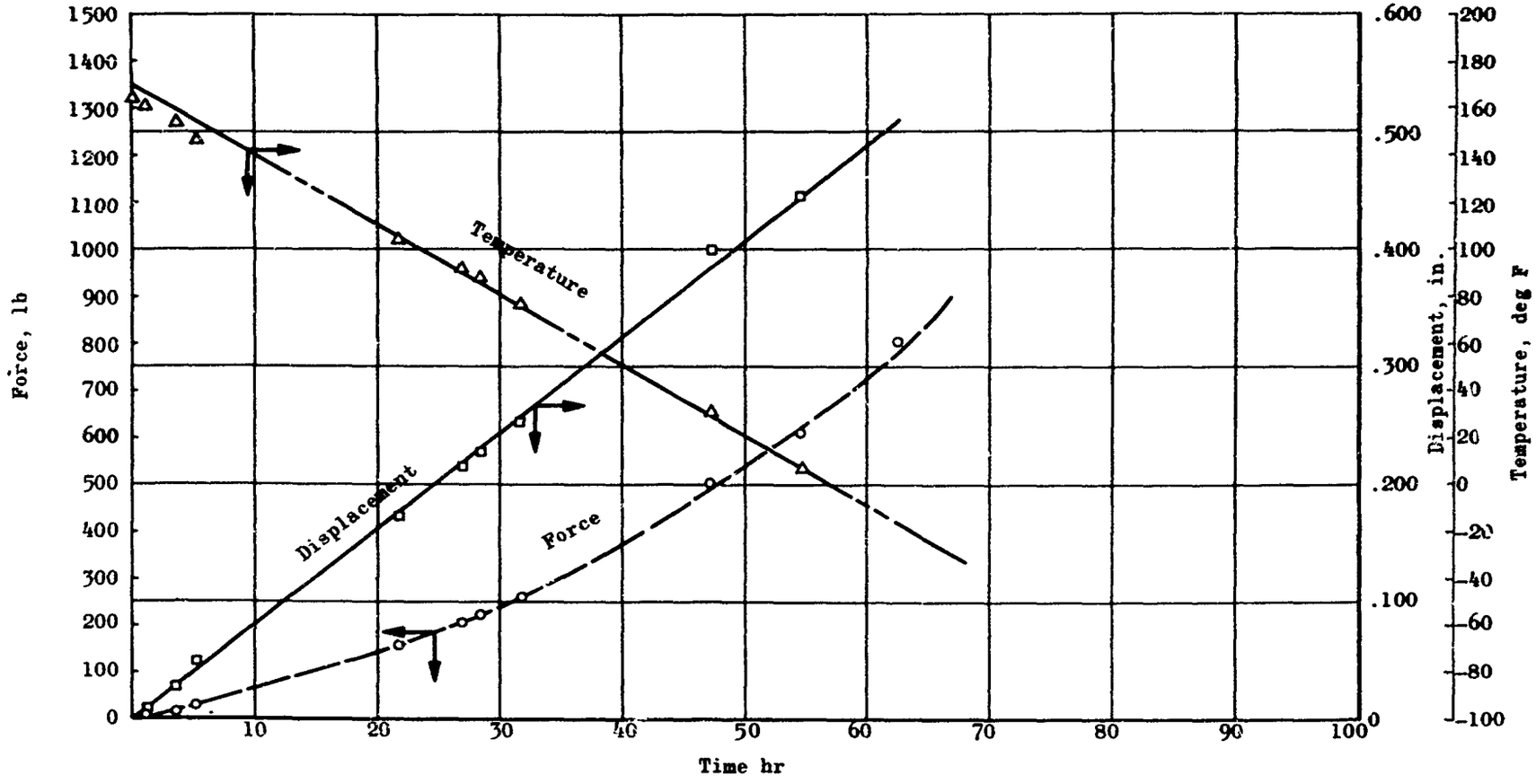

Strain Rate = 4.84×10^{-5} in.in./min; Cooling Rate = 3 F/hr; Crack Type Failure Observed after 68 hours.

Figure 47. Concluded

APPENDIX IV

MACHINE COMPLIANCE AND POKER CHIP TESTS

Page 150 is blank

APPENDIX IV

MACHINE COMPLIANCE AND POKER CHIP TESTS

To better understand conditions existing at the boundaries of a poker chip specimen during a pull on the Instron tester, it was necessary to determine the load-vs-deformation curve, or compliance, of the machine and the related poker chip apparatus as one unit. These tests were conducted with the same hardware (Instron tester and related poker chip attachment) as was used in the Cumulative Damage poker chip test program. The only difference was that instead of being bonded between two platens, propellant specimens were bolted together with three 0.5-inch bolts. Two different Instron load cells (5 and 10K) were used in the tests. All tests were conducted at 77 F at 0.2, 0.2, and 20.0 in./minute crosshead speed. Figure 48 shows related hardware in position on the Model TTD Instron, S/N 1572. Figure 48 also shows the position from which the crosshead deflection was measured.

Tables XIX through XXIV summarize data obtained at the three conditions of crosshead speed for the two load cells. Table XXV summarizes data from a test in which all the poker chip test apparatus was removed and a direct connection was made between the Instron 10K cell and the crosshead (via a 1.5-inch length of 1.25-inch steel bar stock). This last test was conducted to ascertain the maximum stiffness obtainable with the Instron machine alone.

Figures 49 through 51 are plots of the data given in Tables XIX through XXIV. In Fig. 49 and 50, the relationship between load and deformation appears to be independent of crosshead speed to the extent of reproducing the hysteresis loop.

The curve for the machine only, Fig. 51, is based on the 0.02-in./min rate data only. However, tests were also conducted at 0.2 in./min; but since all previous data indicated no effect from rate changes, these data were not reduced.

The load deformation curves differ considerably from those expected. It was expected that the stiffness of the machine alone would be above 1.0×10 lb/in. The value obtained is approximately 110,000 lb/in. over the 0- to 3000-pound range. This means that the poker chip specimen has a much higher stiffness than the machine (3×10^6 compared to 1×10^5 lb/in.). Therefore, one can postulate that a constant rate of displacement at the boundary is not being obtained.

Displacement time curves for the machine crosshead can be obtained by plotting data from Tables XIX through XXV. In general, these plots show a reasonably repeatable relationship except at 20.0 in./min crosshead speeds.

This effort was sponsored by Rocketdyne as a portion of a larger in-house program. It is reported herein because of the pertinence of the data in support of the triaxial poker chip experimental tests conducted during the course of the Cumulative Damage program.

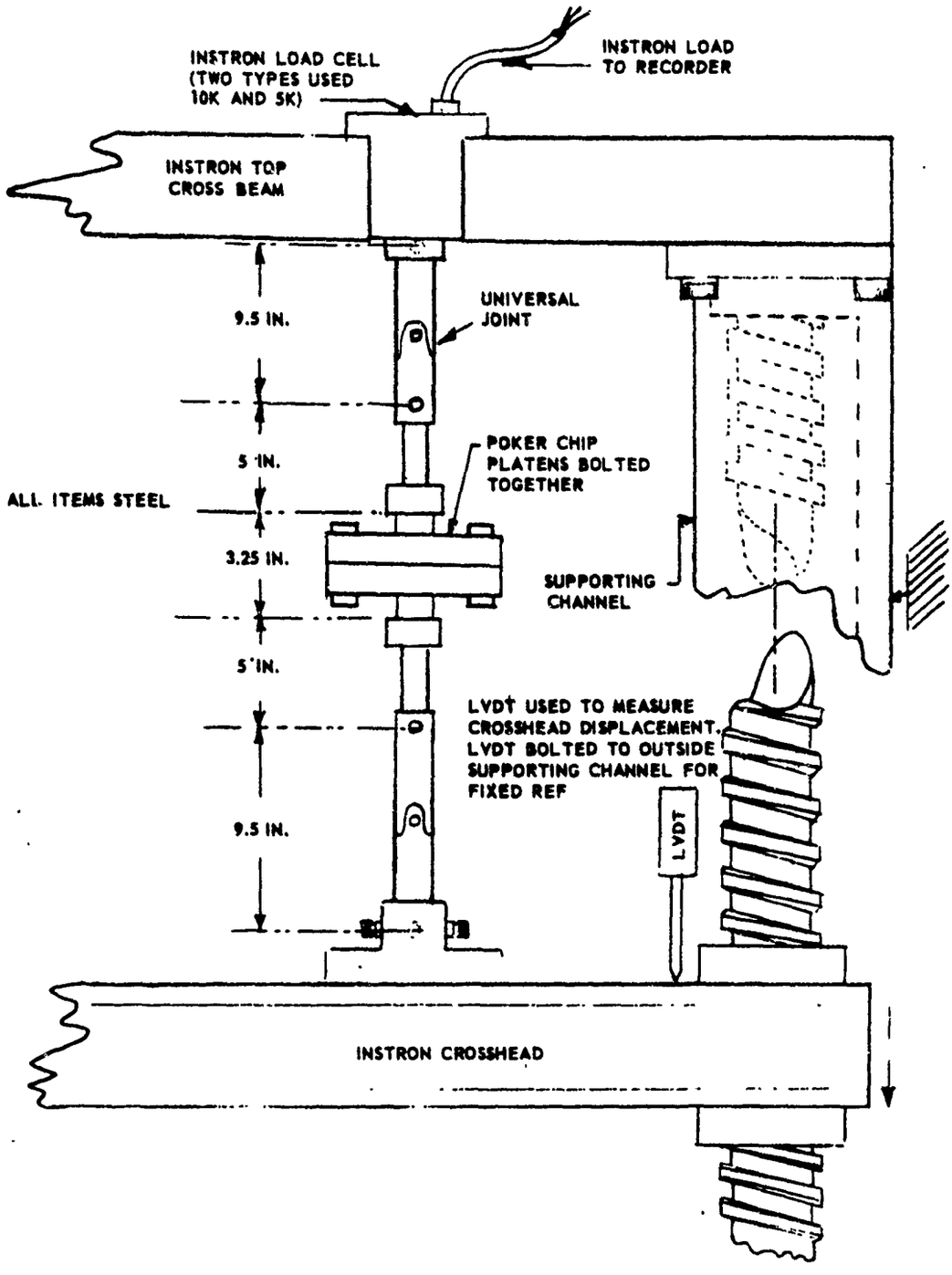

Figure 48. Arrangement of Poker Chip Apparatus on Instron Model TTD Tester in Determining Compliance for Hardware Alone

TABLE XIX. SUMMARY OF DATA FOR POKER CHIP COMPLIANCE TEST*

Time, sec	Instron Load, lb	Crosshead Deflection (LVDT), in.	
30	323	0.0085	Increasing Load
60	733	0.0173	
90	1260	0.0265	
120	1865	0.0360	
150	2530	0.0440	
180	3270	0.0524	
210	4020	0.0605	
240	4720	0.0685	Holding
270	4700	0.0685	
300	4690	0.0685	
330	4000	0.0625	
360	3122	0.0544	Return
390	2370	0.0460	
420	1685	0.0373	
450	1088	0.0286	
480	590	0.019	
510	212	0.0098	
540	0	0	

*Test Conditions: 5K load cell Instron TTD S/N 1572. Crosshead 0.02 in./min at 77 F with poker chip apparatus (see Fig. 48)

TABLE XX. SUMMARY OF DATA FOR POKER CHIP COMPLIANCE TEST*

Time, sec	Instron Load, lb	Crosshead Deflection (LVDT), in.	
3.2	402	0.010	Increasing Load
6.2	826	0.019	
9.2	1355	0.0282	
12.2	1990	0.0372	
15.2	2680	0.0455	
18.2	3390	0.0538	
21.2	4100	0.0610	
23.54	4690	0.0673	
27.2	4685	0.0673	Holding
30.2	4660	0.0673	
33.2	4650	0.0673	
36.2	4500	0.0665	Return
9.2	3550	0.0581	
42.2	2760	0.0500	
45.2	2030	0.0420	
48.2	1395	0.0333	
51.2	835	0.0235	
54.2	410	0.0150	
57.2	102.2	0.0060	
59.2	0	0	

*Test Conditions: 5K load cell Instron Model TTD S/N 1572. Crosshead speed 0.2 in./min at 77 F with poker chip apparatus (see Fig. 48)

TABLE XXI. SUMMARY OF DATA FOR POKER CHIP COMPLIANCE TEST*

Time, sec	Instron Load, lb	Crosshead Deflection (LVDT), in.	
0.02	71	0.004	Increasing Load
0.04	213	0.0075	
0.06	406	0.0122	
0.08	684	0.0184	
0.10	1070	0.0255	
0.12	1588	0.033	
0.14	2200	0.040	
0.16	2860	0.047	
0.18	3640	0.056	
0.20	4440	0.063	
0.02	4110	0.071	Return
0.04	3800	0.0672	
0.06	3390	0.0622	
0.08	2890	0.0575	
0.10	2350	0.0505	
0.12	1770	0.0428	
0.14	1205	0.0355	
0.16	695	0.0266	
0.18	290	0.0172	
0.20	0	0	

*Test Conditions: 5K load cell Instron Model TTD S/N 1572. Crosshead speed 20.0 in./min at 77 F with poker chip apparatus (see Fig. 43)

TABLE XXII. SUMMARY OF DATA FOR POKER CHIP COMPLIANCE TEST*

Time, sec	Instron Load, lb	Crosshead Deflection (LVDT), in.	
30	224	0.006	Increasing Load
60	620	0.0125	
90	1060	0.0185	
120	1600	0.0240	
150	2190	0.030	
180	2640	0.0355	
210	3400	0.0405	
240	4000	0.0460	
270	4620	0.0522	
300	5200	0.0575	
330	5820	0.0635	
360	6260	0.0695	
30	5420	0.0635	Return
60	4660	0.0575	
90	3980	0.052	
120	3320	0.045	
150	2700	0.040	
180	2110	0.035	
210	1560	0.029	
240	1080	0.0234	
270	607	0.0172	
300	264	0.0105	
330	26.4	0.005	
350	0	0	

*Test Conditions: 10K load cell Instron Model TTD S/N 1572. Crosshead speed 0.02 in./min at 77 F with poker chip apparatus (see Fig. 48)

TABLE XXIII. SUMMARY OF DATA FOR POKER CHIP COMPLIANCE TEST*

Time, sec	Instron Load, lb	Crosshead Deflection (LVDT), in.	
1.0	65	0.0048	Increasing Load
4.0	606	0.0145	
7.0	1440	0.0245	
10.0	2320	0.0335	
13.0	3190	0.0415	
16.0	4300	0.0505	
19.0	5330	0.060	
22.0	6250	0.069	
3.0	4830	0.0588	Return
6.0	3722	0.0485	
9.0	2700	0.0400	
12.0	1690	0.032	
15.0	1002	0.0228	
18.0	344	0.0128	
21.0	0	0.002	
22.0	0	0	

*Test Conditions: 10K load cell Instron Model TTD S/N 1572. Crosshead speed 0.2 in./min at 77 F with poker chip apparatus (see Fig. 48)

TABLE XXIV. SUMMARY OF DATA FOR POKER CHIP COMPLIANCE TEST*

Time, sec	Instron Load lb	Crosshead Deflection (LVDT), in.	
0.02	105	0.0024	Increasing Load
0.04	251	0.0062	
0.06	555	0.0110	
0.08	965	0.0174	
0.10	1505	0.0224	
0.12	2230	0.0290	
0.14	3020	0.037	
0.16	3900	0.0456	
0.18	4700	0.053	
0.20	5580	0.061	
0.22	6420	0.069	
0.24	6880	0.074	

*Test Conditions: 10K load cell Instron TTD S/N 1572. Crosshead speed 20.0 in./min at 77 F with poker chip apparatus (see Fig. 48)

TABLE XXV. SUMMARY OF DATA FOR INSTRON ALONE COMPLIANCE TEST*

Time, sec	Instron Load, lb	Crosshead Deflection (LVDT), in.
30	498	0.0088
60	1295	0.0172
90	2460	0.0260
120	3810	0.0350
150	5200	0.0420
180	6520	0.0500
210	8040	0.0582
216	8320	0.0600
0	8080	0.0605
30	5520	0.0522
60	3380	0.044
90	1780	0.035
120	615	0.0265
150	50	0.0175
180	0	0.00850

*Test Conditions: 10K load cell Instron TTD S/N 1572. Crosshead speed 0.02 in./min at 77 F. Direct coupling between 10K load cell and crosshead (1.5-inch length of 1.25-inch steel rod)

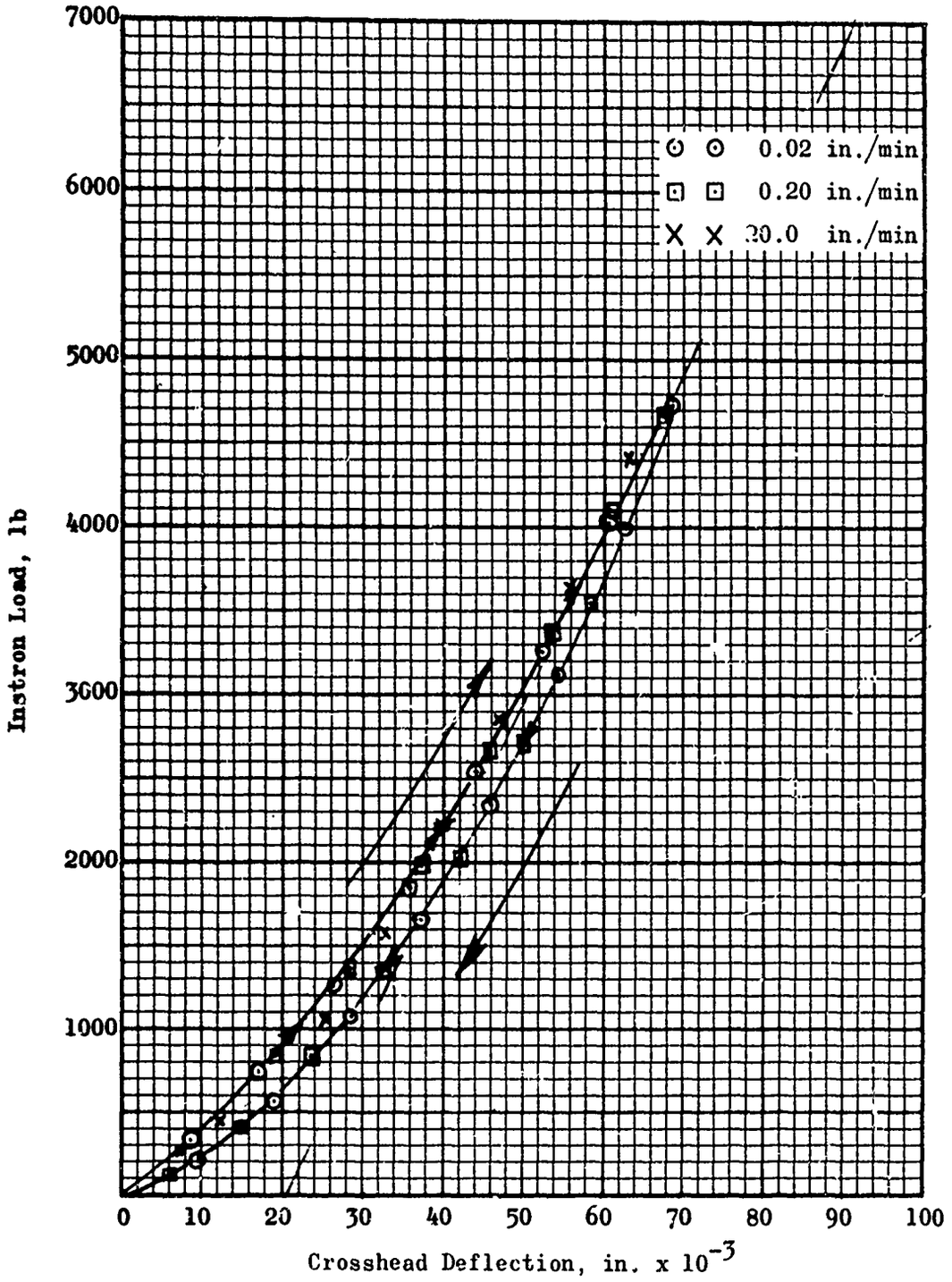

Figure 49. Compliance Curve (Load vs Deflection) for Poker Chip Apparatus with 5K Instron Load Cell

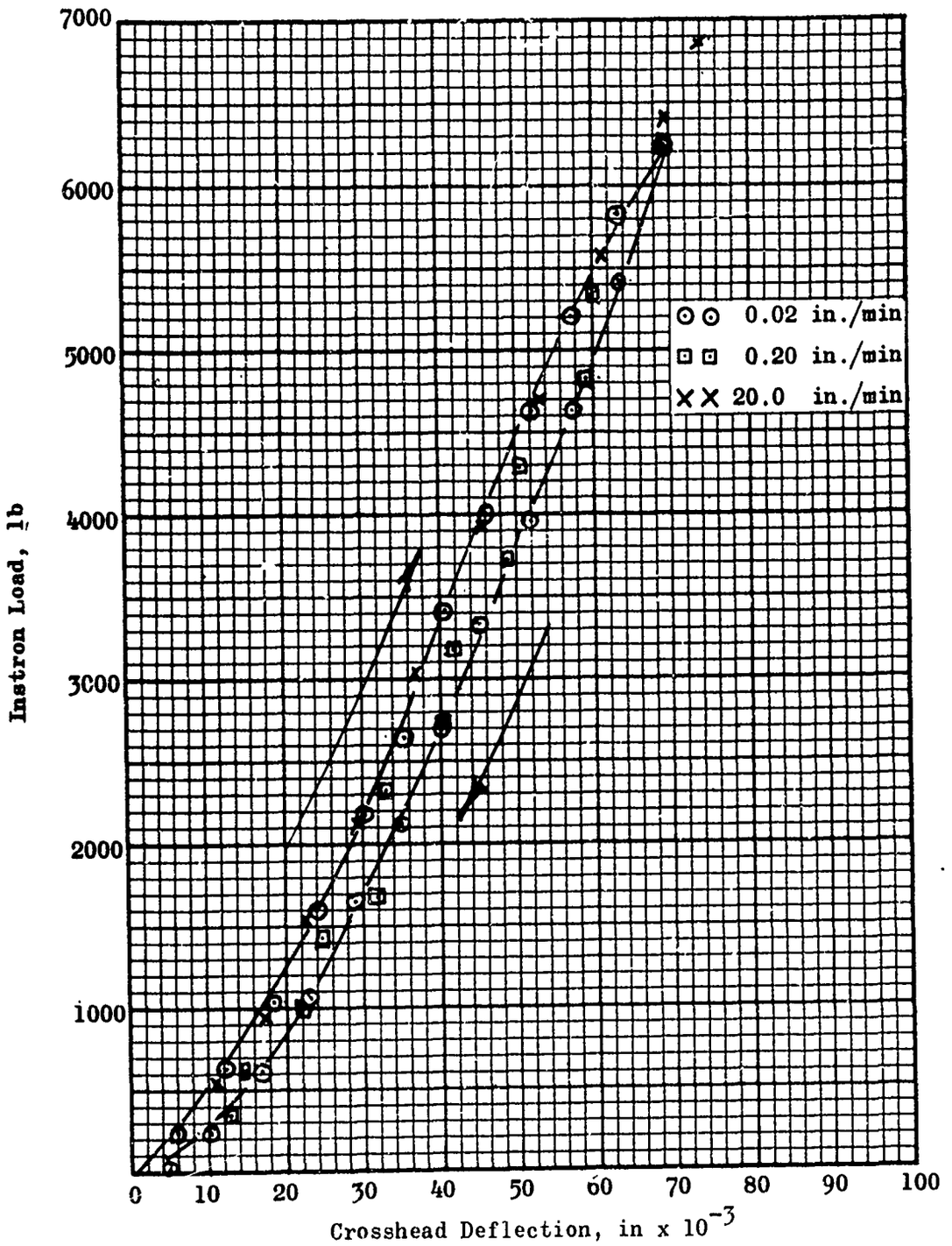

Figure 50. Compliance Curve (Load vs Deflection) for Poker Chip Apparatus with 10K Instron Load Cell

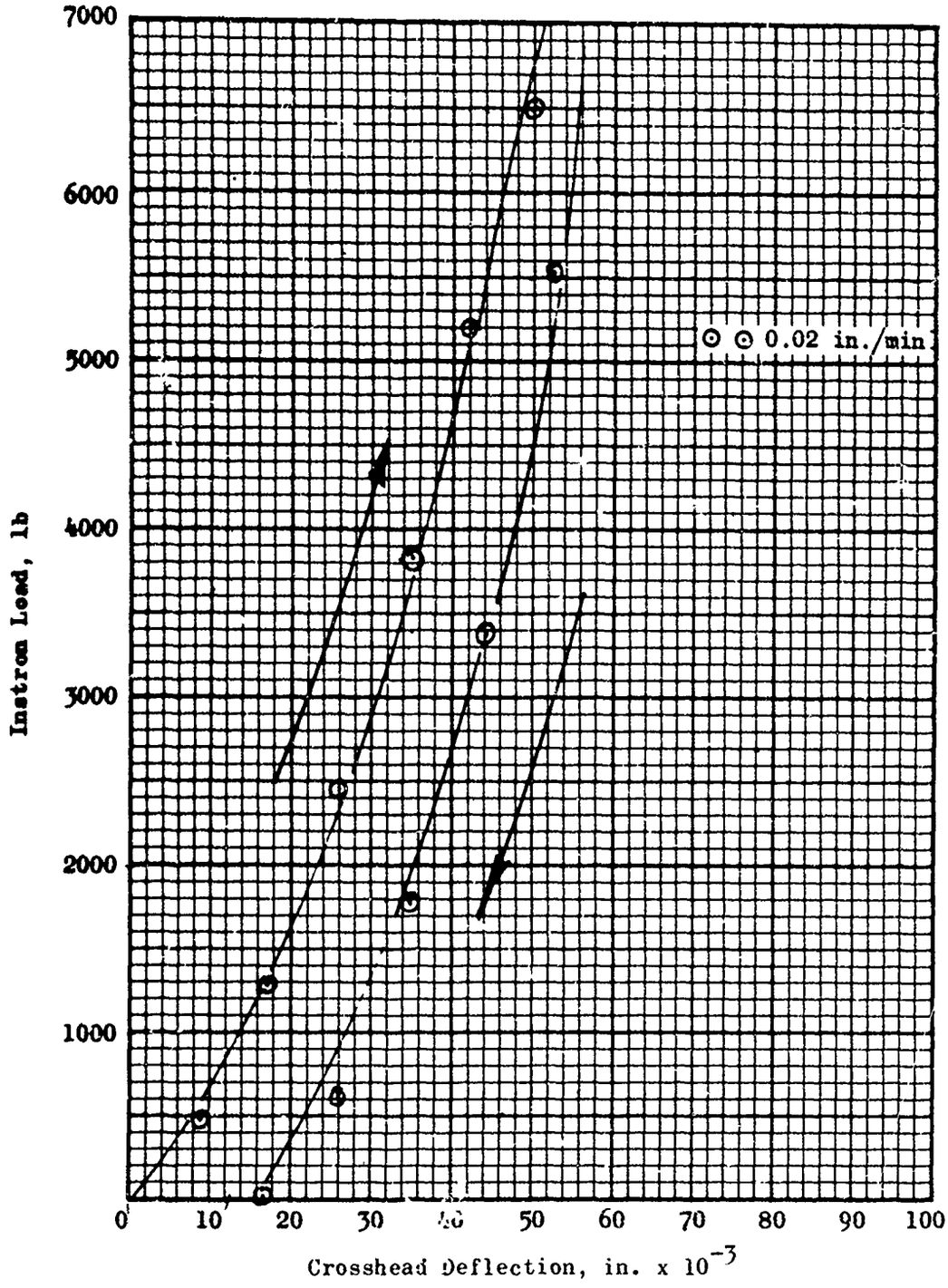

Figure 51. Compliance Curve (Load vs Deflection) for Instron Model TTD S/N 1572 with 10K Load Cell

APPENDIX V

MATERIAL PROPERTIES

Page 164 is blank

APPENDIX V

MATERIAL PROPERTIES

This appendix is included to familiarize the reader with the sequence of events and methods used to obtain the material property results presented in this report.

Uniaxial experimental relaxation data was furnished to Rocketdyne by Lockheed Propulsion Company (12); and limited biaxial relaxation data, also furnished by LPC, was shifted at Rocketdyne to determine a temperature-time equivalence relationship.

Using the experimental uniaxial and biaxial relaxation modulus curves, the creep compliance curves were computed from the relation (32)

$$D_{crp}(t)\, E_{rel}(t) = \frac{\sin n\pi}{n\pi} \tag{139}$$

where n is the logarithimic slope of the relaxation modulus curve.

Since, the theory of fracture mechanics, successive integrals of the creep compliance and relaxation modulus curves are necessary to compute γ, the characteristic energy release rate constant for different kinds of loading histories, a short discussion of the method used to obtain them will be in order.

When the creep compliance curve is obtained from Eq. 139, a Prony series is written for the curve which is typically of the form

$$D_{crp}(t) = D_e - \sum_i D_i e^{-t/\tau_i} \tag{140}$$

This gives an approximation to the curve which can be easily integrated term-by-term. The notation that will be used for the first time integral of the creep compliance is

$$D^{(1)}(t_o) = \int_o^{t_o} D_{crp}(t)\, dt \tag{141}$$

the second integral is

$$D^{(2)}(t_o) = \int_o^{t_o} \int_o^{\beta} D_{crp}(\alpha)\, d\alpha\, d\beta \tag{142}$$

and so on. Likewise, a Prony series for the relaxation modulus is of the form

$$E_{rel}(t) = E_e + \sum_i E_i e^{-t/\tau_i} \tag{143}$$

and the integral will be defined in the same way as before, i.e.,

$$\begin{aligned} E^{(1)}(t_o) &= \int_o^{t_o} E(\tau)\, d\tau \\ E^{(2)}(t_o) &= \int_o^{t_o}\int_o^{\beta} E(\alpha)\, d\alpha\, d\beta \end{aligned} \tag{144}$$

This same reasoning can be extended to the nth integrals defined as

$$D^{(n)}(t) = \int_o^t D^{(n-1)}(\alpha)\, d\alpha$$

and (145)

$$E^{(n)}(t) = \int_o^t E^{(n-1)}(\alpha)\, d\alpha$$

The results of some integrations of the Prony series are as follows

$$E^{(1)}(t_o) = E_e t_o - \sum_i \tau_i E_i \left[e^{-t_o/\tau_i} - 1\right] \tag{146}$$

$$E^{(2)}(t_o) = E_e \frac{t_o^2}{2} + \sum_i \tau_i^2 E_i \left[e^{-t_o/\tau_i} - 1\right] + t_o \sum_i \tau_i E_i \tag{147}$$

$$E^{(n)}(t_o) = E_e \frac{t_o^n}{n!} + (-1)^n \sum_i E_i \tau_i^n \left[e^{-t_o/\tau_i} - 1\right] + \sum_{m=1}^{n-1} \left\{ \sum_i \frac{t_o^m}{m!} (-1)^{n-m-1} (\tau_i)^{n-m} E_i \right\} \tag{148}$$

$$D^{(1)}(t_o) = D_e t_o + \sum_i D_i \tau_i \left[e^{-t_o/\tau_i} - 1\right] \tag{149}$$

$$D^{(2)}(t_o) = D_e \frac{t_o^2}{2} - \sum_i D_i \tau_i^2 \left[e^{-t_o/\tau_i} - 1\right] - t_o \sum_i D_i \tau_i \tag{150}$$

$$D^{(n)}(t_o) = D_e \frac{t_o^n}{n!} + (-1)^{n+1} \sum_i D_i \tau_i^n \left[e^{-t_o/\tau_i} - 1\right] + \sum_{m=1}^{n-1} \left\{ \sum_i \frac{t_o^m}{m!} (-1)^{n-m} \tau_i^{n-m} D_i \right\} \tag{151}$$

The power law for the relaxation modulus is

$$E_{rel}(t) = \frac{E_g - E_e}{(1 + t/\tau_o)^n} + E_e \qquad (152)$$

where

E_g = glassy modulus
E_e = rubbery modulus
τ_o = that time when $E_{rel}(t) = E_g/2^n$
n = the slope of the log curve

The power law constants for uniaxial and biaxial relaxation formulas follow in Table XXVI.

TABLE XXVI. RELAXATION FORMULA CONSTANTS

	E_g, psi	E_e, psi	n, num.	τ_o, sec
Uniaxial	200,000	100	-0.194	1.44×10^{-15}
Biaxial	470,000	170	-0.204	5.13×10^{-15}

The Prony series coefficients are given in Table XXVII for $E_{rel}(t)$ and $D_{crp}(t)$ for both uniaxial and biaxial curves.

The plots of $E^{(1)}$, $E^{(2)}$, $E^{(3)}$, $E^{(4)}$, $D^{(1)}$, $D^{(2)}$, $D^{(3)}$, and $D^{(4)}$ for both uniaxial and biaxial cases are included in Fig. 52 through 55. They have been normalized by multiplying each $E^{(n)}$ or $D^{(n)}$ by $\frac{n!}{t^n}$ so that they can be plotted on the same graph. In addition, the shift factor (a_T) for both uniaxial and biaxial data are included in Fig. 56 and 57, respectively.

Based on the biaxial relaxation modulus, the storage (E') and loss (E") moduli were derived and are plotted vs frequency in Fig. 58.

Other physical properties furnished by Lockheed pertinent to STV propellant include:

Glass Transition Temperature	-82 C (-116 F)
Coefficient of Thermal Expansion	$5.27 \pm 0.28 \times 10^{-5}$ in./in./deg F
Density	0.0633 ± 0.00184 lb/cu in.

TABLE XXVII. PRONY SERIES COEFFICIENTS

Uniaxial				Biaxial			
τ_i	E_i	τ_i	D_i	τ_i	E_i	τ_i	D_i
10^5	12	10^6	0.00054	10^6	20	10^7	0.00028
10^4	48	10^5	0.001085	10^5	12	10^6	0.0004
10^3	28	10^4	0.00162	10^4	65	10^5	0.0006
10^2	19	10^3	0.001355	10^3	40	10^4	0.0006
10^1	55	10^2	0.00162	10^2	110	10^3	0.0008
10^0	125	10^1	0.000946	10^1	110	$10^{2.2}$	0.0007
10^{-1}	185	10^0	0.000757	10^0	273	$10^{1.2}$	0.0006
10^{-2}	320	$10^{-0.8}$	0.000488	10^{-1}	400	$10^{0.2}$	0.0007
10^{-3}	470	$10^{-1.6}$	0.0005	10^{-2}	900	$10^{-0.8}$	0.0004
10^{-4}	790	$10^{-2.7}$	0.0004	10^{-3}	1,200	$10^{-1.7}$	0.00035
10^{-5}	1,100	$10^{-3.7}$	0.00023	10^{-4}	2,400	$10^{-2.7}$	0.00015
10^{-6}	1,700	$10^{-4.7}$	0.000159	10^{-5}	2,700	$10^{-3.7}$	0.00012
10^{-7}	3,000	$10^{-5.7}$	0.00012	10^{-6}	5,800	$10^{-4.7}$	0.00006
10^{-8}	4,400	$10^{-6.7}$	0.000065	10^{-7}	8,000	$10^{-5.7}$	0.000046
10^{-9}	6,700	$10^{-7.7}$	0.000036	10^{-8}	10,800	$10^{-6.2}$	0.000028
10^{-10}	10,400	$10^{-8.8}$	0.00003	10^{-9}	19,000	$10^{-7.7}$	0.000019
10^{-11}	17,300	$10^{-9.7}$	0.000015	10^{-10}	34,000	$10^{-8.7}$	0.000009
10^{-12}	27,000	$10^{-10.7}$	0.000011	10^{-11}	50,000	$10^{-9.7}$	0.000006
10^{-13}	40,000	$10^{-11.8}$	0.000009	10^{-12}	70,000	$10^{-10.7}$	0.0000046
10^{-14}	40,000	$10^{-12.7}$	0.000006	10^{-13}	110,000	$10^{-11.7}$	0.0000028
10^{-15}	23,000	$10^{-13.8}$	0.000001	10^{-14}	110,000	$10^{-12.7}$	0.0000015
10^{-16}	18,000	10^{-15}	0.0000012	10^{-15}	25,000	$10^{-13.9}$	0.0000006
10^{-17}	5,348	10^{-16}	0.0000006			$10^{-14.8}$	0.0000002
		10^{-17}	0.0000002			10^{-16}	0.0000001

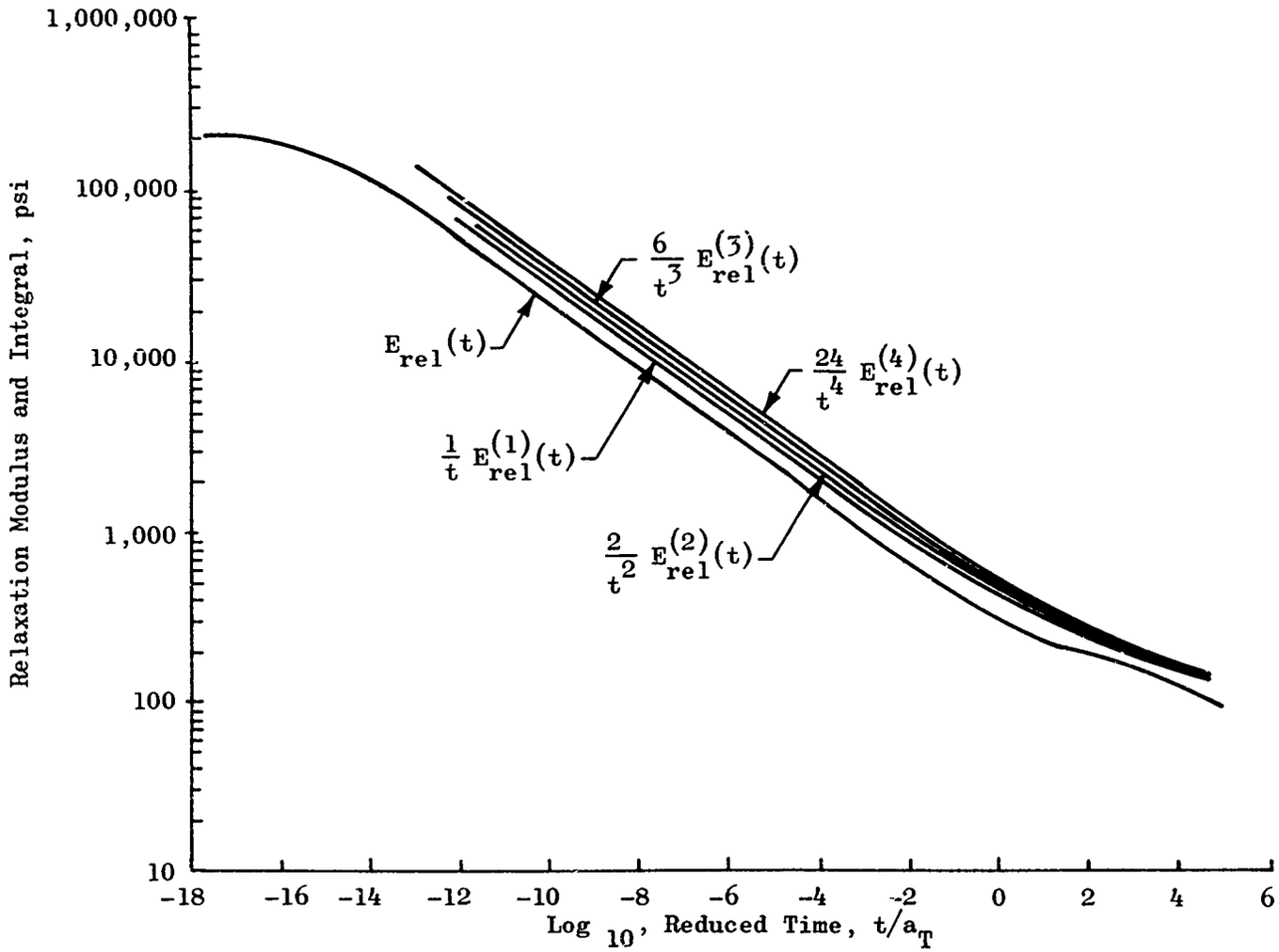

Figure 52. Uniaxial Stress Relaxation Modulus and the First Four Time Integrals vs Reduced Time (0064-61E STV Propellant, Tested November 1967)

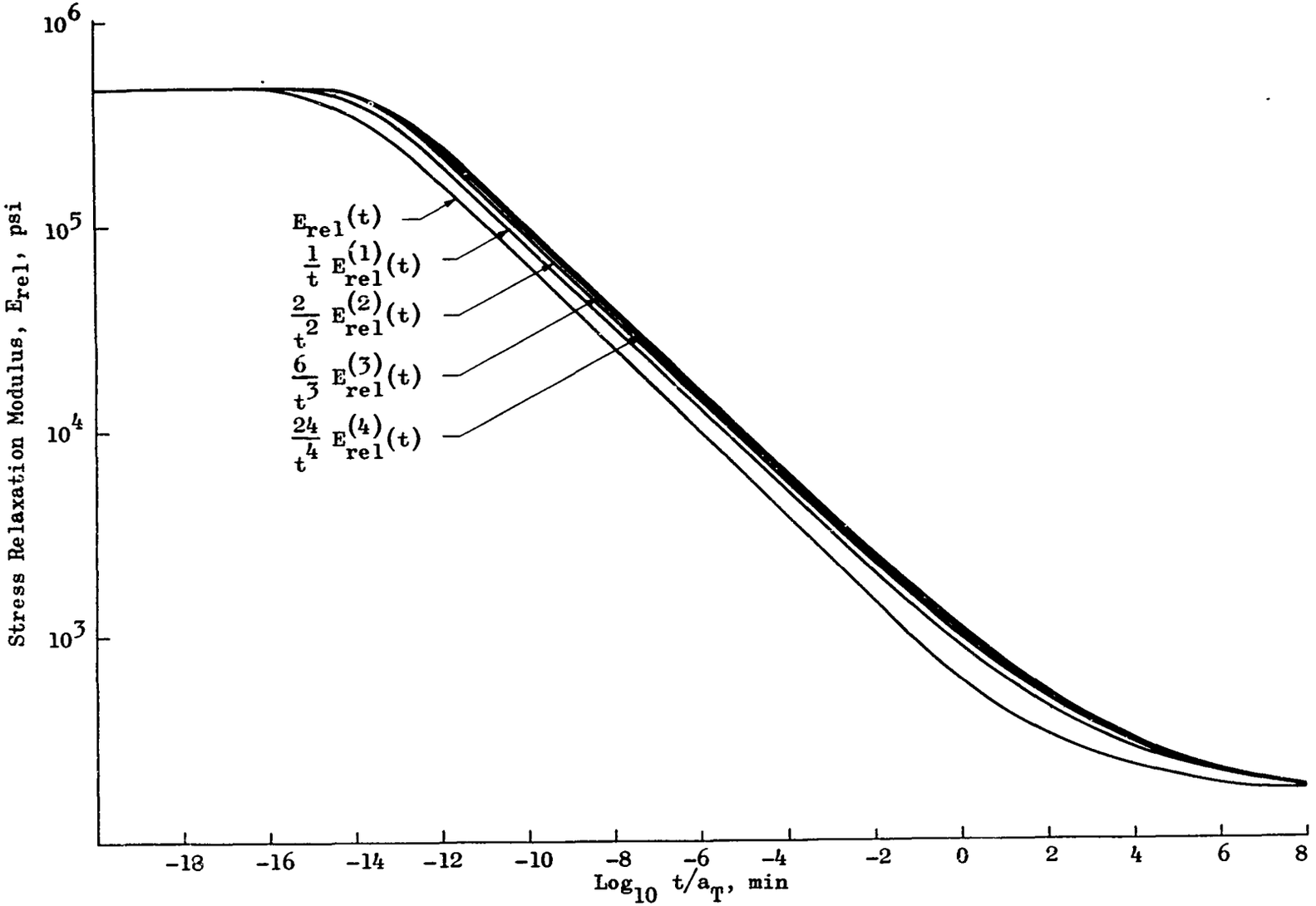

Figure 53. Biaxial Stress Relaxation Modulus and the First Four Time Integrals vs Reduced Time

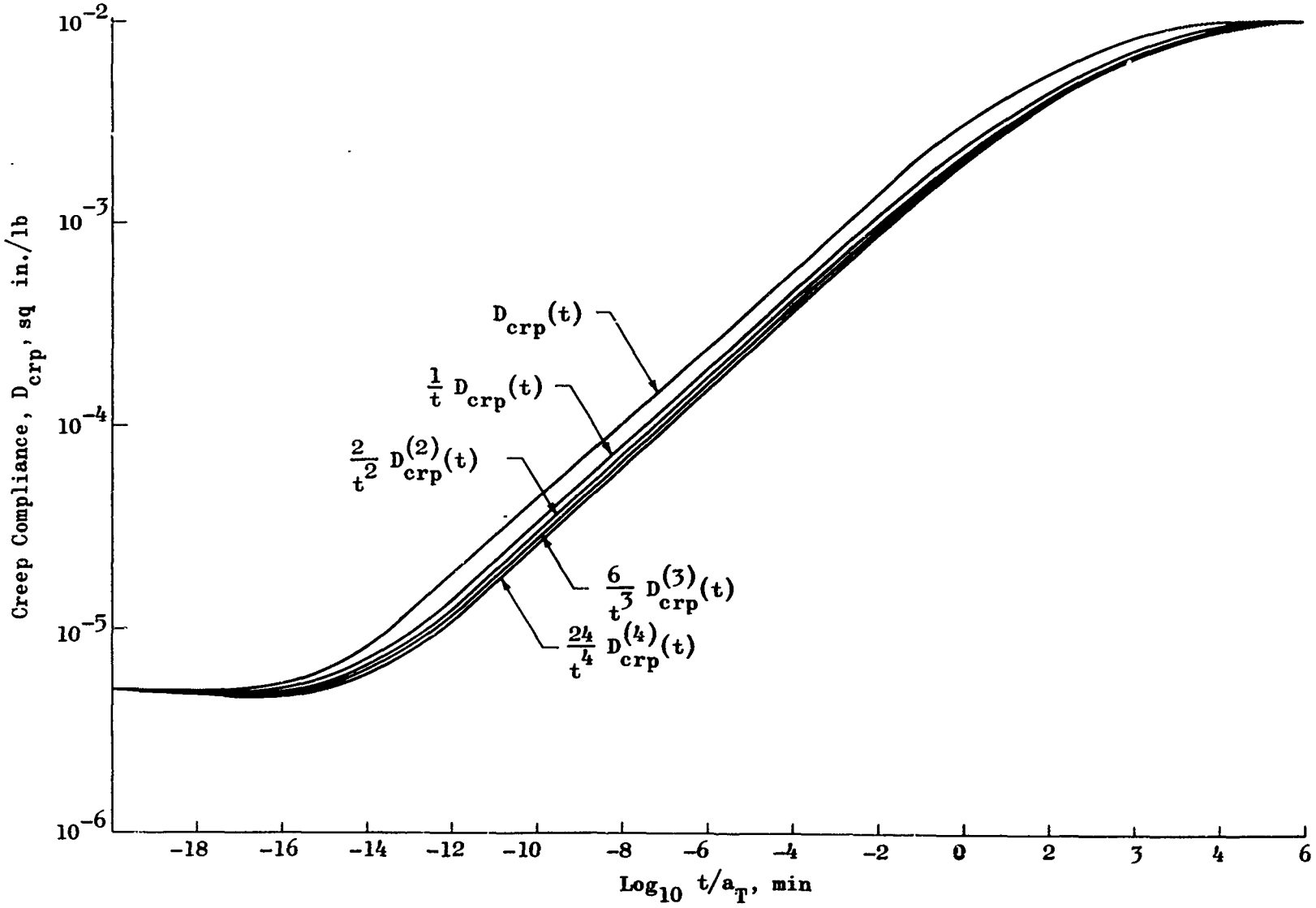

Figure 54. Uniaxial Creep Compliance and the First Four Time Integrals vs Reduced Time

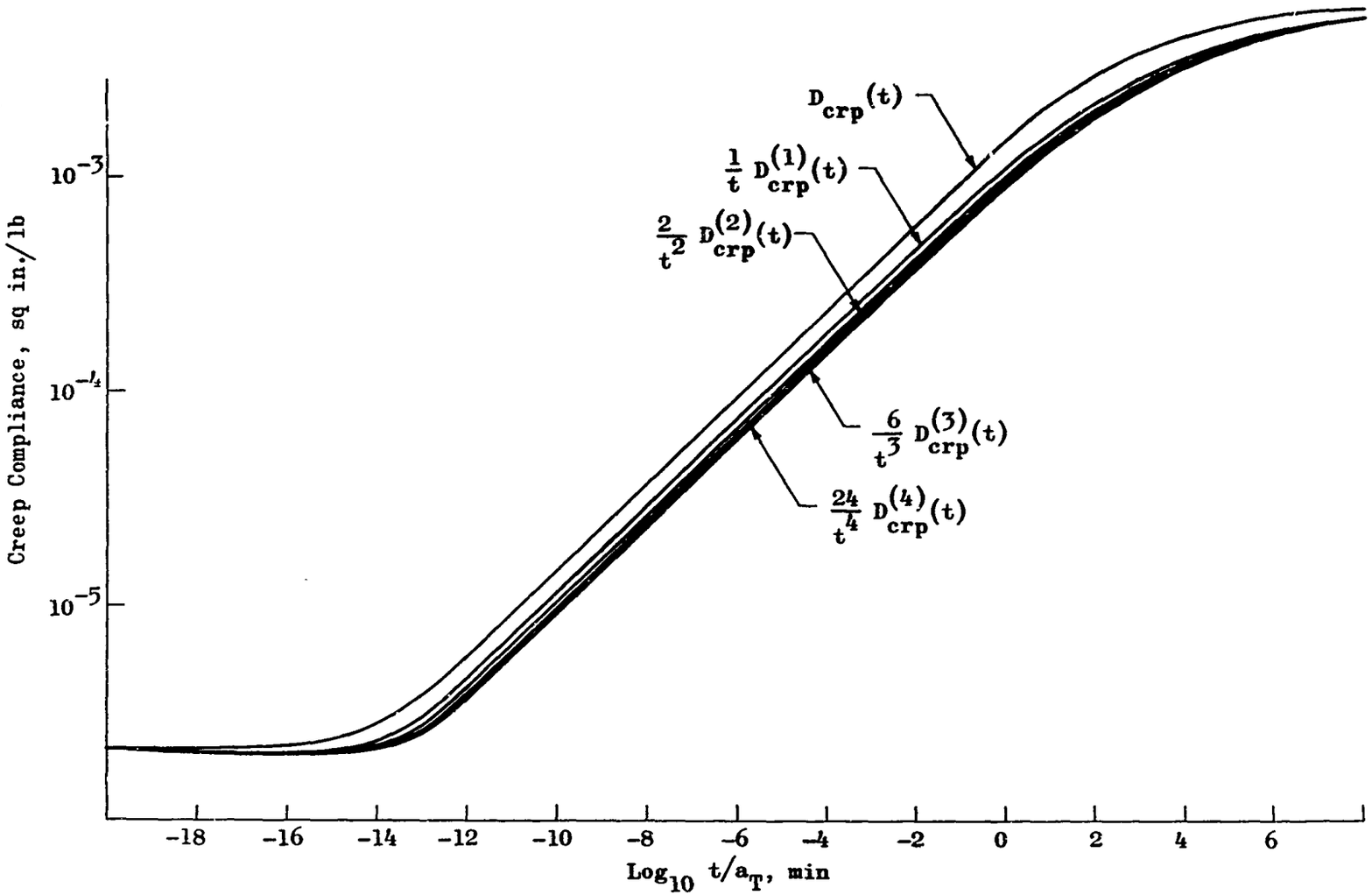

Figure 55. Biaxial Creep Compliance and the First Four Time Integrals vs Reduced Time

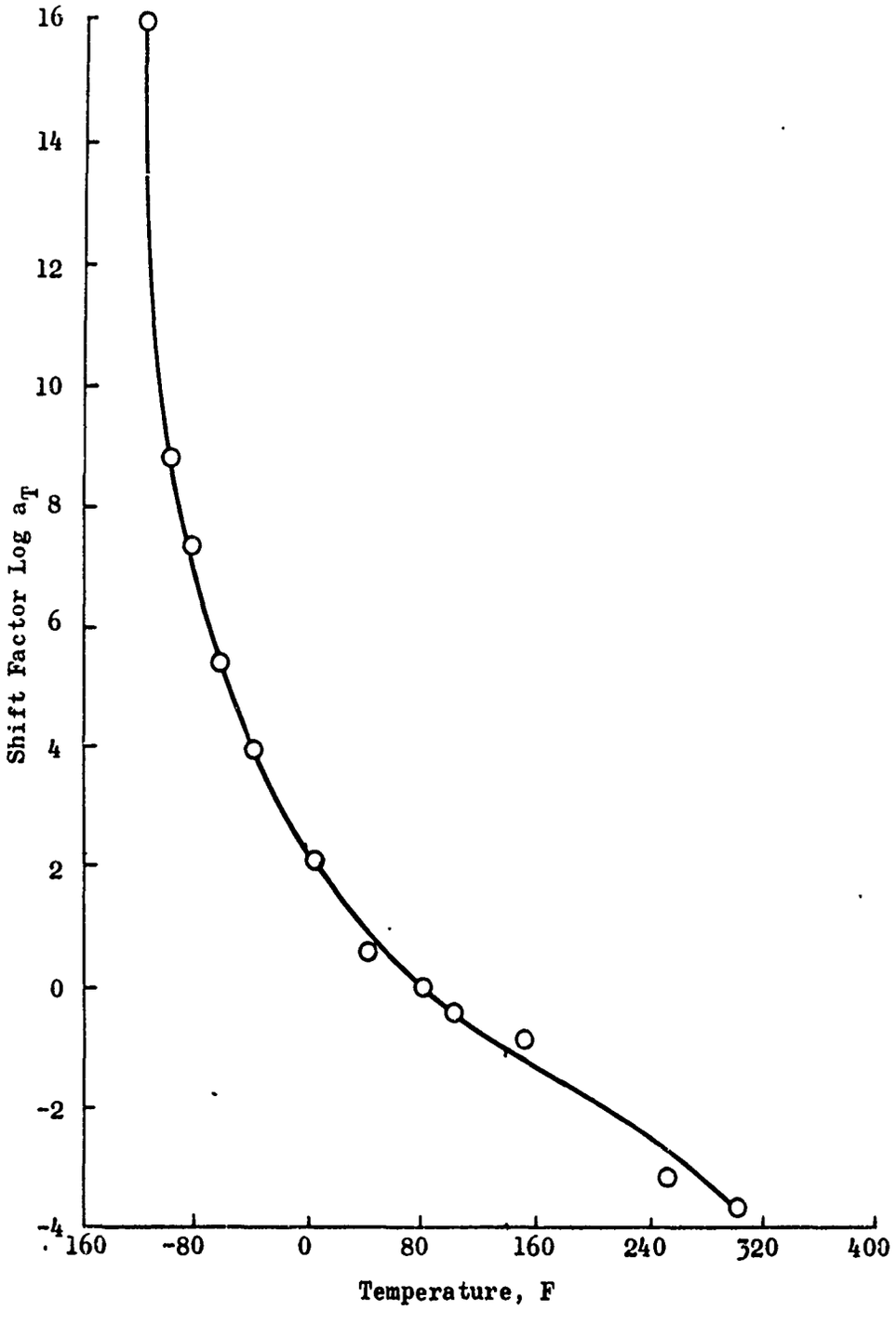

Figure 56. Uniaxial Shift Factors for Lockheed STV Propellant

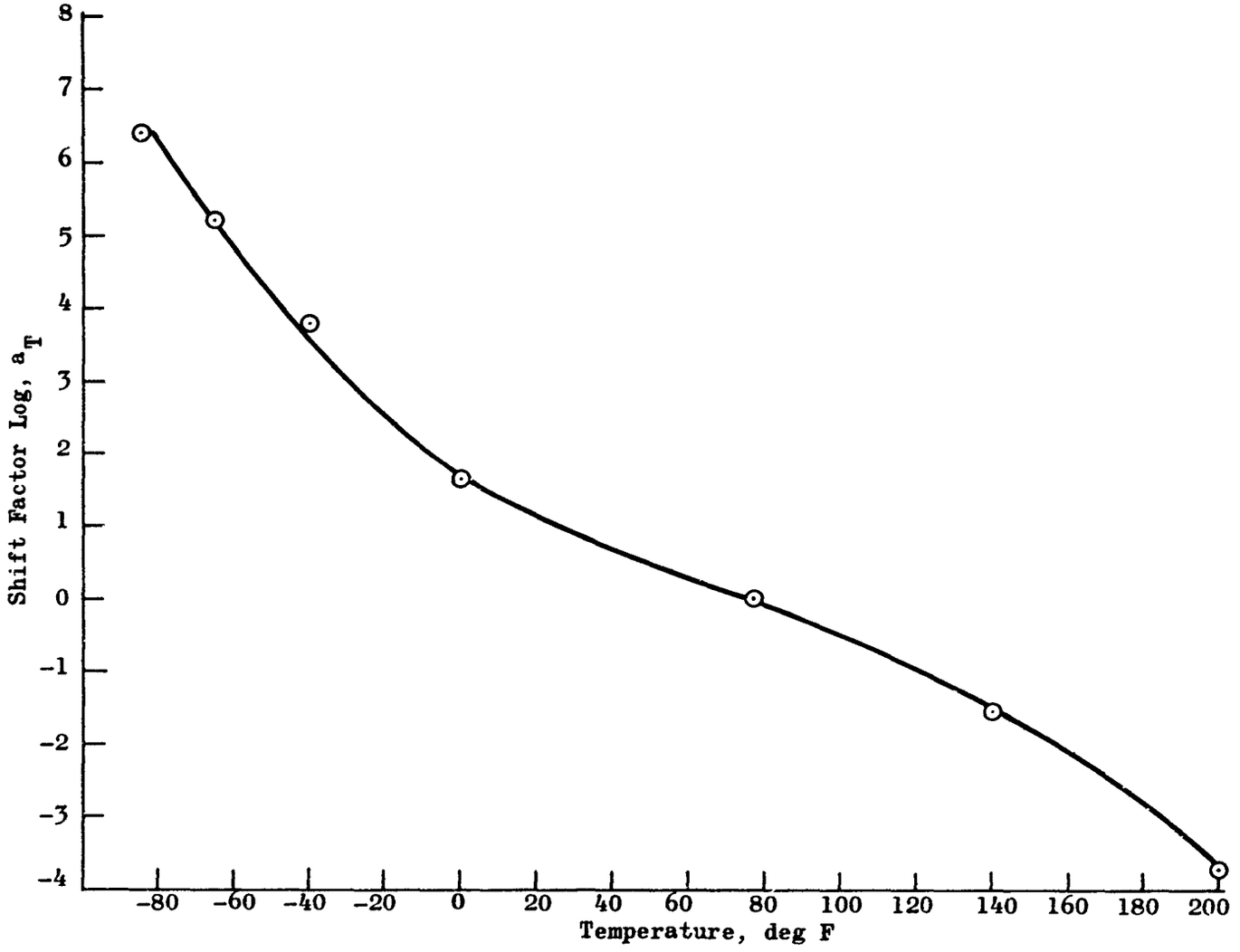

Figure 57. Biaxial Shift Factor, a_T for Lockheed STV Propellant

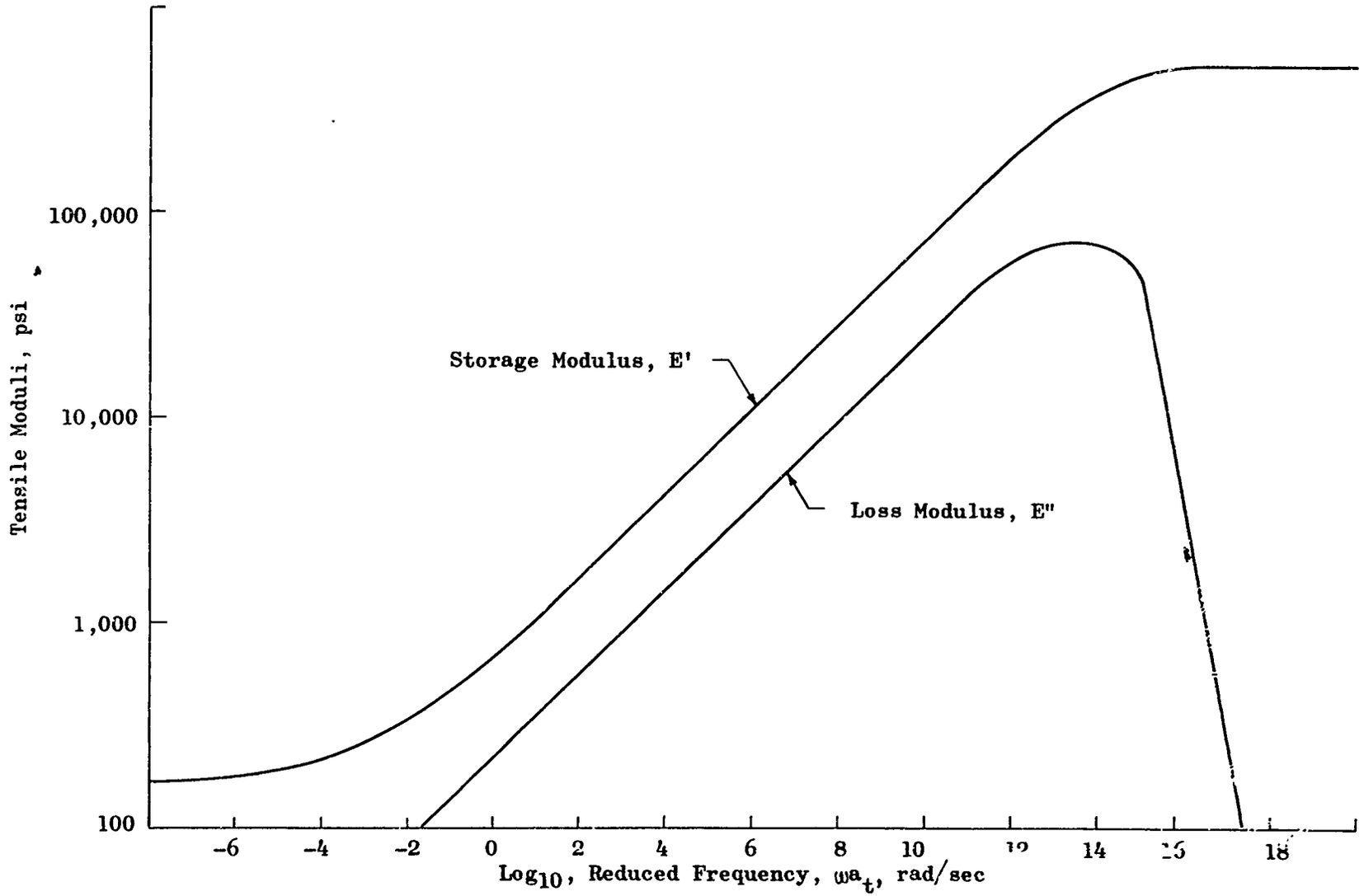

Figure 58. Dynamic Moduli (Propellant from Biaxial Tests)

Page 176 is blank

APPENDIX VI

CUMULATIVE DAMAGE TESTING

Page 178 is blank

APPENDIX VI

CUMULATIVE DAMAGE TESTING

The unique test apparatus furnished by Rocketdyne was designed and built by MTS Systems, Minneapolis, Minnesota, specifically to Rocketdyne specifications for use on the AFRPL Cumulative Damage program. This machine is considered unique because it provides for the first time the means of determining fatigue life for strip biaxial specimens of solid propellant. With the MTS tester, fracture data can be generated over a wide range of conditions including various combinations of displacements, frequency, and temperature.

The tester consists of three basic units: load frame, control console, and hydraulic power unit. Figure 59 shows the control console and the load frame with a biaxial test specimen mounted ready for testing.

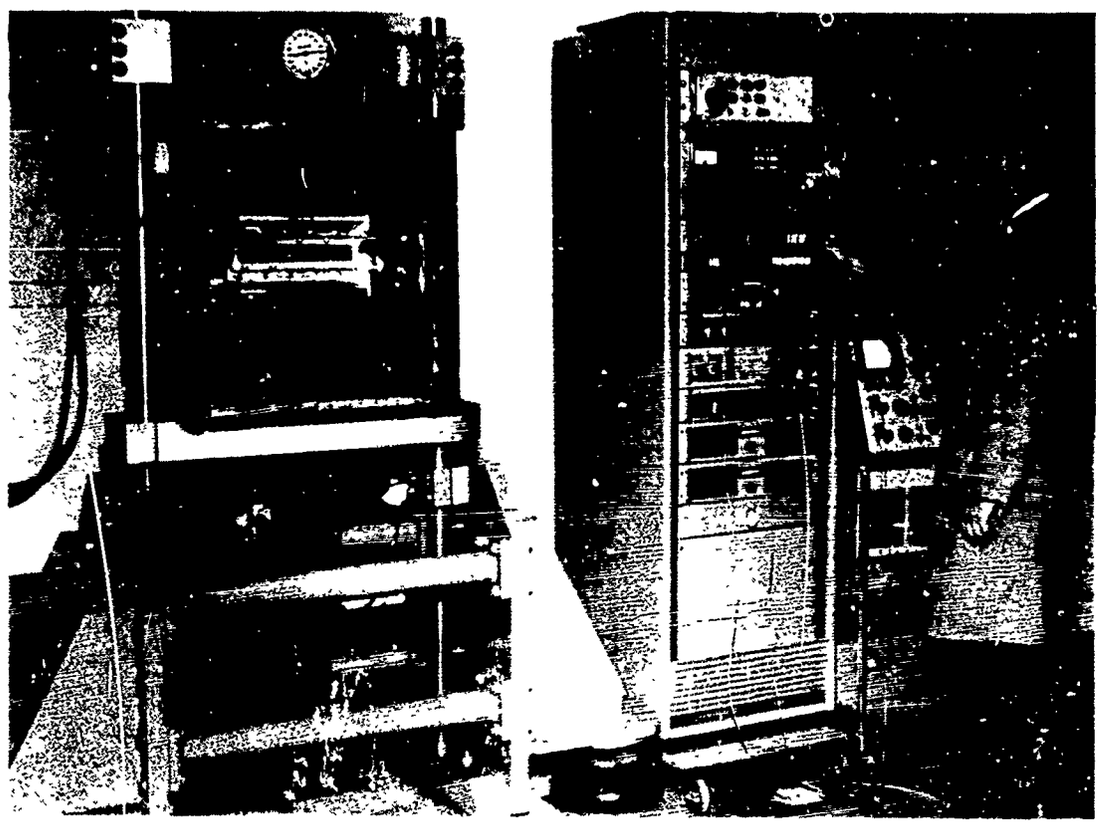

Figure 59. Cumulative Damage Tester

The large metal base supporting the load frame is not part of the original design. Originally, the load frame was to be bolted to a seismic mass of about 11,000 pounds (a cube of concrete extending below the laboratory floor lead). However, excessive frame movements were occurring at 50 cps and other certain critical frequencies. Excessive frame movements induced inertia loadings which generated false output from the force load cells. This made it impossible to interpret the force data at higher frequencies. The problem was eliminated by suspending the large supporting frame on the four air bellows. These bellows exert enough force upward to lift the load frame as well as the original seismic mass. Thus, the load frame and the cube of concrete are floating on air. This technique very effectively eliminated the high-frequency vibration problem.

Driving force for loading the specimen is derived from a double-acting, hydraulically operated actuator which receives pressurized hydraulic fluid through an electronically controlled servovalve that meters fluid to either end of the piston, Fig. 60. Servovalve position is controlled by an electronic circuit that puts out a command depending on the error detected between a desired voltage function and the output from one of three transducers, which is following a physical change in the test specimen. Through this "closed loop" arrangement it is possible to make the actuator or driver follow any desired movement within the mechanical and hydraulic limitations of the driver itself. Thus, it is possible to vary the displacement of the system independently of the load in the specimen and, conversely, to program a load time function independently of the displacement or strain in the specimen. These operations can be conducted to control specified displacement strain and load functions on the specimen while separate static transient or cyclic temperature environments are induced. The temperature control point can be either the specimen temperature or the ambient air temperature in the box.

Characteristics of the system are

Max tensile or compressive, 4500 lb
Max stroke, 2.0 in.
Max ram speed, 2600 in./min
Min ram speed, 4×10^{-5} in./min

Environmental Box
- Max temperature, 350 F
- Min temperature, -100 F
- Rate of change in temperature (wide range of rates possible using ramp generator as command)

Electronic Wave Form Inputs
- Sine
- Square
- Triangle
- Ramp (Linear, bilinear)

Maximum Ram Stroke at Sine Frequency
- 0.010, 150 Hz
- 0.250, 50 Hz
- 2.0, 1 Hz

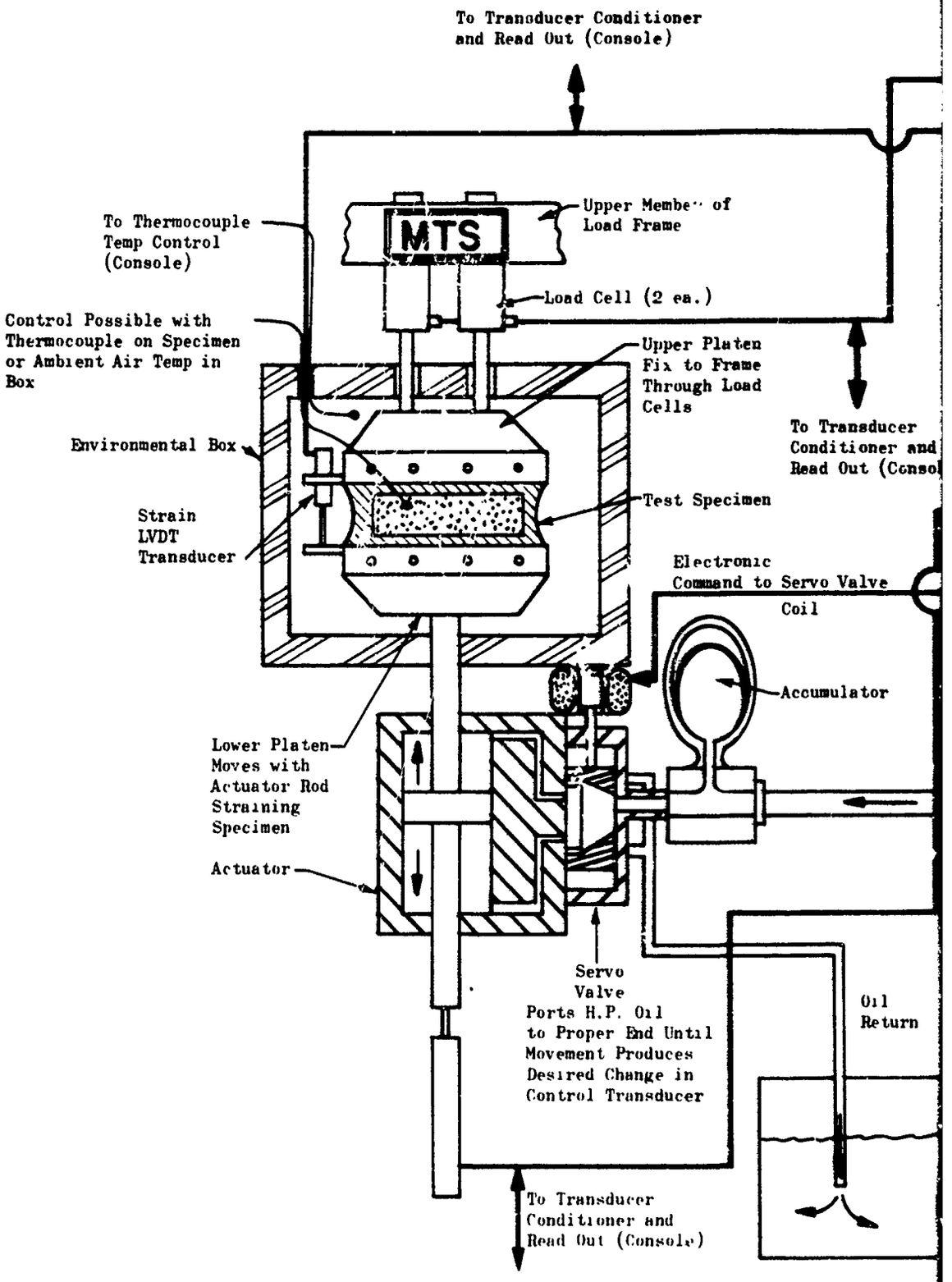
To Tranoducer Conditioner
and Read Out (Console)
To Thermocouple
Temp Control
(Console)
MTS
Upper Membe·· of
Load Frame
Load Cell (2 ea.)
Control Possible with
Thermocouple on Specimen
or Ambient Air Temp in
Box
Upper Platen
Fix to Frame
Through Load
Cells
To Transducer
Conditioner and
Read Out (Consol
Environmental Box
Test Specimen
Strain
LVDT
Transducer
Electronic
Command to Servo Valve
Coil
Accumulator
Lower Platen
Moves with
Actuator Rod
Straining
Specimen
Actuator
Servo
Valve
Ports H.P. Oil
to Proper End Until
Movement Produces
Desired Change in
Control Transducer
Oil
Return
To Transducer
Conditioner and
Read Out (Console)

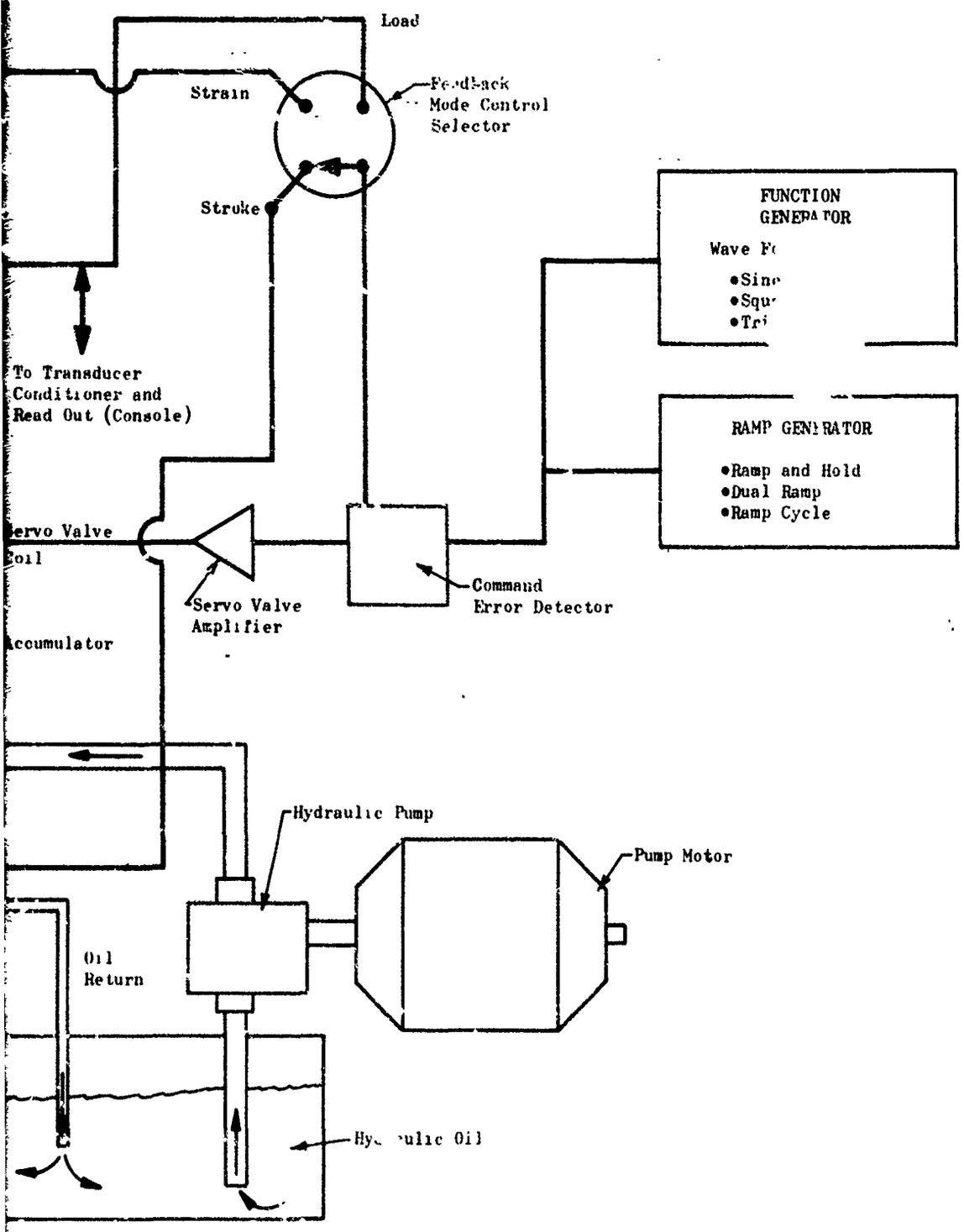

Figure 60. Sketch Showing Operating Principle of "Closed Loop" MTS Test Equipment

Page 182 is blank

APPENDIX VII

SINUSOIDAL FORCE LOADING OF BIAXIAL STRIP SPECIMENS

Page 184 is blank.

APPENDIX VII

SINUSOIDAL FORCE LOADING OF

BIAXIAL STRIP SPECIMENS

This appendix presents experimental failure data obtained from biaxial strip specimen tests. The boundaries of the specimens were subjected to a varying tensile displacement chosen to force the total load to vary sinusoidally with time.

The 13.25- x 0.375- x 2.80-inch specimen was placed between two aluminum platens and bonded to each surface. The force through the machine linkage was monitored by two transducers which supplied a signal to a command unit; this signal was then compared to an incoming signal from a sinusoidal function generator. The voltage resulting from the difference in these two signals was amplified and operated an electromechanical servo-valve which controlled oil flowing from a reservoir to either side of a piston which was moved by the oil pressure.

The harmonically varying force boundary was applied at frequencies of 5, 15, and 45 hertz. At each frequency level, peak-to-peak loads of 230, 200, and 180 pounds were input. The load form was displayed on an oscilloscope and the number of cycles was recorded electronically. The specimen was observed and when a crack appeared, the cycle number and time was recorded.

The data and a typical sinusoidal wave form are presented in Fig. 61 and 62. The theoretical waveform would be

$$F(t) = F_o + F_o \sin \omega t \tag{153}$$

which would look like the following:

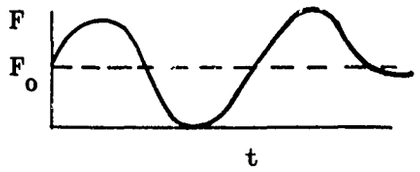

What was actually imposed was

$$F(t) = F_1 + F_2 \sin \omega t \tag{154}$$

giving a curve such as:

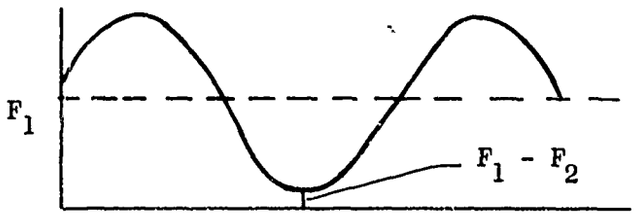

So the machine control proved to be incapable of imposing a step load with a superposed sinusoidal load of exactly the same amplitude. However, observed variations, $F_1 - F_2$, were always less than 5% of the peak force.

Figure 61 shows the number of cycles to failure following various stress levels. Stresses were calculated by dividing peak forces, $F_1 + F_2$, by the nominal specimen cross-sectional area.

Figure 62 shows a typical force-vs-time history from one of these tests. The curve varies slightly from the desired sinusoidal shape.

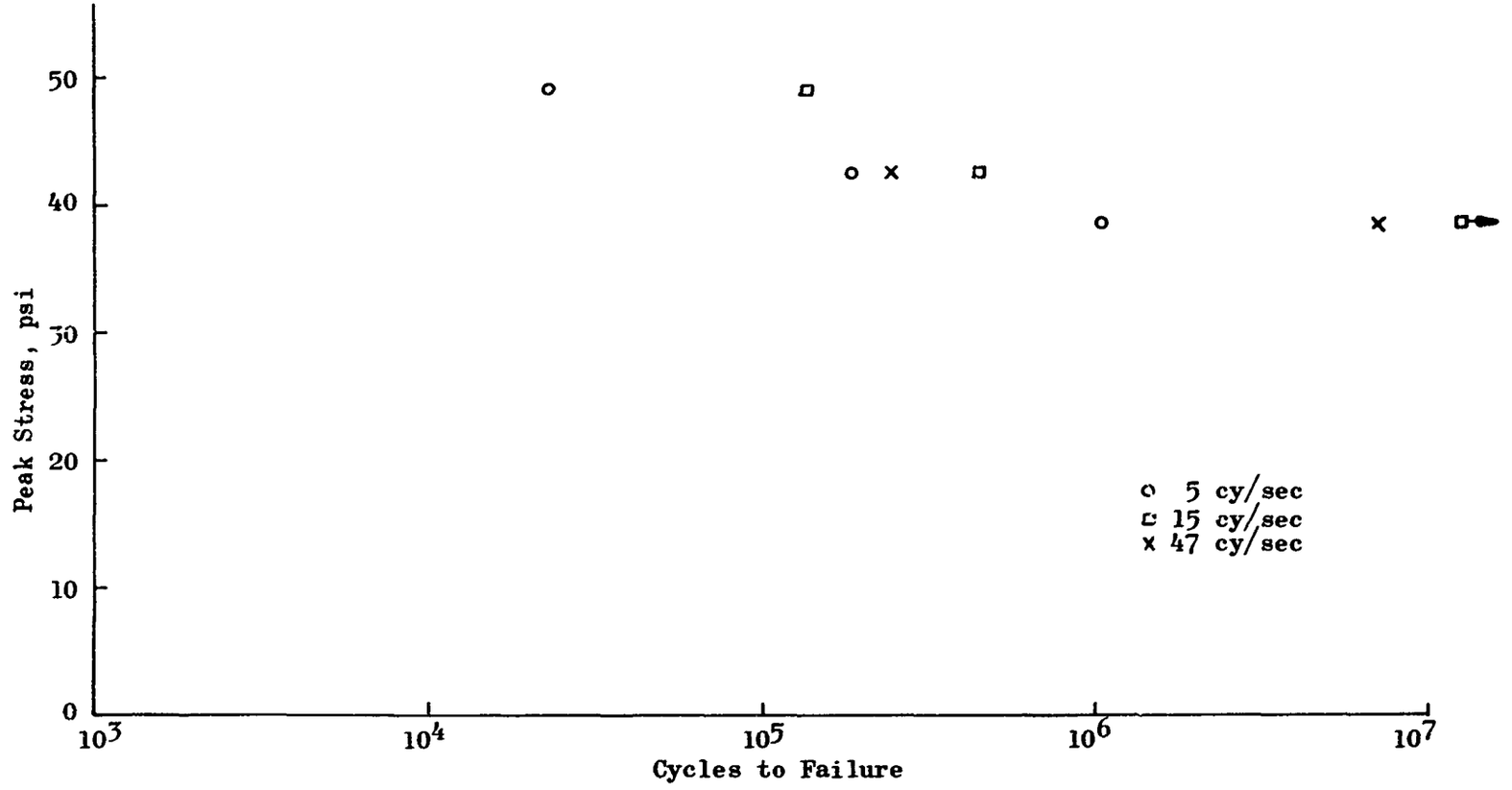

Figure 61. Experimental Failure Data from Biaxial Strip Specimen Test (Force Boundary Prescribed)

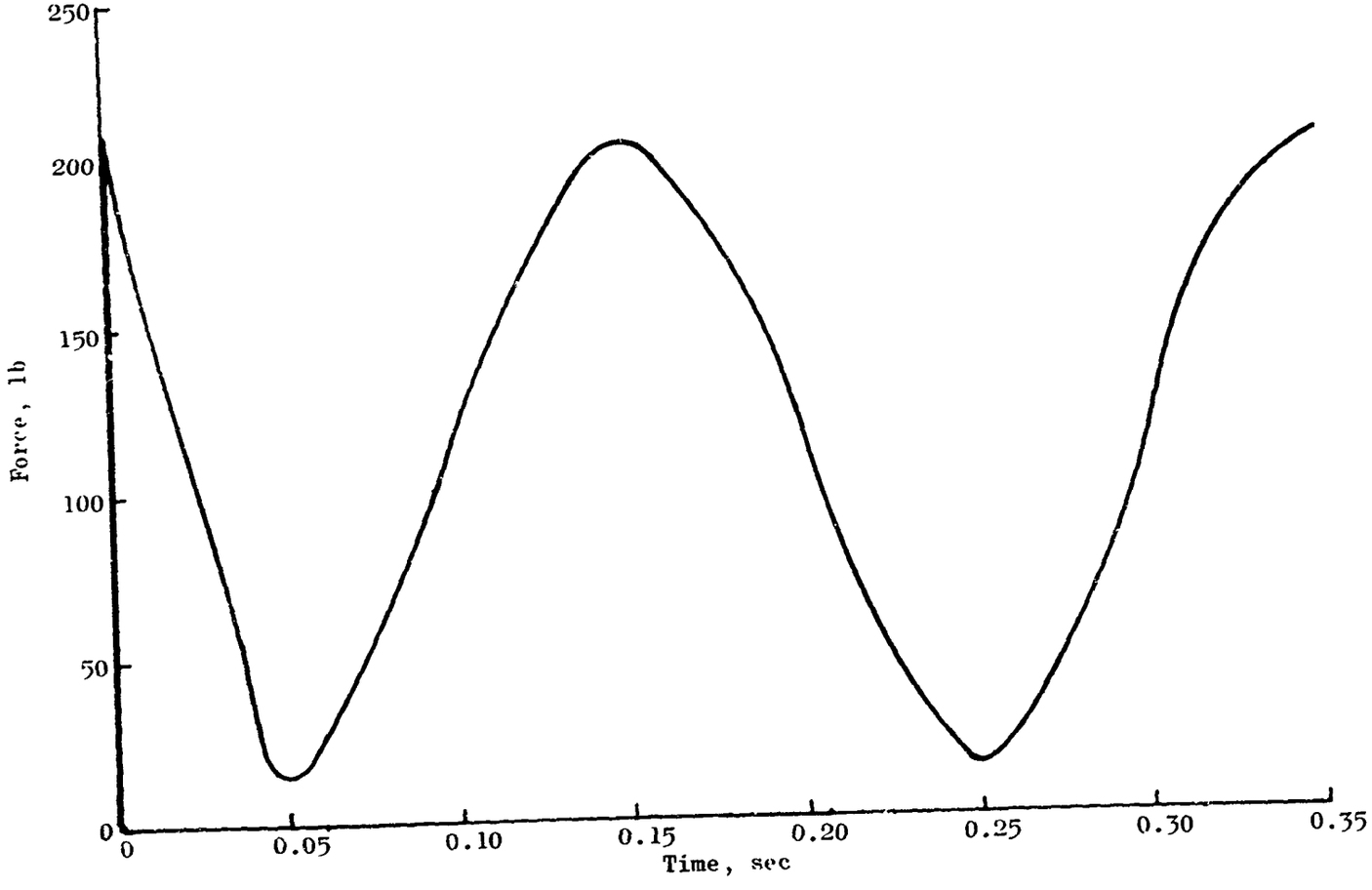

Figure 62. Typical Sinusoidal Waveform

APPENDIX VIII

MEASUREMENT OF CRACK GROWTH DURING BIAXIAL FATIGUE TESTS

Page 190 is blank

APPENDIX VIII

MEASUREMENT OF CRACK GROWTH

Although recording the rate of crack growth across the specimen following initial failure was not a contractual requirement of the Cumulative Damage program, it soon became evident that unless this rate of crack growth was recorded much valuable data would be lost. To accomplish this, it was necessary to photograph the specimen at some precise time interval at the point where the specimen had reached its maximum extension during the cycle. An existing Hulcher 70 mm sequence camera was modified to expose a single frame upon command. Exposure was accomplished by first opening an auxillary shutter then discharging an electronic flash unit (having a 15-microsecond duration) whose trigger circuit was energized by the voltage output from the appropriate MTS transducer (stroke or force) at the right point on the wave form. To accomplish these functions, it was necessary to design and build a special sequence timer and triggering circuit. This activity was performed by Engineering Test personnel and supported totally by Rocketdyne.

It was not possible to obtain a photographic record for each fatigue test because testing had to progress simultaneously with the building and development of the sequence timer and triggering unit. However, 19 tests were photographed, and the data were reduced (see Fig. 63). The camera was normally used to monitor the specimen for crack initiation--it was set to take photographs at relatively infrequent intervals. The time between photographs was greatly reduced after a crack initiated. Crack initiation varied from specimen to specimen. When the crack started on the back side of the specimen (away from the viewing window) it progressed through the specimen and appeared abruptly on the fron side with an appreciable initial length (~0.5 inch). Such crack growth was measured during the rapid-growth phase as depicted in Fig. 64d through 64h. When the crack initiated on the front (viewing) side of the specimen, it was noted that the time required for the initial surface crack to work through the thickness of the specimen was quite significant (Fig. 64a through 64d). Front-surface propagations always progress in the manner depicted in Fig. 64a through 65g. All specimens tested were milled specimens and, therefore, dod not have a binder-rich layer as would be the case in full-scale motors. Mechanical damage incurred from the milling process produces many sites where large perchlorate crystals have been crushed, and these apparently influence the failure initiation.

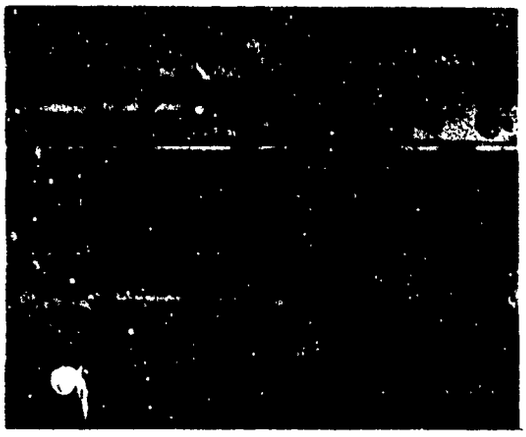

a. 63,900 Cycles

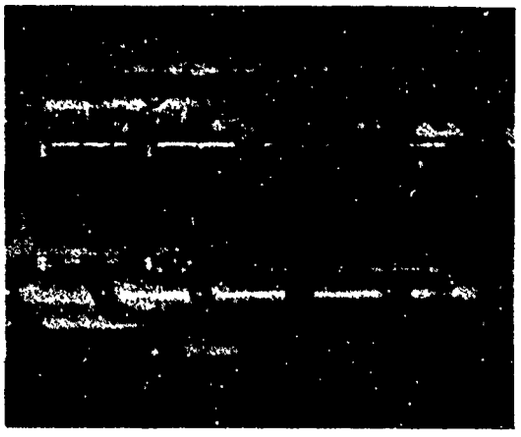

b. 74,200 Cycles

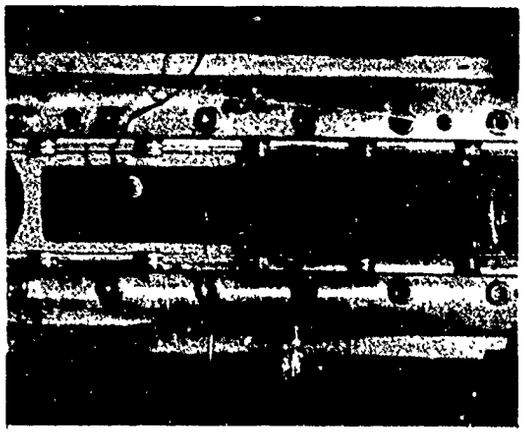

c. 85,700 Cycles

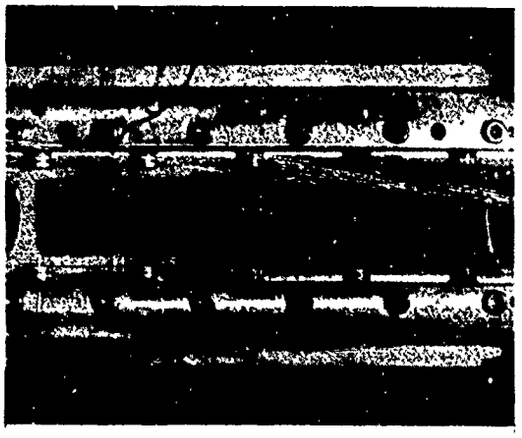

d. 87,200 Cycles

Figure 63. Sequential Photographs Showing a Growing Cracks(s) in a Biaxial Strip Specimen During Displacement Vibration Test

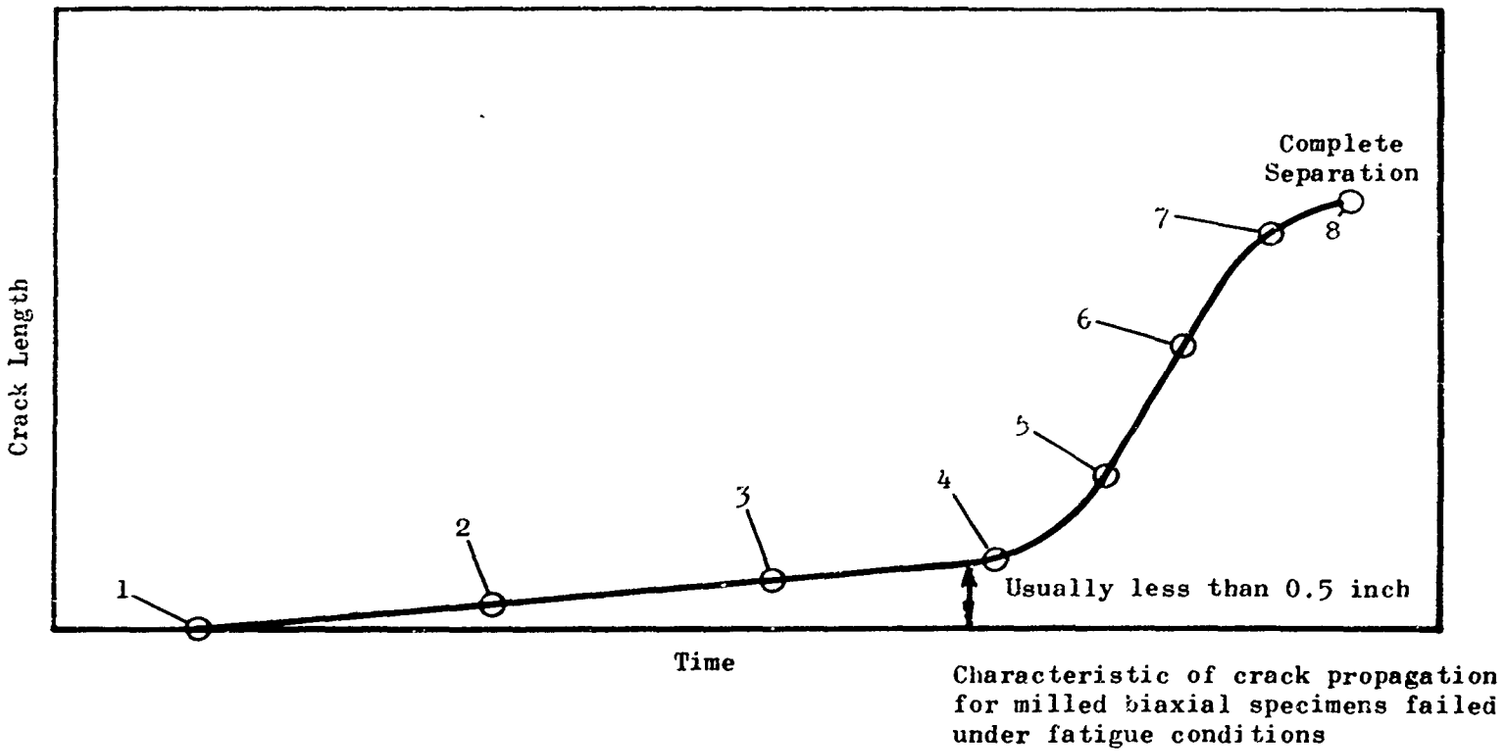

Figure 64. Typical Crack Development and Relative Growth for Biaxial Specimen in Fatigue Test

(Times between figures are not uniform. Longer periods occurred between a, b, c, and d than occurred between e, f, g, and h. Sequence camera did not photograph small initial cracks between a and d.)

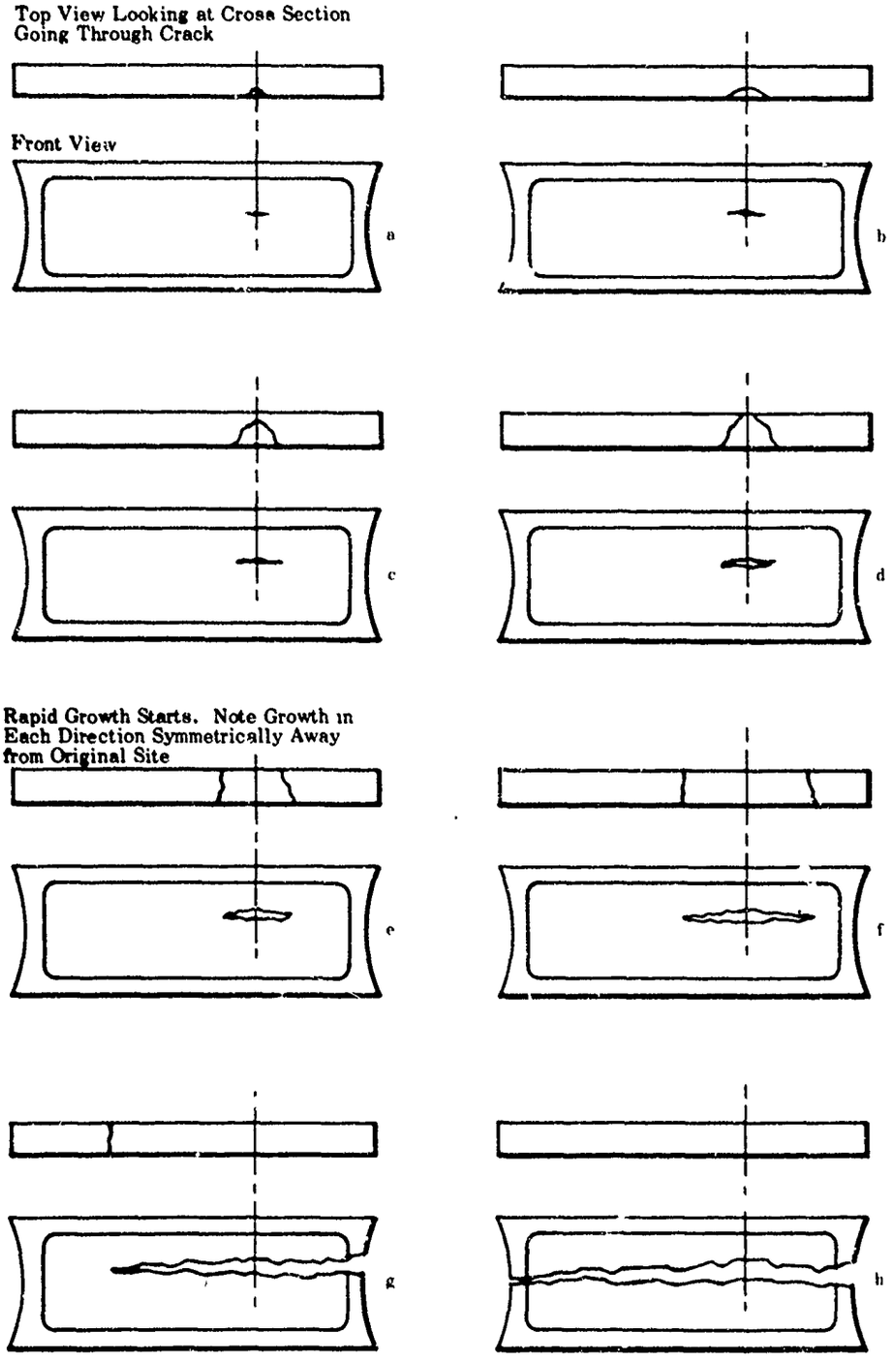

Figure 64. Concluded

Replots for the crack growth data are included for the 19 tests (Fig. 65 through 83. Seven of these replots reflect the low initial rate as depicted in Figure 64b. The remaining twelve curves do not. In most cases the crack suddenly appeared from the back side, and it was not possible to track the initial small surface crack in these cases, as mentioned earlier.

Average rates shown on these replots are based on the growth of the crack after it had worked completely through the thickness of the specimen from the initial surface crack and growth had started toward the edges.

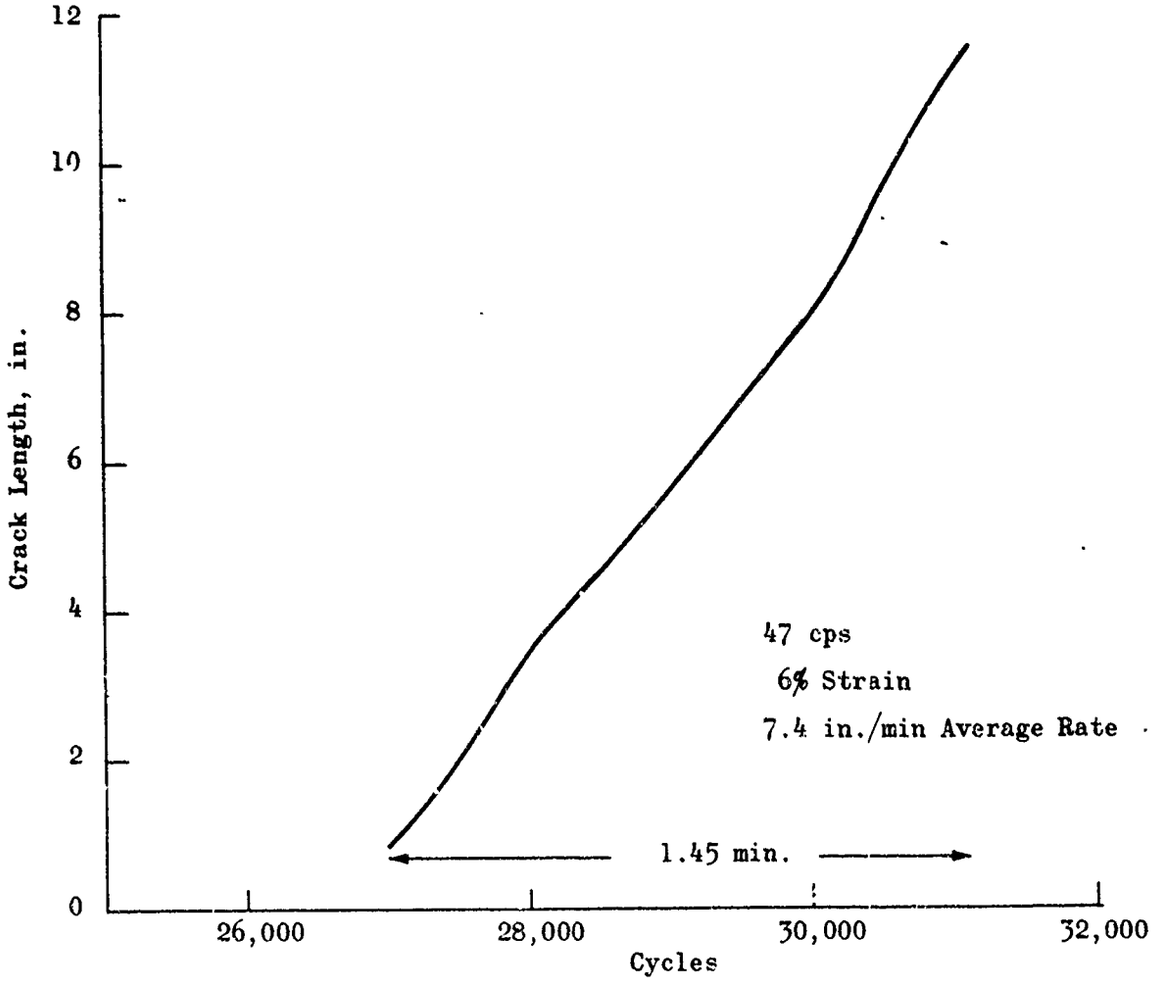

Figure 65. Biaxial Fatigue Test 92

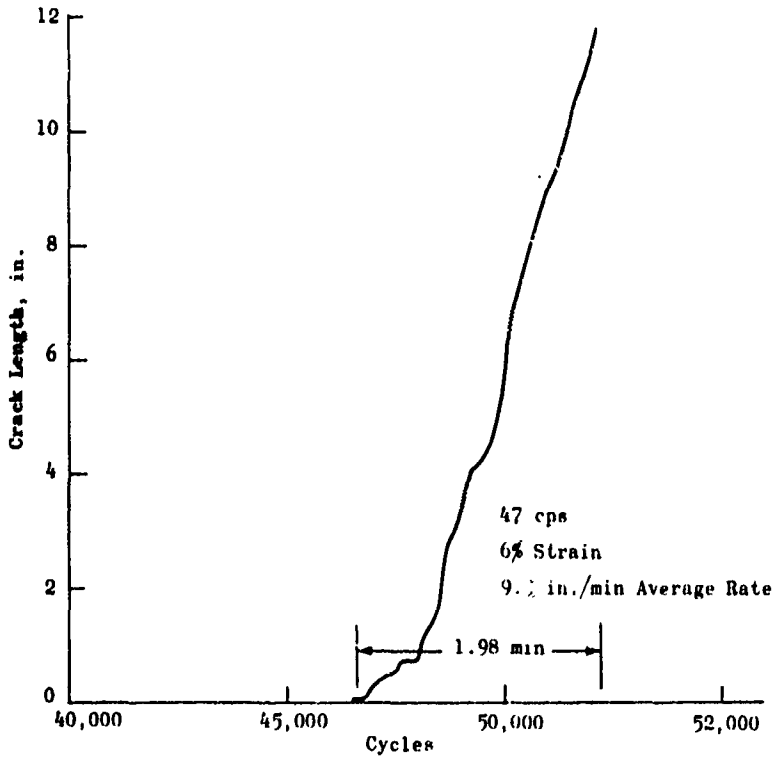

Figure 66. Biaxial Fatigue Test 93

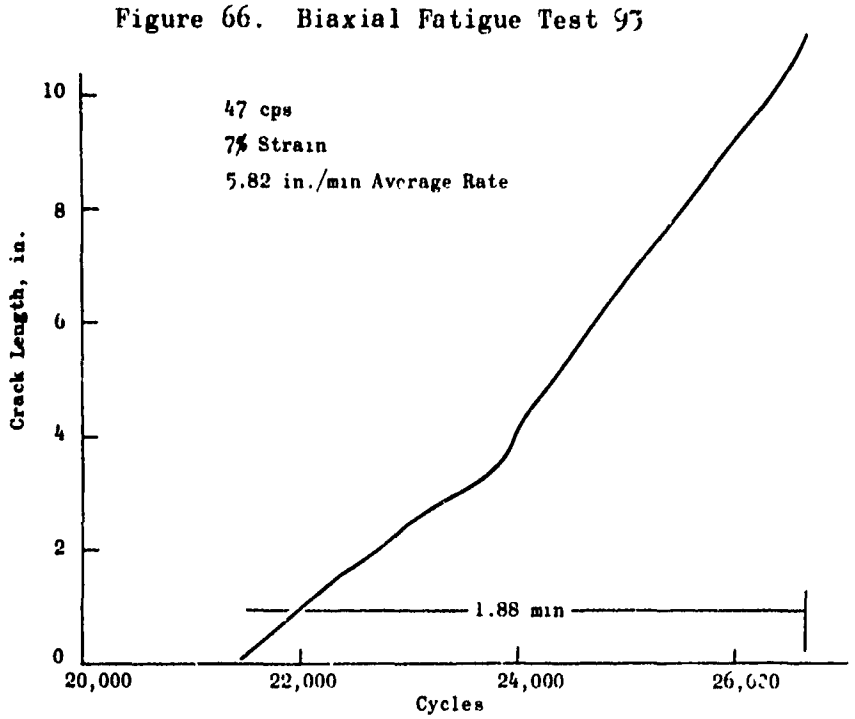

Figure 67. Biaxial Fatigue Test 94

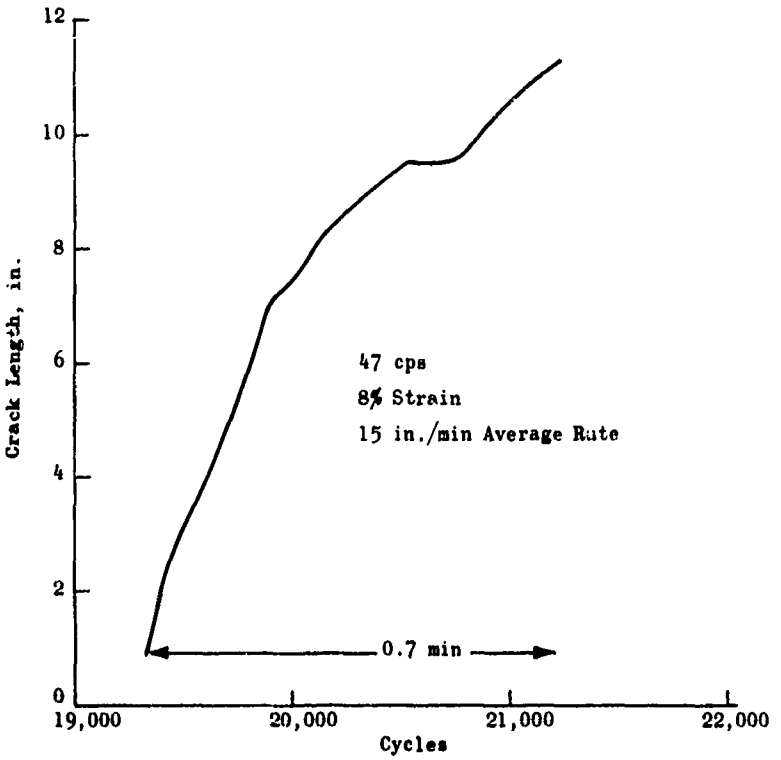

Figure 68. Biaxial Fatigue Test 95

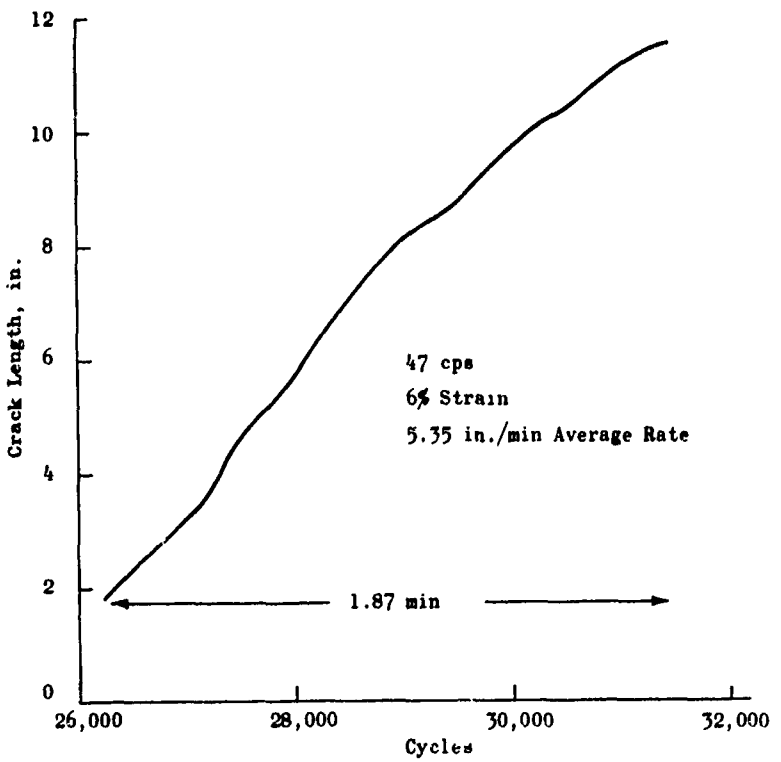

Figure 69. Biaxial Fatigue Test 96

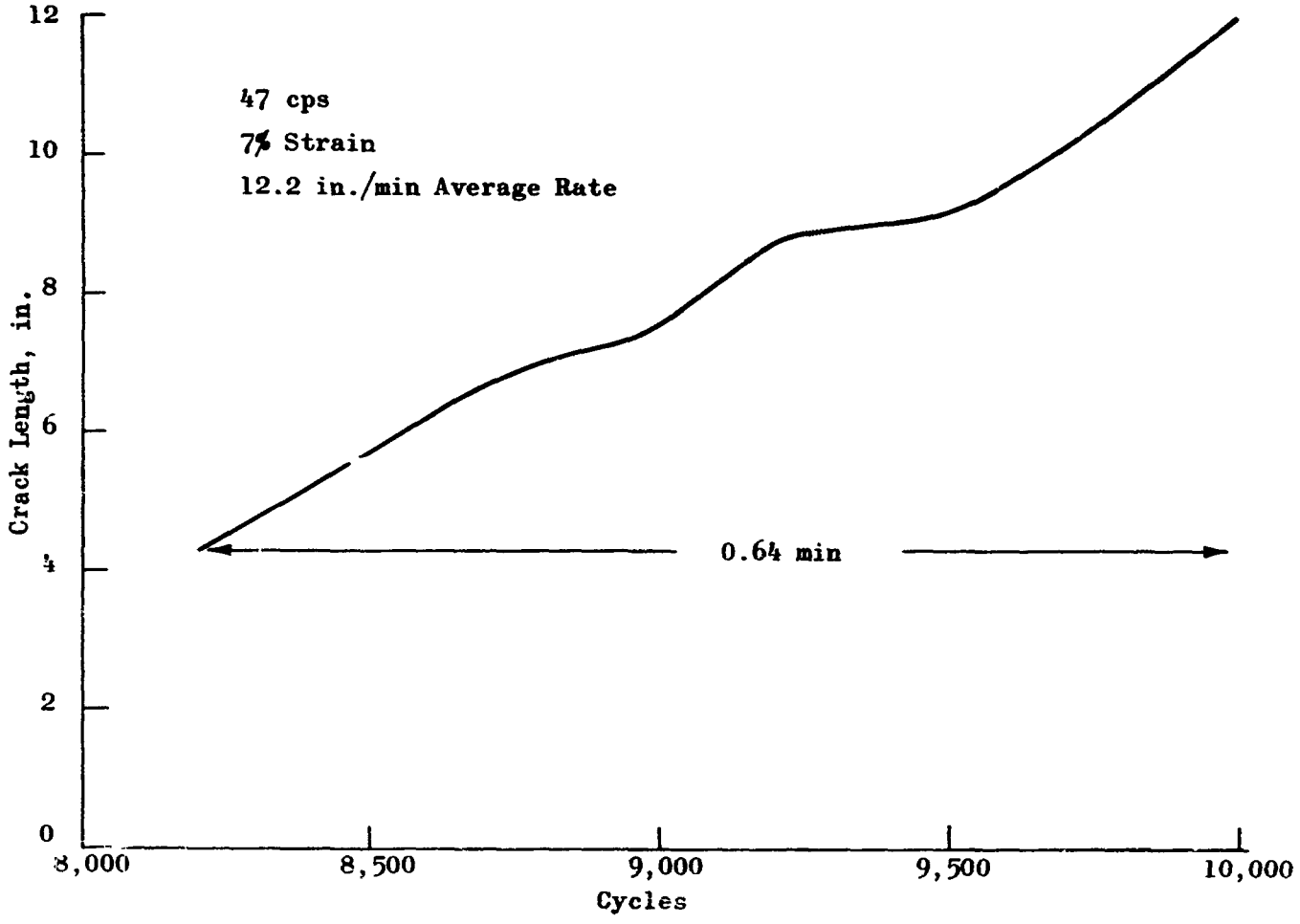

Figure 70. Biaxial Fatigue Test 97

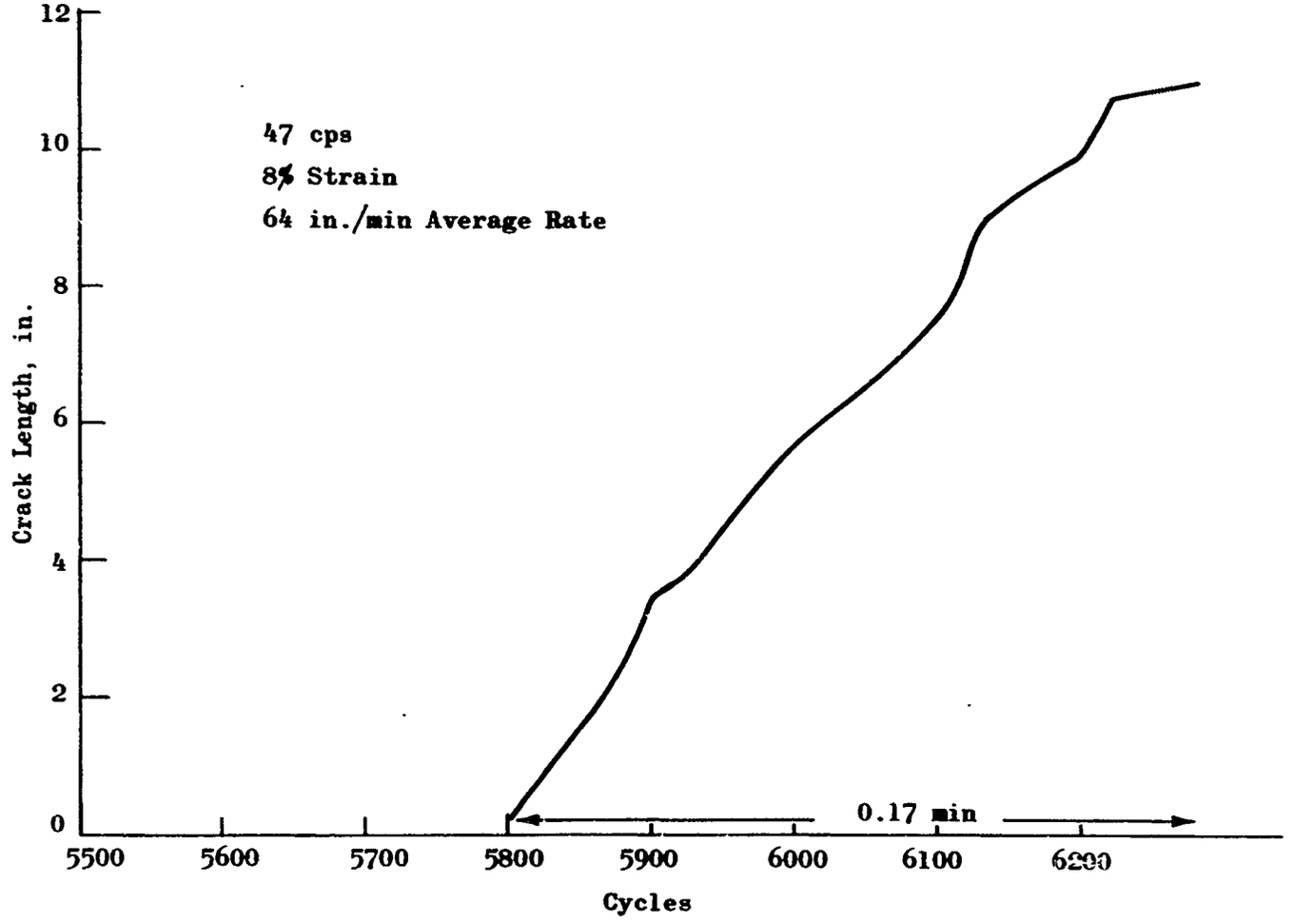

Figure 71. Biaxial Fatigue Test 98

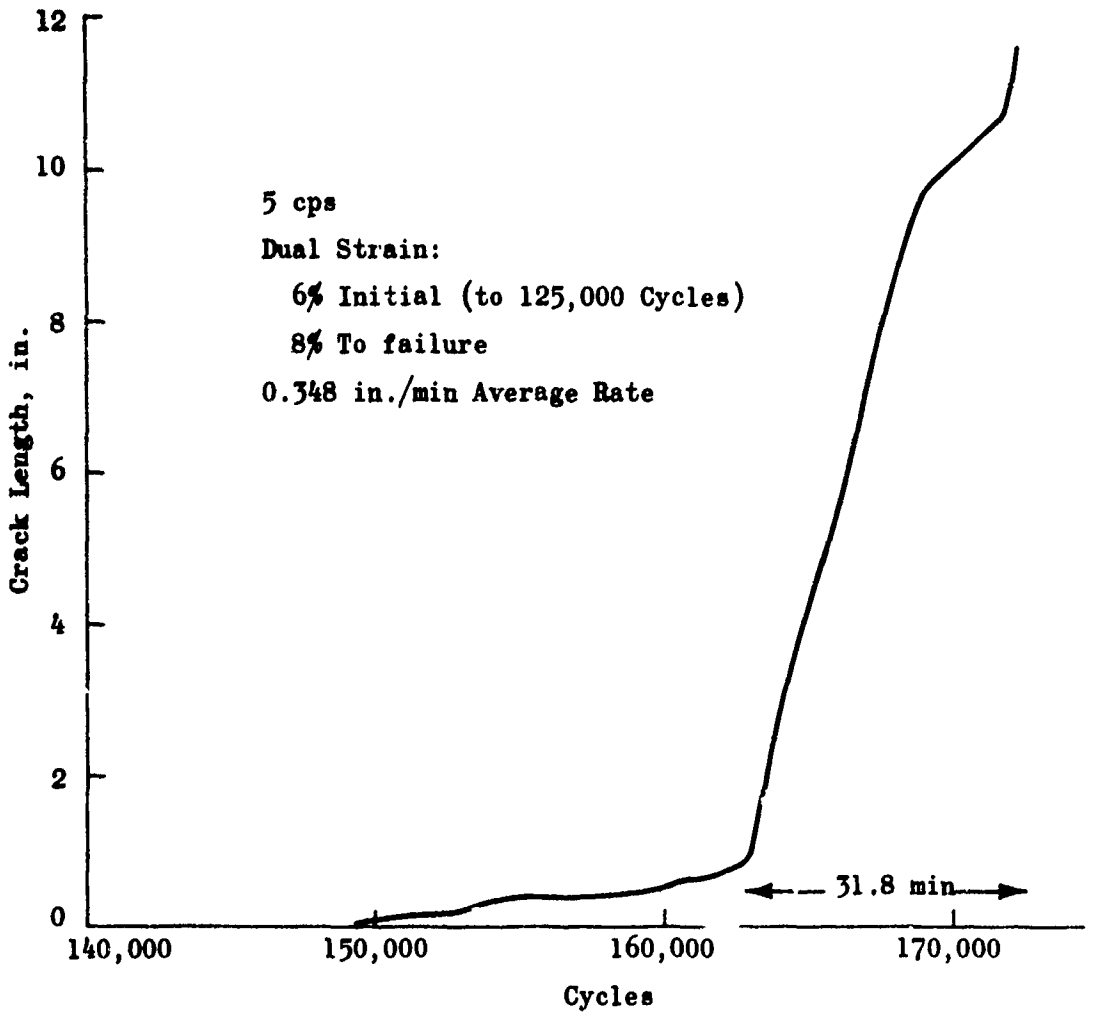

Figure 72. Biaxial Fatigue Test 100

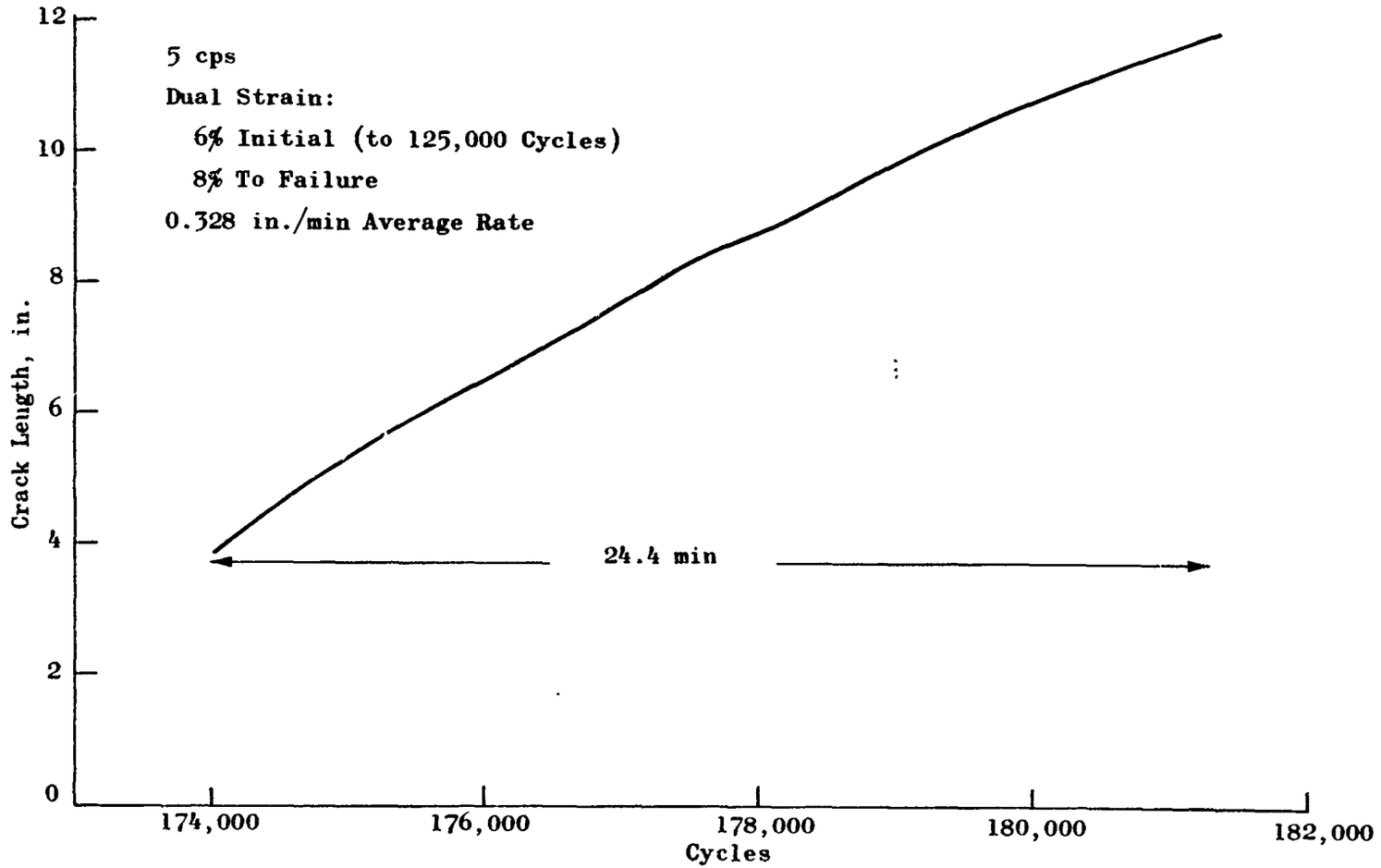

Figure 73. Biaxial Fatigue Test 101

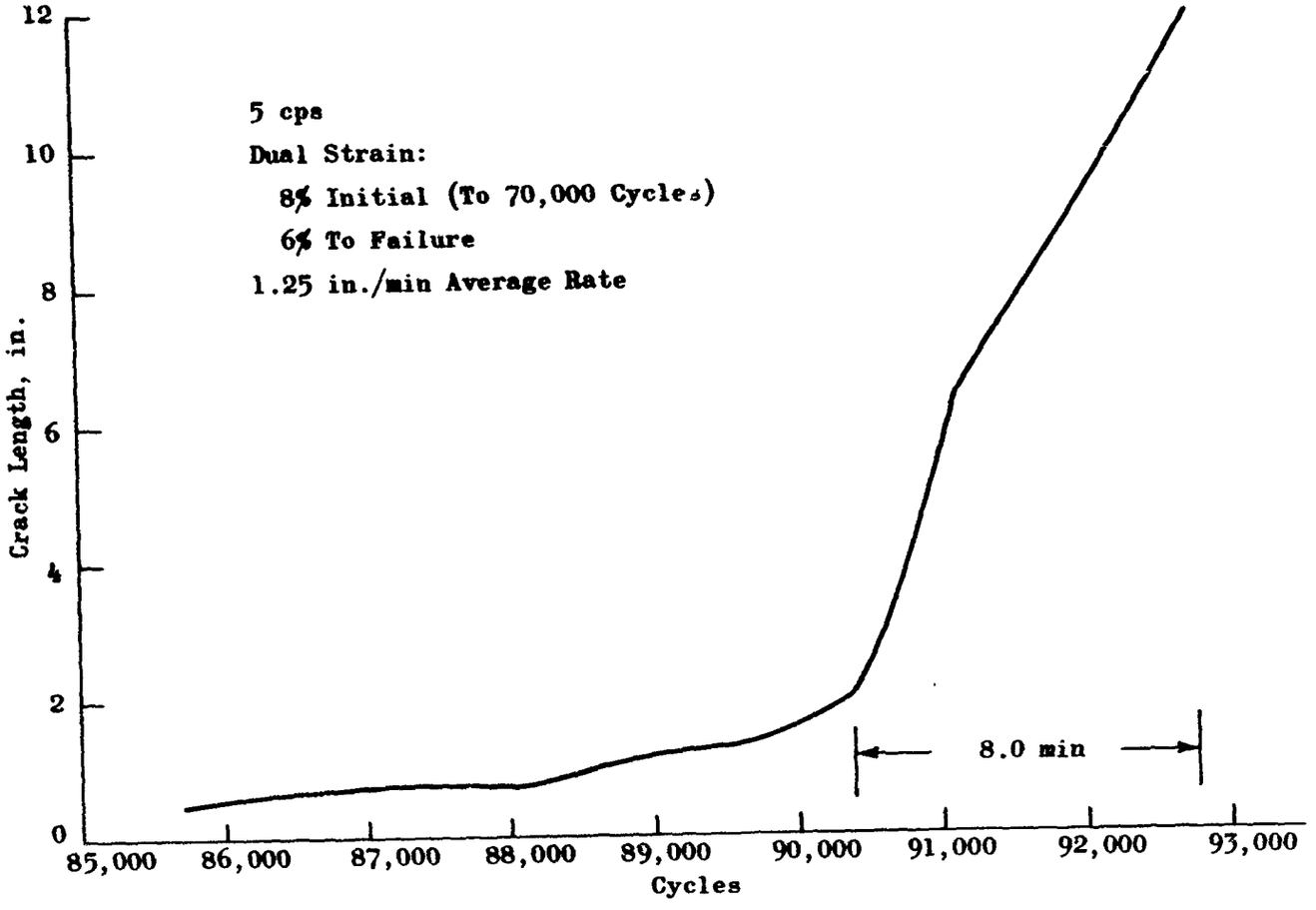

Figure 74. Biaxial Fatigue Test 102

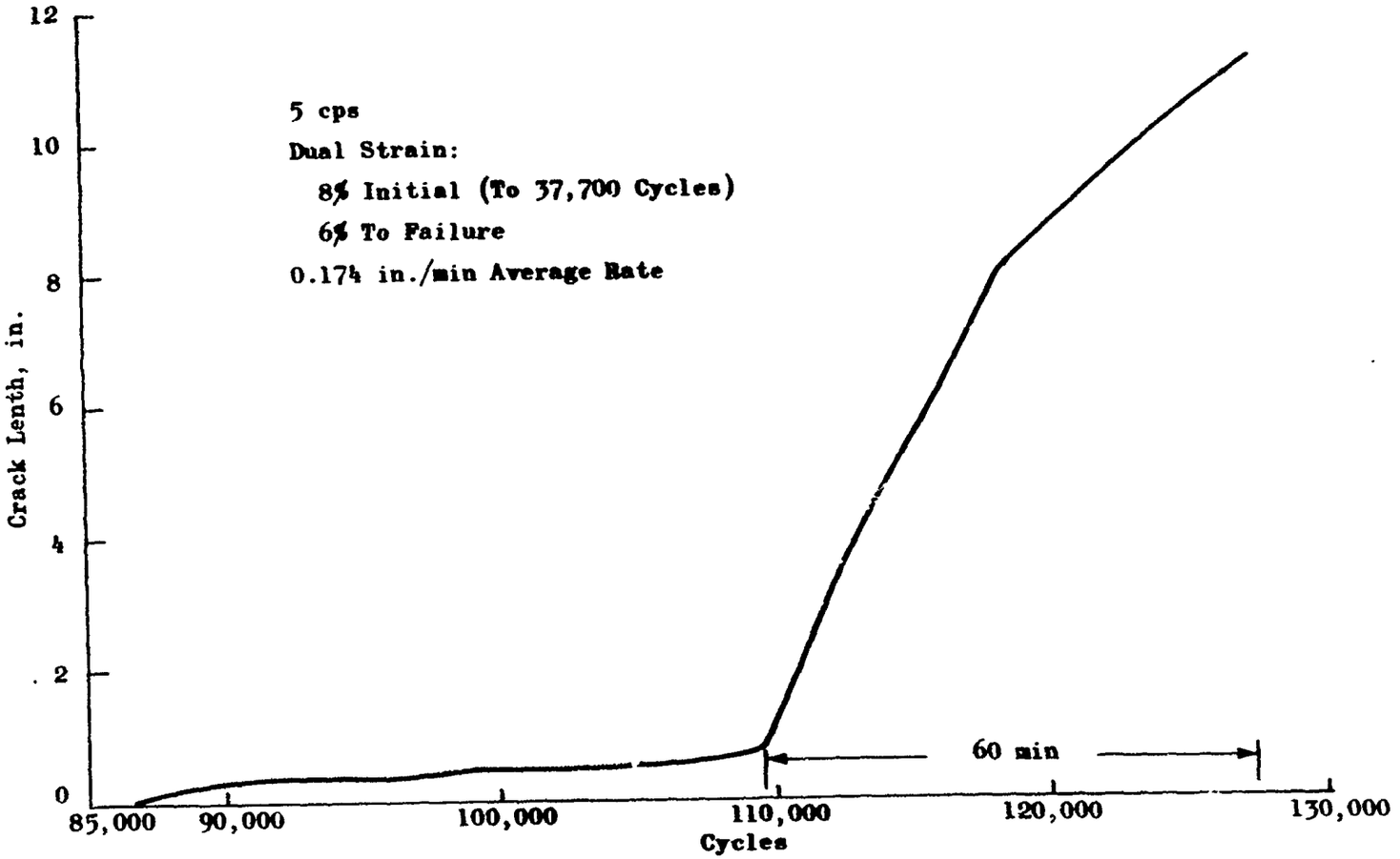

Figure 75. Biaxial Fatigue Test 103

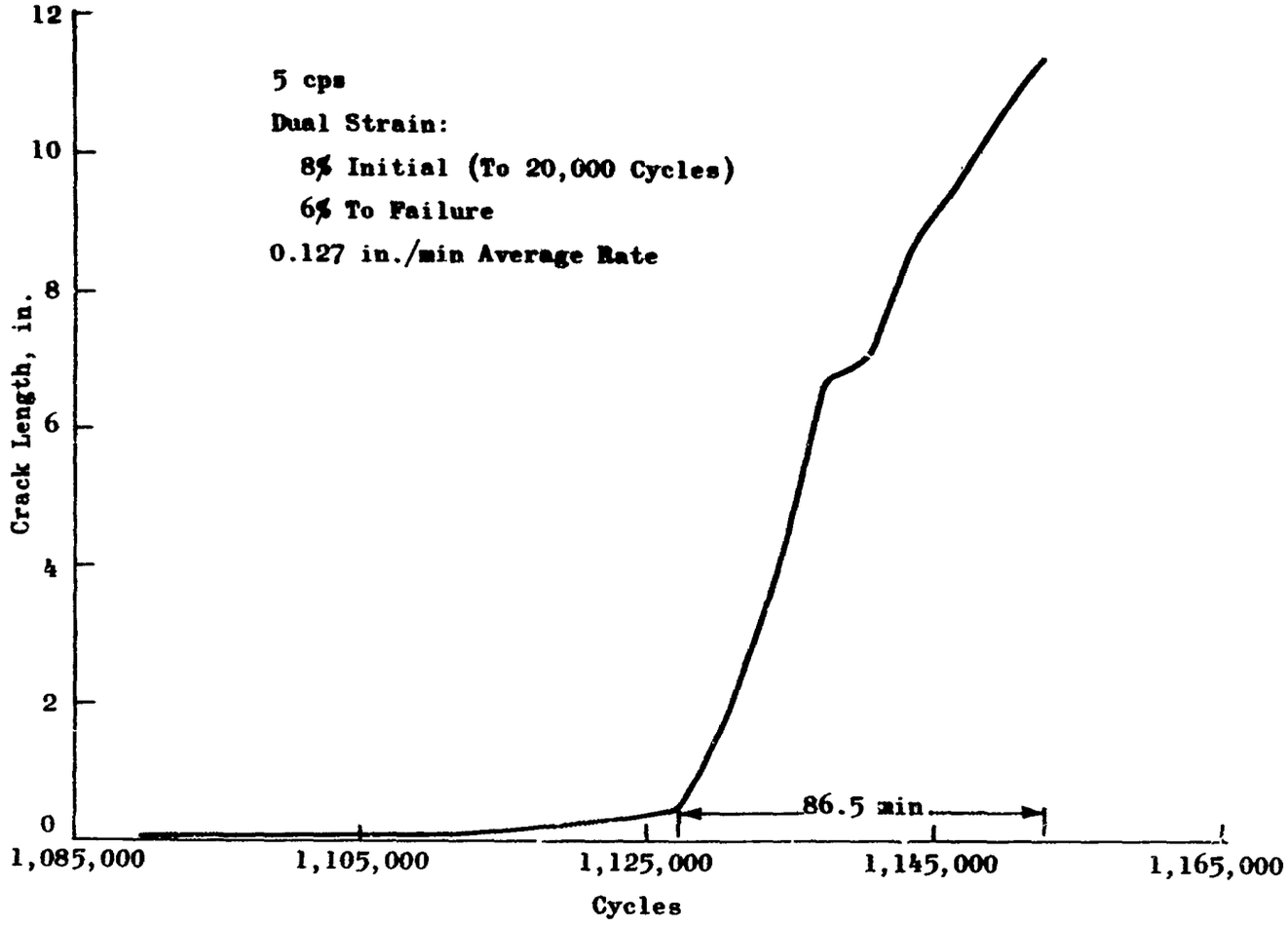

Figure 76. Biaxial Fatigue Test 104

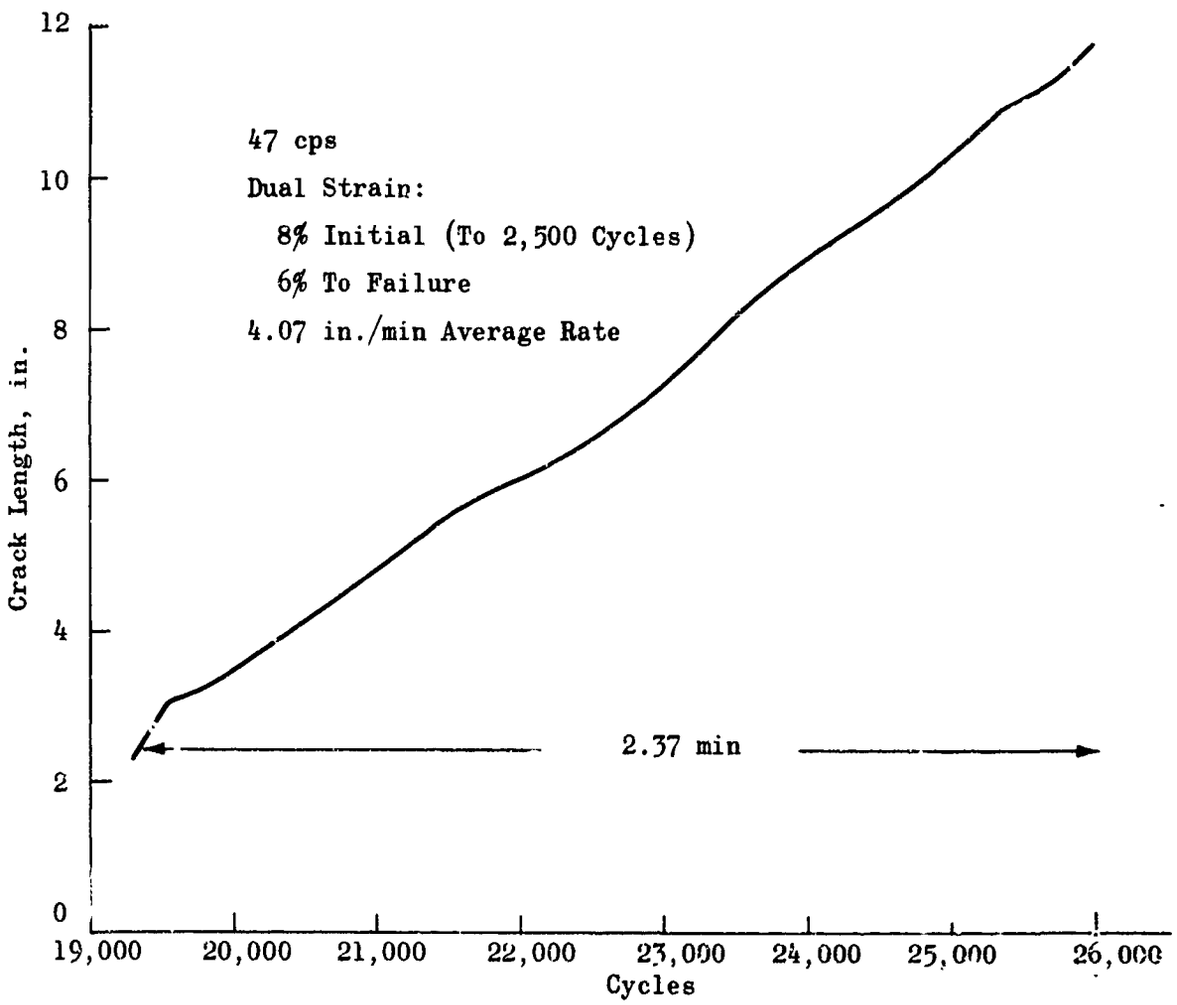

Figure 77. Biaxial Fatigue Test 105

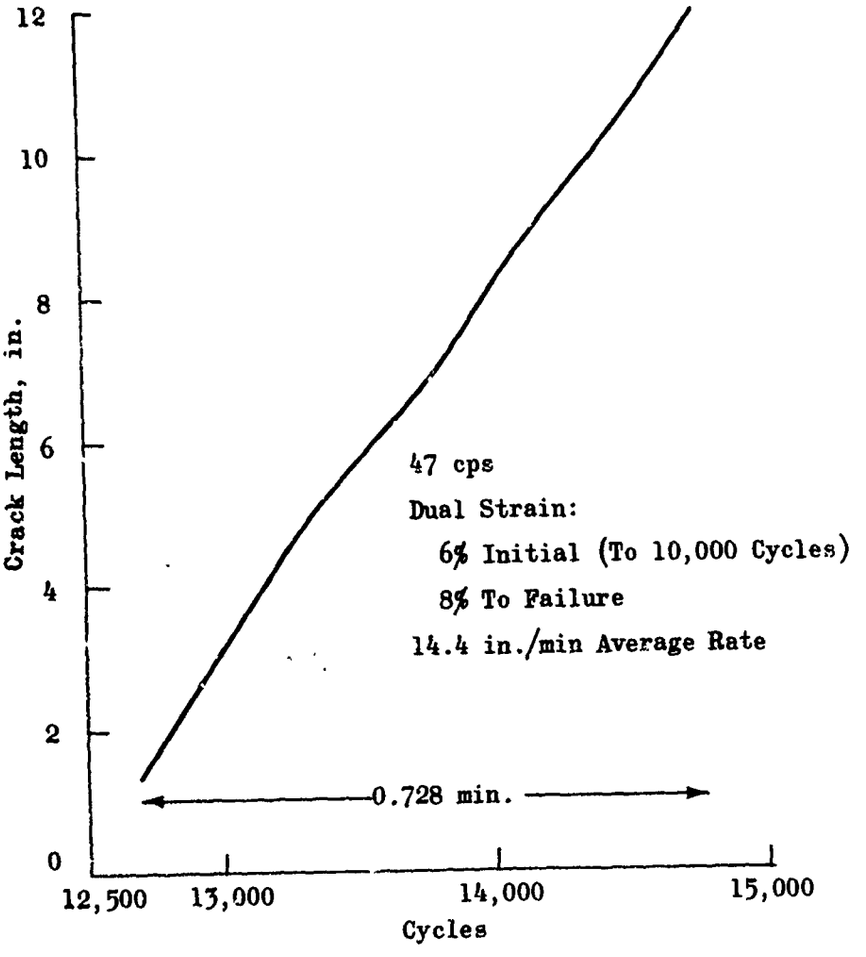

Figure 78. Biaxial Fatigue Test 106

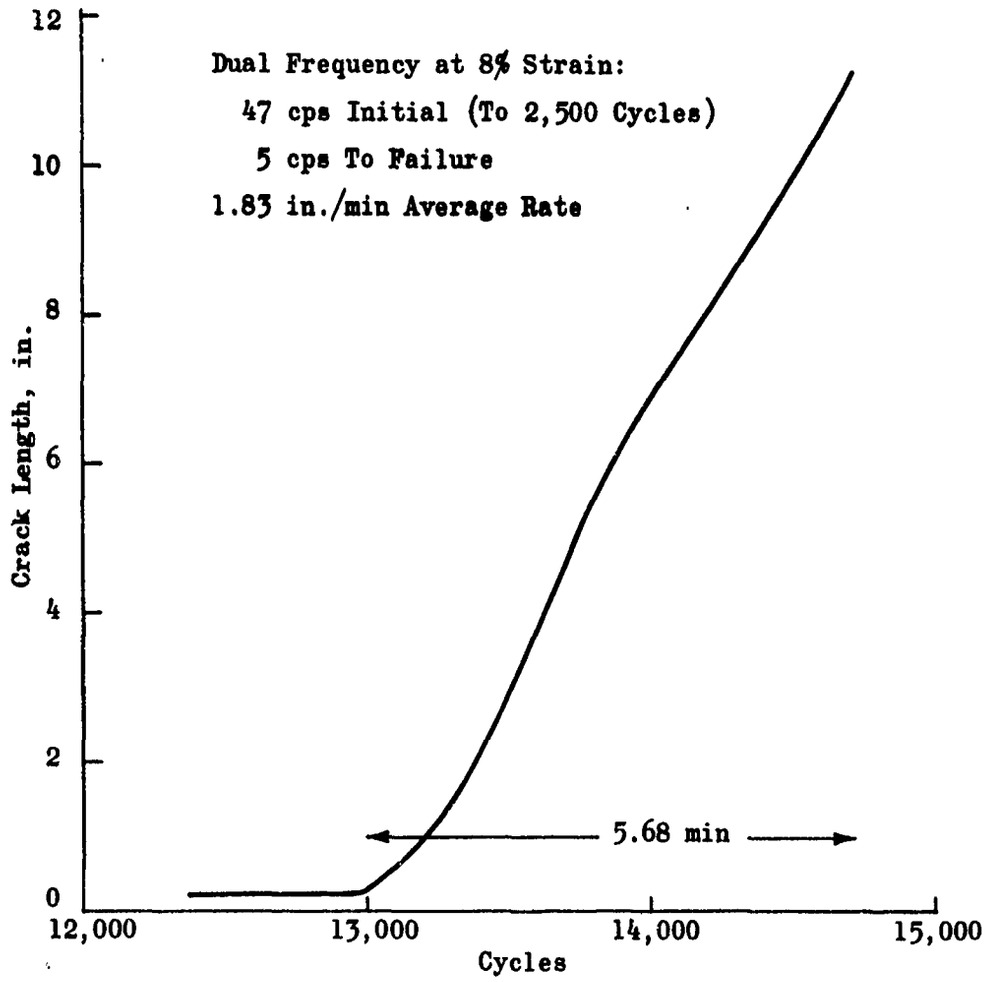

Figure 79. Biaxial Fatigue Test 107

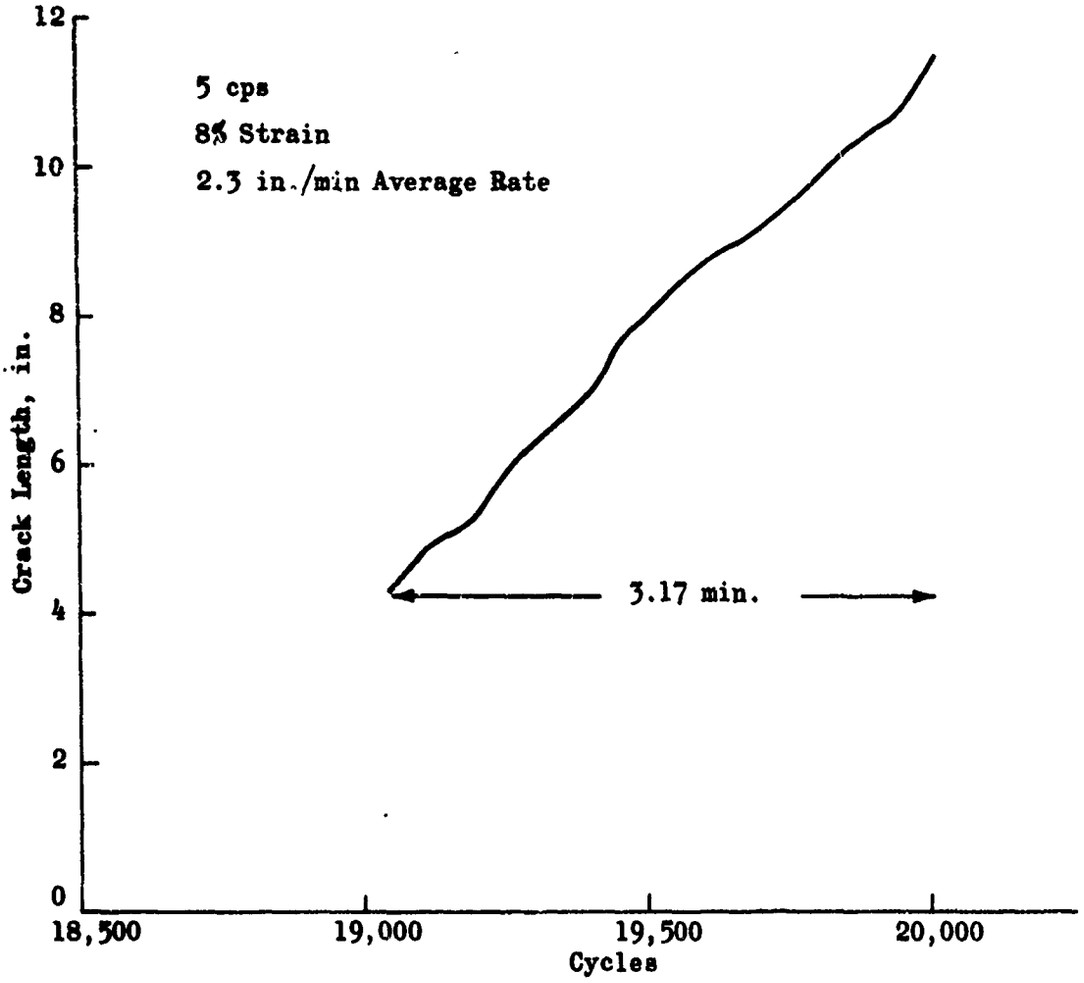

Figure 80. Biaxial Fatigue Test 103

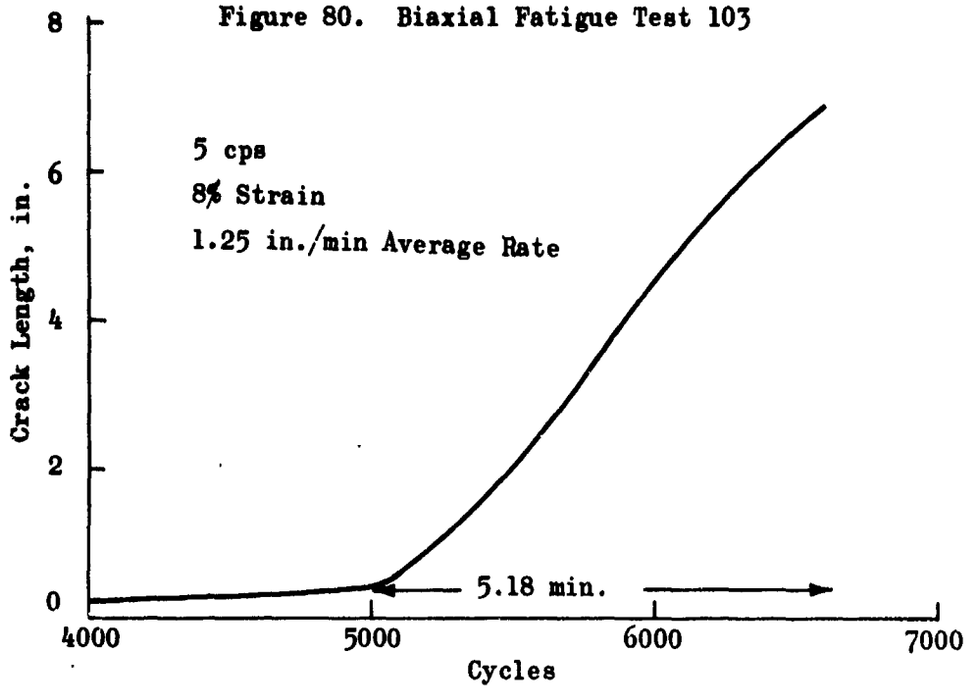

Figure 81. Biaxial Fatigue Test 110

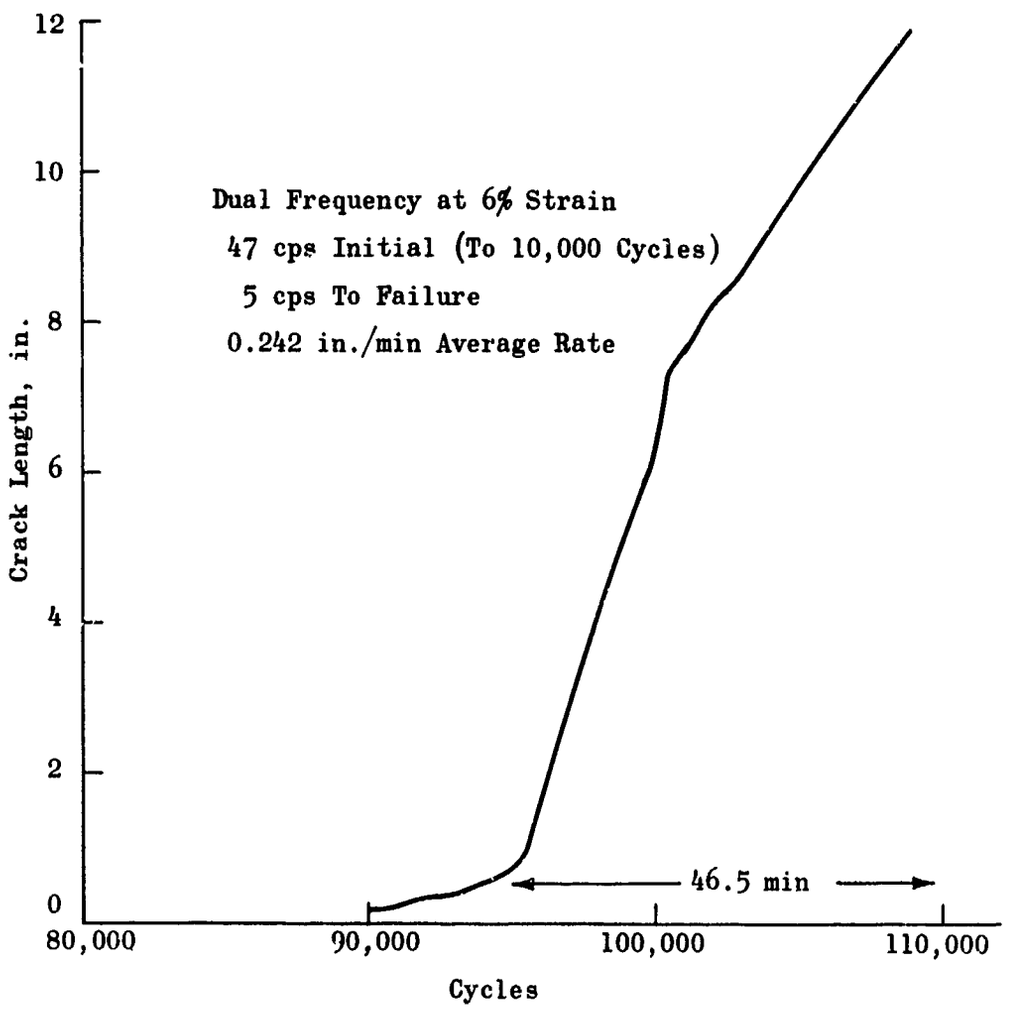

Figure 82. Biaxial Fatigue Test 112

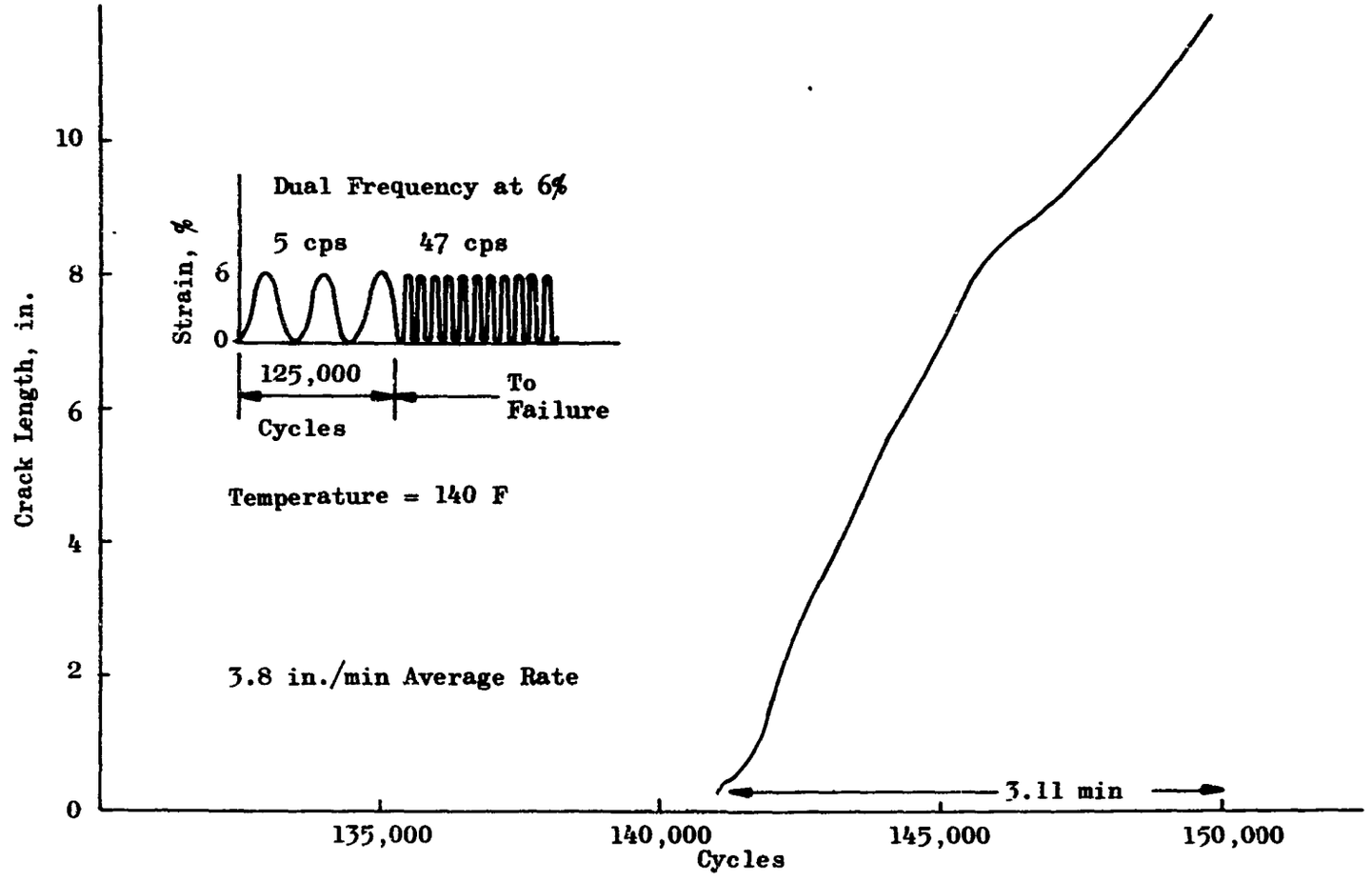

Figure 83. Biaxial Fatigue Test 113

APPENDIX IX

UNIAXIAL VS BIAXIAL PROPERTIES

Page 212 is blank

APPENDIX IX

UNIAXIAL VS BIAXIAL PROPERTIES

During the conduct of the tasks required on the Cumulative Damage Program data have become available which provide additional information for a direct comparison of propellant mechanical properties obtained from both uniaxial and multiaxial specimens. Engineers within the industry have long questioned the validity of property data determined under one state of stress for predicting behavior under other states of stress. But the expense and technical difficulty of performing satisfactory multiaxial tests has limited efforts to define the magnitude of the discrepancies. However, Rocketdyne's past experience with poker chip tests coupled with many recent biaxial tests conducted over a broad spectrum of conditions provided the data necessary to make quantitative conclusions concerning these discrepancies.

The discrepancies between uniaxial and triaxial tests have previously been discussed by Harbert (33, 34). This appendix is limited mainly to a discussion of discrepancies between uniaxial and biaxial conditions as found in a more recent testing sequence.

VIBRATION FATIGUE TESTS

Vibration fatigue tests were performed using the Cumulative Damage Testing machine with biaxial strips 13.25 x 3/8 x 2.8 inches long. In all cases the specimen surface temperature was maintained at a constant 140 F during the entire test duration. Fatigue loadings were harmonic (in time) extensions of the form

$$U(t) = U_o + U_o \sin \omega t \qquad (155)$$

applied to the 2.8-inch gage length

The resulting forces and the ambient temperature were both monitored. Also, the time a crack first becomes visible and the growth of that crack as a function of time (or number of cycles) was recorded. The force-time and force-displacement records were photographic prints of oscilliscope traces reflecting force transducer and linear variable differential transformer (LVDT) outputs. Examples of these traces are shown in Fig. 84.

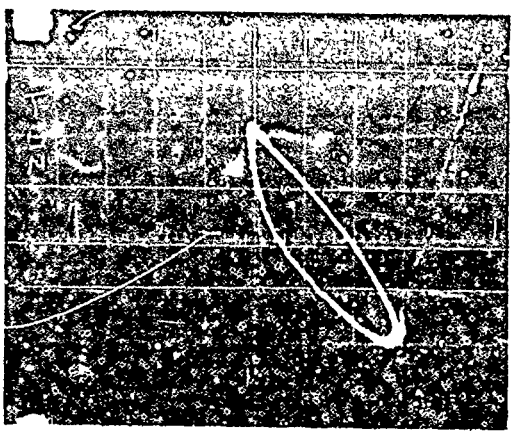

a. Lissajous Pattern after Only a Few Cycles

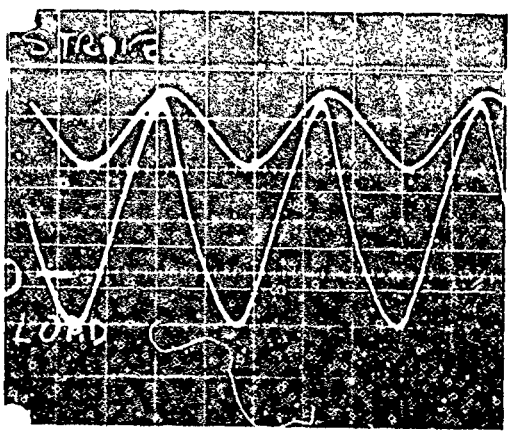

b. Displacement-time and Force-time Pattern after Only a Few Cycles

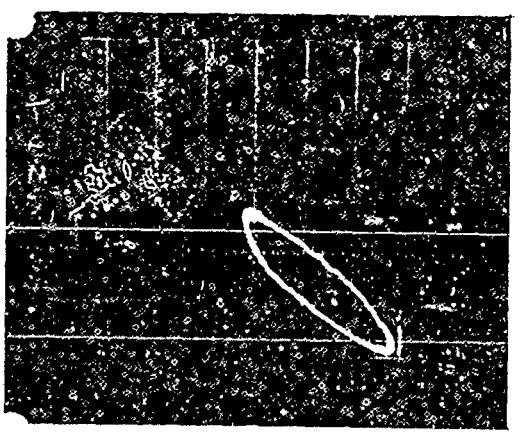

c. Lissajous Pattern after 50,000 Cycles

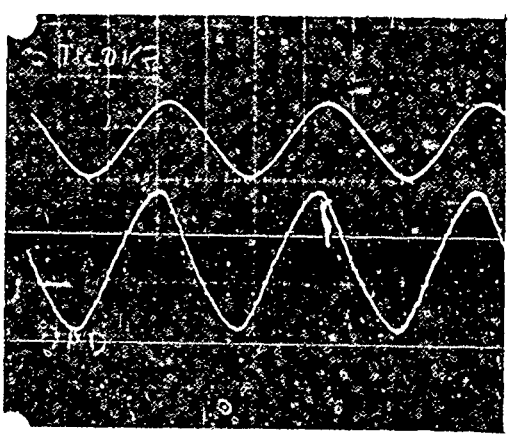

d. Displacement-time and Force-time Pattern after 50,000 Cycles

Figure 84. Oscilloscope Traces Resulting from Biaxial Fatigue Tests on Cumulative Damage propellant (Maximum extensions were 0.1875 inch applied at 15 cps. Specimen surfaces were held at 140 F.)

The tests were conducted to determine (using the number of cycles to failure) apparent values of the characteristic strain energy release rate and intrinsic flaw size. These parameters, once established, can then be used to predict times to failure following more complicated loading histories. The idealized model upon which these predictions are to be based consists of an initial spherical (or cylindrical) flaw in an incompressible spherical (or cylindrical) body of linear viscoelastic material. Analytical expressions based upon fracture mechanics for the time to the growth of the flaw in idealized models of this type have been derived in the literature for several typical loading histories (20, 21). These histories include that defined by Eq. 55.

These tests were all performed using a CTPB propellant furnished for the Cumulative Damage program studies. An extensive characterization for this propellant was provided by Lockheed Propulsion Company in support of the multicontractor Cumulative Damage program (35). Of particular importance to the Rocketdyne fracture mechanics approach was the relaxation modulus reproduced in Fig. 85. These uniaxial data were obtained using an Instron machine at strain levels of approximately 2.5%. The specimens had the standard JANAF dimensions but were tab-ended. Displacements were quickly imposed (2.0 in./min crosshead speed) and then held constant while the Instron load cell monitored the force deterioration. These measurements were continued for 20 minutes; data collected before four loading times had elapsed were disregarded. Test temperatures ranged from -120 to 300 F to generate the curve of Fig. 85. The time-temperature shift factors, a_T, used for the curve are shown in Fig. 86.

To apply the relaxation (or transient) modulus of Fig. 85 to the harmonic displacement input of the fatigue tests it became necessary to convert these data to the dynamic format implied when one writes

$$\sigma(t) = E^* \, \epsilon(t) \tag{156}$$

If the displacement (and in turn, the strain) is a specified harmonic function in time

$$\epsilon(t) = \epsilon_0 e^{i\omega t} \tag{157}$$

then the resulting stress may be written

$$\sigma(t) = \sigma_0 e^{i(\omega t + \delta)} \tag{158}$$

where δ is the angle by which the resulting stress leads the applied strain. From these one can deduce the value for a dynamic modulus, E*, by writing

$$E^* = \frac{\sigma}{\epsilon} = \frac{\sigma_o e^{i(\omega t + \delta)}}{\epsilon_o e^{i\omega t}} \tag{159}$$

so

$$E^* = \frac{\sigma_o}{\epsilon_o} e^{i\delta} = \frac{\sigma_o}{\epsilon_o} (\cos \delta + i \sin \delta) \tag{160}$$

The stress was decomposed into two vectorial components, one in-phase with the strain and the other 90° out of phase. Correspondingly the modulus E* has an in-phase component, E', and an out-of-phase component, E", and is written as the complex number

$$E^* = E' + i\, E'' \tag{161}$$

where from Eq. 160 the real and imaginary parts are seen to be, respectively[1]

$$E' = \frac{\sigma_o}{\epsilon_o} \cos \delta; \quad E'' = \frac{\sigma_o}{\epsilon_o} \sin \delta \tag{162}$$

Noting the decaying character of the relaxation modulus, Schapery (16) has suggested the use of a finite Prony series to analytically represent the experimentally measured time function. The series of terms is written

$$E_{rel}(t) = E_e + \sum_1^n E_k e^{-t/\tau_k} \tag{163}$$

where the several E_k's and τ_k's can be selected by collocation. Further, the term-by-term Laplace transformation of the functions yields the image

$$\bar{E}_{rel}(p) = E_e + \Sigma \frac{E_k p \tau_k}{\tau_k p + 1} \tag{164}$$

[1] $\left\{E'^2 + E''^2\right\}^{1/2} = \sigma_o/\epsilon_o$

Prony Series Coefficients	
Log τ_k	E_k
5	12
4	48
3	28
2	19
1	55
0	125
-1	185
-2	320
-3	470
-4	790
-5	1,100
-6	1,700
-7	3,000
-8	4,400
-9	6,700
-10	10,400
-11	17,300
-12	27,000
-13	40,000
-14	40,000
-15	23,000
-16	18,000
-17	5,348

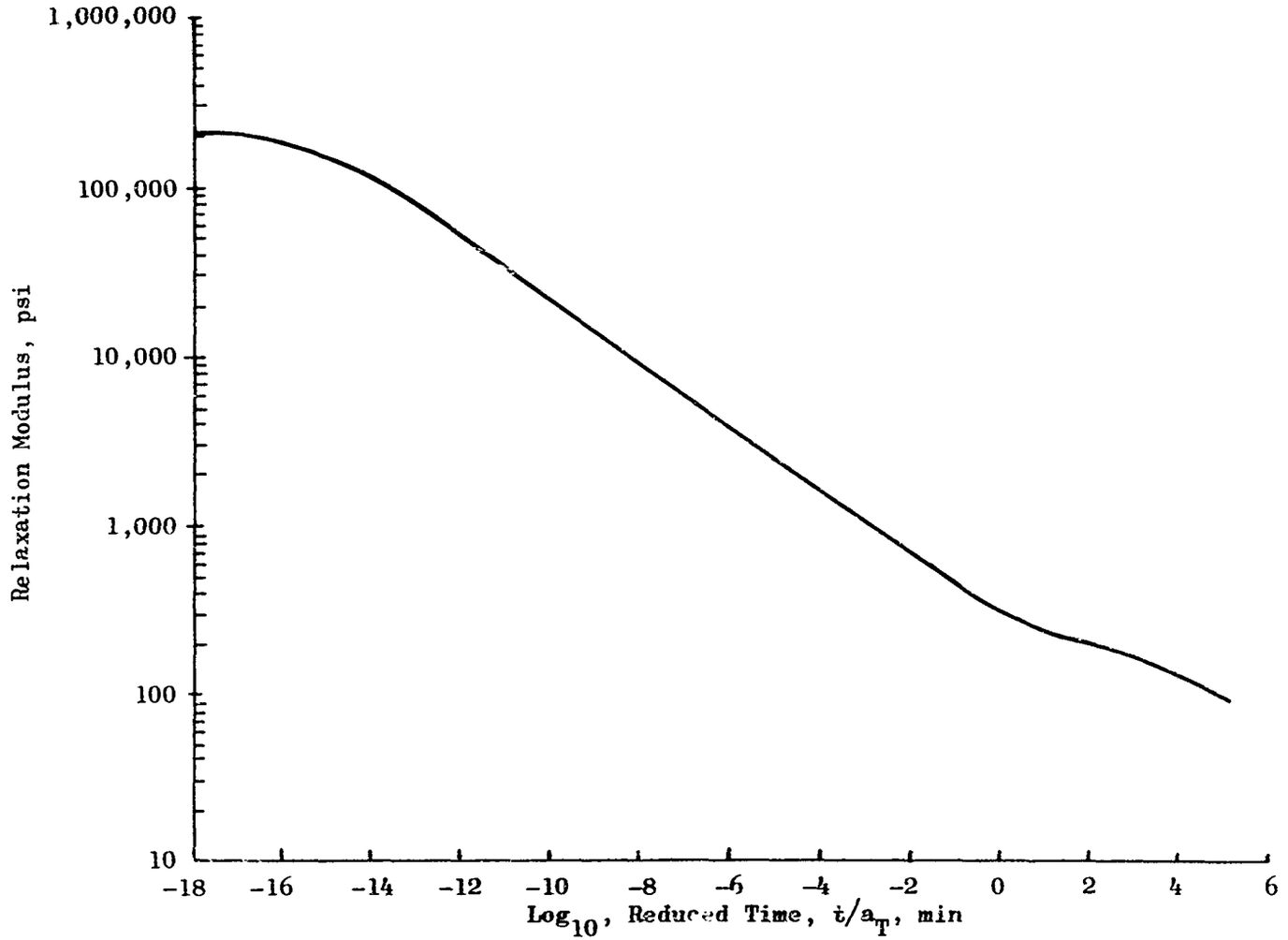

Figure 85. Stress Relaxation Modulus vs Reduced Time (0002-61E STV Propellant—Furnished by LPC and Tested in November 1967)

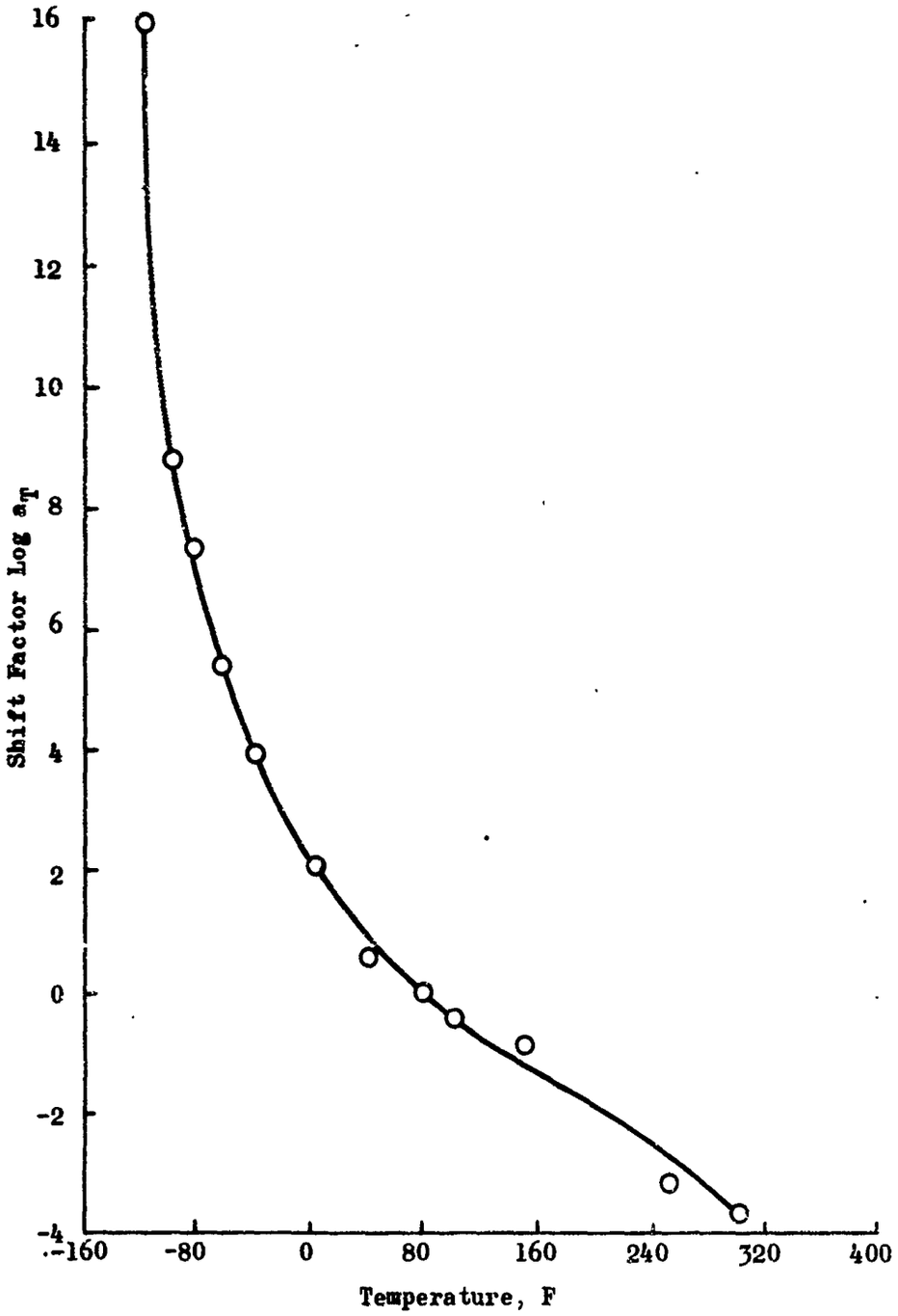

Figure 86. Time-Temperature Shift Factors Corresponding to the Uniaxial Relaxation Data of Fig. 85

The bar implies that the function has been transformed. The interrelationship of the dynamic properties with these so-called transient properties can be determined simply by replacing the transform parameter p with $\pm i\omega$. The function becomes a complex number, the real part of which corresponds to E' and the imaginary part E". By following this line of reasoning as suggested in (36), when $p = \pm i\omega$

$$E(\pm i\omega) = E_r + \sum_{n=o}^{N} \frac{\pm i\omega \tau_n E_n}{1 \pm i\omega \tau_n} \tag{165}$$

or

$$E(\pm i\omega) = E_r + \sum_{n=o}^{N} \frac{(\omega \tau_n)^2 E_n}{(\omega \tau_n)^2 + 1} + i \sum_{n=o}^{N} \frac{\omega \tau_n E_n}{(\omega \tau_n)^2 + 1} \tag{166}$$

$$= E' + i\,E'' \tag{167}$$

In polar rotation

$$E(\pm i\omega) = \left\{ \left[E_r + \sum_{n=o}^{N} \frac{(\omega \tau_n)^2 E_n}{(\omega \tau_n)^2 + 1} \right]^2 + \left[\sum_{n=o}^{N} \frac{\omega \tau_n E_n}{(\omega \tau_n)^2 + 1} \right]^2 \right\}^{1/2} x$$

$$\left\{ e^{\pm i \tan^{-1} \left[\frac{\sum_{n=o}^{N} \frac{\omega \tau_n E_n}{(\omega \tau_n)^2 + 1}}{E_r + \sum_{n=o}^{N} \frac{(\omega \tau_n)^2 E_n}{(\omega \tau_n)^2 + 1}} \right]} \right\} \tag{168}$$

Comparing Eq. 156 and 168 one has

$$|E^*| = \frac{\sigma_o}{\epsilon_o} = \left\{ \left[E_r + \sum_{n=o}^{N} \frac{(\omega \tau_n)^2 E_n}{(\omega \tau_n)^2 + 1} \right]^2 + \left[\sum_{n=o}^{N} \frac{\omega \tau_n E_n}{(\omega \tau_n)^2 + 1} \right]^2 \right\}^{1/2} \tag{169}$$

$$\delta = \tan^{-1}\frac{E''}{E'} = \tan^{-1}\frac{\sum_{n=0}^{N}\frac{\omega\tau_n E_n}{(\omega\tau_n)^2+1}}{E_{r+}\sum_{n=0}^{N}\frac{(\omega\tau_n)E_n}{(\omega\tau_n)^2+1}} \qquad (170)$$

The relaxation modulus of the Lockheed propellant (shown in Fig. 85) was numerically expanded into a Prony series (Eq. 163) of 23 terms in addition to the rubbery modulus, E_e. The best value for the coefficients E_k and τ_k are shown in the table on the left side of Fig. 85. These coefficients have been used to calculate both the corresponding storage modulus, E', and loss modulus, E", as indicated by Eq. 166 and 168. These functions of the vibrating frequency, ω, are shown plotted in Fig. 87.

It was intended that these data; $E_{rel}(t)$, $E''(\omega)$, and $E'(\omega)$; would be used with the viscoelastic fracture mechanics equations for the growth of a spherical or cylindrical flaw. The remaining parameters could be chosen to give the best fit to the number of cycles to failure observed during the fatigue tests. These parameters would then permit the use of the theory for predicting failure following more complicated loading histories; i.e., a numerical evaluation of the cumulative damage. But first a cursory comparison of the properties determined from uniaxial relaxation tests with those deduced from the responses of the dynamic tests of biaxial strips was made. This step was performed to confirm the validity and check the accuracy of the calculations utilizing the uniaxial relaxation properties.

COMPARISON

The test data used for these calculations was that collected from a biaxial strip specimen subjected to a harmonic tensile displacement with a frequency of 94.5 radian/sec. The equation for the platen movement was

$$u(t) = 0.09375 + 0.09375 \sin 94.5t$$

where t is time in seconds and u(t) the displacement in inches. This proved to be a trouble-free, valid test.

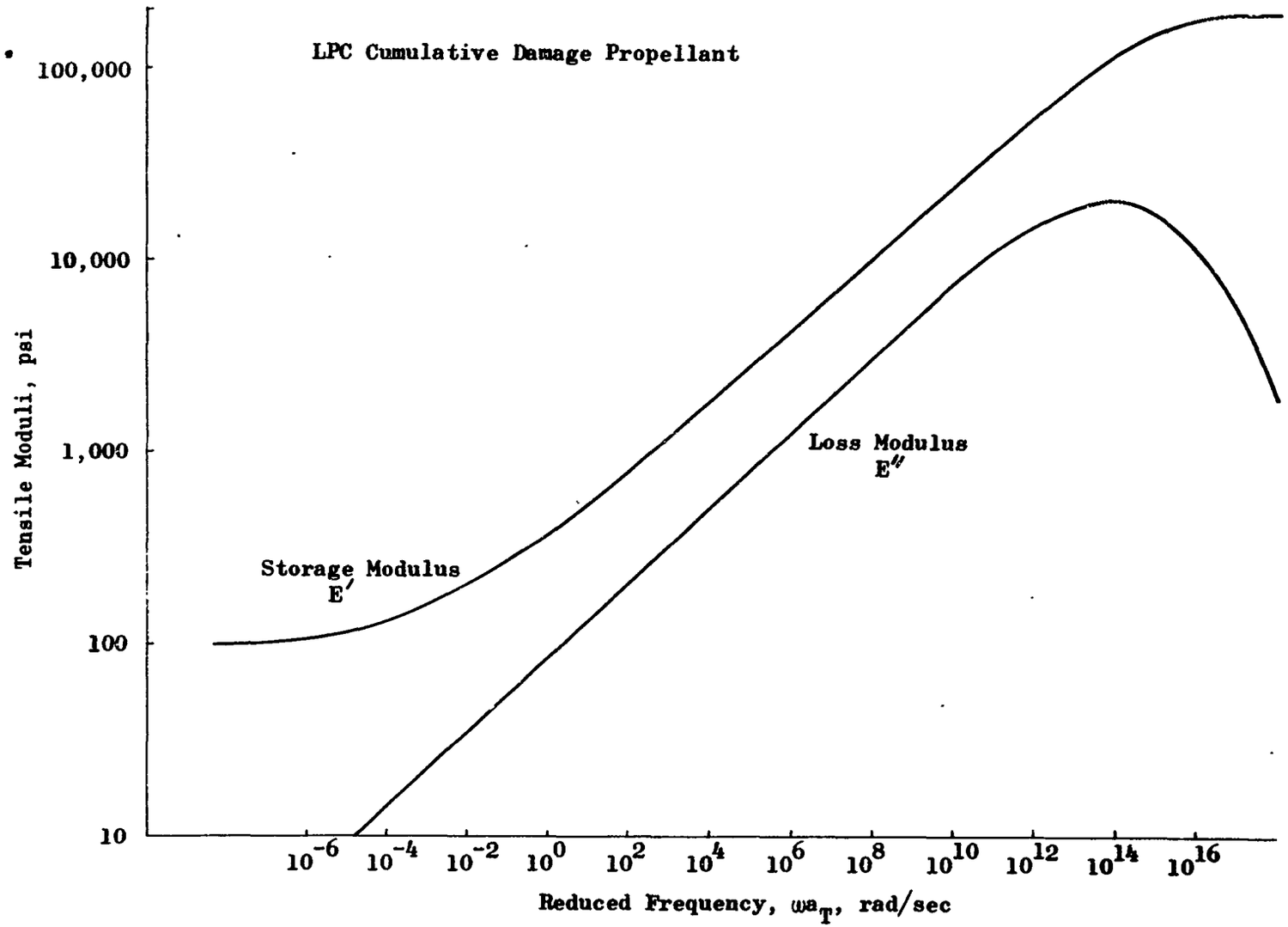

Figure 87. Dynamic Moduli as Calculated from the Uniaxial Relaxation Modulus

Figure 88 shows replots of the hysteresis loops shown as photographs in Fig. 84. But also shown are the predicted stresses and strains corresponding to the uniaxial relaxation modulus and the dynamic properties of Fig. 87. The differences are seen to be the largest at a low number of cycles even though this is where one would logically believe the results should be best because the nonlinearity due to dewetting from cycling has not fully come into play.

Because the material properties are a vital part of the equations derived from the fracture theory, it was felt that some resolution of this discrepancy should be accomplished before the effort continued. This work resulted from the attempt to understand these phenomena and intelligently reconcile theory and test results.

BIAXIAL CONSTANT STRAIN RATE TEST

The discrepancies between the measured dynamic response of the biaxial specimen with the predicted response using properties determined from static tests of uniaxial specimens caused us to attempt to determine just which new condition our analytics could not handle, the two dimensional stress state or the dynamic loading. To do this we ran a single sawtooth displacement test where a linear cross-head rate first tensed and then relieved a biaxial specimen (see Fig. 89a). The resulting measured forces are shown in Fig. 89b. Those forces predicted using the modified power law as derived from the uniaxial relaxation data are also shown. This four-parameter representation is of the form

$$E_{rel}(t) = \frac{E_g - E_e}{(1 + t/\tau_0)^n} + E_e \qquad (170)$$

and the procedure for using it to predict the response of constant strain rate tests is discussed in (12). The results of this procedure are shown by the curve labeled "Predicted" in Fig. 89b.

RELAXATION TO CONSTANT RATE TESTS

There are two possible sources for the discrepancies described in the previous paragraphs. One is that the relaxation modulus (the ratio of the time-dependent stress to strain in constant strain test) for the propellant cannot be used to predict constant strain rate behavior even under a like stress state. The other is that the uniaxial properties are not appropriate for biaxial or other stress states. To check the importance of the first of these differences for the Lockheed propellant, predictions of the time-dependent force due to a linear strain rate were made. These predictions were then compared to the forces as reported by Lockheed in their constant rate characterization tests of uniaxial specimens.

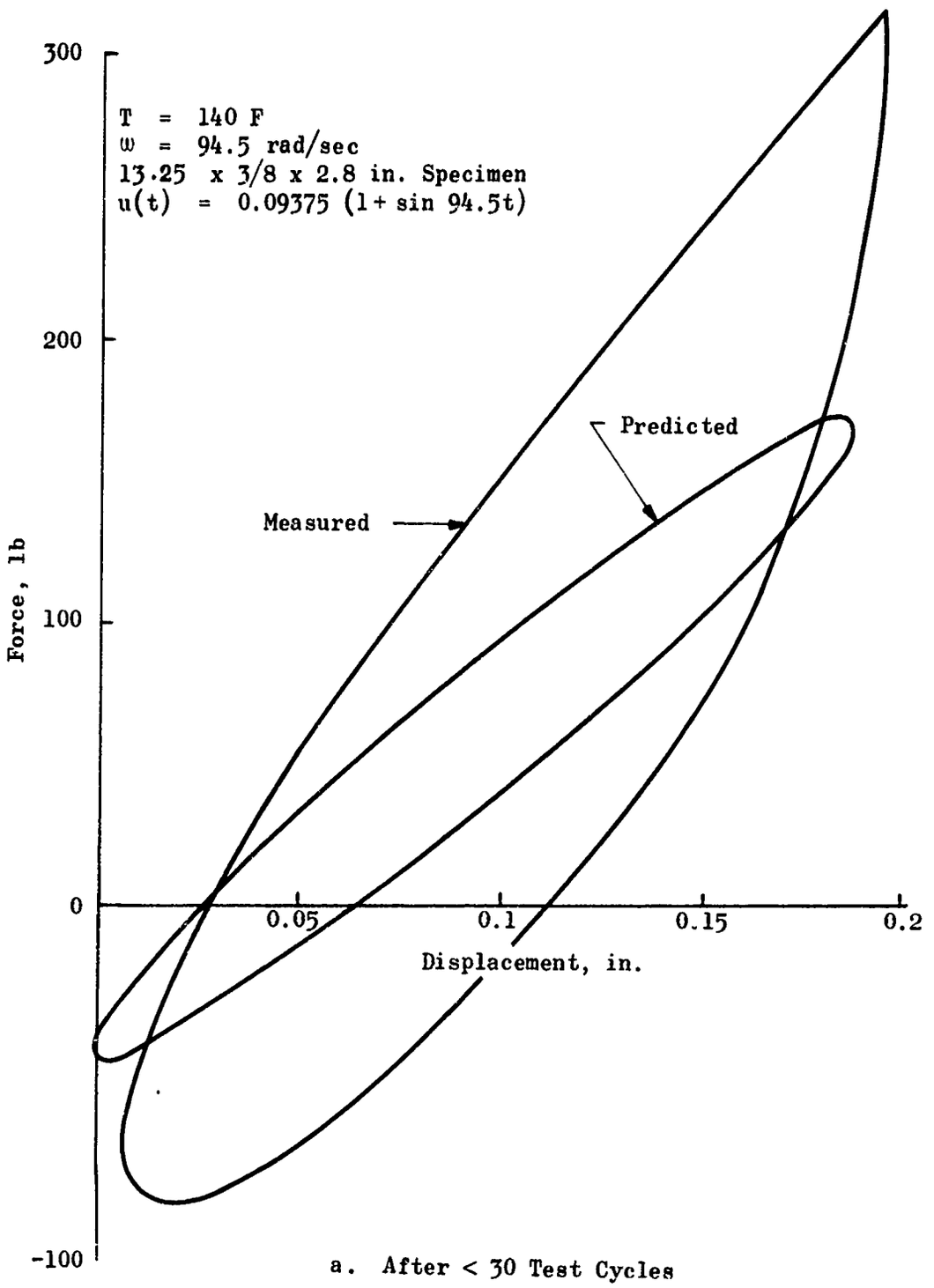

a. After < 30 Test Cycles

Figure 88. A Comparison of the Biaxial Force-Displacement Curves as Measured and Predicted

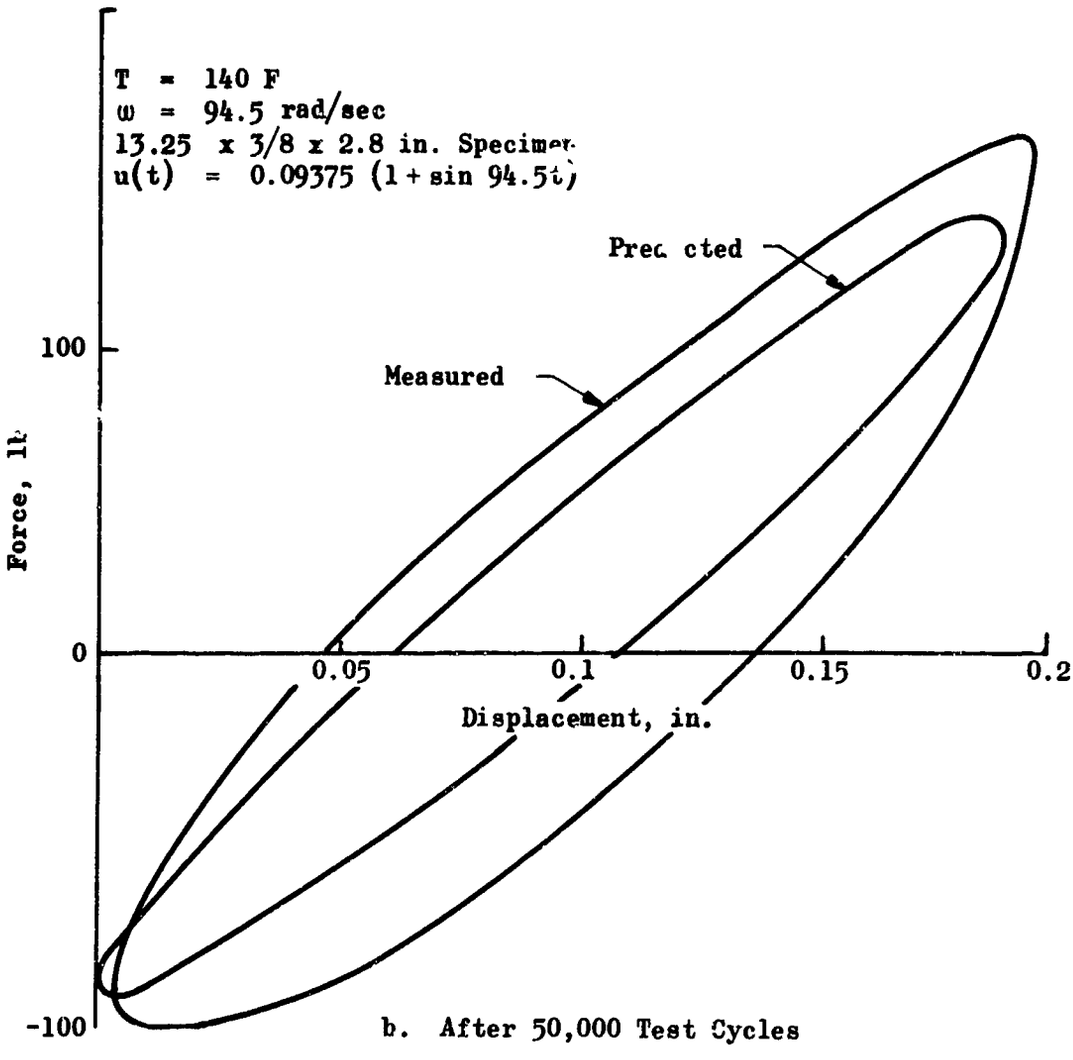

b. After 50,000 Test Cycles

Figure 88. Concluded

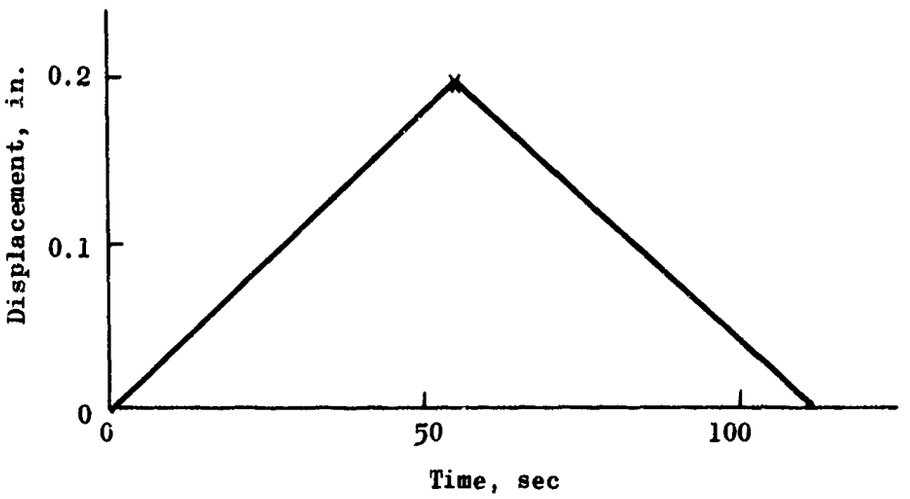

a. Imposed Displacement History

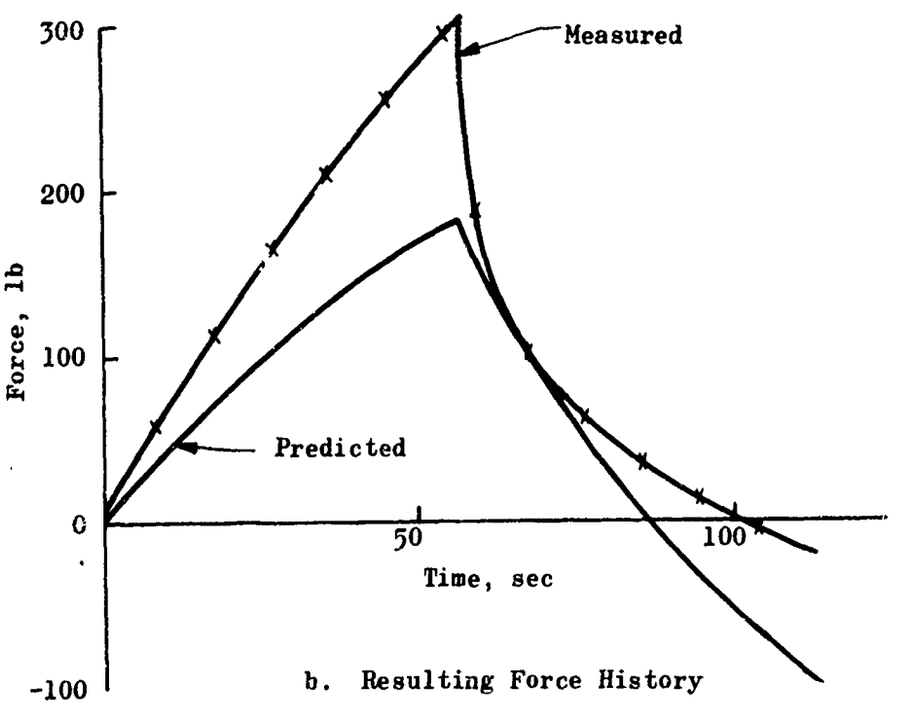

b. Resulting Force History

Figure 89. Comparisons of the Biaxial Force-Time Curves, Measured and Predicted, Resulting from the Sawtooth Displacement-Time History

The predictions were made using equations of linear viscoelasticity and the superposition principle beginning with the convolution integral

$$\sigma = \int_0^t E_{rel}\,(t - \tau)\,\frac{d\epsilon}{dt}\,d\tau \qquad (171)$$

which, when evaluated for a constant strain rate history becomes

$$\sigma = (Rt)\,\frac{1}{t}\int_0^t E_{rel}\,(\xi)\,d\xi \qquad (172)$$

which when $Rt = \epsilon(t)$ is substituted becomes

$$\sigma(t) = \epsilon(t)\,\frac{1}{t}\int_0^t E_{rel}\,(\xi)\,d\xi \qquad (173)$$

The predicted forces are compared to those experimentally determined in Fig 90 for strains of less than 8%. It will be noted that the variations (especially at the lower rates) are small. So it is concluded that a significant portion of the errors discussed in this report are due to the state-of-stress rather than the kind of loading history.

BIAXIAL VS UNIAXIAL RELAXATION MODULUS

As a consequence of the comparisons outlined in the preceding paragraphs a biaxial relaxation characterization was requested of LPC. In response they furnished the results of a series of biaxial relaxation tests with the specimens subjected to an average strain of 2.5%. Three points over two decades of time at each of seven temperatures were reported. The raw plots are shown in Fig. 91.

To compare the relaxation modulus indicated by these tests with that predicted using the previously reported uniaxial tests, the series of curves of Fig. 91 were shifted using factors corresponding to the curve of Fig. 86. The results are indicated in Fig. 92 as is the comparison with the uniaxial prediction. While at first glance the prediction looks good, a closer inspection shows that for some temperatures discrepancies as large as 30% are present. Also it is evident that except for the hottest temperature the stiffness prediction based on uniaxial tests are lower (more compliant) than are observed in the actual biaxial tests. This result implies, of course, that uniaxial data give unconservative predictions of biaxial stresses.

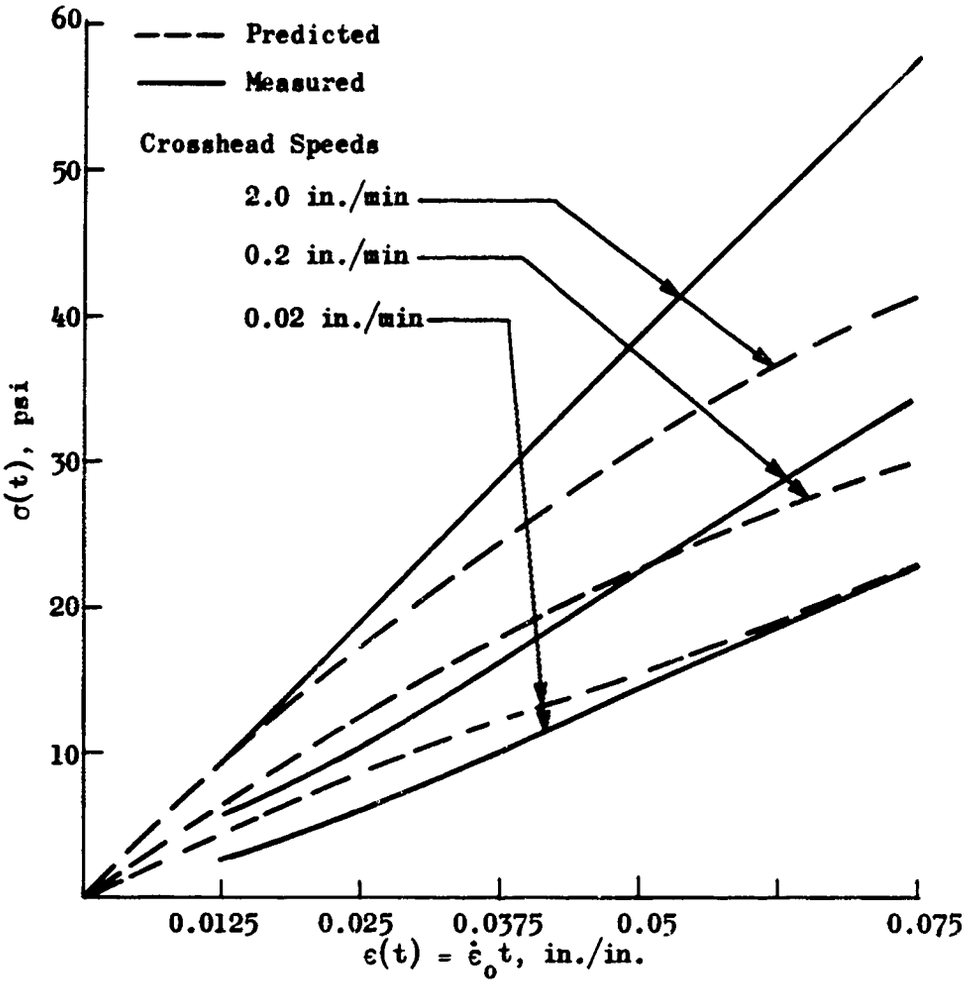

Figure 90. Comparisons of the Stresses, Predicted and Measured, Resulting from Uniaxial Constant Strain Rate Tests-- (Predictions Based on Uniaxial Relaxation Data)

CONCLUSIONS

Analytical predictions of the stress levels in realistic stress fields based on material properties deduced from tests of uniaxial specimens give erroneous results. For simple biaxial strip vibration and tensile tests the predicted force response was less than two-thirds of that measured. The comparison of biaxial and uniaxial relaxation test results confirm this trend. Such inaccuracies in predicting the responses of carefully controlled and monitored laboratory tests make the prediction of real motor stress responses an apparent impossibility.

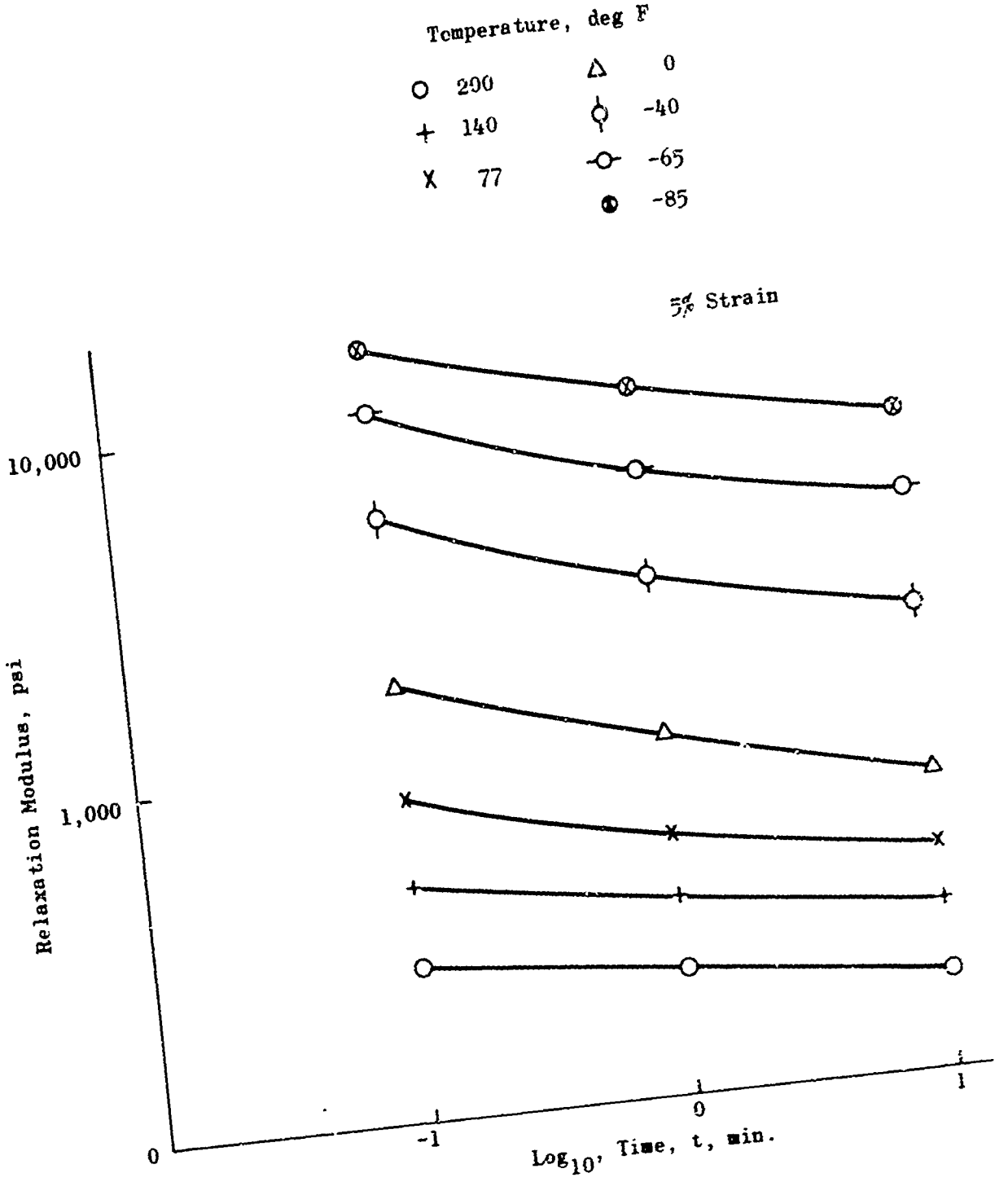

Figure 91. Raw Biaxial Relaxation Data as Furnished by LPC

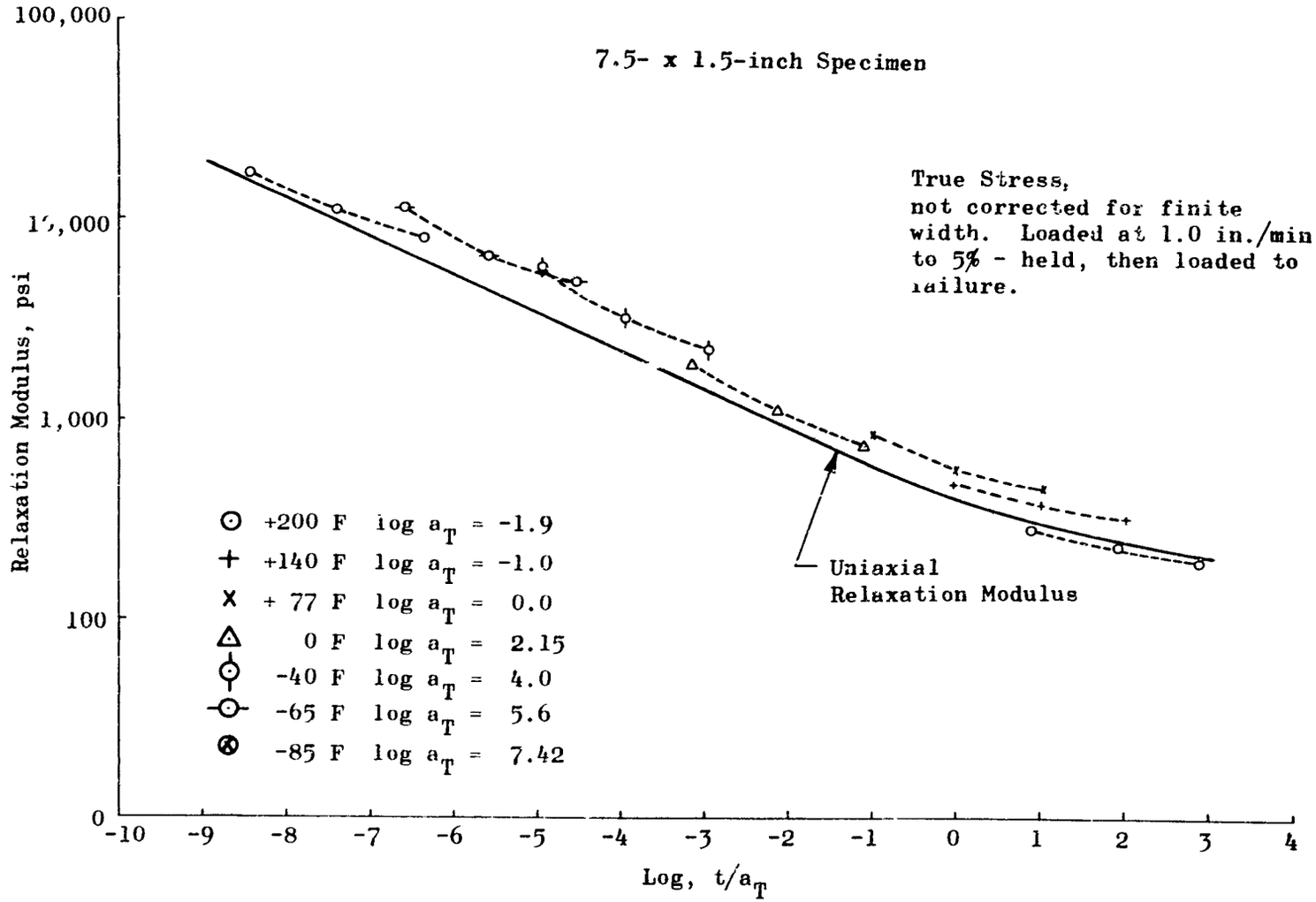

Figure 92. Comparison of the Biaxial Relaxation Data to the Relaxation Modulus as Determined from Uniaxial Tests (Biaxial Data has been Shifted According to the a_T's of Fig. 85)

This variability of the composite propellant properties with stress-state has previously been noted by others. Schapery has discussed the propellant nonlinearities resulting from the method of tests (37) and, as noted earlier, Harbert has discussed the differences he has discovered between uniaxial and triaxial moduli. But the magnitude and importance of this effect may have been minimized to facilitate arriving at early answers.

REFERENCES

Page 232 is blank

REFERENCES

1. Williams, M. L.: "The Fracture of Viscoelastic Material," Fracture of Solids, Interscience Publishers, New York, 1963.

2. Williams, M. L.: "Initiation and Growth of Viscoelastic Fracture," International Journal of Fracture Mechanics, Vol. 1, No. 4, 1965.

3. Williams, M. L.: "Fatigue Fracture Growth in Linearly Viscoelastic Material," Journal of Applied Physics, Vol. 38, No. 11, Oct 1967.

4. Griffith, A. A.: "The Theory of Rupture," Proceedings of First International Congress of Applied Mechanics, Delft, 1924, pp 55-63.

5. Inglis, C. E.: "Stresses in a Plate Due to the Presence of Cracks and Sharp Corners," Transactions, Inst. Naval Architects, Vol. 60, 1913.

6. Sokolnikoff, I. S.: Mathematical Theory of Elasticity, 2nd Edition, McGraw-Hill Book Co., 1956.

7. Berry, J. P., et al: Fracture Processes in Polymeric Solids: Phenomena and Theory, Bernard Rosen, Editor, Interscience Publishers, New York, 1964.

8. Rivlin, R. S. and A. G. Thomas: "Rupture of Rubber, I. Characteristic Energy for Tearing," Journal of Polymer Science, Vol. 10, 1952, p 291.

9. Irwin, G. R.: "Fracture Dynamics," Fracturing of Metals, American Society of Metals, Cleveland, 1948.

10. Orowan, E.: "Energy Criteria of Fracture," Welding Research Supplement, Vol. 20, 1955.

11. Greensmith, H. W. and A. G. Thomas: "Rupture of Rubber. Part III. Determining of Tear Properties, Journal of Polymer Science, Vol. 18, 1955, p 189.

12. Williams, M. L., P. J. Blatz, and R. A. Schapery: SM 61-5, Fundamental Studies Relating to Systems Analysis of Solid Propellants, Final Report, California Institute of Technology, February 1961.

13. Lee, E. H.: Technical Report No. 8, NORD11496, Stress Analysis in Viscoelastic Bodies, Brown University, 1954.

14. Biot, M. A.: "Dynamics of Viscoelastic Anisotropic Media," Proceedings of the Fourth Midwestern Conference on Solid Mechanics, September 1955.

15. Biot, M. A.: "Theory of Stress-Strain Relations in Anisotropic Viscoelastic and Relaxation Phenomena," Journal of Applied Physics, Vol. 25, 1954, p 1385.

16. Schapery, R. A.: "Approximate Methods of Transform Inversion for Viscoelastic Stress Analysis," Proceedings of the Fourth U.S. National Congress on Applied Mechanics, 2, 1075, 1962.

17. Ferry, J. D.: Viscoelastic Properties of Polymers, John Wiley and Sons, New York, 1961.

18. Tobolsky, A. V.: "Stress Relaxation Studies of the Viscoelastic Properties of Polymers," Journal of Applied Physics, Vol. 27, July 1956, p 673.

19. Williams, M. L., R. F. Landel, and J. D. Ferry: "The Temperature Dependence of Relaxation Mechanisms in Amorphous Polymers and Other Glass-Forming Liquids," Journal of the American Chemical Society, Vol. 77, 1955.

20. Burton, J. D. and J. S. Noel: "Viscoelastic Fracture in Plane Stress and Plane Strain Fields," Bulletin of the 6th Meeting, ICRPG Mechanical Behavior Working Group, 1967.

21. Jones, W. B., Jr., F. R. Wagner, and M. L. Williams: "Cumulative Damage in the Mechanics of Viscoelastic Fracture," ICRPG Bulletin, 6th Meeting of the Mechanical Behavior Working Group, CPIA No. 158, Vol. 1, December 1967.

22. AFRPL-TR-67-72: Determination of Optimum Length of End Release for Case-Bonded Solid Propellant Rocket Motors, Rocketdyne Final Report, March 1967.

23. Swanson, S. R.: "Crack Propagation in Double-Base Propellants Under Ignition Loading," Bulletin of the 7th Meeting, ICRPG Mechanical Behavior Working Group, Orlando, Florida, November 1968.

24. Williams, M. L., and R. A. Schapery: "Spherical Flaw Instability in Hydrostatic Tension," International Journal of Fracture Mechanics, Vol. 1, No. 1, 1965.

25. Blatz, P. J.: "An Elastodynamic Theory of Fracture," Polymer Science Report, North American Science Center, April 1967.

26. Lindsey, G. H., R. A. Schapery, M. L. Williams, and A. R. Zak: "The Triaxial Tension Failure of Viscoelastic Materials," Aerospace Laboratories Report, ARL 63-152, September 1963.

27. Messner, A. M.: "Stress Distribution in Poker Chip Tensile Specimens," Bulletin of the 2nd Meeting, ICRPG Mechanical Behavior Working Group, CPIA Publication No. 27, 1963.

28. Williams, M. L., R. A. Schapery, A. R. Zak, and G. H. Lindsey: "The Triaxial Tension Failure of Viscoelastic Materials," SM-63-6, Interim Status Report (January--December 1962), California Institute of Technology, Pasadena, California, February 1963.

29. AFRPL-TR-68-130· Solid Propellant Structural Test Vehicle, Systems Analysis and Cumulative Damage Program, LPC Final Report on Contract F04(611)-67-C-0100.

30. Blatz, P. J.: Application of Finite Elastic Theory to the Behavior of Rubberlike Materials," Rubber Chemistry and Technology, 36, No. 5, December 1963.

31. Bateman Manuscript Project: Higher Transcendental Functions, Vol. 3, 1955, p 206.

32. Prony, R.: "Essai Experimentale et Analytique," J. Ecole Polytechnique, 1, Paris, (1795) pp 24--76.

33. Harbert, B. C.: "Triaxial Testing of Solid Propellants," 4th Bulletin of the ICRPG Mechanical Behavior Working Group, CPIA Publication No. 94 U, 1 October 1965.

34. Harbert, B. C. and S. C. Britton "Influence of Solids Particle Size on Propellant Mechanical Behavior in a Triaxial Stress Field," 5th Bulletin of the ICRPG Mechanical Behavior Working Group, CPIA Publication No. 119, 1 October 1966.

35. Leeming, H. et al: AFRPL-TR-68-130, STV, CD and Systems Analysis, Final Report, Lockheed Propulsion Company, October 1968.

36. Rocketdyne Report R-4282: MK 38 MOD 0 Solid Propellant Rocket Motor Product Improvement Program Summary Report, USN Contract NOw 63-0591d, 8 May 1964.

37. Schapery, R. A.: "Nonlinear Viscoelastic Characterization and Stress Analysis of Solid Propellants," Solid Rocket Structural Integrity Abstracts, October, 1966, Lead Article.

Page 236 is blank

Unclassified

Security Classification

DOCUMENT CONTROL DATA - R & D

(Security classification of title, body of abstract and indexing annotation must be entered when the overall report is classified)

1. ORIGINATING ACTIVITY *(Corporate author)* Rocketdyne, A Division of North American Rockwell Corp, McGregor, Texas	2a. REPORT SECURITY CLASSIFICATION Unclassified 2b. GROUP

3. REPORT TITLE

Fracture Mechanics Approach to Cumulative Damage

4. DESCRIPTIVE NOTES *(Type of report and inclusive dates)*

Final Report (15 May 1967--19 August 1968)

5. AUTHOR(S) *(First name, middle initial, last name)*

J. S. Noel, J. D. Burton, and B. C. Harbert

6. REPORT DATE	7a. TOTAL NO. OF PAGES	7b. NO. OF REFS
December 1968	235 + xi	37

8a. CONTRACT OR GRANT NO.	9a. ORIGINATOR'S REPORT NUMBER(S)
F04611-67-C-0103	R-4521
b. PROJECT NO.	
c.	9b. OTHER REPORT NO(S) *(Any other numbers that may be assigned this report)*
d.	

10. DISTRIBUTION STATEMENT

This document is subject to special export controls and each transmittal to foreign governments or foreign nationals may be made only with prior approval of AFRPL (RPPR/STINFO), Edwards, California 93523.

11. SUPPLEMENTARY NOTES	12 SPONSORING MILITARY ACTIVITY
	AFRPL

13. ABSTRACT

~~This~~ report documents a 12-month program conducted ~~by Rocketdyne~~ to study cumulative structural damage in solid rocket propellant. Tests conducted and experimental data obtained therefrom are described, and conclusions drawn from the study are presented. The theory of fracture in viscoelastic materials provides the analytical expressions for evaluating damage to propellant during loading histories comparable to those which might be experienced by rocket motor grains. Poker chip and biaxial strip tensile tests were used to simulate the states of stress typically occurring in actual motors. Simple constant rate tests were used to evaluate the constants necessary to apply the fracture equations to histories involving sequences of loadings.

DD FORM 1 NOV 65 1473

Unclassified

Security Classification

14. KEY WORDS	LINK A		LINK B		LINK C	
	ROLE	WT	ROLE	WT	ROLE	WT
Solid propellant, Cumulative damage, Crack-type failure predictions, Biaxial stress, Biaxial strain						